Evaluation of the contribution of the isotopic exchange mechanism to the retention of radioactive iodine

Hantao Lin

Thèse de doctorat de Sorbonne Université

Ecole doctorale de Chimie Physique et Chimie Analytique de Paris Centre 388

Évaluation de la contribution du mécanisme d'échange isotopique à l'épuration de l'iode radioactif

Par Hantao LIN

Thèse de doctorat de Chimie physique

Présentée et soutenue publiquement le 14 Avril 2022

Devant un jury composé de :

Mme Pascaline PRÉ	Professeure / IMT Atlantique	Rapporteur
Mme Cécile VALLIERES	Professeure / Univ. Lorraine	Rapporteur
M. Thierry LOISEAU	Directeur de recherche / Univ. Lille	Président
M. Denys GREKOV	Maitre de conférence / IMT Atlantique	Examinateur
M. Jean-Christophe SABROUX	Chercheur / Retraité	Examinateur
M. Mouheb CHEBBI	Chercheur / IRSN	Co-encadrant
Mme Céline MONSANGLANT-LOUVET	Chercheuse / IRSN	Co-encadrante
M. Denis DOIZI	Professeur / CEA	Directeur de thèse
M. Bruno AZAMBRE	Maitre de conférence - HDR / Univ. Lorraine	Invité

Résumé

La nécessité de limiter les rejets de substances radioactives dans l'environnement a toujours été un défi majeur dans le domaine de la radioprotection et de la sûreté des installations nucléaires que ce soit en exploitation normale, en situation d'incident ou en conditions d'accident grave. Une attention particulière est accordée aux espèces radioactives iodées (notamment I_2 et CH_3I) compte tenu de leurs grandes mobilités dans l'environnement et de leurs affinités spécifiques pour la thyroïde. En exploitation normale, la diminution attendue des autorisations de rejets implique des travaux de recherche et de développement en particulier sur les performances ou l'amélioration des procédés existants d'épuration.

Les dispositifs industriels actuels d'épuration de l'iode gazeux peuvent être classés en deux catégories : les procédés utilisant un piège liquide, dits filtres à barbotage et les procédés utilisant des adsorbants solides poreux. Ce dernier type est connu pour être plus prometteur que les filtres à barbotage, en raison de sa plus grande efficacité d'élimination (vis-à-vis des organo-iodés volatils en particulier) et de son faible coût de maintenance. Le choix de l'adsorbant dépend du type d'effluent à épurer, de son emplacement et du scénario envisagé. Les charbons actifs (CA) sont connus pour être largement utilisés dans les pièges à iode (PAI) implantés au sein des réseaux de ventilation des installations nucléaires. Ces PAI ont pour vocation de piéger les espèces iodées volatiles dans des conditions normales ou dégradées. Le choix d'un tel adsorbant découle de son réseau microporeux (d_{pore} < 2 nm) bien développé favorisant ainsi la capture du CH_3I par des phénomènes non spécifiques de type physisorption dans des conditions de température et d'effluents maitrisées (humidité relative (HR) < 40% et température ~ 20 °C). Par ailleurs, une dégradation drastique des performances de ces adsorbants est connue sous l'effet de l'humidité (notamment les HR dépassant 90%). Ceci est dû à des phénomènes d'adsorption compétitive entre la vapeur d'eau et l'iodure de méthyle. Une fonctionnalisation à façon est ainsi nécessaire pour garantir un piégeage efficace et sélectif vis-à-vis de l'iodure de méthyle dans des conditions plus humides. Les imprégnants les plus utilisés dans le domaine nucléaire sont la triéthylènediamine (TEDA, ≤ 5 w.t%) et l'iodure de potassium (KI, 1 w.t%). Différents mécanismes de rétention régissent l'interaction de ces imprégnants avec CH_3I.

D’une part, le piégeage de CH_3I par la TEDA est basé sur une réaction chimique (d’où le nom chimisorption), dont le mécanisme exact est dépendant des conditions opératoires. Ce mécanisme a été largement étudié ces dernières années en couplant des approches expérimentales (courbes de percée, isothermes d’adsorption) à des méthodes de calcul en chimie théorique (DFT par exemple). D’autre part, la réactivité de KI est basée sur une réaction appelée échange isotopique. Ce procédé consiste dans la redistribution de différents isotopes de l’iode (entre KI stable et CH_3I radioactif) sans modification chimique des espèces. Malgré la présence historique de KI dans les charbons actifs utilisés pour l’industrie nucléaire, l’apport de l’imprégnation au KI n’a pas été démontré d’une manière précise. La contribution ainsi que le mécanisme de cette réaction ont été rarement abordés. De plus, il n’existe pas d’études permettant de faire de lien direct entre les caractéristiques intrinsèques des CA et les performances de piégeage du CH_3I, tout en explicitant clairement la contribution des différents mécanismes potentiellement mis en jeu (physisorption, chimisorption, échange isotopique).

Dans ce contexte, cette thèse porte sur la quantification de la contribution de l’échange isotopique en se basant sur différentes méthodologies d’essai. Il s’agit d’un défi majeur pour l’industrie du nucléaire, où ces pièges à iode sont testés annuellement sur site avec de l’iode radioactif. La procédure de test mise en place induit parfois d’une manière paradoxale, les seules émissions en iode-131 à l’environnement de l’installation contrôlée. Ainsi, la substitution de ces méthodes anciennes de test par des méthodes non-radioactives constitue un enjeu fort pour la radioprotection et la sûreté nucléaire. La validité d’un tel test se repose néanmoins sur deux axes de recherche importants : (i) le premier concerne l’utilisation d’une méthode d’analyse chimique suffisamment sensible en comparaison de la spectrométrie γ, pour pouvoir envisager d’effectuer des tests de performances non destructifs des pièges à iode (c’est-à-dire très en deçà des capacités d’adsorption du charbon actif). Ce point sera abordé lors de prochaines études ayant pour vocation de qualifier les performances de capteurs innovants tels que la spectroscopie photo-acoustique (ii) le deuxième point concerne le cœur de ce sujet de thèse, qui a pour but de quantifier la contribution de l’échange isotopique dans l’adsorption de CH_3I dans certaines configurations (charbons actifs à façon, conditions opératoires données). Cette quantification doit permettre *in fine* de vérifier la validité d’un coefficient de transposition entre le coefficient d’épuration (CE) mesuré à l’iode radioactif et le CE mesuré à l’iode non radioactif.

Le manuscrit se découpe en plusieurs chapitres.

Dans le chapitre I, des informations globales sur la rétention des espèces iodées par les CA sont présentées. Une bibliographie la plus complète possible est faite notamment sur la caractérisation des CA, mais également sur leurs performances dans un contexte nucléaire. A cet égard, peu d'articles sur l'échange isotopique en phase gaz-solide ont été trouvés.

Dans le chapitre II, les charbons actifs étudiés, les moyens mis en œuvre pour leurs caractérisations, ainsi que les résultats obtenus sont présentés. Les adsorbants étudiés sont des charbons actifs synthétisés à façon à l'échelle industrielle à partir du même précurseur utilisé pour les charbons destinés à l'industrie nucléaire. Un large éventail de configurations d'imprégnation a été visé de manière à pouvoir étudier séparément les rôles joués par les imprégnants (KI et TEDA). Au total, 20 CA ont été considérés pour ce travail de thèse (charbon non imprégné, charbons imprégnés au KI, charbons imprégnés à la TEDA, charbons co-imprégnés au KI et à la TEDA).

Parmi les informations d'intérêt à sonder à travers les charbons étudiés, on peut citer en particulier la quantité et la spéciation de l'imprégnant, la composition chimique de surface, la structure poreuse et le comportement d'adsorption avec H_2O. Des collaborations ont dû être mises en place avec le Centre interdisciplinaire de Nanoscience de Marseille (CINaM) afin de caractériser un certain nombre d'adsorbants avec des techniques complémentaires notamment la spectroscopie photoélectronique aux rayons X (XPS).

Dans un premier temps, une méthodologie basée sur l'extraction des CA dans l'acétonitrile suivie par le dosage par spectroscopie UV-Visible, a été mise en place pour vérifier les teneurs en KI et TEDA indiquées par le fournisseur. Une relation quasi-linéaire a été observée en comparant les teneurs expérimentales et théoriques pour tous les CA testés. Néanmoins, une déviation de 23%, 15% et 27% par rapport à la quantité théorique a été trouvée pour les CA imprégnés à la TEDA, au KI et les CA co-imprégné, respectivement. Les écarts observés pour la TEDA sont expliqués par l'inaccessibilité de l'acétonitrile à toutes les molécules incorporées à l'intérieur de la microporosité des charbons testés. En effet, des analyses élémentaires (CHNS) effectués au Laboratoire de Génie des Procédés–Environnement–Agro-alimentaire (GEPEA), ont montré des quantités moyennes en TEDA en bon accord avec les données théoriques. Par la suite, les charbons ont été désignés avec leurs teneurs théoriques, compte tenu des résultats CHNS et de l'écart linéaire

aux donnés du fabriquant, mis en évidence dans les analyses basées sur l'extraction et le dosage par spectroscopie UV-Visible.

Des informations supplémentaires concernant la spéciation de l'imprégnant et la surface de l'échantillon de CA peuvent être déduites à partir de l'analyse XPS. D'une part, la nature carbonée (88 - 90 at.% en carbone) des CA testés a été confirmée par les analyses XPS, EDX et CHNS. De plus, la spéciation similaire entre tous les charbons étudiés pour le carbone (C1s, 285 eV) et l'oxygène (O1s, 530 eV) est conforme avec l'utilisation du même lot pour la production des différents CA étudiés. D'autre part, une spéciation similaire de l'azote et de l'iode a été mise en évidence entre les CA simplement ou co-imprégnés. Ceci indique l'absence d'interaction particulière entre les molécules de TEDA et de KI incorporées dans le réseau poreux des CA. D'autres analyses par DRX et MEB/EDX montrent l'absence d'agglomération des imprégnants (> 100 nm) sur la surface externe, indiquant que le KI et la TEDA sont bien dispersés dans la porosité interne des matériaux étudiés. La comparaison entre les données d'analyse par EDX et XPS a également fourni des renseignements sur la distribution élémentaire (C, O, N, I, K) entre la surface et le cœur de certains des CA testés.

La structure poreuse des CA étudiés a été déterminée par la porosimétrie de N_2 à 77 K. Les isothermes d'adsorption/désorption obtenues pour tous les CA considérés présentent une isotherme de type I caractéristique des matériaux microporeux. Des surfaces spécifiques élevées autour de 1000 $m^2 \cdot g^{-1}$, avec une contribution importante de la microporosité (V_{micro} / V_{pore} > 94%) peuvent également être soulignées en accord avec les charbons actifs issus de la noix de coco. Le diamètre moyen calculé des pores d'environ 0,5 nm rend les CA testés appropriés pour le piégeage du CH_3I (diamètre cinétique : 0,5 – 0,6 nm) par des phénomènes de physisorption. De plus, les propriétés texturales (S_{BET} et le V_{micro}) présentent une évolution générale décroissante avec le ratio molaire d'imprégnation totale à cause de la présence des molécules KI, TEDA à l'entrée et/ou au sein des micropores, comme souligné par les méthodes de caractérisations précédentes. Ce phénomène de blocage partiel de la microporosité devient plus significatif pour un taux d'imprégnation molaire total dépassant 0,4 % (environ 3 w.t% pour la TEDA et 5 w.t% pour le KI).

Dans le chapitre III, les performances des CA pour le piégeage du CH_3I marqué à l'iode 131 sont évaluées en utilisant la mesure des coefficients d'épuration (CE) normalisés sur un large panel de

configurations de matériaux (CA non imprégné, CA imprégné au KI et/ou à la TEDA). L'objectif est d'étudier l'effet des imprégnants séparément dans des conditions semi-pilotes, ce qui est rarement étudié dans la littérature avec des tests non-radioactifs ou avec des teneurs limitées en TEDA ou KI dans les mesures des CE. Pour la première fois, une corrélation entre les performances de rétention par les CA et leurs propriétés de départ (chapitre II) est établie afin de mieux comprendre les mécanismes mis en jeu, ainsi que le rôle des imprégnants KI ou TEDA, en fonction des conditions opératoires.

L'étude du comportement d'adsorption du CH_3I marqué à l'iode 131 à des HR de 40% et 90% (T d'environ 20 °C) a permis de révéler différents comportements. Dans le premier jeu de conditions (T = 20 °C, HR = 40 %), tous les CA testés présentent de bonnes performances de piégeage de CH_3I, avec un CE jusqu'à 2.2×10^5 en bon accord avec les performances requises pour les CA actuellement mis en œuvre dans l'industrie nucléaire française. L'évolution similaire du CE entre les CA simplement et co-imprégnés permet de confirmer l'absence d'interactions entre les imprégnants comme observé dans le chapitre de caractérisation. L'évolution du CE pour les CA imprégnés à la TEDA montre une augmentation jusqu'à 5 w.t% suivie d'une légère diminution. Cependant, une évolution décroissante du CE avec l'imprégnation de KI est observée. Dans ces conditions, le mécanisme de piégeage dominant (physisorption) s'avère être décroissant pour l'imprégnation à la TEDA et KI mais pour des raisons différentes. En raison de la teneur en TEDA bien dispersée qui contribue à la chimisorption, l'évolution du CE pour la TEDA dans ce premier jeu de conditions, s'avère être un compromis entre la diminution de la microporosité disponible et l'augmentation de la chimisorption *via* la TEDA, avec une imprégnation optimale de la TEDA à 5 w.t%. En revanche, l'échange isotopique par le KI est absent en considérant cette première méthodologie d'essai. La performance du CA imprégné au KI étant dominée par la physisorption elle-même déterminée par l'eau pré-adsorbée. En effet, une relation quasi-linéaire a pu être mise en évidence pour la première fois entre l'efficacité de piégeage (exprimée en utilisant $\eta(\%)$) et le volume des micropores disponibles après l'étape d'équilibration effectuée au préalable sous humidité. Ce volume des micropores, qui serait disponible pour le piégeage de CH_3I a été déduit en combinant le volume microporeux calculé à partir de la porosimétrie de N_2 d'une part, et la prise en masse de la vapeur d'eau déterminée expérimentalement à partir des isothermes d'adsorption de H_2O (T = 25 °C, HR = 30 %).

Dans le second jeu de conditions (T = 20 °C, HR = 90 %), une diminution drastique du CE est observée pour tous les CA, avec des CE environ inférieurs d'un facteur 1000 par rapport aux CE mesurés dans le premier jeu de conditions (HR = 40 %). L'imprégnation optimale à HR = 90% est obtenue avec 1 w.t% au KI et 5 w.t% à la TEDA, en accord avec la composition des CA de qualité nucléaire. L'augmentation du CE avec la TEDA et le KI dans les conditions humides est directement liée à la chimisorption et à l'échange isotopique, respectivement. L'importance de la chimisorption et de l'échange isotopique correspondants est mise en évidence par la diminution significative de la microporosité disponible (fraction de pore remplie d'eau dépassant 90% selon les isothermes d'adsorption de H_2O), indiquant que la physisorption comme étape préliminaire des phénomènes d'adsorption n'est plus dominante dans les conditions actuelles. Les différentes évolutions du CE pour les CA imprégnés au KI à HR = 40% (absence de l'échange isotopique) et 90% (présence de l'échange isotopique avec une mauvaise performance) mettent en évidence l'importance des différentes phases pendant le test d'adsorption. Une hypothèse est donc proposée selon laquelle l'échange isotopique n'est observé que pendant la phase de percée, conformément à une ancienne étude de G. O. Wood.

Dans le chapitre IV, un nouveau dispositif expérimental ainsi qu'une méthodologie d'essai spécifique sont développés pour la comparaison des courbes de percée entre CH_3I stable et CH_3I radioactif. L'étude comparative qui est réalisée sur différentes teneurs en KI, permet de présenter un premier élément important concernant la quantification de ce mécanisme, et ceci au cours de l'adsorption.

L'objectif principal est d'élucider l'importance de la réaction d'échange isotopique en mesurant les courbes de percée du $CH_3{}^{127}I$ et du $CH_3{}^{131}I$ pour les CA imprégnés au KI. Les conditions opératoires sont aussi similaires que possible sur les 2 bancs d'essais utilisés de façon à pouvoir comparer les différents résultats. D'une part, les mesures de l'adsorption dynamique de CH_3I stable ont été réalisées sur un banc existant avec la mesure en ligne par la chromatographie en phase gazeuse couplée à un détecteur de type PD-ECD. D'autre part, un nouveau dispositif expérimental est développé pour les mesures des courbes de percée de CH_3I radioactif.

En ce qui concerne les mesures des courbes de percée du CH_3I stable (T = 30 °C, HR = 0 %, $[CH_3I]_0$ = 10 ppmv, temps de séjour = 0.2 s), des performances similaires ont été observées pour

les CA imprégnés au KI en général. Cette tendance est en accord avec leur microporosité similaire et l'occurrence uniquement des phénomènes de type physisorption pour les CA étudiés (non-imprégné + CA imprégnés au KI). Une amélioration significative peut être observée après l'imprégnation à la TEDA, en termes de durée de la phase de rétention et de stabilité de piégeage, avec une durée totale d'environ 12 h contre 5 h pour les CA imprégnés au KI. Ceci confirme l'occurrence simultanée des réactions de chimisorption (mécanisme d'alkylation de type S_N2).

Concernant les courbes de percée du CH_3I radioactif (T = 20 °C, HR = 0 %, $[CH_3I]_0$ = 10 ppmv, débit de génération de l'iode 131 = 150 $Bq \cdot min^{-1}$, temps de séjour = 0.2 s), une zone de rétention similaire est observée dans un premier temps pour les CA imprégnés au KI. A cet égard, les comportements des CA imprégnés au KI et à la TEDA (profil d'adsorption similaire entre CH_3I stable et radioactif) pendant la phase de rétention se sont avérés cohérents avec les mesures précédentes de CE à HR = 40 %. En effet, la phase de rétention similaire pour les CA imprégnés de KI envers le piégeage du CH_3I radioactif confirme l'absence d'échange isotopique dans des conditions modérément humides. En revanche, une amélioration significative de la rétention de CH_3I est observée en raison de la réactivité de la TEDA interagissant *via* un mécanisme d'alkylation dans ces conditions. Deuxièmement, une amélioration significative des performances des CA concernant le piégeage du CH_3I radioactif pendant la phase de percée est observée après l'imprégnation progressive de KI, ce qui est clairement dû à l'échange isotopique. En général, les améliorations de rétention observées dues à l'apparition d'un échange isotopique après la percée du CA sont en accord avec les mesures de CE à HR = 90 % indiquant des coefficients de perméations élevés. Par conséquent, l'hypothèse proposée peut finalement être confirmée.

La contribution de l'échange isotopique est ensuite évaluée dans un premier temps à travers les comparaisons de la capacité d'adsorption à saturation ainsi que les constantes de vitesse déduites du modèle de Thomas pour les deux configurations. Plus particulièrement, une augmentation significative de la capacité d'adsorption à saturation vis-à-vis du $CH_3{}^{131}I$ après imprégnation au KI peut être mise en évidence. Par exemple, une contribution d'environ 70% due à l'échange isotopique peut être calculée pour un CA imprégné à 5 w.t% en KI, contre 30% pour les phénomènes de type physisorption. Cependant, l'utilisation actuelle des PAI dans les réseaux de ventilation se concentre principalement sur des performances très éloignées de la saturation (principalement 1% de percée). Des comparaisons supplémentaires des capacités d'adsorption à

différentes percées montrent que la contribution de l'échange isotopique augmente progressivement après une percée de 5%. Une contribution d'environ 19% pour le CA imprégné à 5 w.t% en KI est estimé pour 1% percée de $CH_3{}^{131}I$ par exemple.

Pour conclure, les performances des charbons actifs avec différentes combinaisons d'imprégnation pour le piégeage du CH_3I (stable et radioactif) ont été finement étudiée à la fois en laboratoire et à l'échelle semi-pilote. Le KI et la TEDA présentent non seulement des mécanismes de piégeage différents pour le CH_3I, mais conduisent également à des comportements différents dans les courbes de percée. L'effet de la TEDA se traduit principalement par l'augmentation de la durée de la phase de rétention accompagnée d'une amélioration de la stabilité du piégeage. Alors que l'effet du KI contribue plutôt à une phase de percée plus importante, indiquant un retardement de la percée de l'iode 131 sous l'effet de la redistribution progressive des isotopes entre CH_3I radioactif en phase gazeuse et KI stable en phase adsorbée. Les résultats présentés dans ce sujet de thèse constituent une première évaluation directe de l'effet de l'échange isotopique, pour lequel une étude dans le futur est encore nécessaire. Par ailleurs, des améliorations techniques du montage expérimental devraient être effectuées afin de mesurer des courbes de percée sous un plus grand panel de conditions opératoires (spécialement pour les HR) pour vérifier cet effet spécifique de l'échange isotopique pendant la phase de percée. La comparaison des courbes de percée de CH_3I radioactif obtenues pour les CA co-imprégnés sera nécessaire pour assurer l'extrapolation aux charbons actifs de qualité nucléaire.

Acknowledgements

The following manuscript represents three years and a half of work that I was able to complete thanks to the help of many people. I don't know how to express my heartfelt thanks to everyone in a few sentences, but I owe a thankful heart to everyone who supported me during my difficult times.

This thesis was carried out at IRSN in the *Laboratoire d'Expérimentations sur le Comportement des Equipements et de la Ventilation (LECEV)*, within the *Service du Confinement et de l'Aérodispersion des polluants (SCA)* in Saclay. I must thank our head of department Laurant Bouilloux for giving me the opportunity to share my PhD experience in this friendly and sympathetic department.

I would like to express my sincere gratitude to my PhD director Denis Doizi. Thank you for your positive attitude and enthusiasm throughout each discussion, as well as your assistance during my PhD.

I would like to thank Pascaline Pré and Cécile Vallières for accepting to review my PhD thesis and the constructive exchanges during the defense. I am also very grateful to Jean-Christophe Sabroux for your valuable remarks in the manuscript to improve the thesis quality. I would like to sincerely thank Bruno Azambre, for reviewing this manuscript but also for the helpful discussion during the difficult moment of my PhD. Special thanks to Denys Grekov for the valuable exchanges as well as the experimental characterization. I am also thankful to Thierry Loiseau for accepting to be the president of the jury.

Certainly, I give my endless appreciation to the PERSÉE team of LECEV:

First of all, a huge thank you to my supervisor Céline Monsanglant-Louvet, for all the guidance, constant supervision, and moral support in completing this PhD. It was a great pleasure to do my research under your direction.

Next, I'd want to express my gratitude to you, Mouheb Chebbi, for believing in me and allowing me to develop as a researcher during the previous two years. It's been a genuine joy to share my

scientific enthusiasm with you. Apart from providing scientific advice, you would never pass up any opportunity to raise my spirits or assist me. Thank you for your unwavering patience, great sense of humor and endless support. I can't express how grateful I am to you in words.

I also want to express my gratitude to Benoit Marcillaud and Audrey Roynette. Every day of my PhD has been a pleasure, thanks in large part to the pleasant working environment you all have created in PERSÉE. Thank you for always being willing to assist me throughout these years.

Of course, I would never forget the happy moments during my PhD with all my colleagues in SCA:

The first person on the list is reserved to Lina Giannakandropoulou, the Rudolph singer, co-bureau de la pièce 17. Thank you, my friend, for bringing so much fun and dynamics in our office. I will not forget your warm words during the challenging time of my PhD. Hope that a “diamond” life is ahead of you.

A special dedication to the lovely PhD students of SCA: thank you Gwenichou, Amel and Samuel (ex-PhD students), for the unforgettable moments that we shared together. You made an excellent example of PhD student for me to follow. Modou and Karim, the new generation of PhD students of bât 389, the conversations with you guys whether they were work-related or not, have been a real pleasure. I would also like to thank Zeinab, Marie, Jonathan, Alexis, Benjamin et Delphine in other buildings of SCA, for the happy moments we spent together.

This thesis would not turn into reality without the help of my colleagues: Stéphane, Cécile, Laure, Sylvain, Carina, Pauline, Pascal, Soleiman… Because the list is so long, I'd like to express my gratitude to all of the SCA.

Special thanks to Eason Chan and Wu Bai & China Blue, for their company during the manuscript writing.

My gratitude also goes to my family, who have been a constant source of encouragement. Your support, advice, and constant presence have been crucial in the success of this thesis, and I am grateful for that.

Table of contents

List of Figures

List of Tables

Glossary

Latin letters

a	Coefficient associated with the macropore properties	[-]
$A(CH_3I)$	Activity of the γ-labelled CH_3I	[Bq]
$A_{downstream}$	Downstream activity (Bq)	[Bq]
$A_{upstream}$	Upstream activity (Bq)	[Bq]
A_λ	Absorbance of the medium at wavelength λ	[-]
b	Langmuir constant	[$m^3 \cdot mol^{-1}$]
C	Gas concentration	[$mol \cdot m^{-3}$]
C_{BET}	BET constant according to the relation: $C_{BET} = exp((E_1-E_{liq})/RT)$	[-]
C_{inlet}	Inlet concentration	[$mol \cdot m^{-3}$]
C_{outlet}	Outlet concentration	[$mol \cdot m^{-3}$]
c_λ	Concentration of molecules that absorb at wavelength λ	[$mg \cdot L^{-1}$]
D	Volume flowrate	[$L \cdot min^{-1}$]
d_{micro}	Micropore diameter	[nm]
D_p	Certificate flowrate of the permeation tube depending on the temperature of the permeation oven	[$\mu g \cdot min^{-1}$]
E_1	Molar energy of adsorption of the first layer	[$kJ \cdot mol^{-1}$]
E_{liq}	Molar energy of liquefaction of the adsorbate	[$kJ \cdot mol^{-1}$]
Ep	Activation energy of permeation	[$kJ \cdot mol^{-1}$]
G_{IDF}	Isotopic dilution factor between the ^{131}I and ^{127}I in the permeate CH_3I flow	[-]
$I(E)$	Emission abundance of the radionuclide at the given energy	[%]
K	Performance index	[s^{-1}]
K_{BA}	Adams-Bohart rate constant	[$L \cdot mg^{-1} \cdot min^{-1}$]
K_F	Freundlich constant	[-]
k_r	Coefficient dependent on the mean diameter of the micropores	[-]
K_{Th}	Thomas rate constant	[$L \cdot mg^{-1} \cdot min^{-1}$]
K_{YN}	Yoon-Nelson rate constant	[min^{-1}]
L	Bed depth	[cm]
l	Optical path of the cell	[cm]
L_p	Length of the permeation tube	[cm]

L_T	Length of mass transfer zone	[cm]
m	Mass of the adsorbent	[g]
m'	Characteristic constant of the interactions between the adsorbate and the adsorbent for Freundlich isotherms	[-]
$M(CH_3I)$	Molar mass of CH_3I	[mg·mol^{-1}]
n	Adsorption amount	[mol·m^{-3}]
$N(E)$	Net counting surface of the peak at the given energy;	[-]
N_0	Saturation concentration	[mg·L^{-1}]
n^a	Amount of adsorbed substance per gram of adsorbent	[mol·g^{-1}]
N_A	Avogadro constant	[-]
$n^a{}_m$	Amount of adsorbable substance necessary to cover the surface of the solid with a monomolecular layer	[mol·g^{-1}]
n_m	Maximum adsorption amount in monolayer	[mol·m^{-3}]
P	Penetration	[%]
p	Partial saturation pressure of the adsorptive gas in equilibrium	[Pa]
P'	Constant of permeation coefficient	[cm^2·s^{-1}·pa^{-1}]
p_0	Gas saturation pressure	[Pa]
P_0’	Permeation coefficient	[cm^2·s^{-1}·pa^{-1}]
p_e	External partial pressure of permeation tube (pa);	[Pa]
p_i	Internal partial pressure of permeation tube (pa);	[Pa]
$Q_{5\%}$	Adsorption capacity at 5% breakthrough	[mg·g^{-1}]
Q_p	Permeate flowrate	[cm^3·s^{-1}]
Q_{sat}	Adsorption capacity at saturation	[mg·g^{-1}]
Q_{Th}	Adsorption capacity from the Thomas model	[mg·g^{-1}]
R	Gas constant	[J·K^{-1}·mol^{-1}]
r_e	External permeation tube radius	[cm]
r_i	Internal permeation tube radius	[cm]
R_{IDF}	Isotopic dilution factor between the adsorbed $CH_3{}^{127}I$ and $CH_3{}^{131}I$	[-]
r_m	Distance of separation between two molecules	[nm]
s	Specific surface area calculated from the iodine number	[m^2·g^{-1}]
S_{BET}	Specific surface area	[m^2·g^{-1}]
T	Temperature	[K]
t	Measurement time	[s]
$t_{5\%}$	Time at $C_{outlet} = 5\% \times C_{inlet}$	[s]
$t_{95\%}$	Time at $C_{outlet} = 95\% \times C_{inlet}$	[s]
U_0	Linear velocity	[m·min^{-1}]

$V(CH_3I)$	Volume of the γ-labelled CH_3I	[mL]
V_{LJ}	Lennard-Jones potential between two molecules	[kJ·mol^{-1}]
V_m	Molar volume of the liquid adsorbate	[cm^3·mol^{-1}]
$V_m(CH_3I)$	Molar volume of CH_3I	[L·mol^{-1}]
V_{micro}	Microporous volume	[cm^3·g^{-1}]
V_{pore}	Total pore volume	[cm^3·g^{-1}]
w	Pore width	[nm]

Greek letters

η	Retention efficiency	[%]
ε	Depth of the potential well	[kJ·mol^{-1}]
ε_λ	Specific coefficient of molar absorbance	[L·mg^{-1}·cm^{-1}]
$\eta(E)$	Detection efficiency at the given energy E	[-]
ρ	Density of the CH_3I in liquid phase	[g·cm^{-3}]
σ	Finite distance at which the potential is zero	[nm]
σ_m	Area occupied by a N_2 molecule adsorbed on the surface of the solid covered with a monomolecular layer	[m^2]

Abbreviation

AC	Activated carbon
ANR	Agence nationale de la recherche
BTC	Breakthrough curve
CE	Coefficient d'épuration
CVD	Chemical vapor deposition
DECA PF	Diagnostic de l'état d'un cœur accidenté par la mesure des produits de fission dans l'enceinte
DF	Decontamination factor
DFT	Density functional theory
DL	Detection limit
DVS	Dynamic vapor sorption
ECD	Electronic capture detector
FAU	Faujasite structural type of zeolites
FCVS	Filtered containment venting systems

FEP	Fluorinated ethylene propylene copolymer
FTIR	Fourier-transform infrared spectroscopy
GC	Gas-chromatography
HEPA	High-efficiency particulate air filter
IUPAC	International Union of Pure and Applied Chemistry
MIRE	Mitigation of Releases to the Environment in the event of a nuclear accident
MTZ	Mass transfer zone
PASSAM	Passive and active systems on severe accident source term mitigation
PDECD	Pulsed discharge electron capture detector
PTFE	Polytetrafluoroethylene
PWR	Pressurized water reactor
py-GCMS	Pyrolysis gas chromatography mass spectrometry
RH	Relative humidity
SBA-15	Santa Barbara Amorphous-15 mesoporous silica
TGA	Thermogravimetric analysis
TPD	Temperature-programmed desorption

General introduction

The extensively developed nuclear industry in France has raised debates due to the possible occurrence of severe nuclear accidents. Regardless of the nuclear accident level, or even in normal operating conditions, the trapping of radioactive species constitutes a capital safety issue but also a societal challenge for the nuclear energy acceptability. Among the fission products potentially emitted, a special attention should be paid to iodine because of its high radiological impact towards the thyroid gland as well as its high volatility (mainly I_2 and CH_3I) [1][2]. In that respect, activated carbon (AC) is largely used within the nuclear ventilation networks [3], more particularly in the French nuclear facilities, to capture these volatile iodine species. The *nuclear grade* AC industrially implemented in the iodine trap is characterized by high removal efficiency under normal conditions, simple design and low maintenance costs. These good performances are assigned to their well-developed microporosity [4] (d_{pore} < 2 nm) promoting therefore the capture of CH_3I by physisorption phenomena. However, the AC performances for CH_3I trapping are known to be drastically reduced under humid conditions due to the competitive adsorption between water vapor and CH_3I [5]. The AC affinity towards CH_3I must be enhanced by impregnation with organic or inorganic compounds. The most employed impregnants in the nuclear field [6] are triethylenediamine (TEDA, ≤ 5 w.t%) and potassium iodide (KI, 1 w.t%) interacting with CH_3I through different retention mechanisms [7][8][9][10].

In the nuclear facilities, an annual test of the iodine traps is performed to verify their efficiency towards volatile iodine species. These annual tests are carried out by an *in-situ* measurement on the iodine trap installed within the ventilation network by means of a radioactive iodine measurement. The test procedure induces paradoxically the major release of radioactive iodine to the environment by the controlled nuclear facilities [11]. Therefore, the replacement of this traditional testing procedure by a novel non-radioactive method is a critical issue in the field of radioprotection and nuclear safety. However, the validity of such a non-radioactive method relies on two important research developments:

(i) the first one is related to the use of a sufficiently sensitive analytical method in comparison with γ-spectrometry, to perform non-destructive performance tests for iodine traps (*i.e.*,

well below the adsorption capacities of AC). These researches will be addressed in future studies to quantify the performance of innovative and promising sensors such as photo-acoustic spectroscopy according to the previous works conducted within the frame of DECA PF project [12];

(ii) the second one concerns the quantification of isotopic exchange reaction yield for the total trapping of iodine species. At the beginning of this thesis, an ambitious objective was to characterize and then quantify the isotopic exchange mechanism under different conditions. The initial aim was to determine a transposition coefficient between the measured AC performances from radioactive to non-radioactive test methodologies. Due to the scale of the experimental devices to be designed and implemented as well as the COVID 19 outbreak, efforts were rather oriented to the identification of this mechanism through complementary test methodologies. An attempt was achieved afterwards to give an initial quantification of the contribution of this mechanism for a given experimental configuration.

Based on this context, the first part of this PhD project is devoted to better assess the role played by KI and TEDA molecules towards the capture of CH_3I under semi-pilot configuration. The main objective is to establish correlations between the adsorbents parameters and retention properties depending on the water vapor content. First insights about the different trapping mechanisms involved will be therefore presented.

The second objective is to quantify the contribution due to isotopic exchange mechanism for KI AC through the comparison between stable and radioactive CH_3I dynamic adsorption experiments. In that respect, a new experimental setup as well as a specific test methodology were developed.

The manuscript is organized as follows:

Chapter I is devoted to the bibliographical study. The first part is dedicated to the description of the context as well as the trapping technologies used for the iodine species. The second part will present some adsorption generalities. The third part will present a state of the art on CH_3I trapping performances by different porous adsorbents. A particular attention will be paid to the AC behavior, by reporting on the influencing parameters as well as the involved retention mechanisms. Finally, considering the gaps in the literature, a conclusion will be presented to justify the investigations performed during this PhD thesis.

Chapter II is dedicated to the characterization of the tested AC using a combination of physico-chemical analyses. Firstly, experimental protocols about the employed techniques are presented. Then, information about impregnant amount is given as deduced from an extraction procedure followed by UV-Visible spectroscopic analysis. Complementary insights about the surface composition as well as the morphology of some of the tested adsorbents are deduced from XPS and SEM/EDX characterizations. Finally, the porous structure of the different impregnated AC is discussed from N_2 porosimetry at 77 K and H_2O adsorption isotherms at 298 K.

Chapter III presents the performances of AC towards the capture of γ-labelled CH_3I at the semi-pilot scale. Firstly, the experimental setup and the test protocol are presented in detail. Then, attention is focused on the AC performances at different operating conditions (RH = 40 and 90 % at T = 20 °C). Attempts are made to establish a structure – activity correlation between the physico-chemical characteristics of AC and the decontamination factor (DF) under the studied conditions. Finally, a discussion about the involved retention mechanisms, namely the isotopic exchange reaction is presented based on the obtained results.

Chapter IV is dedicated to compare the breakthrough curves (BTC) for both stable and γ-labelled CH_3I using KI impregnated AC. Firstly, experimental procedures for the BTC determination are reported. A particular attention is devoted to describe the newly designed experimental setup as well as the developed methodology for γ-labelled CH_3I BTC measurements. The obtained BTC under similar conditions are finally compared for stable and radioactive CH_3I. Finally, a first quantification related to the isotopic exchange occurrence is presented under a specific experimental configuration.

Chapter I: State of the art on iodine species removal by impregnated AC

1. Context

1.1 General information on nuclear industry in France

Energy production was a crucial political choice for countries like France after WWII for the development and the energy independence of these countries. Since 1971, 58 reactors have been built in France, with 1 still under construction [13]. In 2019, about 71% of the total produced electricity in France is of nuclear origin (379.5 TWh) [13]. In addition, France has established an entire related industry, ranging from uranium mining, fuel manufacturing and enrichment to reprocessing and waste disposal (Figure 1) [14].

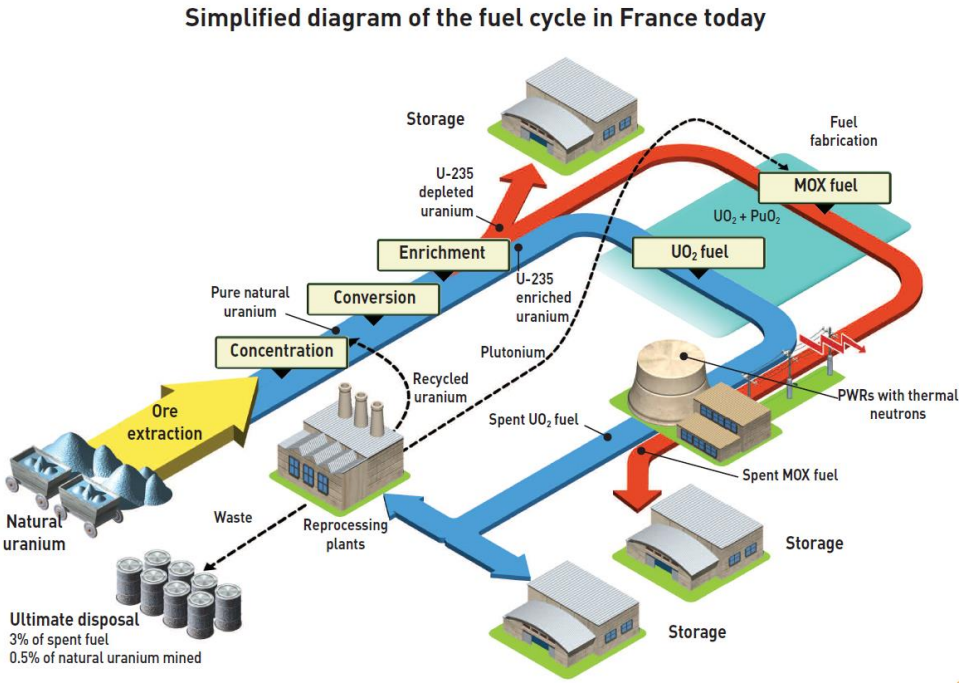

Figure 1. Simplified diagram of the nuclear fuel cycle in France [14]

Meanwhile, there is currently a huge debate about the use of this energy source with the same rate and importance. This debate is partly due to the possible occurrence of major nuclear accidents

characterized by low probabilities and severe consequences. More particularly, Chernobyl (1986) [15] and Fukushima (2011) [16] disasters have resulted in dramatic consequences in terms of radioactive releases into the environment and population contamination. In that respect, the efficient capture of radioactive species potentially released from nuclear facilities in all scenarios (from normal operating conditions to severe accident situations) remains a major issue to improve nuclear safety and nuclear energy acceptability.

1.2 Exhaust from nuclear facilities

Among the most hazardous radionuclides, special attention should be paid to iodine isotopes presenting the largest part of released radioactivity in a nuclear accident: for instance, the total releases of radioactive iodine were about 408 PBq, including 197 PBq of ^{131}I and 168 PBq of ^{132}I during the Fukushima Daiichi accident [17]. Furthermore, the radioactive isotopes of iodine (especially ^{131}I and ^{133}I at the short term) display a high radiological impact owing to the special affinity of iodine element towards the thyroid gland. Finally, iodine element is characterized by a high mobility due to its ability to be present under volatile forms (mainly molecular iodine I_2 and methyl iodide CH_3I)[1][2]. CH_3I formation results from reactions between I_2 and organic materials existing in the nuclear buildings. This molecule is known to be the most penetrating form of volatile iodine species. Therefore, the present PhD project will be focused only on CH_3I removal efficiency.

In addition to the release of these species from nuclear power plants, other anthropogenic origins can also be involved [18]:

Release from spent nuclear fuel reprocessing

The main attention during fuel reprocessing is devoted to ^{129}I isotope retention (half-life of 1.6×10^7 years) [19]. Taking "*La Hague reprocessing plant"* as an example, it can be stated that the ^{129}I activity discharged within the effluents was about 1.84×10^{12} Bq in 1999 (99% in the liquid effluents). The rejection of ^{131}I is at least 100 times lower than that of ^{129}I [18].

Medical release of radioactive iodine

The medical use of radioactive iodine includes mainly ^{123}I and ^{131}I: ^{123}I is used for radio diagnostics, while ^{131}I is used for the medical treatment of thyroid cancers [20]. It is reported that the medical

release of ^{131}I can be more than 60 kBq per day at New York [21]. Unlike the airborne emission of ^{131}I in nuclear facilities, the ^{131}I generated by medical treatment is collected at wastewater treatment plant through sewage transport [22].

Annual testing of iodine traps at nuclear facilities

In the nuclear facilities, an annual test of the iodine traps is carried out in order to verify the retention efficiency of such a barrier. These annual tests are performed by an *in-situ* measurement on the iodine trap installed within the ventilation network by means of radioactive iodine injection and followed by γ-spectrometry measurements. The test procedure induces paradoxically the major release of the radioactive iodine to the environment of most of the controlled nuclear facilities [11].

The next section will present the different trapping technologies for volatile iodine species.

1.3 Trapping technologies of the iodine species

1.3.1 Generalities

Different technologies can be used to trap the volatile iodine species. Schematically, these methods may be classified into two categories: wet and dry processes. On the one hand, wet processes use a solvent to scrub iodine from gas phase. More precisely, these scrubbing methods encompass alkaline (caustic) scrubbing, mercurex and iodox processes. More details can be found in Table 1 [23].

Table 1. Summary of wet scrubbing methods [23][24][25]

Method	Principle	Method example	Performance
Mercurex [$Hg(NO_3)_2/HNO_3$]	Iodine is transferred to the solution and converted to iodates and mercury complexes.	SCK/CEN (Belgium)	DF up to 150 for gaseous iodine
Iodox (HNO_3)	Oxidation of iodine in solution.	LMFBR (U.S.A)	DF up to 106 for ^{131}I
Caustic (NaOH)	Conversion of elemental iodine to iodide and iodate in solution.	La Hague (France)	DF of 50-150

DF: Decontamination Factor (see definition in section 2.3.1)

However, these processes display numerous disadvantages such as:

(i) manipulation of toxic and corrosive solutions;

(ii) liquid waste generation;

(iii) high maintenance cost, etc.

Hence, a reliable and robust operation seems to be difficult using this kind of technology.

On the other hand, dry process using adsorption is one of the effective operations to capture the volatile radioactive contaminants from gas streams [26]. Dry process is known to be more promising than wet processes due to its high removal efficiency and adsorption capacities, simple design and low maintenance costs. Industrially, activated carbons, silver-loaded adsorbents (zeolites, alumina or silica) are commonly used as adsorbent materials for the capture of radioactive iodine. A summary of their main industrial application is presented in Table 2. Another class of materials such as titanosilicate, mesoporous silica and metal-organic-framework (MOF: ZIF-8(Zn), MIL-53(Al), MIL-100(Al), UiO-66(Zr), HKUST-1(Cu), CAU-1(Al) and MIL-120(Al), etc. [27][28]) are also investigated but only for academic purposes [7]. An overview of the behavior of these porous adsorbents towards the capture of I_2 and CH_3I is summarized in Table 5 (see Section 3).

Table 2. Summary of the industrial adsorbent application

Adsorbent material	Application	Example
Activated carbon	Ventilation networks	Ventilation system of nuclear facilities
Silver-loaded zeolites	Nuclear reactor accident Spent fuel reprocessing	Fukushima accident, Japan [29] La Hague, France [30]
Silver-impregnated silica (AC-6120)	Spent fuel reprocessing	Karlsruhe reprocessing plant (WAK), Germany [2]
Silver-impregnated alumina	Spent fuel reprocessing	Tokai spent fuel processing plant, Japan [7]

In the category of industrial adsorbents, zeolites are widely used within nuclear reactor and the spent fuel reprocessing plant for an accidental scenario thanks to their thermal stability, radiation resistance as well as tunable properties (structure, pore connectivity and size, Si/Al ratio). Since the Fukushima disaster in 2011, efforts were deployed more particularly within the ANR PIA MIRE project (MItigation of Releases to the Environment in the event of a nuclear accident) [31] and the European PASSAM project (Passive and Active Systems on Severe Accident source term

Mitigation) [32]. These projects aim to revisit and improve the existing mitigation technologies that could be implemented in order to limit the dissemination of radioactive species (namely I_2 and CH_3I) into the environment in the case of severe nuclear accident. Ag-exchanged zeolites were found to be the best adsorbents towards the capture of I_2 and CH_3I among all the other tested cations (Na^+, Cu^{x+}, Pb^{2+}, etc.) [33]. This was explained by the high affinity displayed by silver for iodine to form thermally stable AgI precipitates. Moreover, it was shown that the retention performances were mainly dependent on the content of silver well dispersed within the internal porosity (silver cations + small charged or metallic clusters) [33]. In that respect, zeolites belonging to the faujasite structural type (FAU) exhibited the highest retention performances (adsorption capacities higher than 200 $mg \cdot g^{-1}$ [28], AgI precipitates fraction of 70-80% [28]). Additional experiments were also carried out within the framework of MIRE project extension to explore the behavior of such silver zeolitic sorbents using more representative conditions. More precisely, the effects of temperature, water vapor [34] as well as some chemical inhibitors (NO_X, CO_X, SO_X) under accidental or ageing conditions were further assessed.

As a comparison, AC is not suitable to be used within the Filtered Containment Venting Systems (FCVS) [35][36][37] implemented in PWR to overcome the radiological consequences of a severe nuclear accident (core damage). Indeed, AC present serious drawbacks for this application such as: low auto-ignition temperature (around 400°C according to ASTM D-3466) [38] and reduced performance in different types of severe atmospheres (high temperature, water in large excess, challenging irradiation and oxidizing conditions [7][39]). In addition, nitrogen oxide (NO_x) is known to be present mainly in the off-gas generated from spent nuclear fuel reprocessing plant. Owing to the adverse reactions between NO_X and AC, this sorbent cannot be considered as primary sorbent for the spent fuel reprocessing plant off-gas [40]. The next section will be devoted to the description of their use in the nuclear field.

1.3.2 Utilization of activated carbon in the nuclear context

There is worldwide interest in AC for their common use within the nuclear ventilation networks [3], more particularly in the French nuclear facilities. In a nuclear facility, ventilation networks ensure a dynamic confinement as a complement of the static confinement [41]. As depicted in Figure 2, the dynamic confinement is achieved by a series of negative pressure differentials (P1 <

P2 < P3) for a classic static confinement containing three or more containment systems, so that the pressure is the lowest in the areas where the radioactive substances are contained [41]. Filtration and purification devices installed on the extraction networks for each containment system are depending on the targeted chemical forms and can be composed of:

- **iodine traps (composed by AC) for volatile iodine species;**
- high-efficiency particulate air (HEPA) filters for aerosols;
- detritiation systems dedicated to tritium removal;
- gas washing for chemical or radioactive components in gaseous form.

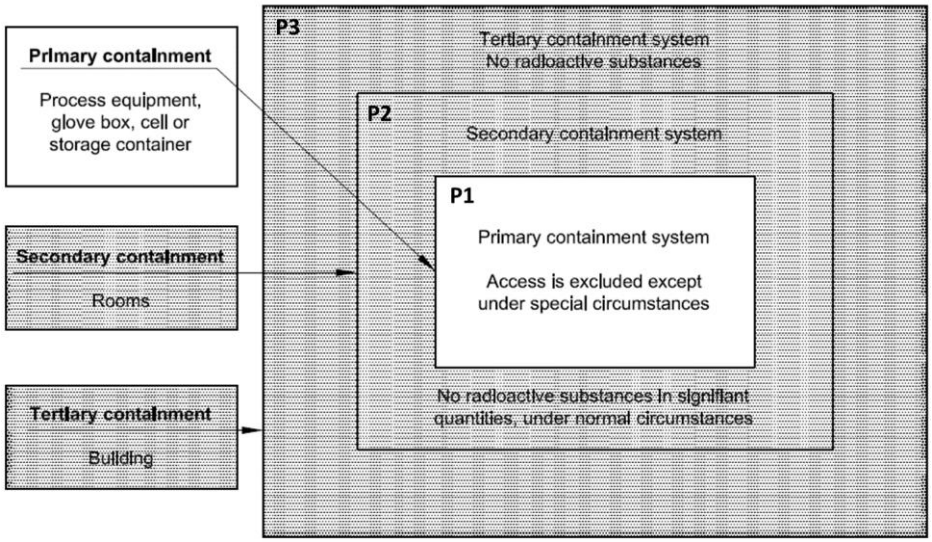

Figure 2. Schematic drawing of a three-containment system [41]

An example of an industrial iodine trap (*Acticarb, CAMFIL)* is shown in Figure 3. This iodine trap is composed of a specific formulation of AC noted as *nuclear grade AC*. More precisely, it consists of a granular AC derived from coconut shell with KI (potassium iodide) and TEDA (triethylenediamine) impregnations. According to the supplier specifications, this iodine trap can be used for temperatures lower than 80°C and relative humidity (RH) below 40% [42]. Indeed, AC implemented in the French nuclear ventilation networks are generally equipped with a heating apparatus, preheating the gas stream in order to reach a RH of about 40% due to the adverse effect of higher humidity on the retention performances of a given AC [3][43] (Table 3). More details about iodine traps use within the nuclear facilities (conditions, safety criteria, replacement criteria, etc.) are summarized in Table 3.

The safety criterion of DF (10 or 100, Table 3) represents the minimal performances required for a safe operation within the nuclear facilities. However, the DF replacement criterion (100 or 300, Table 3) corresponds to the minimal authorized performances during periodic tests, allowing a security margin with respect to the safety criterion. Such DF performances which are considered acceptable, may be no longer acceptable if the functional integrity of these protective systems is to be assured in other thermodynamic conditions (high RH, and even condensation) envisaged in an incident situation.

Based on this context, R&D efforts are necessary to gain knowledge about the retention behavior under different conditions as well as about the involved mechanisms for the current iodine traps. These investigations will be conducted in the frame of a dedicated R&D program, which is presented in the next section.

Figure 3. Commercial iodine trap containing *nuclear grade* AC (Acticarb, Camfil) [42]

Table 3. Summary of the iodine traps for the nuclear facilities [42][43][44]

Temperature	< 30 °C
RH	< 40% (with upstream heater)
	< 70% (without upstream heater)
Inspection intervals for the iodine traps	From 6 to 12 months
Safety criteria of the decontamination factor (DF)	10 or 100 depending on the operating systems (CH_3I)
Replacement criteria of the decontamination factor (DF)	100 or 300 depending on the operating systems (CH_3I)
Acceptance criterion of DF after the iodine trap replacements	> 1000 (CH_3I)

**DF: decontamination factor* (see Section 2.3.1)

1.4 New challenges for the iodine traps

The trapping efficiency of I_2 and CH_3I by porous adsorbents has been an active field of research depending on the context (Figure 4). More particularly, it can be noticed that the bibliometrics seems to be directly related to the construction of reactors in France (1970s – 2000s) but also to the occurrence of severe nuclear accidents (for instance, Fukushima in 2011).

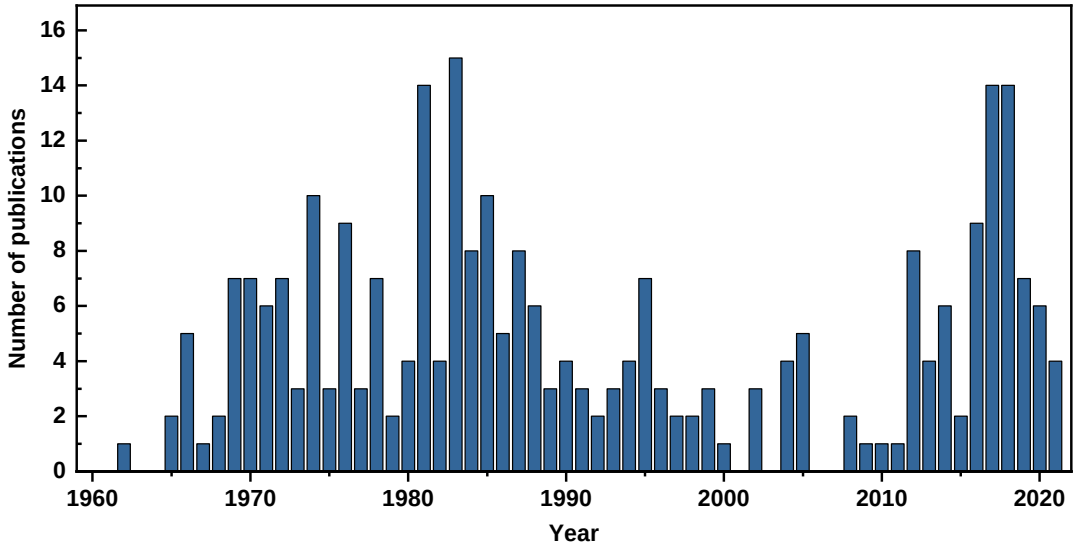

Figure 4. Global number of publications over time (keywords: iodine/radioiodine/iodide/filter/epuration, SCOPUS)

As the knowledge of iodine filtration and severe accidents has progressed, new materials and improvements in iodine measurement technologies have emerged, offering promising prospects for improving the retention performance of molecular iodine and its organic compounds. In that respect, a specific R&D program (IODE [11]) was initiated within the SCA department of IRSN. Among the challenges of this project, a special emphasis is devoted to the development of new methods for evaluating the trapping performance of AC. As previously stated, the current annual test procedure may paradoxically result in the most significant radioactive release for nuclear facilities. As a result, the replacement of this traditional testing procedure with a novel non-radioactive method is a critical issue in the field of nuclear safety and radioprotection by reducing the potential radioactive release into the environment. However, the validity of such a non-radioactive method relies on two important points: (i) the first one concerns the use of a sufficiently sensitive analytical method in comparison with γ-spectrometry, to be able to perform non-destructive performance tests for iodine traps (*i.e.*, well below the adsorption capacities of AC). These researches will be addressed in future studies to qualify the performance of innovative sensors such as photo-acoustic spectroscopy [12]. (ii) the second one is about the quantification of isotopic exchange contribution in the adsorption of $CH_3{}^{131+127}I$. This quantification should finally allow to verify the validity of a transposition coefficient between the DF measured with radioactive iodine and the DF measured with non-radioactive iodine. The PhD works will be focused on the (ii) research axis.

In the following sections, adsorption generalities are firstly presented. A particular attention is devoted to the AC which was used as a reference adsorbent during this PhD project. Then, the state of the art about the iodine removal by AC is summarized regarding both the adsorbent characteristics and the operating conditions. Finally, concluding remarks and the methodology of this PhD project is presented.

2. Generality of the adsorption

2.1 Definition of the adsorption

Adsorption is a process in which molecules of a fluid (gas or liquid) settle on the surface of a solid. The phase consisting of the adsorbed molecules is called "adsorbate" and the solid is named

"adsorbent". In the particular case of the present PhD project, the AC is the adsorbent and CH_3I is the adsorbate. The surface of the solid comprises external and internal surfaces generated by the network of pores and cavities within the adsorbent.

The gas/solid adsorption is an analogy to liquid/vapor equilibrium where the solid imposes a potential field upon the adsorbed phase [45]. This interaction between solid surface and adsorbed phase is mainly due to Van der Waals forces. As a distance-dependent interaction, the Van der Waals forces are often interpreted by the Lennard-Jones potential model (Figure 5) presented as follows [46]:

$$V_{LJ}(r_m) = 4 \times \varepsilon \times \left[\left(\frac{\sigma}{r_m}\right)^{12} - \left(\frac{\sigma}{r_m}\right)^{6}\right] \quad (1)$$

Where V_{LJ} Lennard-Jones potential between two molecules (kJ·mol^{-1});
ε depth of the potential well (kJ·mol^{-1});
σ finite distance at which the potential is zero (nm);
r_m distance of separation between two molecules (nm).

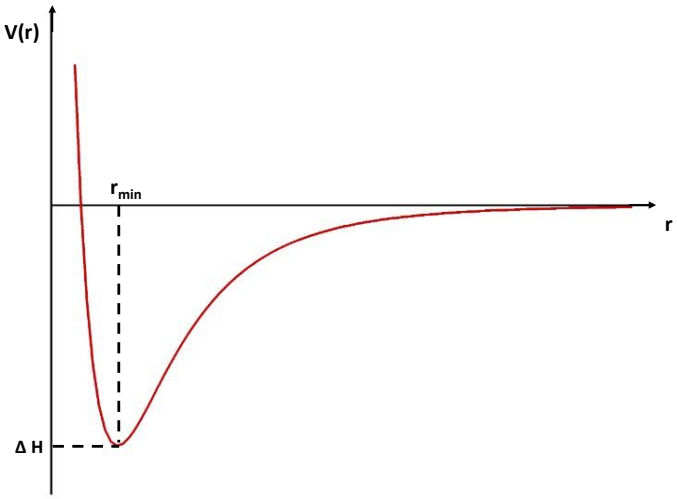

Figure 5. Lennard-Jones potential energy

At short distances, as the adsorbate molecule approaches the adsorbent surface, the electronic clouds of the adsorbate and adsorbent molecules interact, causing a repulsive force (term $(\sigma/r_m)^{12}$). On the contrary, over relatively large inter-molecular distances, the molecular interactions are of attractive nature, and the potential energy between two molecules is dominated by $(\sigma/r_m)^6$. In this

case, the attractive nature of these interactions contributes to the physisorption phenomenon [47]. Physisorption occurs without modification of the molecular structure and is totally reversible.

In the case of chemical adsorption, the process results from a chemical reaction with formation of chemical bonds between the adsorbate molecules and the adsorbent surface. The binding energy is much stronger than in the case of physical adsorption and the process is much less reversible and even sometimes irreversible [48].

As depicted in Figure 5, the minimum potential at r_{min} of the order of a few kJ·mol^{-1} constitutes the adsorption energy. For physisorption, this value corresponds to the distance for which the molecule is stable. The adsorption energy brought into a physisorption reaction can reach up to 50 kJ·mol^{-1}[49]. For the case of chemisorption where a chemical bond is formed between the solid and the adsorbed molecule, the adsorption energy can reach a few hundred kJ·mol^{-1} [49].

The AC is widely chosen as an adsorbent in gas phase due to its large specific surface areas (300 – 4000 m^2/g [7]) and good accessibility of internal pores. Pores of different dimensions can be classified into three categories (Figure 6) according to the definition of International Union of Pure and Applied Chemistry (IUPAC) [50]:

- micropore (under 2 nm diameter);
- mesopore (2-50 nm diameter);
- macropore (above 50 nm diameter).

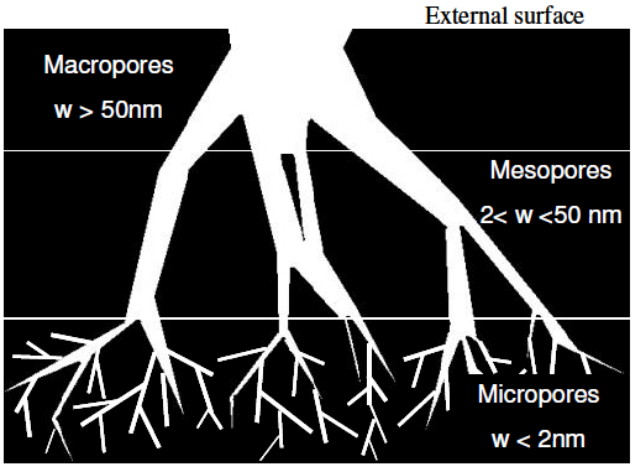

Figure 6. Schematic representation of the pore network of carbon material [51]

The major part of the internal surface area or specific area of AC is provided by the micropores, which play a key role for volatile iodine species retention considering the kinetic diameters of I_2 and CH_3I of about 0.5 and 0.6 nm, respectively [52], corresponding to the micropores range. Generally, the specific surface of AC is between 500 and 1500 $m^2 \cdot g^{-1}$, and can reach up to 3600 $m^2 \cdot g^{-1}$ when a two-step technique combining liquid phase impregnation with chemical vapor deposition (CVD) is used [53][54].

The adsorption phenomenon can be studied experimentally using adsorption isotherms or breakthrough curves resulting from dynamic experiments. The difference between these two configurations is described below.

2.2 Adsorption isotherms

2.2.1 Definition

The thermodynamic equilibrium between the adsorbate and the adsorbent can be represented using adsorption isotherms, adsorption isobars as well as adsorption isosteres. The adsorption isotherm, which shows the quantity of molecules adsorbed per unit mass of adsorbent as a function of relative pressure at a given temperature, is the most common of these representations. The adsorption isotherm can be acquired by manometric (ex: N_2 porosimetry at 77 K) or gravimetric measurements (ex: H_2O adsorption isotherms) at various relative pressures or relative humidities when studying the water vapor adsorption. For a given temperature, an adsorption isotherm corresponds generally to a collection of equilibrium states for relative pressures between 0 and 1, with 1 corresponding to the saturated vapor pressure.

For the isotherms of a gas-solid system (the case of CH_3I adsorption with AC), both the concentrations and the partial pressures can be used as parameter units while for a liquid-solid system the concentrations are used. The majority of adsorption isotherms observed can be classified into six types according to the IUPAC [48] (Figure 7):

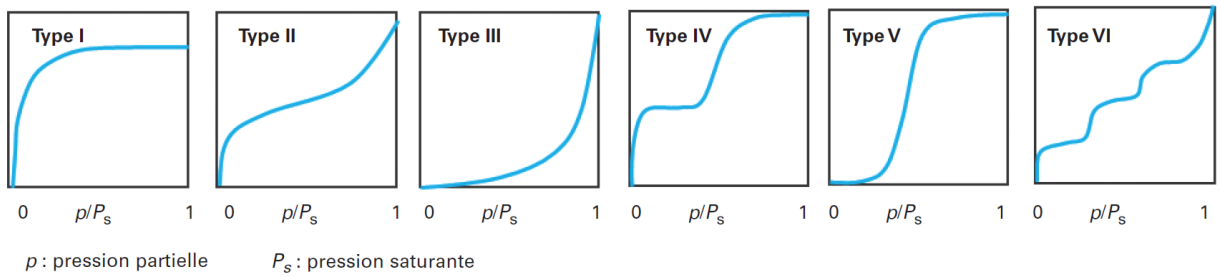

Figure 7. Classifications of adsorption isotherms for gas adsorption systems [48]

- Type I isotherms: in the case of microporous adsorbents with progressive saturation of substantially equivalent adsorption sites, type I isotherms are typically obtained;
- Type II and III isotherms: adsorbents with broad pore size distributions show Type II and III isotherms, with a continuous transition from monolayer adsorption to multilayer adsorption to capillary condensation;
- Type IV isotherm: when the interactions between the adsorbate molecules and the solid surface are stronger than the interactions between the adsorbed molecules, the formation of two successive adsorbate layers on the surface of the solid can result in a type IV isotherm. The second layer's adsorption sites do not begin to fill in until the first layer is nearly complete in this case;
- Type V isotherm: the type V isotherm indicates the presence of significant intermolecular interactions, with weak interactions between adsorbate molecules and the solid.
- Type VI isotherm: the successive formation of layers adsorbed on each other on a non-porous and homogeneous surface causes the type VI isotherm to form different levels.

Here, attention is given to the most used adsorption isotherms models: Langmuir and Freundlich isotherms. Details about these adsorption isotherms are presented below.

Langmuir isotherm [55]

$$n = \frac{n_m bC}{1 + bC} \tag{2}$$

Where n adsorption amount ($mol \cdot m^{-3}$);
n_m maximum adsorption amount in monolayer ($mol \cdot m^{-3}$);
b Langmuir constant ($m^3 \cdot mol^{-1}$);
C gas concentration ($mol \cdot m^{-3}$).

Langmuir model describes the Type I adsorption isotherms with saturation to a high gas concentration (where $b \times C >> 1$) and is consistent with Henry's model at low pressures. It should be noticed that the use of this model is based on five main assumptions:

(i) the adsorbed gas is considered as a perfect gas;
(ii) the maximum adsorption corresponds to a monolayer covering of the surface;
(iii) the adsorbent surface is energetically homogeneous (characterized by a single energy affinity coefficient designated by *b* which is the same for all the adsorption sites);
(iv) interactions between adsorbed molecules are negligible;
(v) migration phenomena between adsorption sites are neglected.

The Langmuir isotherm is widely used thanks to the simplicity of its mathematical formula, even though the hypotheses are not always satisfied. It should be noticed that the Langmuir isotherm is generally inadequate in describing adsorption of heterogeneous system such as AC regarding the assumption (iii)) [56]. Besides, the two last assumptions are rarely achieved experimentally.

Freundlich isotherm

The empirical Freundlich isotherm is reported to be capable of describing heterogeneous structures of the adsorbing surfaces [48][57]:

$$n = K_F C^{m'} \quad (3)$$

Where K_F Freundlich constant;
m' characteristic constant of the interactions between the adsorbate and the adsorbent;
C gas concentration ($mol \cdot m^{-3}$).

A limitation of the Freundlich model is that it does not imply the maximum quantity of adsorption because the proposed equation assumes an infinite increase as a function of the concentration [58].

2.2.2 Experimental determination

In this PhD project, particular interests on the adsorption isotherms are devoted to the characterization of the starting AC rather than the adsorption behavior of CH_3I. More particularly, different AC will be characterized using adsorption isotherms through two different aspects:

- Porous structure (specific surfaces, microporous volumes and distributions) deduced from the N_2 adsorption isotherm determined by a manometric method;
- Behavior with respect to the water vapor from H_2O adsorption isotherms based on gravimetric measurements.

More information about the experimental techniques and protocols used to determine the corresponding adsorption isotherms, as well as the results obtained will be presented in detail in Chapter II.

2.3 Dynamic adsorption

In the previous section, the definition and the details of the static adsorption are presented. However, the static adsorption does not represent the real adsorption behavior for AC within the ventilation networks. Indeed, the adsorbent is placed in a fixed position with a continuous stream of the adsorbate fluid. This behavior is better assessed by the dynamic adsorption experiments.

2.3.1 Generality of dynamic adsorption

In the present configuration, the dynamic adsorption takes place in an open system: the fluid (CH_3I) passes continuously on the fixed bed of adsorbent (AC), and the upstream and downstream concentrations are continuously measured. An example of the dynamic adsorption experiment system is given in the work of B. S. Choi *et al.* [52] for investigating the adsorption dynamics of CH_3I towards silver ion-exchanged zeolite (Figure 8). The zeolite sample (bed depth = 0.6 m) is fixed at a thermostated adsorption column (up to 400 °C). Then, continuous flow of CH_3I (2.5×10^{-5} mol·L^{-1}, linear velocity = 18 cm·s^{-1}) passes through the sample. An *in-situ* outlet gas concentration measurement is achieved by GC with a Pulse Discharge Detector (GC-PDD [59]).

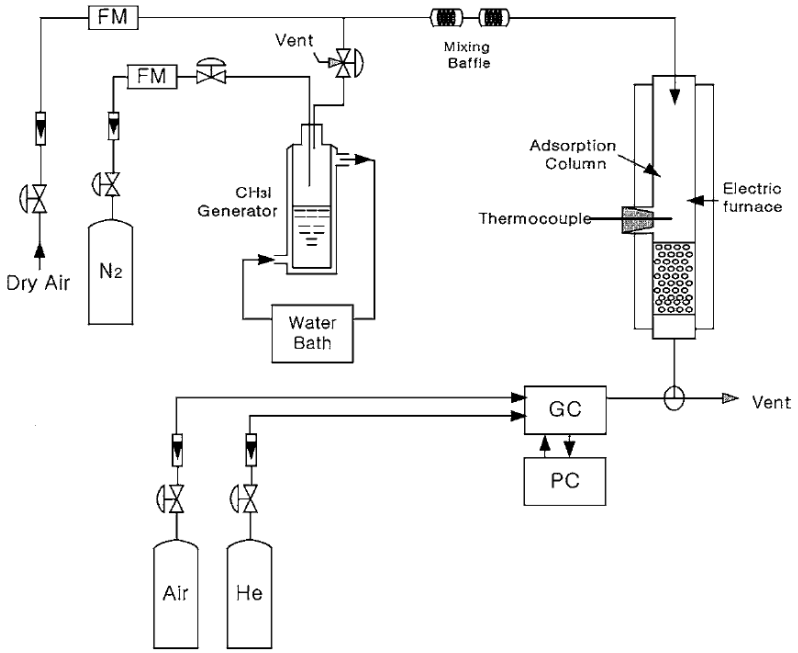

Figure 8. Schematic experimental apparatus for CH_3I adsorption [52]

The dynamic adsorption is usually accompanied by the breakthrough curve (BTC) measurement. An example is presented in Figure 9. The BTC results from the outlet concentration (C_{outlet}) monitoring of an adsorbent bed (AC for example) fed continuously with specific adsorbate (CH_3I for example) at a given inlet concentration (C_{inlet}).

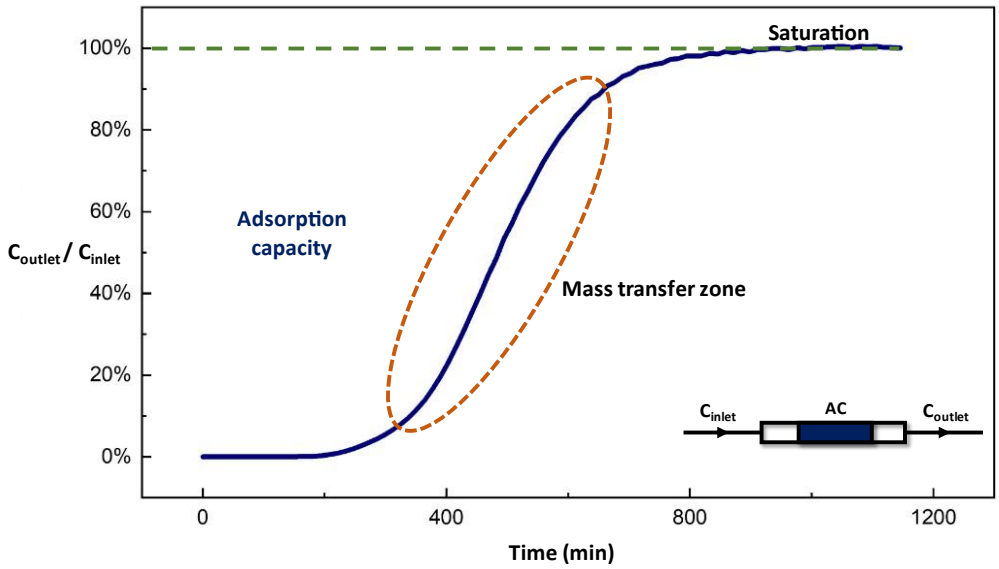

Figure 9. An example of BTC from CH_3I adsorption by a given AC ([CH_3I] = 10 ppmv, T = 30 °C, bed depth = 5 cm, linear velocity = 25 $cm \cdot s^{-1}$, residence time = 0.2 s):

It can be noticed from Figure 11 that a BTC can be schematically divided into three parts:

(i) The retention phase

This region corresponds to a « total » retention of the incoming CH_3I molecules by the adsorbent bed. Indeed, no CH_3I molecules at the outlet are detected by the instrument used due to its detection limit (DL). This region is largely used to evaluate the trapping performances of industrial adsorbents in nuclear facilities [60]. The limit of use for the adsorbent in the ventilation networks of the nuclear facilities depends on the correspondent safety criterion. As previously shown in the Table 4, a maximal value of DF (*DF: Decontamination factor* – see below) of around 100 can be highlighted for the AC. Hence the saturation of the adsorbent filter will never happen in real conditions.

In the nuclear context, the performances of various adsorbents towards the capture of iodine species are commonly compared within the retention phase in terms of the following parameters:

- Decontamination factor (DF) or CE (Coefficient d'Epuration) in French:

$$DF = \frac{C_{inlet}}{C_{outlet}} \tag{4}$$

Where DF decontamination factor;
C_{inlet} inlet concentration at the adsorbent bed (ppmv);
C_{outler} outlet concentration at the adsorbent bed (ppmv).

- Retention efficiency (η (%)):

$$\eta = \frac{100 \times (C_{inlet} - C_{outlet})}{C_{inlet}} = 100 \times \left(1 - \frac{1}{DF}\right) \tag{5}$$

- Penetration (P (%)):

$$P = \frac{100 \times C_{outlet}}{C_{inlet}} = \frac{100}{DF} \tag{6}$$

- Performance index (K (s^{-1})):

$$K = \frac{1}{residence\ time\ (s^{-1})} log(DF) \quad (7)$$

According to these formula, the relationships between same orders of magnitude for these aforementioned parameters are presented in Figure 10.

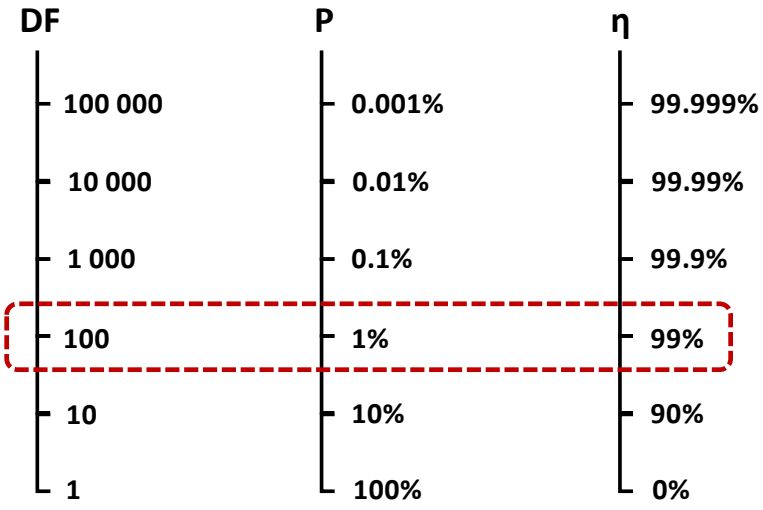

Figure 10. Relationship between DF, P and η [61]

The evaluation of these parameters requires the measurement of the outlet gas concentration, which is dependent on the detection limit (DL) of the analytical instrument for CH_3I online monitoring. Thus, it seems crucial to employ very sensitive technology for the detection of this molecule. In that respect, gas-chromatography coupled with electronic capture detectors (GC-ECD) was widely used in the literature in order to measure traces of CH_3I with high accuracy (theoretical DL up to 0.1 pptv) [62]. Despite its lower sensitivity (DL = 15 ppmv) [60], a Fourier-transform infrared spectroscopy methodology (FTIR coupled with a gas cell of V = 0.19 L and optical pathlength of 2 m) was used in recent works with the aim to finely monitor CH_3I with a high temporal resolution (every 2 minutes) but also to detect the possible by-products resulting from its interaction with silver-exchanged zeolites. According to the conditions used during this study (C_{inlet} = 1333 ppmv, DL around 15 ppmv [60]), the decontamination factors (DF) were found to be around 100. Thus, the use of a very sensitive analytical instrument like GC-ECD or GC-PDECD for CH_3I is essential in order to ensure the measurement of larger DFs with better accuracies.

(ii) the mass transfer zone

After a certain time (so-called the breakthrough time), the CH_3I molecules breakthrough becomes important since the adsorption sites available initially within the porous framework become insufficient to retain all the incoming gas. In the studies devoted to the adsorption phenomena, an adsorption capacity at breakthrough ($Q_{5\%}$) [60][63] is also introduced in order to gain insights about the working capacity displayed by the sorbent in real condition. This adsorption capacity ($Q_{5\%}$ as example) can be calculated from the following equation:

$$Q_{5\%} = \frac{M(CH_3I) \times D \times \int_0^{t5\%} (C_{inlet} - C_{outlet})\, dt}{m \times V_m(CH_3I)} \quad (8)$$

Where
- $Q_{5\%}$ adsorption capacity at 5% breakthrough ($mg \cdot g^{-1}$);
- $M(CH_3I)$ molar mass of CH_3I ($mg \cdot mol^{-1}$);
- D volume flowrate ($L \cdot min^{-1}$);
- $t_{5\%}$ time at $C_{outlet} = 5\% \times C_{inlet}$ (min);
- C_{inlet} concentration at the adsorbent bed inlet (ppmv);
- C_{outlet} concentration at the adsorbent bed outlet = $5\% \times C_{inlet}$ (ppmv);
- m mass of the adsorbent (g);
- $V_m(CH_3I)$ molar volume of CH_3I ($L \cdot mol^{-1}$).

Then, an increase of C_{outlet} is observed. This increase is rapid with a vertical slope for an ideal adsorbent. However, mass transfer phenomena occur in the real application (more particularly for AC grains) due to diffusional limitations. This mass transfer zone (MTZ) was defined in several studies through its length denoted by L_T as deduced from Eq. (9) [64]:

$$\frac{L_T}{L} = \frac{t_{95\%} - t_{5\%}}{t_{95\%}} \quad (9)$$

Where
- L bed length (cm);
- L_T length of mass transfer zone (cm);
- $t_{95\%}$ time at $C_{outlet} = 95\% \times C_{inlet}$ (s);
- $t_{5\%}$ time at $C_{outlet} = 5\% \times C_{inlet}$ (s).

When L_T is small compared to L, most of the adsorption capacity has been successfully used until the breakthrough point. Therefore, a narrow value of L_T/L lengths are known to be convenient for an effective use of the adsorbent [65].

(iii) The saturation of adsorbent bed

As the C_{outlet} continues to increase, it will finally reach a saturation value, where C_{outlet} equals C_{inlet}. At this time, the adsorption capacity at saturation Q_{sat} can be defined, which reflects the maximum quantity of adsorbed molecules for a given C_{inlet}. The Q_{sat} can be determined through Eq. (8) using equilibrium time instead of $t_{5\%}$.

2.3.2 Dynamic adsorption models

The measured BTC allows to calculate practical features of the dynamic adsorption column such as adsorption capacity (breakthrough or saturation), mass transfer zone, rate constant, etc. These features can be deduced by using appropriate dynamic adsorption models. In that respect, several models have been developed in the literature in order to better understand the adsorption process.

Most of the dynamic adsorption models are based on the assumption of axial dispersion, external mass transfer, intraparticle diffusion and nonlinear isotherms [66]. The Bohart-Adams model [67], the Thomas model [68] and the Yoon-Nelson model [69] represent three models that are the most used in the adsorption field to determine the adsorption characteristics of a fixed bed column. More particularly, these three models were reported to be mathematically equivalent [70]. Indeed, they can both be reformulated in terms of the following equation:

$$ln\left(\frac{C_{inlet}}{C_{outlet}} - 1\right) = A - \mathrm{B} \times t \qquad (10)$$

The parameters A and B are summarized in Table 4.

Table 4. Summary of the parameters deduced from the Adams-Bohart model, the Thomas model and the Yoon-Nelson model [67] [68][69][71]

<table>
<tr><th colspan="2">Bohart-Adams</th><th colspan="2">Thomas</th><th colspan="2">Yoon-Nelson</th></tr>
<tr><td colspan="2">Assumptions:
Adsorption rate proportional to both the residual capacity of the adsorbent and the concentration of the adsorbate
no axial dispersion
negligible film and particle resistances</td><td colspan="2">Assumptions:
Langmuir isotherms
Second-order reversible reaction kinetics
no axial dispersion.
negligible film and particle resistances</td><td colspan="2">Assumptions:
rate of adsorption proportional to adsorbate and adsorbent breakthrough.</td></tr>
<tr><td colspan="2">$A = \frac{k_{BA} N_0 L}{U_0}$
$B = k_{BA} C_{inlet}$</td><td colspan="2">$A = \frac{k_{Th} Q_{Th} m}{D}$
$B = k_{Th} C_{inlet}$</td><td colspan="2">$A = k_{YN} t_{50\%}$
$B = k_{YN}$</td></tr>
<tr><td>K_{BA}</td><td>Bohart-Adams rate constant ($L \cdot mg^{-1} \cdot min^{-1}$)</td><td>$K_{Th}$</td><td>Thomas rate constant ($L \cdot mg^{-1} \cdot min^{-1}$)</td><td rowspan="2">$K_{YN}$</td><td rowspan="2">Yoon-Nelson rate constant (min^{-1})</td></tr>
<tr><td>N_0</td><td>saturation concentration ($mg \cdot L^{-1}$)</td><td>Q_{Th}</td><td>adsorption capacity ($mg \cdot g^{-1}$)</td></tr>
<tr><td>L</td><td>height of bed in adsorption column (m)</td><td>m</td><td>mass of adsorbent (g)</td><td rowspan="2">$t_{50\%}$</td><td rowspan="2">time at C_{outlet} = 50% × C_{inlet} (min)</td></tr>
<tr><td>U_0</td><td>linear velocity ($m \cdot min^{-1}$)</td><td>D</td><td>flowrate of gas ($L \cdot min^{-1}$);</td></tr>
</table>

It can be noticed from Table 4 that regardless of the same mathematical expression, the required assumptions vary between these models. For example, a second-order reaction kinetics is assumed for the Thomas model, while the Yoon-Nelson model does not require any hypothesis regarding the reaction kinetics [72]. In addition, it is outlined that the aforementioned Thomas model is in reality the Bohart–Adams model in disguise, with their parameters interchangeable [73]. The real Thomas model is found to be too computational difficult for an analytical resolution [73]. It should also be noticed that the mathematical modification of the aforementioned models is also reported in the literature which allows to take into account the unsymmetric nature of the obtained breakthrough curves. The improved versions of the fixed bed models are presented with the following expressions [74]:

$$(Improved\ Bohart-Adams)\ ln\left(\frac{C_{inlet}}{C_{outlet}}-1\right)=K_{BA}\ln\left(\frac{N_0 L}{U_0}\right)-K_{BA}\ln\left(C_{inlet}t\right) \quad (11)$$

$$(Improved\ Thomas)\ ln\left(\frac{C_{inlet}}{C_{outlet}}-1\right)=K_{Th}\ln\left(\frac{Q_{Th}m}{D}\right)-K_{T}\ln\left(C_{inlet}t\right) \quad (12)$$

$$(Improved\ Yoon-Nelson)\ ln\left(\frac{C_{inlet}}{C_{outlet}}-1\right)=K_{YN}\ln\left(t_{50\%}\right)-K_{YN}\ln\left(t\right) \quad (13)$$

Among these models, a particular attention was devoted to the Thomas model based on the Langmuir isotherms and second-order reversible reaction kinetics. Indeed, this approach allows the direct determination of physical parameters related to the adsorption, essential for the quantitative comparison of retention performances for different adsorbents. On the one hand, an adsorption capacity at saturation (Q_{Th}) can be determined. On the other hand, information about the adsorption kinetics can be deduced from the calculated rate constant (K_{Th}). This model was also used in previous works [75] devoted to I_2 and Kr dynamic adsorption by carbonated materials. More particularly, a good fitting quality was observed when using this model to describe I_2 and Kr BTC using 10 w.t% hollow carbon nano-polyhedron impregnated titanosilicate for dry conditions and at temperatures about 35-45°C [75].

To sum-up, the improved Thomas model was used during the present PhD project to give insights on the CH_3I adsorption behavior for various AC and under several experimental configurations (see chapter IV). In the next section, the comparison of different industrial adsorbents for the removal of volatile iodine is presented. Then particular attention is given to the state of the art on iodine species adsorption by AC.

3. Comparisons of the adsorbents for the removal of iodine species

As mentioned in Section 1.3, the porous adsorbents reported in the literature for trapping volatile iodine species can be divided into two families:

- the first includes the adsorbents already used industrially to trap iodine species either in NPP or in fuel reprocessing plants (AC, silver-doped zeolites and silver-doped silica/alumina);
- the second category comprises sorbents reported only in academic works. These adsorbents have shown promising trapping performances but they present a certain number of technological obstacles for their implementation in a real application (titanosilicate, mesoporous silicas and MOF).

A summary is presented in Table 5 to compare the performances of these main adsorbents. Then, a particular attention is paid to AC in the next section as the studied material of this PhD project.

Table 5. Summary of different sorbents for removal of volatile iodine

Materials	S_{BET} ($m^2 \cdot g^{-1}$)	Adsorption capacity / Efficiency	Main advantages (+) and drawbacks (-) [7]
Silver exchanged zeolite	500-800	Q_{max} > 200 $mg \cdot g^{-1}$, 80% of trapping under AgI precipitates (Ag-Y zeolite, T = 100 °C, [CH_3I] = 1333 ppmv) [28] DF : 10^4-10^5 (Ag-Clino zeolite, T = 140 °C, water content up to 42 w.t%) [76][77]	(+): high thermal and chemical stability, radiation resistance, tunable pore size and chemistry, more appropriate to severe nuclear accident (potential material for the FCVS system in French Nuclear Power Plants), good trapping performances (formation of thermally stable and insoluble AgI precipitates) [28]; (-): expensive, negative effects of NOx on performance, alteration of the adsorption performance due to organic compounds. [28]
Impregnated AC	1000-1500 $V_{micro} \approx 80\%$	Q_{max} = 470 $mg \cdot g^{-1}$ (6.5 w.t% TEDA, T = 30 °C, [CH_3I] = 1460 ppmv) [78] Q_{max} ~ 320 mg/g (without impregnation, T = 30 °C) [79]	(+): well-defined microporous network, good adsorption performances with TEDA and KI impregnations, low production cost, high stability in basic and acidic conditions, reference material for the trapping of volatile iodine species in the ventilation systems (*Acticarb Camfil* in France, T < 80 °C, RH < 40 %) [42]; (-): ill-defined surface chemistry and heterogeneity, alteration of the adsorption performance due to aging, low autoignition temperature especially in the NOx presence, decline in performances in high temperature and RH, not appropriate for severe nuclear accident context (T ~ 140 °C, water content > 70 w.t%) [80].
Silver-doped silica and alumina (Ag/SiO_2, Ag/Al_2O_3)	~100	DF > 500 ([CH_3I] = 30 ppmv, 150 °C) [81]	(+): increase of the adsorption performances in the presence of NOx (1–10 vol.%), good adsorption performance up to 150 °C, less expensive than silver-exchange zeolite, adsorbents commonly used in the fuel reprocessing units (*AC-6120*) (-): loss of efficiency at temperatures of > 200 °C, high operating cost, loss of performance in the presence of a large excess of organic contaminants and in humid conditions.
Titanosilicate	~200	Q_{max} = 243 $mg \cdot g^{-1}$ (T = 80 °C, $P(I_2)$ = 0.047 bar, $P(H_2O)$ = 0.47 bar) [82]	(+): good adsorption performances after silver incorporation (rather similar to those displayed by of silver-doped zeolites); (-): few studies on the influence of humidity and/or inhibitors (NOx, organics, etc.).
MOFs	~2000	Q_{max} = 1740 $mg \cdot g^{-1}$ (30 °C, [CH_3I] = 150 ppmv) [83] Q_{max} = 1250 $mg \cdot g^{-1}$ (77 °C, $P(I_2)$ = 0.014 atm) [84]	(+): high specific surfaces areas, excellent adsorption performance towards I_2 after amine functionalization (R-NH_2), large range of existing MOFs, possibility of adjusting properties; (-): interactions only based on physisorption for the trapping of CH_3I [27], few studies on the influence of humidity and/or inhibitors (NOx, organics, etc.), expensive for a large scale application (shaping under a controlled grain size distribution is required).
Mesoporous silica	~700	Bismuth SBA-15: Q_{max} = 540 $mg \cdot g^{-1}$ at 200 °C, [I_2] not mentioned [85] Silver doped SBA-15: Q_{max} = 143 $mg \cdot g^{-1}$ (10 °C, [CH_3I] = 450 $mg \cdot L^{-1}$, adsorption in liquid phase [86])	(+): high adsorption capacities towards I_2 after aminated functions grafting, silver or bismuth doping [87][86]; (-): limited thermal stability when functionalized, few studies on the influence of humidity and/or inhibitors (NOx, organics, etc.), expensive for a large-scale application (shaping under a controlled grain size distribution is required).

4 Activated carbons

AC is industrially applied to remove volatile iodine species more particularly within the nuclear ventilation networks owing to its reasonable cost and effectiveness. The retention of iodine molecules by this class of material, assigned to physisorption phenomena, is enhanced by their well-developed microporosity as well their large specific surface areas. In addition, some modification steps (impregnation with TEDA, KI, silver, etc.) are required in order to enhance the affinity of these adsorbents towards I_2 and CH_3I. In this part, attention is devoted to the main preparation steps of AC. Generalities about the effect of the synthesis method on the physico-chemical properties of the resulting AC will also be addressed.

4.1 Preparation of activated carbons

The preparation process of AC comprises generally the main following steps: treatment of raw materials, carbonization (also called pyrolysis) and activation. These steps are sometimes followed by a further modification (physical, chemical or biological) depending on the application [4].

4.1.1 Treatments of raw materials

The wise choice for the starting material is crucial depending on the desired application. The nuclear grade AC are commonly produced from coconut shell [88] owing to its mechanical strength and its ability to yield high solid content during the subsequent pyrolysis step [89][90]. In addition, the coconut shell presents interesting environmental properties due to its low nitrogen and sulfur content [89]. Finally, this crude material is known to be associated with the fabrication of highly microporous AC [89][91][92]. This property is suitable for I_2 and CH_3I capture (kinetic dimeter of 0.5 and 0.6 nm, respectively [52]).

The treatment aims generally to prepare the raw material for the further steps. It consists for example of drying, cleaning the crude material but also of the selection of specific grain size range depending on the nature of crude material and its application. Some examples of raw material treatment are reported in Table 6.

Table 6. Treatments of different raw materials

Crude materials	Treatments	Application
Coconut shell [93]	Dry (sunlight), size selection (2–3.5 mm), determination of the moisture content.	Ventilation network for nuclear installation [8]
Cotton [94]	Dry (room temperature), separation: gross mass, stems, balls and roots.	Supercapacitors and batteries [95]
Eucalyptus bark [96]	Cleaning (water), dry (4 h, 105 °C), crush and sieve (mesh number 10, approximately 2 mm), impregnation with 50 mL phosphoric acid, manual stir (3 min)	Water purification [97]
Birch [98]	Size selection (0.5 – 1mm), impregnation with phosphoric acid	Water purification [99]
Bamboo [100]	Dry	Ventilation network for nuclear installation [100]
Rubber wood sawdust [101]	Conversion of logs into sawn timber, dry (105 °C), particle size analysis	Volatile organic compound (COV) adsorption [102]
Silver berry [103]	Cleaning (water), dry (48 h, 105 °C), crush and sieve (1–2mm)	Gas purification [104]

4.1.2 Carbonization

The carbonization process is a thermal treatment for the raw materials with a temperature range generally between 600 and 900 °C [51]. This process is indispensable for the AC production since the micropore structure begins to form during carbonization. When the raw material is treated with carbonization, elements other than carbon are volatilized leading to the increase of both the void spaces in the solid phase and the carbon content [105]. The resulted carbonaceous material (so-called char) is mainly amorphous (random distribution) with some entities presenting a short-range periodicity (ordered part) [106]. On the one hand, the disordered carbon (non-graphitizing carbon structure with pentagonal, heptagonal and hexagons rings, Figure 11 (A)) includes both amorphous carbon and aliphatic chains. On the other hand, the ordered structures consist of small aromatics units linked together by ether and olefin type bonds (Figure 11 (B)). The heteroatoms (namely oxygen and hydrogen) are inserted within the carbon matrix. The structural properties of the final char depend mainly on the pyrolysis temperature. Higher temperatures are known to increase the content of carbon within the obtained char [107]. In addition, the carbon structure becomes more ordered and graphitized (Figure 11 (B)), which increases the size of the crystallites [106].

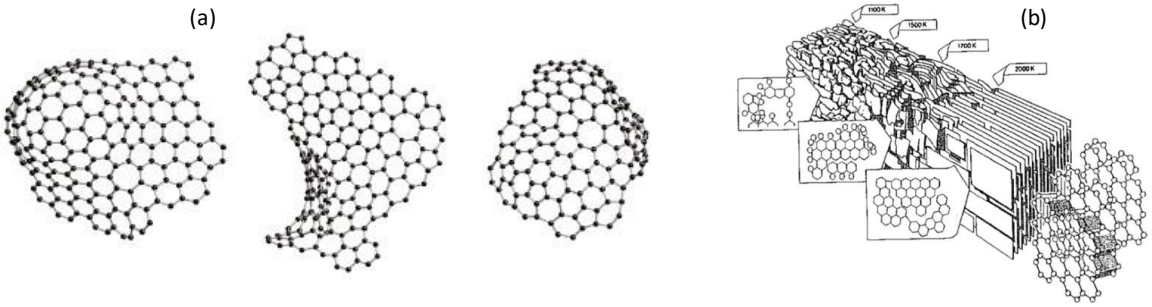

Figure 11. (a) Non-graphitizing carbon structure with pentagonal, heptagonal and hexagons rings [108], (b) Evolution of the carbon structure as a function of the pyrolysis temperature [106]

4.1.3 Activation

The activation process has the vocation to enhance the micropore structure generated in the carbonization process in order to improve its adsorption ability. Similar to the carbonization, the activation process also requires a high temperature but with a different objective: the oxidation of certain carbon atoms to form volatile compounds in order to create a well-developed microporous structure. There are two different ways of activation: physical activation and chemical activation ($ZnCl_2$, H_3PO_4, KOH, etc.). Only the physical activation is employed on nuclear grade AC. Hence, this process will be presented below.

A temperature of about 800 to 1000 °C is needed for the physical activation. Two reagents are commonly used (water vapor and carbon dioxide). Both steam activation and carbon dioxide activation are endothermic, which explains the requirement of an external heating to maintain the activation reactions [51].

During the physical activation, the disordered carbon present in the interstices between the graphene sheets reacts with the gaseous phase leading to CO and CO_2 formation, cleaning therefore the char porosity. The carbonaceous structure reacts also with the gaseous phase leading to the formation of new pores as well as to the increasing size of the existing pores.

The nature of gas employed in the course of activation will influence the textural properties of the final AC. Indeed, activation with CO_2 is known to be associated with well-developed microporous materials. However, activation with water vapor is rather responsible for the development of different kinds of porosities (micro, meso and macroporosity). The duration and temperature for

the activation process have also a significant effect on the pore size distribution as well as the specific surface area of the AC.

The activation allows also the chemisorption of heteroatoms on the carbonaceous structure. Apart from carbon, the trace of other elements can be found on the AC surface, like in most cases, oxygen and hydrogen with various quantities or even chlorine, phosphorus, sulfur, etc. More precisely, the hydrogen and oxygen found on the AC surface come from the functional groups located at the ends of the polyaromatic units. Some work on the quantification of these functional groups showed that the acidic groups are in the majority on the pore surface, such as carboxylic acid, lactone and phenol functional groups. On the other hand, some basic groups of the chromene and pyrone can also be found. An example of some functional groups commonly observed on the AC surface is presented in Figure 12. Generally, the activation under steam is expected to induce an enhancement of the surface pH of the AC and to increase the oxygenated compounds [106].

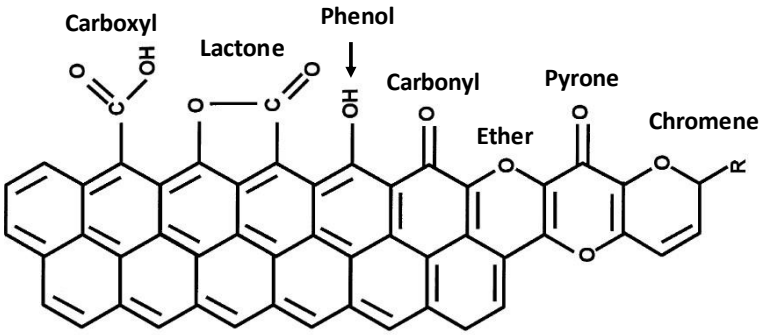

Figure 12. Examples of oxygen functions present on the AC surface [109]

4.1.4 Modification

A final step (called modification) is required depending on the desired application. An extensive literature review dealing about the existing modification techniques was conducted by C. Y. Yin *et al*. [4]. Authors have categorized the performed techniques into three groups: chemical, physical and biological modification. Nevertheless, these modifications may lead to an alteration of some intrinsic properties of the initial AC. An overview about the advantages and the disadvantages of the physical and chemical modification is summarized in Table 7.

Table 7. Advantages and disadvantages of existing modification techniques [4]

Modification	Treatment	Advantages	Disadvantages
Physical modification	Heat	Increases specific surface area and pore volume;	Decreases oxygen surface functional groups
Chemical modification	Acidic	Increases acidic functional groups on AC surface;	Decreases specific surface area and pore volume; May give off undesired SO_2 (treatment with H_2SO_4) or NO_2 (treatment with HNO_3) gases
	Basic	Enhances uptake of organics;	May decrease the uptake of metal ions;
	Impregnation	Enhances in-built adsorption capability	May decrease specific surface area and pore volume

In the nuclear context, the chemical modification consisting of the introduction of new active sites (so-called impregnation) is the most commonly used in order to improve the trapping stability and efficiency towards iodine species under humid conditions and at high temperatures. The nuclear grade AC are generally co-impregnated with both TEDA and KI molecules (about 1 w.t% KI and 5 w.t% TEDA) [6]. More details about the choice of impregnants as well as their influence on retention performances are presented in the next section.

4.2 Review on AC used in the nuclear context

The retention performance of AC towards the iodine species is found to be a function of many variables. Indeed, the influencing parameters reported in the literature studies can be classified in two categories:

(i) Parameters related to the adsorbent: nature of the raw material, preparation method, nature of impregnant and its content, functional surface type, grain size, etc.;
(ii) Parameters related to the operating conditions: temperature, RH, presence of inhibitors, gas velocity, etc.

The next section is dedicated to the state of the art of AC towards CH_3I removal.

4.2.1 Effect related to the adsorbent

The raw material nature and the production method (carbonization, activation and further modification) of AC play a key role for iodine species removal. Indeed, these parameters could influence the textural properties (specific surface areas, pore size distribution, pore volume) as well as the chemical characteristics (surface functional groups, speciation and content of the impregnated molecules) as stated in Part 4.1. Some insights about the relationship existing between iodine removal performances and the sorbent parameters are presented here.

4.2.1.1 Selection of the impregnants

The selection of the impregnants is reported to be dependent on the targeted adsorbate. It is claimed that the impregnation is required in order to remove CH_3I from highly humid atmosphere. However, this requirement is not indicated clearly for I_2 whose trapping seems to be easier either by physical or chemical adsorption [3]. It is even stated that the adsorption capacity of a given AC towards I_2 is dependent mainly on the surface area and the pore size of the investigated sorbent [110][111][112]. Hence, most of the studies about the impregnant selection are devoted especially to the capture of CH_3I by AC.

Numerous investigations about the appropriate impregnant for the CH_3I removal have been performed since the 1960s. A particular attention should be paid on the work of S. Kitani *et al.* [113], who investigated 27 different impregnants for the trapping of γ-labeled CH_3I by AC (prepared from coconut shell). The results are summarized in Table 8.

Table 8. CH_3I removal efficiency by various impregnated AC (T = 70 °C, RH = 90 %, [CH_3I] = 15 ppmv) [113]

Inorganic	Efficiency	Organic	Efficiency
6 w.t% Cl_2	45.5%	10 w.t% $CH_3ClCOOH$	14.7%
10 w.t% Br_2	98.9% (DF = 91)	10 w.t% $(CH_3)_2SO$	5.5%
10 w.t% $HgCl_2$	45.1%	10 w.t% $(CH_3CH_2)_2S$	23.8%
1 w.t% HgI_2	71.0%	10 w.t% $(CH_2)_6N_4$	70.3%
10 w.t% KF	6.2%	10 w.t% $H_2N(CH_2)_6NH_2$	20.3%
10 w.t% KSeCN	13.2%	10 w.t% $CH_3(CH_2)_4COONa$	8.2%
10 w.t% KSCN	93.5% (DF = 15)	10 w.t% $CH_3(CH_2)_8COONa$	7.3%
1 w.t% $AgNO_3$	16.4%	10 w.t% $(HOCH_2CH_2)_3N$	16.4%
10 w.t% $AgClO_4$	35.4%	10 w.t% $(-CH_2NHCH_2CH_2NH_2)$	53.9%
10 w.t% NaCN	56.8%	10 w.t% $(CH_3CH_2)_3N$	50.0%
10 w.t% KCN	27.0%	10 w.t% CH_3CSNH_2	4.0%
10 w.t% Na_2S	34.9%	10 w.t% $CS(NH_2)_2$	17.3%
10 w.t% Na_2SO_3	17.2%	10 w.t% $(C_6H_5O)_3P$	4.3%
1 w.t% SeI_2	91.5% (DF = 12)	10 w.t% TEDA ($C_6H_{12}N_2$)	98.4% (DF = 63)
10 w.t% I_2	88.1%		
10 w.t% KI	93.6% (DF = 16)		

The experimental conditions were: T = 70 °C, RH = 90 % with 15 ppmv of γ-labeled CH_3I. The test section is composed of five carbon cartridges, with a thickness of 5 mm for each one, but other experimental conditions (face velocity, residence time) were not mentioned. It was found that potassium thiocyanate (KSCN), stannous iodide (SeI_2), potassium iodide (KI), triethylenediamine (TEDA) and bromine (Br_2) were effective (trapping efficiency higher than 90%, Table 8). However, the use of bromine should be avoided due to its corrosive nature on the stainless steel. The efficiency difference of these impregnants was not explained by the author. Besides, S. Kitani *et al.* [113] tested molecular sieves 4A and silica gel with hydrophile surfaces with 5% KI and 10% KSCN impregnation. Results show that the efficiency of these materials for the trapping of γ-labeled CH_3I is nearly 0%. Then he proposed that adsorption of CH_3I on the base material may take place prior to the reaction between the CH_3I and the impregnant.

D. A. Collins *et al.* [114] investigated more than 50 impregnants (both organic and inorganic) for the trapping of γ-labeled CH_3I at room temperature and RH of 98%. Table 9 presents the most

efficient impregnants among the tested molecules during this study. Similar trends can be depicted as the study of S. Kitani et *al.* [113], where good retention performances were obtained mainly for iodine/bromine derivate molecules and TEDA.

Table 9. Different impregnates and their efficiencies towards CH_3I (100 µg $CH_3{}^{131}I \cdot g^{-1}$ carbon, 15 min of injection, 4 h of elution, 98-100% RH at room temperature) [114]

Impregnate	Efficiency (Residence time = 1.5 s)	Impregnate	Efficiency (Residence time = 0.25 s)
5 w.t % I_2	99.999 %	5 w.t % Br_2	99.999%
3 w.t % HI	99.999 %	0.5 w.t % CsI	99.999 %
10 w.t % KI	99.999%	2 w.t % NaI	99.998%
5 w.t % KBr	99.995%	5 w.t % TEDA	99.992%

It should be outlined that these findings are not explained from a fundamental or mechanistic point of view, and no additional studies on these molecules (CsI, Br_2, etc.) have been published in the literature. For the nuclear grade AC, two specific molecules (KI: potassium iodide and TEDA: triethylenediamine) are known to be widely used to remove CH_3I under highly humid conditions. TEDA impregnation allows the enhancement of chemical interaction leading to the trapping of CH_3I as a stable ammonium salt, which remains fixed to the porous structure [89]. Other literature studies indicate a significant increase of the AC breakthrough time after KI impregnation thanks to isotopic exchange reactions with the incoming $CH_3{}^{131}I$ [115]. As a comparison between these two impregnation agents, it is reported that TEDA impregnated AC are more efficient for the CH_3I removal than KI impregnated AC especially in highly humid conditions [7]. Thus, a combination of KI and TEDA is generally used in the nuclear context in order to counterbalance the humidity effect.

Some insights about the involved retention mechanism for KI and TEDA are presented in Part 4.2.3. The reported factors influencing iodine species removal are presented in the following for AC impregnated, mostly with KI and TEDA.

4.2.1.2 Effect of TEDA and KI contents

Studies have been carried out in order to evaluate the influence of impregnant content on the removal performances of AC towards CH_3I. The results are also reported to be a function of the

operating conditions. In configurations mainly governed by physical adsorption (low temperature, high concentration and absence of water vapor), the progressive impregnation induces a decrease of the global adsorption capacity as a correlation with the partial blockage of the microporosity (reducing CH_3I molecules accessibility to active sites). However, the impregnation seems to be crucial in order to ensure the capture of CH_3I under more realistic conditions (high temperature, high relative humidity low concentrations, etc.) mainly dominated by chemisorption phenomena. In that respect, the impregnation (up to a certain threshold) allows to enhance the trapping stability as well as the specific storage of CH_3I molecules even in the presence of water vapor in large excess. Some examples from the literature are reported below and summarized in Table 10.

Studies investigated by S. W. Park *et al.* [116] using adsorption isotherms at T = 30 °C (dry condition) have shown that the adsorption amount in low concentration ranges (< 1 ppmv) increases with the impregnation ratio, whereas a decrease is observed after impregnation for higher concentrations (> 5 ppm). In that respect, the authors indicated that chemisorption dominates at low adsorbate concentrations but physical adsorption become dominant at high adsorbate concentrations.

According to the work performed by D. A. Collins *et al.* [114] under humid condition (RH = 98 – 100 %, room temperature, residence time = 0.2 s), it was outlined that the best performances are obtained in the impregnation range of 5 - 10 w.t% for TEDA, and 0.1 - 1 w.t% for KI [114]. However, F. Billard reported that a 5w.t% TEDA AC has nearly the same performance as a 5w.t% KI AC [117]. These different observations of the optimal content of a given impregnant may be assigned to the differences in the manufacture procedures, raw materials as well as the operating conditions. Furthermore, M. Gourani *et al.* [118] investigated the influence of KI impregnation on coconut shell AC characteristics. A significant decrease of the specific surface was observed for KI content higher than 2 w.t%. Thus, it seems that a compromise in the TEDA and KI contents should be determined to ensure the efficient retention of CH_3I without altering the intrinsic properties of the AC. This compromise seems to be a content lower than 5 w.t% for TEDA and a content of 1 w.t% for KI in the commonly used nuclear grade AC [6].

Table 10. Specific surface and adsorption capacity of AC in different impregnation ratios

	Conditions	Impregnation	1%	2%	4%-5%	10%
M. Gourani *et al.* [118]	/	KI	S_{BET} = 980 $m^2 \cdot g^{-1}$	S_{BET} = 952 $m^2 \cdot g^{-1}$	S_{BET} = 596 $m^2 \cdot g^{-1}$	S_{BET} = 305 $m^2 \cdot g^{-1}$
D. A. Collins *et al.* [114]	Room temperature, RH = 98- 100% [CH_3I] = 100 $\mu g \cdot g^{-1}$	KI	The best performance is in the impregnation range 0.1-1 w.t%			
		TEDA	The best performance is in the impregnation range 5-10 w.t%			
H. K. Lee *et al.* [56]	Isotherms 30 °C, dry	TEDA	-	1320 $mg \cdot g^{-1}$	1190 $mg \cdot g^{-1}$	-
		NI	1500 $mg \cdot g^{-1}$			
S. W. Park *et al.* [116]	Isotherms 30 °C, dry	TEDA	Langmuir isotherms: Q_m (2.4% TEDA) = 6.37 $mol \cdot kg^{-1}$, Q_m (4.9% TEDA) = 5.04 $mol \cdot kg^{-1}$			

4.2.1.3 Effect of grain size

The retention efficiency of CH_3I is reported generally to be enhanced for decreasing grain size of AC whatever the nature of the impregnant [92][26]. This well-known trend in the adsorption field of research is assigned to the enhancement of mass transfer phenomena of CH_3I for lower grain size [119]. An example from J. L. Kovach *et al.* [120] is presented in Table 11, in order to elucidate the influence of grain size on $CH_3{}^{131}I$ retention for both KI and TEDA impregnated coconut AC. The best performances are generally obtained for a grain size between 1 and 1.19 mm according to Table 11. To compare with, the average grain size indicated by the suppliers of nuclear grade AC is generally about 8 × 16 mesh (between 2.36 and 2.5 mm) [42]. A lower grain size will however lead to a more significant problems related to pressure drop.

Table 11. Effect of particle grain size for KI and TEDA impregnated AC (T = 30 °C, RH = 95 %) [120]

Particle size (mm)	Residence time: 0.25 s Linear velocity: 20 $cm \cdot s^{-1}$ Bed depth: 5 cm		Residence time: 0.125 s Linear velocity: 420 $cm \cdot s^{-1}$ Bed depth: 5 cm		Residence time: 0.25 s Linear velocity: 40 $cm \cdot s^{-1}$ Bed depth: 10 cm	
	DF (2w.t% KI)	DF (2w.t% KI + 2w.t% TEDA)	DF (2w.t% KI)	DF (2w.t% KI + 2w.t% TEDA)	DF (2w.t% KI)	DF (2w.t% KI + 2w.t% TEDA)
2.38 - 2.00	26	98	9	18	57	198
2.00 - 1.68	51	263	10	25	111	606
1.68 - 1.41	73	657	17	76	278	3030
1.41 - 1.19	160	1754	30	108	781	11111
1.19 - 1.00	368	3125	42	145	1695	50000

4.2.1.4 Other effects

It is also reported that retention performances are enhanced for increasing adsorbent bulk densities. Indeed, the quantity of available adsorption sites will be enhanced for higher packing densities [3][26]. In addition, the increase of bed depth will also account for an enhancement of the retention performances in general, since the residence time is higher for a fixed linear velocity (see examples in Table 12).

The effect of pore structure on CH_3I adsorption was also investigated by A. J. Juhola *et al.* [121] using different impregnated commercial AC ($KI+I_2$, KI, I_2, KIO_3) at room temperature (RH = 0 – 99%). This study showed that the specific surface area of the obtained sorbent plays a key role towards the retention of CH_3I. Indeed, an empiric relationship was demonstrated between the penetration P and the specific surface area s:

$$ln\left(\frac{P}{100}\right) = ln(a) - k_r s \qquad (14)$$

Where a Coefficient associated with the macropore properties;
k_r Coefficient dependent on the mean diameter of the micropores;
s Specific surface area calculated from the iodine number ($m^2 \cdot g^{-1}$).

The authors also proposed that a can be associated with the penetration at high humidity since the available specific surface area s is very small. The coefficient k_r is inversely proportional to the mean micropore diameter.

4.2.2 Effects of operating conditions

Numerous studies can be found dealing with the effect of operating conditions on the retention performances of AC towards I_2 and CH_3I. In this section, the most prominent factors of the operating conditions for the AC such as the temperature, relative humidity and linear velocity of the carrier gas is presented.

4.2.2.1 Effect of linear velocity

As stated in the previous section, the residence time of adsorbate molecules within the investigated adsorbent should be maintained as high as possible. In that respect, some works [26][92] [120] [122] have confirmed the increase of retention performances for decreasing velocity. An example

is shown in Table 12 from the study carried out by J. L. Kovach *et al.* [120] on commercial AC (denoted as NUSORB KITEG II) for CH_3I adsorption. It is found that the AC performance decreases with the linear velocity: the DF decreases from 108 to 6 when the linear velocity increases from 10 to 40 $cm \cdot s^{-1}$ for a bed depth of 2.5 cm.

Table 12. Effect of velocity on DF of $CH_3{}^{131}I$ for commercial AC (T = 30 °C, RH = 95 %) [120]

Linear velocity ($cm \cdot s^{-1}$)	Bed depth: 2.5 cm		Bed depth: 5.7 cm		Bed depth: 10.0 cm	
	t (s)	DF	t (s)	DF	t (s)	DF
10	0.250	108	0.500	1678	1.000	76923
15	0.166	38	0.333	602	0.666	33333
20	0.125	21	0.250	344	0.500	10753
30	0.084	10	0.166	88	0.333	5263
40	0.063	6	0.125	37	0.25	1351

4.2.2.2 Effect of relative humidity

Several studies related to the RH effect on AC are summarized in Table 13 with different experimental conditions (especially the residence time). The water content in the gas is generally considered to induce a negative effect on CH_3I trapping since pores filled with condensed water will be no longer available for the adsorption of the incoming iodine molecules. More precisely, it was reported that the water molecules located on the AC surface formed clusters that were bound in a network by hydrogen bonds and then filled the porous network of the AC, making the active sites less accessible for iodine species [123]. The presence of water vapor leads to the competitive adsorption between iodine species and H_2O.

According to numerous papers, TEDA was found to counterbalance the detrimental effect of humidity on the adsorption performances of AC. Indeed, the TEDA was proved by first principles density functional theory (DFT) calculations to improve the AC performance by freeing the active sites of the support thanks to the strong affinity displayed by water for TEDA molecules [124]. This result is also in agreement with experimental works conducted by S. W. Park *et al.* [125]. It was found more particularly that the decrease of chemisorption is much smaller than that of physical adsorption when RH is increased from 35 to 75 % at T = 30 °C for AC impregnated with 2.4 w.t% and 4.9 w.t% in TEDA. [125]. Similar results were obtained by K. Ho *et al.* [63], where the contribution of the physisorption is found to be decreasing from around 40% to 10% with the

increasing RH from 0 to 90 % ([CH_3I] = 400 ppmv). More details about the retention mechanism of CH_3I by TEDA under humid conditions is addressed in Section 4.2.3.

In comparison with TEDA, KI molecules do not possess the same counterbalancing effect towards water vapor. According to the study of C. M. Ecob *et al.* [5], a significant decrease of DF from more than 6000 to around 10 was stated for RH increasing from 40 to 98% respectively (residence time = 0.2 s). A similar behavior was outlined by P. Découcière [43], where a drastic decrease of DF from 10^4 to lower than 10^2 for RH higher than 40% was observed using an 1 w.t% KI AC (residence time = 0.125 s). Besides, F. Billard *et al.* [5] have indicated a stability of retention performances for RH up to 40% after KI impregnation within the AC (0.5 - 5 wt %). However, a drastic decrease is observed in general for higher RH (Table 13). Up to now it is difficult to estimate whether KI is directly affected by humidity or by the decrease of adsorption performances attributed only to pore blockage phenomena. This detrimental effect for KI explains the wide use of both TEDA and KI in *nuclear grade* AC [126]. More particularly, retention efficiencies of 97% (DF = 33) and 99% (DF = 100) were recorded for co-impregnated sorbents (2w.t% KI + 2 w.t% TEDA) at RH higher than 90% by S. Kitani *et al*. [113] and H. Deuber *et al.* [127] respectively.

Regarding the detrimental effects of humidity, a correlation has been proposed by IPSN/DPRE/OAR since 1999 [126], with the aim to predict the decrease of CH_3I retention performances of the commercial iodine trap of AC within EDF for RH values exceeding 40% (at temperatures about 30°C). Accordingly, the DF was found to rely on RH through the following equation:

$$\frac{log(DF_f)}{log(DF_i)} = \left(\frac{a_f}{a_i}\right) \times \left(\frac{t_f}{t_i}\right) \times \left(\frac{v_f^{bf}}{v_i^{bi}}\right) \quad (15)$$

Where DF_i and DF_f — decontamination factors at the tested RH and at 90%, respectively;

t_i and t_f — residence times at the tested RH and at 90%, respectively;

v_i and v_f — linear velocities at the tested RH and at 90%, respectively;

a_i, a_f, b_i and b_f — parameters depending only on RH. These parameters have been already defined and adjusted form experiments performed between 1979 and 1980, for particular conditions where $v_i = v_f$.

The proposed formula has been therefore applied industrially in the nuclear field within the French ventilation systems [126]. Nevertheless, it seems important to revisit this correlation with standardized tests performed on the actual nuclear grade AC with new and more accurate methods of instrumentation. In that respect, first extensive measurements were performed within the PERSÉE facility of IRSN. More particularly, tests were carried out for various nuclear grade AC at RH of 40, 70 and 90%. The other experimental parameters have been fixed: (T ≈ 20 °C, linear velocity = 25 cm/s, residence time = 0.2 s, equilibrium duration under humidity of 16 hours at least). Experimental DF as well the predicted values according to the OAR formula are presented on Figure 13. A decrease of experimental DF as a function of RH can be noticed from Figure 13. This behavior is in line with the literature as stated previously. However, a significant deviation from the OAR correlation can be observed especially at high RH. Therefore, a new correlation should be proposed for the actual *nuclear grade* AC, in order to ensure a better accuracy in the determination of DF by these adsorbents for high RH. The work will be performed within IRSN in the frame of the "IODE" R&D program [11].

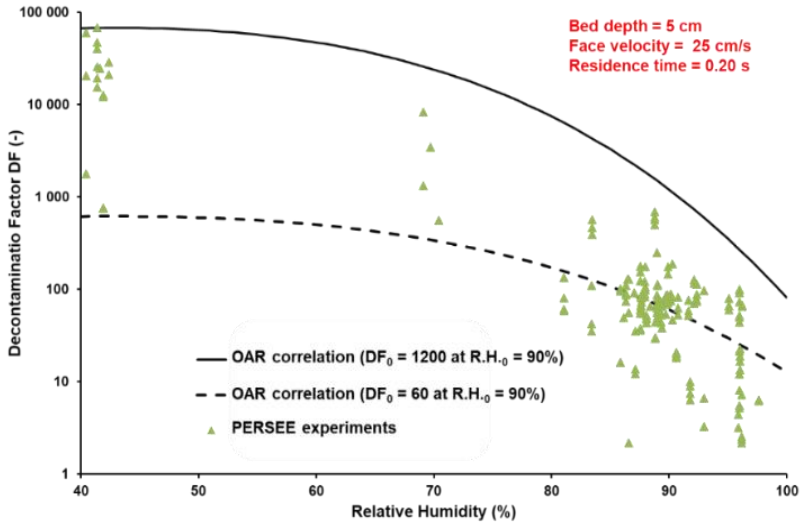

Figure 13. DF evolution towards RH for various *nuclear grade* AC: comparison between OAR correlation and experimental results of PERSÉE (T ≈ 20 °C, bed depth = 5 cm, linear velocity = 25 $cm \cdot s^{-1}$, residence time = 0.2 s, $[CH_3I]_0 \approx 150$ ppbv [11])

Table 13. Different AC performance as a function of RH

	Conditions	Activated carbon	0%	30-40%	70%-90%	90~100%
C. M. Ecob [5]	20-25 °C $[CH_3I]$ = 100 µg·g^{-1} Residence time = 0.2 s 10 min of injection Equilibration of 7 - 8 h	1.5% KI	-	DF=2512	DF=398	DF=100
		5% TEDA	-	-	DF=15848	DF=631
S. W. Park *et al.* [125]	30 °C Adsorption Isotherms	0 – 4.9% TEDA	The total adsorption capacity decreases with RH, and the contribution of chemisorption increases with RH			
K. Ho *et al.* [63]	30 °C $[CH_3I]$ = 400 ppm Bed height = 5 mm Residence time = 0.06 s	3.7% TEDA	126 mg·g^{-1} (total) 58 mg·g^{-1} (physisorbed)	125 mg·g^{-1} (total) 31 mg·g^{-1} (physisorbed)	64 mg·g^{-1} (total) 6 mg·g^{-1} (physisorbed)	64 mg·g^{-1} (total) 5 mg·g^{-1} (physisorbed)
F. Billard *et al.*[117]	25 °C $[CH_3I]$ = 15 µg·g^{-1} Linear velocity = 30 cm/s 15 min of injection	0.5-5%KI	DF=4500-14000	DF=6000-7000	-	DF=12-17
		2%TEDA+ 2%KI	DF=17000	DF=27000	-	-
J. L. Kovach *et al.*[120]	T = 30 °C RH = 95 % Residence time = 0.25 s	Commercial AC KI + TEDA	-	-	DF = 3704 (70% RH) DF = 2083 (80% RH) DF = 935 (85% RH)	DF = 521 (90% RH) DF = 344 (95% RH)

4.2.2.3 Effect of temperature

Numerous studies devoted to the behavior of AC as a function of temperature were performed. Controversial results can be found for temperature effect between the "adsorption" and the "nuclear air cleaning" communities. The different trends observed in the literature are mainly accounted for the different test methodologies. On the one hand, the results from the "adsorption community" are generally expressed in terms of global adsorption capacity which comprises both physical and chemical interactions. Hence, the decrease of global adsorption capacities is always reported by these studies for increasing temperatures owing to the reduction of the physisorption phenomenon. Nevertheless, a closer look to the published data indicates an enhancement of chemical interactions between TEDA and CH_3I for higher temperatures. More particularly, the study of G. I. Park *et al.* [78] has reported a progressive decrease of the CH_3I global adsorption capacity by the impregnated AC (6.5 w.t% of TEDA) from 470 to 105 mg·g^{-1} for temperatures between 30 and 250 °C under dry conditions (Figure 16). This decrease is accompanied by the

enhancement of the fraction of chemisorbed CH_3I from 42 to about 85% at 35 and 250 °C, respectively (Figure 14). This increase is assigned to the enhancement of the reaction between TEDA and CH_3I leading to the quaternary ammonium salt formation at high temperatures [7]. The special affinity of TEDA towards CH_3I also allows to overcome the huge decrease of adsorption capacities for the unimpregnated material from 529 to 21 $mg \cdot g^{-1}$ in the same range of temperatures [78]. Indeed, only physisorption are known to take place for unimpregnated AC for the capture of CH_3I.

On the other hand, tests presented in the nuclear context and more specially in the different nuclear Air cleaning conferences [120] are mostly based on standardized tests [128] aiming to explore the behavior of AC generally under conditions where both chemisorption phenomenon and isotopic exchange reactions can occur to the detriment of physisorption phenomenon. In the corresponding papers, an increase of the retention performances is observed generally at high temperatures owing to the enhancement of diffusion, isotopic exchange rates as well the chemical reactivity with TEDA [120][122]. Some examples are shown in Table 14.

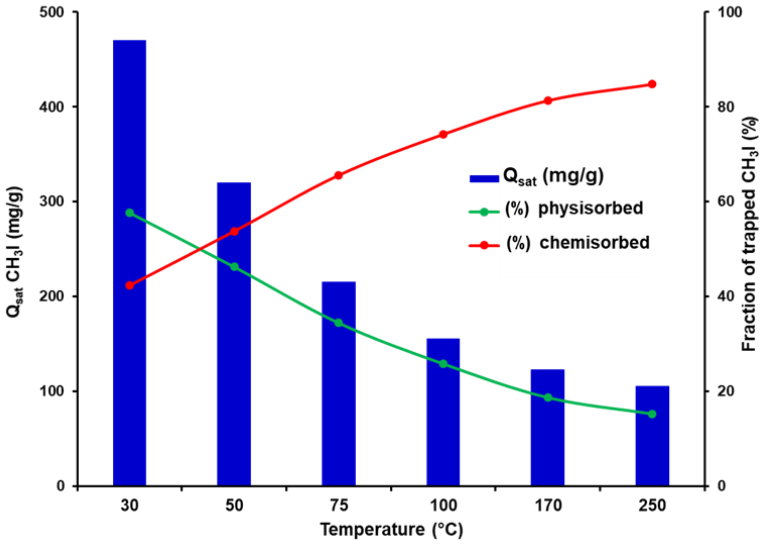

Figure 14. Evolution of physisorption and chemisorption versus temperature [78]

Table 14. Summary of AC performance as a function of temperature

	Conditions	Activated carbon	25-30°C	40-60°C	75-80°C	100°C	>100°C
B. S. Choi *et al.* [52]	Linear velocity = 0.18 $m \cdot s^{-1}$ $[CH_3I] = 2.5 \times 10^{-5}$ $mol \cdot L^{-1}$	Unimpregnated	320 $mg \cdot g^{-1}$	-	50 $mg \cdot g^{-1}$	30 $mg \cdot g^{-1}$	-
G. I. Park *et al.* [78]	Linear velocity = 0.18 $m \cdot s^{-1}$ $[CH_3I] = 4 \times 10^{-6}$ - 6×10^{-5} $mol \cdot L^{-1}$	6.5% TEDA	470 $mg \cdot g^{-1}$	320 $mg \cdot g^{-1}$	215 $mg \cdot g^{-1}$	155 $mg \cdot g^{-1}$	123 $mg \cdot g^{-1}$ (170°C)
		Unimpregnated	529 $mg \cdot g^{-1}$	350 $mg \cdot g^{-1}$	161 $mg \cdot g^{-1}$	74 $mg \cdot g^{-1}$	32 $mg \cdot g^{-1}$ (170°C)
H. Shiomi *et al.* [122]	RH = 70 % CH_3I: 0.1 $mg \cdot m^{-3}$ Linear velocity = 42.4 $cm \cdot s^{-1}$	10% TEDA	DF = 90	DF = 403	DF = 1097	-	-
J.L.Kovach *et al.* [120]	T = 30 °C RH = 95 % Residence time = 0.125s	Commercial AC KI + TEDA	DF = 17 (25°C) DF = 21 (30°C)	DF = 30 (40°C) DF = 39 (60°C)	DF = 105 (80°C)	-	-

In conclusion, temperature seems to enhance the retention performances of iodine species by impregnated AC until a certain threshold. Indeed, the use of AC filter should be limited for temperatures lower than 120 °C to avoid both iodine species desorption and to overcome the possible ignition of the sorbent at higher temperatures. The increase of temperature is known to favor the carbon oxidation phenomena leading to sorbent ignition at temperatures higher than 300 °C generally for parent AC or for AC impregnated only with KI (Table 15). However, AC impregnated with TEDA display lower ignition temperature due to the low flash point of the TEDA molecule. Some examples of ignition temperatures are reported for AC with various KI and TEDA composition in Table 15.

Table 15. Average ignition temperature for some AC [3]

Carbon type	Impregnation	Ignition temperature (°C)
Coconut	5% TEDA	190 - 215°C
Petroleum	5% TEDA	195 - 240°C
Coconut	2% TEDA	215 - 330°C
Coconut	None	340°C
Coconut	5% KI	312 - 333°C

4.2.3 Adsorption mechanisms

Both physisorption and chemisorption exist in the impregnated AC for the retention of CH_3I. However, there exists a third mechanism that needs to be investigated and constitutes a major interest of this PhD project: isotopic exchange. The AC commercially used nowadays for the French nuclear facilities, are co-impregnated with less than 5 w.t % of triethylenediamine (TEDA) and 1 w.t% of Potassium iodide (KI) as reported previously [43]. In this section, the specific adsorption mechanism of chemisorption and isotopic exchange will be discussed using TEDA and KI as impregnants under the nuclear context.

4.2.3.1 Mechanism of CH_3I retention with impregnants

Triethylenediamine (TEDA)

TEDA is an organic compound of nucleophilic amine with the formula $N_2(C_2H_4)_3$ (Figure 15). The melting point and the boiling point of TEDA are 158 °C and 174 °C, respectively [129]. It was reported that a SN_2 nucleophilic substitution reaction between TEDA and CH_3I took place in the AC, which is shown in Figure 15.

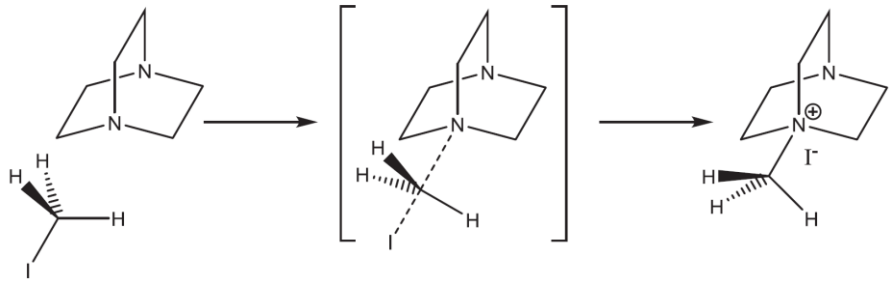

Figure 15. The reaction of TEDA with methyl iodide [130]

According to E. Aneheim *et al.* [130], this reaction can be carried out because of two favorable conditions: the first one is that the nitrogen atom in the amine has a large electron density, which gives it potential to substitute other chemical bond, and the second condition is that a carbon-iodine bond can undergo heterolytic cleavage to form an iodide anion (Figure 15) [130]. The chemical reaction between TEDA and CH_3I leads to the formation of stable quaternary ammonium salts, resulting in the improvement of the adsorption performance of the AC. This reaction was reported firstly to involve several steps as follows [26]:

- diffusion of the adsorbate to the grain surface;

- diffusion of the adsorbate into the pore structure;
- adsorbate adsorption;
- chemical reaction with the adsorbate.

It can be noticed that the physisorption is required as the prior step for the chemisorption by TEDA. In recent years, the huge progress of computational methods such as the density functional theory (DFT) calculations allows to finely investigate the mechanism of CH_3I trapping by TEDA impregnated AC at the molecular scale. It is reported that in dry condition, the capture of the CH_3I is driven by the dissociation (or so-called alkylation) of CH_3I molecule to CH_3 and I entities instead of a direct bond formation between TEDA and CH_3I [124]. This alkylation mechanism is proposed by the significant decrease of the activation barrier of the CH_3I dissociation E_a from 2.27 eV (unimpregnated AC) to 0.1 eV (TEDA impregnated AC) [124]. Then, the dissociated methyl group CH_3 tends to form a TEDA-CH_3 complex through an ionic bond with TEDA, while the dissociated iodine has chemical interactions with both the impregnated AC surfaces and the TEDA (Figure 16), corresponding to the formation of the quaternary ammonium salt [124].

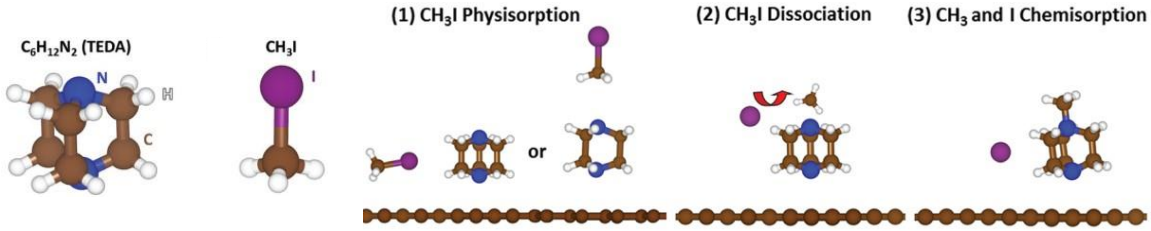

Figure 16. Schematic figures for each reaction step on AC impregnated with TEDA [124]

In humid condition, it is firstly proposed experimentally by K. Ho *et al.* [63] that TEDA combined with condensed water located in the pores of the AC surface promotes the alkylation of CH_3I, resulting in a strong chemisorption. However, a later study using DFT calculations has proposed a different mechanism of the CH_3I retention by protonation mechanism in humid conditions rather than the previously known alkylation mechanisms in dry conditions [131]. More precisely, the potential energy profile of the protonation mechanism is found to be lower than the previous alkylation mechanism under humid conditions (Figure 17), indicating that the chemical interaction of TEDA with CH_3I is significantly enhanced with the presence of H_2O. The reaction of CH_3I with TEDA in the presence of water can be written as below [131]:

$$CH_3I + H_2O + TEDA = CH_3OH + I^- - (H - TEDA)^+ \quad (16)$$

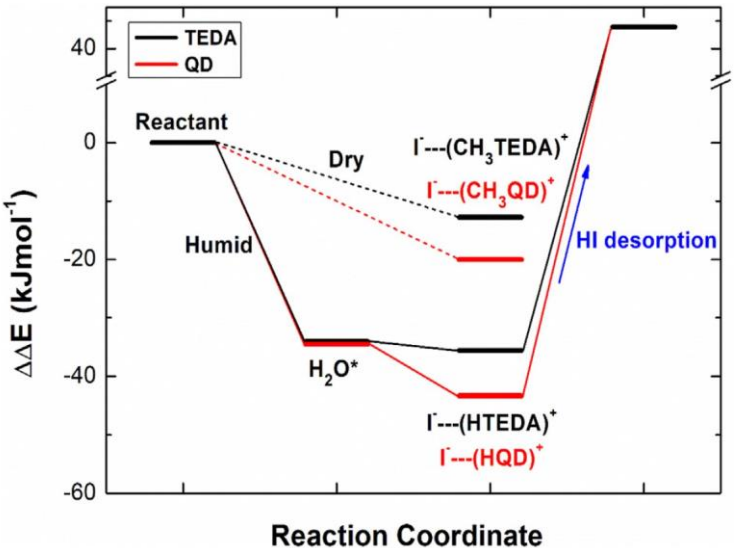

Figure 17. Proposed potential energy profile for the reaction of TEDA with CH_3I under dry and humid conditions [131]

To sum-up, the TEDA impregnation improves the chemisorption of CH_3I through dissociation in dry condition, leading to the improvement of the adsorption performance. Besides, in humid condition, TEDA is able to counterbalance the detrimental effect of humidity on the adsorption capacities of AC by freeing the active sites of the support through the protonation mechanism.

Potassium iodide (KI)

The melting point and boiling point of KI are 686 °C and 1330 °C, respectively. It is used as an impregnant in the AC to improve its adsorption performance through the isotopic reaction as follows:

$$CH_3^{131}I_{(gas)} + K^{127}I_{(ads)} = CH_3^{127}I_{(gas)} + K^{131}I_{(ads)} \quad (17)$$

Because of the reversible nature of this reaction, it is necessary to have an excess amount of reactant ($K^{127}I$ in the solid phase) to guarantee the efficient capture of radioactive iodine species. This condition is generally achieved since the total inlet CH_3I concentration in the nuclear facilities is ranging from 0.1 to 1 ppmv [60], as a comparison with the $K^{127}I$ amount (about 1 w.t% [43]).

According to F. Kepal *et al.* [26], this reaction can proceed until equilibrium when the isotopic composition of iodine in the impregnate is the same as that of iodine in the gaseous phase. However, due to the radioactive decay of $^{131}1$ (half-life of 8.02 days) and other short-lived iodine isotopes, the equilibrium system is perturbed and the isotopic exchange can continue. The $CH_3{}^{131}I$trapping process using KI was reported to be composed of different steps [132]:

- diffusion of active form to the grain surface;
- diffusion of active form into the pores;
- physical adsorption of active form;
- isotopic exchange reaction;
- desorption of inactive form from the surface;
- diffusion of stable form from pores;
- diffusion of stable form into the gas phase.

In general, the mechanism of the isotopic exchange led by KI within the AC has not been studied in a detailed way apart from the theoretical considerations proposed above, which justifies the interest of this PhD project.

4.2.3.2 Quantification of the different adsorption mechanisms

As mentioned before, there are three different mechanisms for the trapping of CH_3I by KI/TEDA impregnated AC: physisorption, chemisorption and isotopic exchange. Previous works were performed to quantify the physisorption and the chemisorption. G. I. Park *et al.* [78] quantified the physisorption and the chemisorption of CH_3I for TEDA-impregnated AC by changing the temperature of the AC after the adsorption experiments. It is concluded that the desorption amount and the residual amount correspond to the physisorption and the chemisorption, respectively [78].

In the context of severe nuclear accident, B. Azambre *et al.* [133] performed a temperature-programmed desorption (TPD) on different types of silver-exchanged zeolites to quantify the relative contribution of the different mechanisms involved during CH_3I uptake by these adsorbents (physisorption, chemisorption and AgI precipitation [134]). The schematic view of the TPD principle is presented in Figure 18. More precisely, an adsorption phase is first performed for a given zeolitic sorbent. The blue area calculated from the BTC corresponds to the total adsorption

capacity. After saturation, an evacuation step was performed under argon at the same temperature until the elimination of physisorbed species. The related purple area corresponds to the physisorption fraction. Afterwards, the zeolitic bed was heated progressively up to 500 °C under argon. The orange area calculated in this period corresponds to the chemisorption fraction. The fraction of trapped CH_3I as silver iodide precipitates was then deduced from the following mass balance:

$$Q_{AgI} = Q_{sat} - (Q_{phys} + Q_{chem}) \quad (18)$$

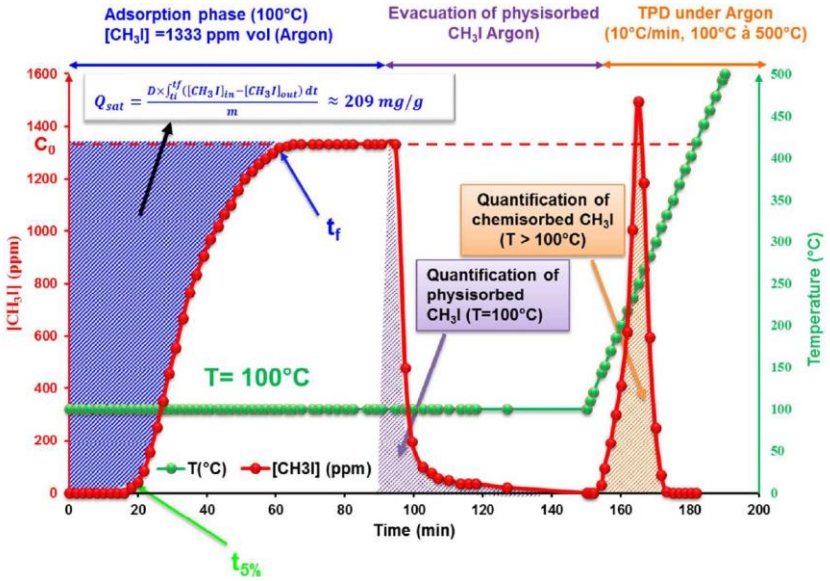

Figure 18. TPD for the study of adsorption and desorption of CH_3I by Ag-Y zeolite ([CH_3I] = 1333 ppm, T = 100°C, dry conditions) [133]

However, to the best of our knowledge, the quantification of the isotopic exchange for the KI-impregnated AC remains unknown. There are only few studies related to the isotopic exchange quantification. Experimentally, the comparison of $CH_3{}^{127}I$ and $CH_3{}^{131}I$ penetrations (C_{outlet}/C_{inlet}) on a 5 w.t% KI_3 (equal amount of KI and I_2) impregnated AC was performed by G. O. Wood *et al.* [135]. As shown in Figure 19 [135], the difference of the cumulative penetrations between the radioactive and stable CH_3I increases progressively after breakthrough, which justifies the presence of isotopic exchange during the dynamic adsorption experiment. However, due to the lack of original data (such as the isotopic dilution), the effect of the isotopic exchange cannot be quantified. Detailed discussion regarding the effect of the isotopic exchange linked to this publication is presented in the chapters III and IV. Furthermore, as depicted in Figure 20 (a), the

plot of $CH_3{}^{131}I$ penetration versus residence time indicated that the $CH_3{}^{131}I$ removal is governed by a simple first order reaction with a rate coefficient of about 3.62 s^{-1}. Besides, the penetration of the $CH_3{}^{131}I$ and total CH_3I are compared for TEDA impregnated AC (Figure 20(b)). It is found that, as expected, CH_3I and $CH_3{}^{131}I$ are removed at equal efficiencies by reaction with TEDA, which highlighted the absence of the isotopic exchange for the TEDA impregnated AC.

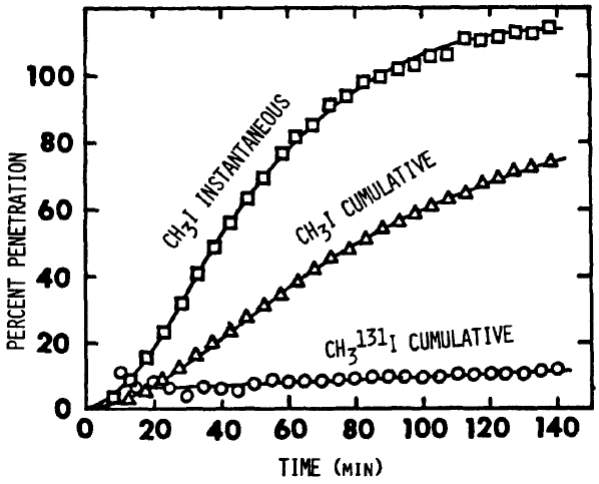

Figure 19. Comparisons of $CH_3{}^{127}I$ and $CH_3{}^{131}I$ penetrations on a 5% KI_3 AC (4625 $Bq \cdot m^{-3}$ of $CH_3{}^{131}I$, RH = 86 %, residence time = 0.75 s, linear velocity = 6.6 $cm \cdot s^{-1}$) [135]

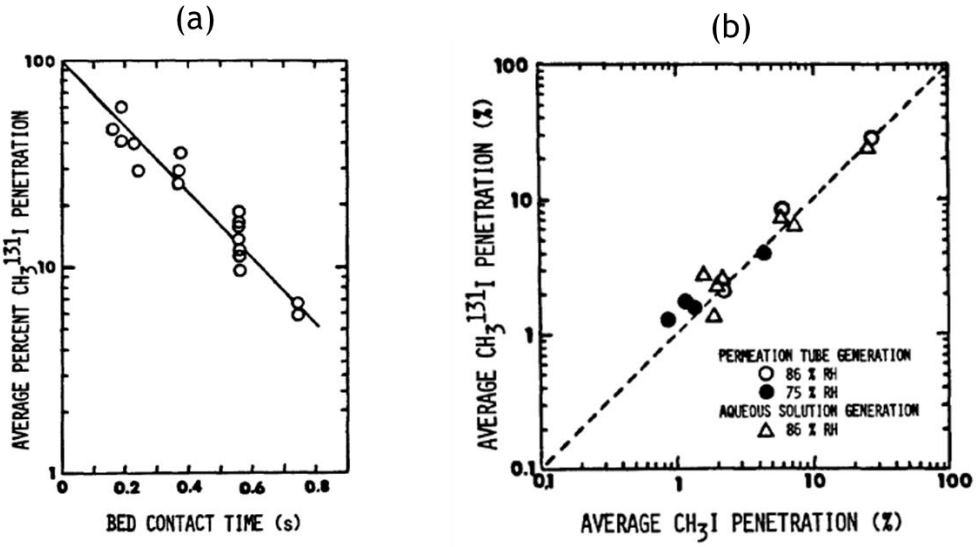

Figure 20. (a) First order rate plot for $CH_3{}^{131}I$ penetration through 5% KI_3 activated carbon; (b) Comparisons of $CH_3{}^{131}I$ and total CH_3I penetrations through TEDA impregnated AC [135]

5. Conclusion and summary of the thesis objectives

This chapter presents global information on the CH_3I retention by AC. Representing one of the largest parts of released radioactivity for the nuclear facility, the radioactive CH_3I receives significant attention for its retention in nuclear facility using AC as adsorbent in the ventilation system. This material with high porosity (around 1000 $m^2 \cdot g^{-1}$) is often impregnated with KI or/and TEDA (less than 5 w.t% of TEDA and 1 w.t% of KI in nuclear facilities) to enhance the trapping stability and efficiency towards iodine species, especially under humid conditions. A variety of studies has been performed to investigate the retention of CH_3I through different aspects regarding the adsorbent properties as well as the operating conditions. In general, RH has a negative effect on the performance of CH_3I retention due to the competitive adsorption between H_2O and CH_3I. However, the temperature effect leads to desperate results according to different test methodologies. One the one hand, a decrease of the global adsorption capacity owing to the reduction of the physisorption was reported, and this decrease is accompanied by the enhancement of the fraction of chemisorption. On the other hand, an increase of the retention performances was observed using standardized tests in the nuclear context owing to the enhancement of the isotopic exchange rates as well as the chemical reactivity with TEDA. More particularly, the mechanism of the chemisorption of TEDA which was finely investigated, is found to be dependent on the RH (alkylation mechanism under dry conditions and the protonation mechanism under humid conditions). On the contrary, few information about the mechanism of the isotopic exchange by KI is reported in the literature, with only one publication that shows a progressive improvement of the trapping performance of the KI_3 impregnated AC after breakthrough under humid conditions.

Numerous studies have been carried out for the iodine filters since the 1970s, corresponding to the massive industrial application of these adsorbents. Then, the academic research ceased around the beginning of the 21st century, making it very difficult to extrapolate these data to areas that have not been explored experimentally. Since the Fukushima disaster in 2011, there has been renewed interest in R&D to improve the existing mitigation technologies in order to limit the radiotoxic releases into the environment in different scenarios. Despite the extensive and historic use of KI impregnated AC within the ventilation networks, some scientific and technological obstacles remained unsolved:

1. Systematic studies of the intrinsic AC characteristics (textural properties, impregnants content and speciation) towards the trapping performance of the γ-labelled CH_3I through standardized tests are rarely investigated. The current investigations of the AC characteristics towards their adsorption performances remain generally at the laboratory scale through BTC or adsorption isotherms. The existing publications based on the DF measurement following standardized procedures are rarely focused on the influence of the intrinsic properties of the adsorbent. In addition, recent studies of the AC performance are mainly focused on the TEDA impregnated AC with limited impregnation ratios, and no structure - activity correlation were determined. Based on this context:

- In Chapter II, the physico-chemical characteristics of the different AC (impregnant quantity, chemical and surface composition, porous structure and the adsorption behavior towards H_2O) are finely investigated using different techniques;
- In Chapter III, the AC performance towards the trapping of γ-labelled CH_3I is evaluated using the normalized DF measurement on a large panel of material configurations (unimpregnated AC, KI and/or TEDA impregnated AC). The objective was to investigate the effect of impregnants separately under semi-pilot conditions, which is rarely studied in the literature with either non-radioactive tests or with limited contents of TEDA or KI. More particularly, the DFs towards γ-labelled CH_3I is discussed depending on the water vapor content. The main objective was to establish relationships between the adsorbent characteristics (data of Chapter II) and its retention properties depending on the studied conditions. Insights about the occurrence of isotopic exchange reaction considering the normalized protocol are also presented for KI impregnated AC.

2. The postulated retention mechanism using KI (isotopic exchange) is rarely studied in the literature and several uncertainties are persisting about the mechanism but also on its contribution for the total CH_3I uptake. The final objective of this PhD project is to quantify the contribution due to this reaction for the trapping of γ-labelled CH_3I by KI impregnated AC, by attempting to studying separately the involved mechanisms. Hence,

- In Chapter IV, a new experimental setup along with a novel testing methodology is developed for the comparison of BTC between stable and γ-labelled CH_3I. The

comparative study performed on different KI contents, will allow to present first important elements about the temporal evolution of this mechanism contribution, considering a given condition in terms of temperature and RH.

- The quantification of this mechanism is of great interest for the nuclear safety and radioprotection field. Indeed, such a quantification will allow the possibility to evaluate a "safety coefficient" to be taken into account when determining a DF based only on the physisorption or the chemisorption of TEDA in different conditions. In this way, a novel "non-radioactive test methodology for the iodine trap" can be considered in the future to limit the release of radioactive iodine into the environment.

Chapter II: Physico-chemical characterization of AC

1. Introduction

In this chapter, a specific attention is devoted to the characterization of the AC by a combination of physico-chemical analyses. The principal objective is to probe the main characteristic parameters (chemical composition, morphology and porous structure) of the starting materials that may influence CH_3I removal efficiency. Firstly, experimental protocols about the different techniques used are presented. The results obtained are presented afterwards. More particularly, information about impregnant (TEDA, KI) amount is presented as deduced from an extraction procedure followed by UV-Visible spectroscopic analysis. Complementary insights about the surface composition as well as the morphology of some of the tested adsorbents are deduced from XRD, XPS and SEM/EDX characterizations. Finally, the porous structure of the different impregnated AC is discussed from N_2 porosimetry at 77 K and H_2O adsorption isotherms at 25 °C.

2. Summary of AC samples

Different formulations of commercial AC (grain size ranging from 2 to 3 mm) are used in this study. The studied materials derived from coco-nut shells were supposed to present well-developed microporosity (d_{pore} < 2 nm [50]), enhancing CH_3I removal by physisorption phenomena. These AC were then impregnated with potassium iodide (KI) and/or triethylenediamine (TEDA) in order to improve their performances towards CH_3I trapping. However, few details were provided regarding the exact synthesis protocol as well as the precise impregnation ratio. Hence, the physicochemical properties of the AC should be characterized in order to reveal the parameters that potentially influence their performances for CH_3I removal:

- Impregnant quantity and speciation;
- Surface morphology;
- Porous structure.

It is worth recalling that all these AC were produced in the same batch in order to limit the dispersions between the AC characteristics. The impregnation ratio of each AC, as reported by the manufacturer, is summarized in Table 16.

Table 16. Summary of the impregnation ratio of the activated carbons used in this PhD project

KI impregnation (w.t%)	TEDA impregnation (w.t%)	Co-impregnation	
		KI (w.t%)	TEDA (w.t%)
0.1	1	0.5	1, 5, 10
0.5	3	1	1, 5, 10
1	5	2	1, 5, 10
2	7		
5	10		

3. Experimental procedures and techniques

In this section, the theoretical principles and experimental protocols of the different physicochemical techniques used to characterize the AC mentioned above is described.

3.1 Determination of KI and TEDA contents

All these commercial AC used in this PhD project are referenced with a factory-made impregnation ratio. Therefore, their actual values should be experimentally verified. The impregnant quantity (KI and TEDA) are determined in this study, using analytical methods based on the extraction from the liquid phase. The principle is to find a solvent capable of extracting with high efficiency KI and TEDA from AC for further analysis without inducing a significant chemical modification of the molecules to be analyzed, especially for selective techniques such as spectroscopic or electrochemical measurements. First, preliminary studies focused on the use of deionized water as a solvent for KI extraction from some impregnated AC. The extraction protocol can be summarized as the following:

- Add 10 g of KI-impregnated AC to 200 mL of deionized water;
- Stirring for overnight at room temperature;
- Recover the solution by filtration.

The iodide concentration in the filtered solution is then analyzed using an iodide-selective electrode. Comparison with global iodine measurements as deduced from ICP-MS analysis was also performed within the *Filab* laboratory. The corresponding KI contents were then deduced assuming a molar ratio I/K about 1. The obtained experimental results of KI loadings for 0.5%KI AC and 5%KI AC are reported in Table 17.

Table 17. Preliminary results of KI contents determination for some KI/AC

AC type	KI% from iodide ion-selective electrode	KI% from ICP-MS
0.5% KI	0.11%	0.15%
5% KI	1.98%	2.81%

From the data gathered in Table 17, a poor recovery fraction (20 - 30% for 0.5%KI AC and 40-60% for 5%KI AC) can be determined using the tested analytical methods. These results are attributed to the solvent nature. Indeed, the well-known hydrophobicity character of AC [136] makes water inappropriate for the extraction from these medias. Based on the literature [137], another extraction method using acetonitrile as a solvent and analysis by ultraviolet–visible spectroscopy was considered. The steps of the extraction protocol are similar to the previous water extraction:

- Add 0.5 g of impregnated AC to 100 mL of acetonitrile;
- Extract overnight at room temperature;
- Recover the solution by filtration and KI or TEDA measurements using ultraviolet–visible spectroscopy.

The impregnant concentration determination is based on the Beer-Lambert law [138]:

$$A_\lambda = \varepsilon_\lambda l c_\lambda \tag{19}$$

Where A_λ absorbance of the medium at wavelength λ;
ε_λ specific coefficient of molar absorbance ($L \cdot mole^{-1} \cdot cm^{-1}$ or $L \cdot mg^{-1} \cdot cm^{-1}$);
l optical path of the cell (cm);
c_λ concentration of molecules that absorb at wavelength λ ($mol \cdot L^{-1}$ or $mg \cdot L^{-1}$).

Firstly, the feasibility of this method using ultraviolet–visible spectroscopy (Figure 21) is investigated for both KI and TEDA. As presented in Figure 21, the absorbances of TEDA (λ = 225 nm) and KI (λ = 247 nm) in acetonitrile both explicit a good linearity (R^2 > 0.999), with a measuring concentration range between 20 – 100 mg·L^{-1} and 5 – 20 mg·L^{-1} for TEDA and KI, respectively.

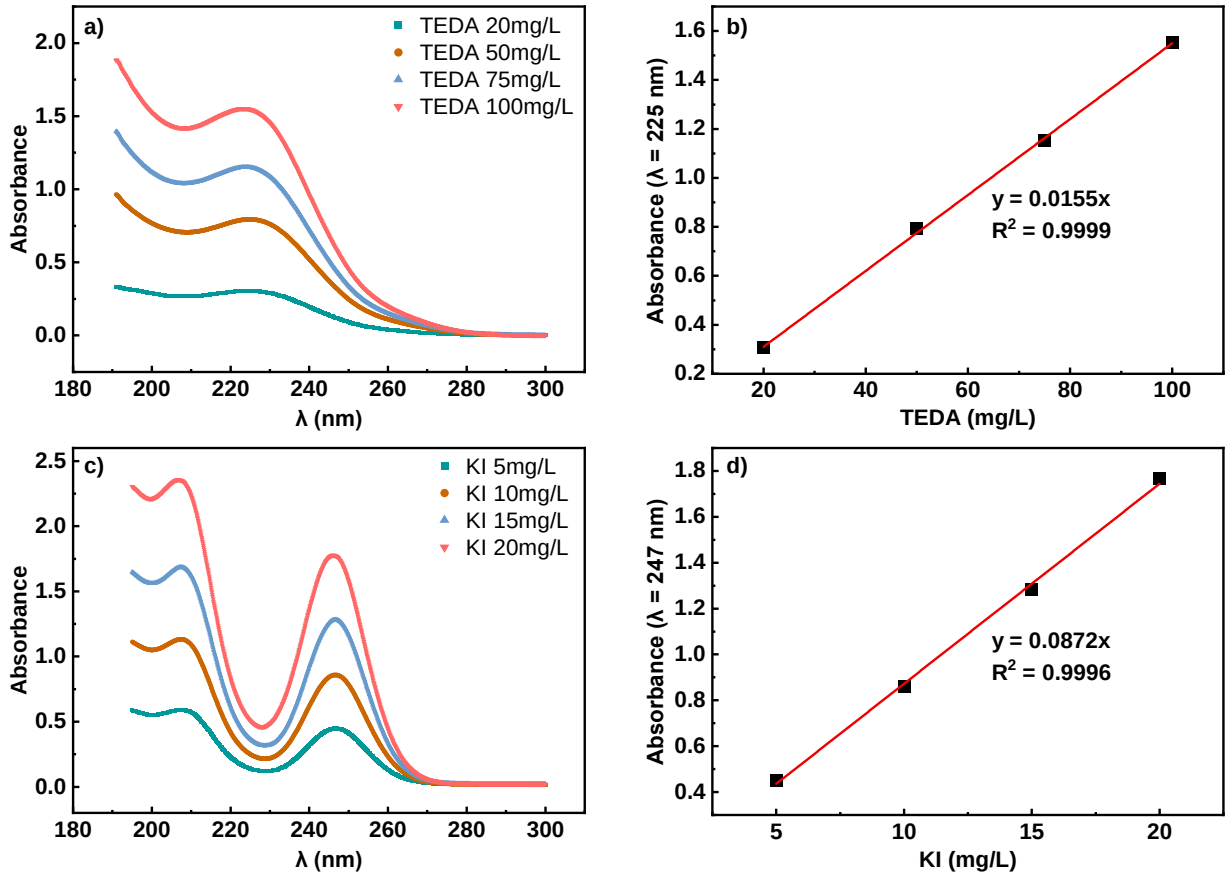

Figure 21. (a) TEDA spectra in acetonitrile for different concentrations (20 - 100 mg·L^{-1}); (b) Corresponding TEDA calibration equation at λ = 225 nm; (c) KI spectra in acetonitrile for different concentrations (5 - 20 mg·L^{-1}); (d) Corresponding calibration equation for KI at λ = 247 nm

In addition, the accuracy of this method was validated using homemade KI or TEDA impregnated AC. The details of the impregnation and extraction conditions are summarized in Appendix 1. It was found that the extraction method using acetonitrile is efficient for both KI and TEDA, with an extraction efficiency higher than 90%.

Nevertheless, precautions were taken for the impregnant analysis. Firstly, a progressive yellow coloration of the solution was observed for increasing KI contents, as depicted in Appendix 2. This yellow coloration may arise from iodide ions (I^-) oxidation leading to the formation of I_2 and I_3^- species. The corresponding KI content will be therefore underestimated. Accordingly, a large excess (mass = 0.5 g) of sodium thiosulfate ($Na_2S_2O_3$) was added during the extraction experiment to avoid such oxidation phenomena. The $Na_2S_2O_3$ introduction allows to preserve the iodide ions I^- speciation as depicted from the correspondent spectrum (Figure 22 (a)), as well as the transparent aspect of the solution during KI extractions.

Secondly, for the co-impregnated AC, the interference between KI and TEDA during extraction may occur for certain impregnation ratio (Figure 22 (b)). Hence, the subtraction of each molecule spectral contribution was made for co-impregnated AC. More precisely, the calibration equations for both KI and TEDA were determined at both λ = 225 and 247 nm. For a given co-impregnated AC, two equations at both λ = 225 and 247 nm can be made containing the unknown concentration of KI and TEDA, using the four calibration equations previously determined (Appendix 3).

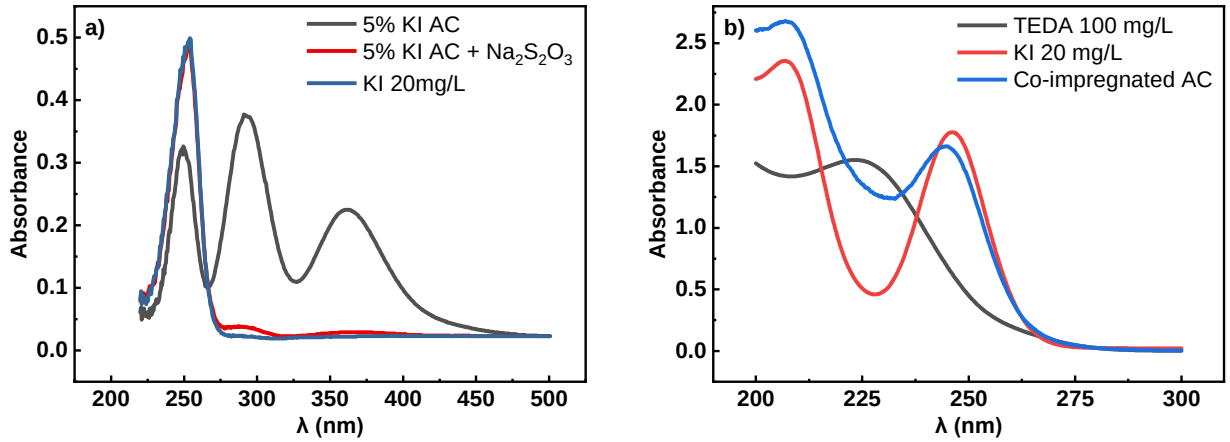

Figure 22. (a) Influence of $Na_2S_2O_3$ during KI extraction; (b) Interference of KI and TEDA during extraction

3.2 Porosimetry with nitrogen at 77 K

3.2.1 Experimental procedure

The N_2 porosimetry at 77 K is used to probe the porous structure of the AC including their specific surface areas, microporous volumes, microporous size distributions as well as total porous

volumes. It is based on the multilayer adsorption of nitrogen on a solid surface at its liquefaction temperature. As shown in Figure 23, the device is composed of three analysis ports, which allows three independent measurements simultaneously. However, only 1 port capable for microporosity measurement (port n°2), was used during the present study in agreement with the expected microporosity for the tested adsorbents. During the measurement, the AC sample (around 100 mg) placed in the measurement chamber is immersed in liquid N_2 at 77 K and the N_2 adsorption/desorption isotherms are recorded. The free volume of the measurement chamber is measured before the N_2-adsorption/desorption using helium at both ambient temperature and 77 K.

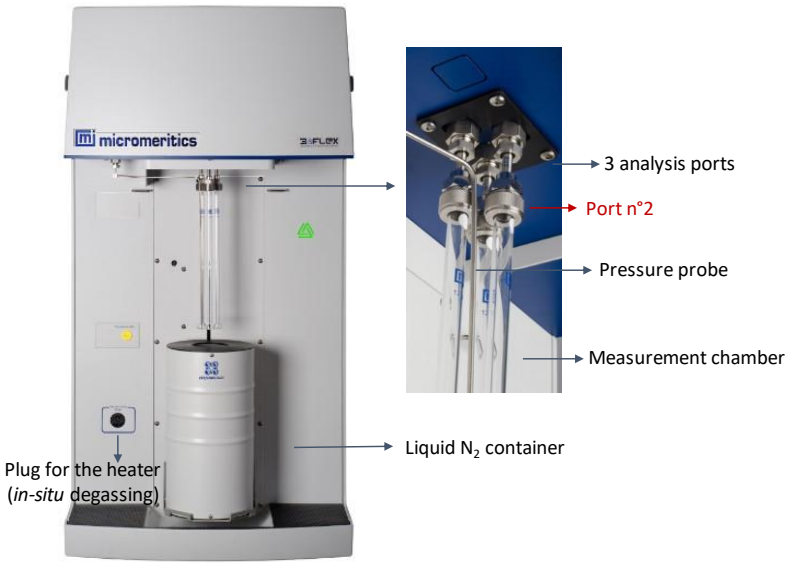

Figure 23. Device used for the N_2-adsorption/desorption analysis (*3FLEX, Micromeritics*)

It should be noticed that the conditioning of the samples before measurement and an appropriate relative pressure program play an important role in the porosity characterization. On the one hand, the micropores of AC are reported to be easily filled with water vapor even in ambient atmosphere [123]. Hence, it is necessary to remove all the moisture content in order to guarantee a good measurement. After different attempts of optimization, a protocol for the conditioning of AC can be summarized as followings:

- *Ex-situ* heating at 120 °C for at least 8 hours;
- *In-situ* degassing until 10^{-5} mbar at 120 °C for 12 hours (heating rate = 5 °C·min^{-1}).

The heating temperature is set to 120 °C to maintain the thermal stability of the impregnants according to TGA [139][140] or py-GCMS [140] investigations on TEDA/AC, and to remain below the melting temperature of these molecules (681 °C and 158 °C for KI and TEDA respectively [141][142]).

On the other hand, a dedicated relative pressure program for microporous adsorbents was inplemented in agreement with the expected nature of the tested AC. More precisely, a specific attention was devoted to monitor with accuracy the pores filling through a predefined criterion to move from a given p/p_0 to another value. Depending on the (p/p_0) range, this criterion was controlled by a given N_2 dose amount and/or a (p/p_0) increment. The relative pressure program used in this PhD project is presented in Table 18.

Table 18. The relative pressure program for the N_2-adsorption/desorption analysis

	Starting pressure (p/p_0)	Pressure increment (p/p_0)	Dose amount (cm^3/g STP)	Equilibration internals (s)	Ending pressure (p/p_0)
1	0		15	20	0.01
2	0.01	0.05	10	10	0.99
3	0.99	0.05	10	10	0.35

Using the aforementioned protocol, adsorption isotherms were measured with good precision. An example for the 0.5% KI AC is presented in the Appendix 4, which exhibits a type I isotherm, characteristic of microporous materials [143].

3.2.2 Exploitation of an adsorption and desorption isotherm

From a given N_2 adsorption/desorption isotherm, different porous characteristics of the AC samples can be determined such as specific surface area, microporous volume, micropore width and the total pore volume. The methods employed for the data processing are presented in the followings:

Determination of specific surface area using the BET method

Specific surface area can be defined as that portion of the total surface area that is available for adsorption of a material per unit of adsorbent mass, a parameter largely used for the porosity characterization of an adsorbent. Among all the possible theories for specific surface area

determination (t-plot method, DR method, etc), Brunauer–Emmett–Teller (BET) theory is the most commonly used to determine this parameter for porous materials [144]. The BET theory describes the multilayer adsorption phenomena, where every adsorption layer is governed by the Langmuir formalism (Appendix 5). The BET equation is used in principle in the monolayer domain (p/p_0 between 0.05 and 0.35) as follows [144]:

$$\frac{1}{n^a \times \left(\frac{p_0}{p} - 1\right)} = \frac{1}{n_m^a \times C_{BET}} + \left[\frac{C_{BET} - 1}{n_m^a \times C_{BET}}\right]\left(\frac{p}{p_0}\right) \quad (20)$$

Where
- n^a amount of adsorbed substance per gram of adsorbent ($mol \cdot g^{-1}$);
- n^a_m amount of adsorbable substance necessary to cover the surface of the solid with a monomolecular layer ($mol \cdot g^{-1}$);
- C_{BET} BET constant according to the relation: $C_{BET} = exp((E_1-E_{liq})/RT)$;
- E_1 molar energy of adsorption of the first layer ($kJ \cdot mol^{-1}$);
- E_{liq} molar energy of liquefaction of the adsorbate ($kJ \cdot mol^{-1}$);
- R gas constant (8.314 $J \cdot K^{-1} \cdot mol^{-1}$);
- T temperature of adsorption (K).
- p partial saturation pressure of the adsorptive gas in equilibrium (Pa);
- p_0 gas saturation pressure (Pa).

When the surface of one gram of solid is completely covered with a layer of adsorbed molecules (Appendix 5), its specific surface area (S_{BET}) can be calculated from the following expression [145]:

$$S_{BET} = n_m^a N_A \sigma_m \quad (21)$$

Here N_A is the Avogadro constant, and σ_m is the area occupied by a N_2 molecule adsorbed on the surface of the solid covered with a monomolecular layer (m^2).

However, it should be noticed that the relative pressure range (p/p_0) proposed by S. Brunauer *et al.* [144] for BET measurement is between 0.05 and 0.35, which is based on the absence of micropores or of any other type of strongly adsorbing sites. For microporous materials, it is difficult to separate the processes of monolayer-multilayer adsorption and micropore filling [143]. Hence, the concept of the monomolecular layer content (n^a_m) in the S_{BET} calculation is inadequate in the presence of micropores where a monolayer has no clear physical or theoretical meaning. Still, the S_{BET} is largely used in the academic field even for microporous materials. Recently, a

new formalism has been proposed by J. Rouquerol [146] in order to extrapolate the applicability of the BET method to microporous adsorbents. This formalism is based on the following criteria:

(i) The term $n^a(1 - p/p_0)$ should continuously increase with p/p_0;

(ii) The deduced n^a_m should be corresponding to a $(p/p_0)_m$ located within the relative pressure range selected for the calculation;

(iii) Alternatively, the $(p/p_0)_m$ can also be recalculated from the Eq. (20) by replacing n^a to n^a_m. The recalculated $(p/p_0)_m$ should be close to that of (ii) with a variation of less than 10%.

An automatic assistance system (*Autofit BET*) already implemented in the software is used to take into account these criteria. An example of the autofit BET calculation is showed in Figure 24 for 0.5%KI AC. It is found that these criteria are allowed to determine automatically the specific surface area of such microporous materials avoiding subjective selection of the pressure range. The determined specific surface area is 1171 $m^2 \cdot g^{-1}$ (Figure 24), which is higher than the value deduced from classic pressure range between 0.05 and 0.35 (873 $m^2 \cdot g^{-1}$). Therefore, an automatic assistance system (*Autofit BET*) using the aforementioned calculation methods is used for all the presented specific surface areas during the present work.

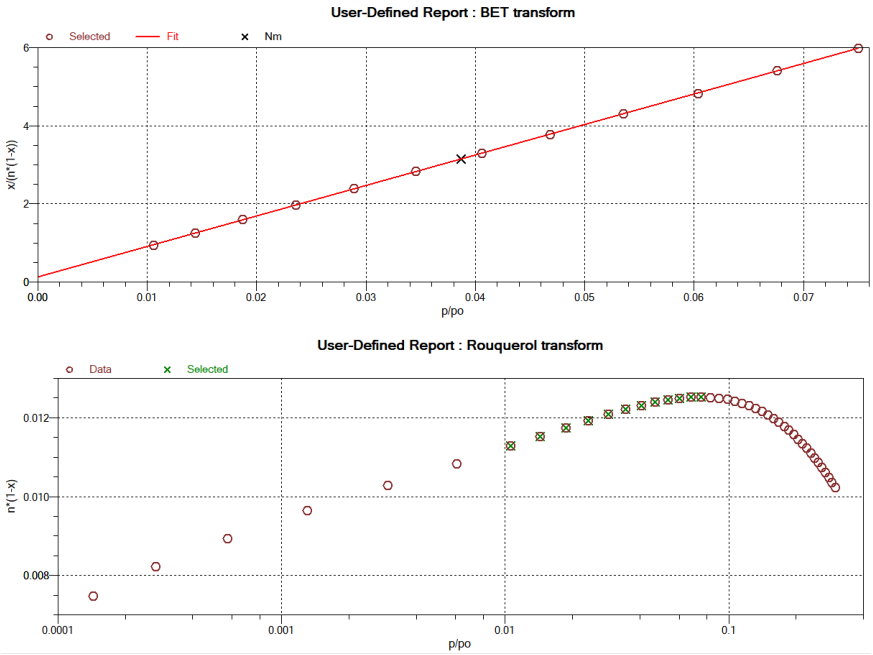

Figure 24. Example of BET calculation for an activated carbon impregnated with 0.5% KI through the Rouquerol criterion

Micropore size distribution analysis

The micropore size distribution analysis for AC is of great importance since the micropores play an important role for the CH_3I retention. Here, the Horvath-Kawazoe (HK) method [147] is employed. As a semi-empirical method, the HK method is largely used to determine the micropore size distribution of the carbonaceous materials using the following expression [147]:

$$\ln\left(\frac{p}{p^0}\right) = \frac{61.23}{(w-0.64)}\left[\frac{1.895\times10^{-3}}{(w-0.64)^3} - \frac{2.709\times10^{-7}}{(w-0.32)^9} - 0.05014\right] \quad (22)$$

Where w is the pore width (nm).

The evolution of the adsorbed volume towards the pore width can then be deduced using the aforementioned expression and the obtained adsorption isotherms. The differentiation of adsorbed gas volume with respect to the effective pore width yields a pore size distribution in the micropore range. Similarly, the micropore volume can be determined using the same expression by selecting effective pore widths in the micropore range (pore width until 2 nm). An example of the micropore size distribution is shown in Appendix 6.

Determination of the total volume

The total pore volume for a micro or mesoporous material can be directly calculated by assuming that pores are filled with liquid adsorbate at a relative pressure close to unity ($0.95 < p/p_0 < 1$) [148]. The total pore volume is expressed as follow:

$$V_{pore} = \frac{pV_{ads}V_m}{RT} = 0.001547 \times V_{ads} \quad (23)$$

Here p and T are the pressure and the temperature in STP conditions, and V_m is the molar volume of the liquid adsorbate (34.65 $cm^3 \cdot mol^{-1}$ for nitrogen at 77K [149]). V_{pore} is calculated from the amount of vapor adsorbed on the adsorption isotherms corresponding to $p/p_0 = 0.99$ all along the present study.

3.3 Water adsorption isotherms

H_2O adsorption isotherms were performed for some AC using a dynamic vapor sorption (DVS) Vacuum microbalance (Surface Measurement Systems, SMS). The objective is to investigate the influence of the water vapor content towards the CH_3I removal for AC, which is known to be highly sensitive to the humidity [7]. Prior to each sorption test, AC samples (mass = 60 - 70 mg) were outgassed at mild conditions (60 °C, 15 hours, vacuum of 10^{-5} Torr) to eliminate the residual humidity without inducing a significant modification of their surface chemistry according to recent works of L. F. Velasco et *al.* [150]. Then, gravimetric measurements are carried out for RH ranging from 0% to 95 % at 25°C. The thermodynamic equilibration for each tested RH was assumed when a mass change of less than 0.0004 % per minute was obtained.

3.4 Characterizations in collaboration

Complementary characterizations were performed within the (CINaM-CNRS) to probe additional information about the morphology, structure as well as surface composition.

X-ray photoelectron spectroscopy (XPS)

X-ray photoelectron spectroscopy (XPS) analysis were performed for some AC to gain insights on the chemical surface groups of the tested sorbents including the impregnants. The XPS

experiments were carried out by Philippe PARENT and Carine LAFFON (CINaM-CNRS). The corresponding experimental setup as well as the protocols are presented in Appendix 7.

Scanning Electron Microscopy (SEM)

The morphology of the AC as well as their surface state were also studied by scanning electron microscopy. The SEM experiments were performed by Olivier GRAUBY (CINaM-CNRS). The experimental protocols are presented in Appendix 8.

X-ray diffraction (XRD)

The X-ray diffraction is used to qualitatively assess the crystallinity of the AC (through the reduction of certain structural peaks) as well as the identification of the possible presence of the impregnants. The XRD experiments were performed by Olivier GRAUBY (CINaM-CNRS). The experimental protocols are presented in Appendix 9.

4. Results and discussion

4.1 Chemical composition

The impregnant quantities of KI and TEDA determined according to the above extraction protocol (Section 3.1) are summarized in Table 19. The deduced molar impregnation evolutions as a function of theoretical data are presented in Figure 25 as average values from three replicates (with k = 2) except for the co-impregnated AC. A quasi-linear relationship can be noticed when comparing experimental and theoretical contents for all the tested AC. Nevertheless, a deviation of 23%, 15% and 27% from the theoretical amount was found for the tested TEDA, KI and co impregnated AC respectively (Figure 25). For example, contents of 0.69 w.t% and 3.85 w.t% were measured for KI and TEDA, respectively, for theoretical contents of 1 w.t% (KI) and 5 w.t% (TEDA) (Table 19). Besides, the absence of KI and TEDA molecules was checked for the unimpregnated AC.

These results were then compared with CHNS analysis (up to six repetitions) performed to validate this methodology for TEDA content in some AC (Appendix 10). The corresponding TEDA contents display some variations due to the heterogeneities of the tested AC and the very low quantity used for this technique (0.5 - 1 mg). Nevertheless, the calculated TEDA loadings as

deduced from the nitrogen quantity were found to be rather close to the expected loadings (Appendix 10). This discrepancy may be related to the presence of more bonded (*i.e.* chemisorbed) molecules that cannot be evidenced by the selected extraction method. Indeed, the molecular diameter of the acetonitrile (0.652 nm [151]) is found to be slightly higher than the pore width of the tested AC (about 0.5 nm in Section 4.3), indicating that the accessibility of the acetonitrile towards certain KI or TEDA sites may be hindered. These strongly bonded or inaccessible molecules can be nevertheless measured by CHNS technique based on a combustion step followed by chromatographic measurements. According to the further exchanges with the AC supplier, all the tested AC were impregnated using specific impregnation protocols (Chemical Vapor Deposition process for example [152]) leading possibly to inaccessible fraction of TEDA and KI molecules using acetonitrile extraction method. Considering the non-measurable TEDA and KI by acetonitrile and the quasi-similar deviation of about 20%, it can be concluded that KI and TEDA are well impregnated in terms of quantity. Most importantly, this quasi-linear evolution between experimental and expected contents allows to use the contents reported by the manufacturer in the following parts of the manuscript for a sake of simplicity.

Table 19. Summary of the impregnation determination from acetonitrile extraction for different AC.

Expected impregnation (w.t%)		Measured impregnation (w.t%)	
KI	TEDA	KI	TEDA
0.1	0	0.07 ± 0.011	0
0.5	0	0.37 ± 0.014	0
1	0	0.69 ± 0.080	0
2	0	1.82 ± 0.13	0
5	0	4.23 ± 0.24	0
0	1	0	0.83 ± 0.16
0	3	0	2.2 ± 0.19
0	5	0	3.8 ± 0.46
0	7	0	5.5 ± 0.52
0	10	0	7.7 ± 1.08
0.5	1	0.38	0.80
0.5	5	0.43	3.7
0.5	10	0.38	7.1
1	1	0.55	0.76
1	5	0.74	3.3
1	10	0.71	6.8
2	1	1.5	1.7
2	5	2.0	4.7
2	10	1.5	7.1

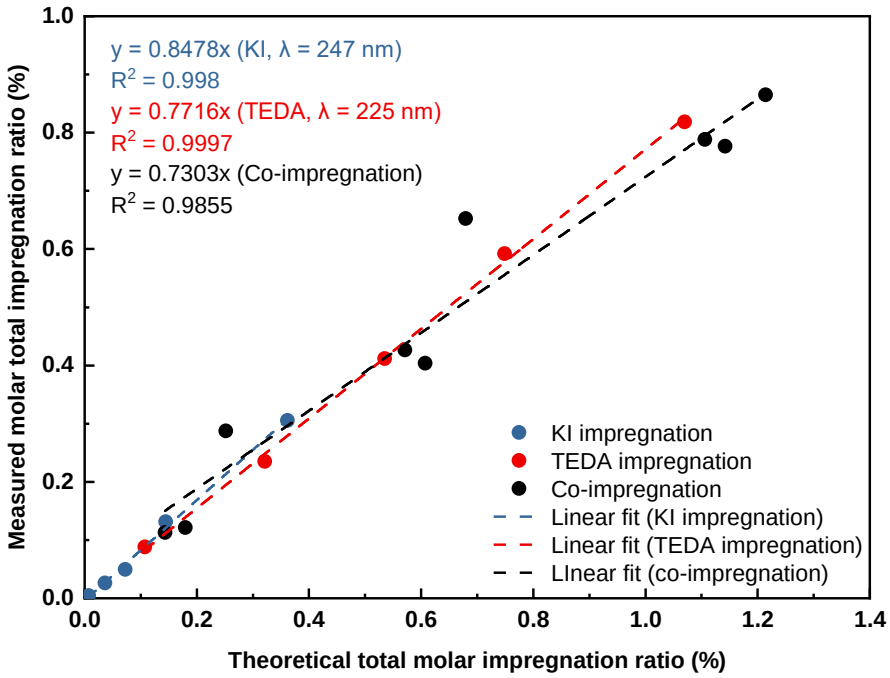

Figure 25. Measured molar impregnation evolution for different AC compared to the "theoretical" impregnation (as reported by the manufacturer)

4.2 Surface composition

Apart from the impregnant quantity, additional information regarding the element speciation (N, K, I, etc.) and the AC surface composition can be deduced from the XPS spectra presented in Figure 26 and Figure 27. As expected, the samples considered are mainly carbonaceous (88 - 90 at.% in carbon), in agreement with the CHNS analysis (Appendix 10). Other elements resulting from the raw material and the further production steps can also be evidenced. We notice, namely, the presence of oxygen (8 - 10 at.%), nitrogen (0.5 - 2 at.%), potassium (0.2 - 1.1 at.%) and iodine (0.1 - 0.5 at.%).

The semi-quantitative analysis using XPS gives also evidence for KI and TEDA impregnations by comparing the chemical composition of both starting and impregnated AC. A quasi-similar amount of nitrogen (1.56 – 1.97 at. %, Figure 27) related to the TEDA species, was found for three adsorbents with 5 w.t% in TEDA. In the meantime, a similar amount of nitrogen (0.51 – 0.74 at. %, Figure 27) was also observed for those without TEDA (NI AC and 5%KI AC), indicating the presence of nitrogen on the starting AC. Using the (2%KI + 5%TEDA) AC as an example, the measured TEDA content obtained by the acetonitrile extraction, CHNS analysis and XPS is

4.73 w.t%, 5.04 w.t% and 4 - 4.5 w.t%, respectively. For the XPS analysis, the obtained TEDA content may be underestimated due to the sublimation of the pure TEDA powders under vacuum of 10^{-7} bar. Therefore, it is proposed that only the strongly bonded TEDA (chemisorbed) on the AC surface can be measured for the XPS analysis. Besides, unlike the acetonitrile extraction and the CHNS analysis which are global analysis, the elemental composition by XPS analysis present a more localized feature. On the one hand, the measuring area for the XPS analysis is in the nanometer scale, which is not sufficient especially for a heterogenous materials such as AC. On the other hand, the specific XPS sensibility to AC surface (depth of about 1 nm) should also be noticed. Hence, using elemental composition of XPS analysis for AC may present a higher variability compared to the global characterization techniques.

Accordingly, a non-linear increase of the iodine surface contents for KI impregnated AC has been observed. Moreover, potassium contents were analyzed in order to check the stoichiometric K/I ratios. In the case of reference KI, a K/I ratio close of unity (~ 0.9) was found. However, a very large deviation from 1:1 stoichiometry was observed at the expense of iodine for 5%KI AC (K/I ~ 2), (1%KI + 5%TEDA) AC (K/I ~ 5) and (2%KI + 5%TEDA) AC (K/I ~ 4). This discrepancy may be attributed to the presence of higher amount of potassium in the starting AC as a comparison with impregnated materials (%K = 1.11 at.% for NI AC, Figure 27), making it difficult to distinguish the native potassium (raw material) from additional potassium due to the KI impregnation.

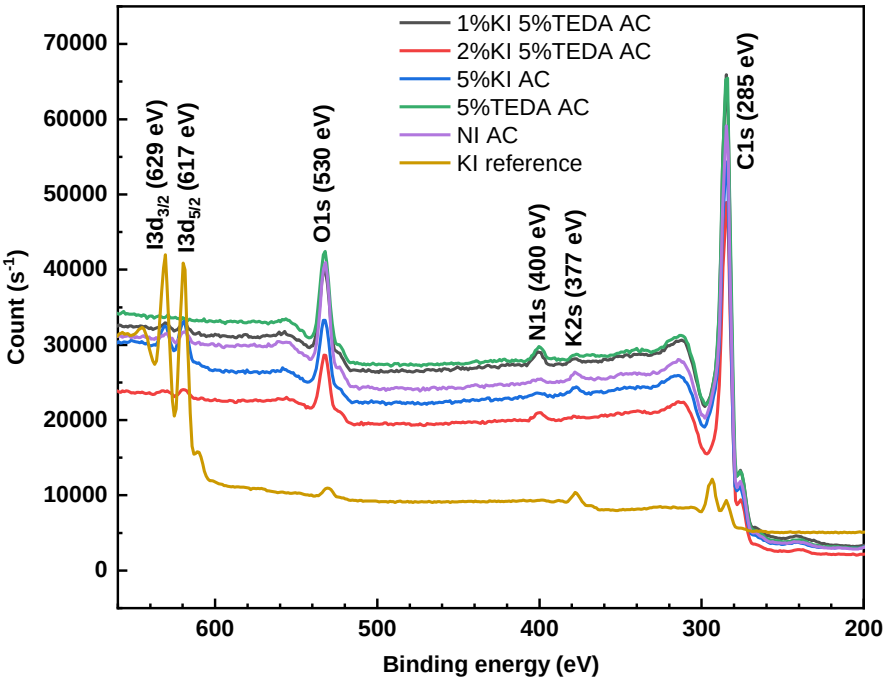

Figure 26. XPS spectra for some AC

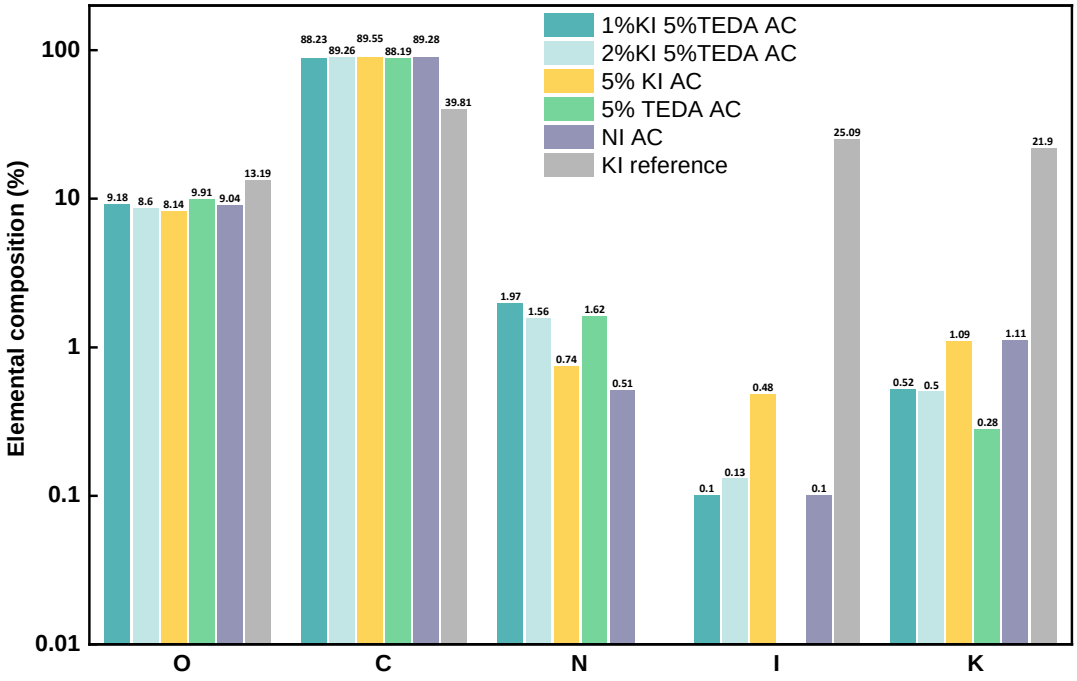

Figure 27. Elemental composition from XPS analysis

The deconvolution of XPS spectra allowed us to gain insights on each element speciation. First of all, it can be mentioned that the tested AC display rather similar C1s (285 eV, Appendix 11) and O1s (530 eV, Appendix 11) speciation, in agreement with the use of the same batch and substrate

for their production. On the one hand, the carbon speciation is mainly dominated by the sp^2 graphitic contribution (Appendix 11) [153]. Other contributions assigned to oxidized carbon species can also be identified (alcohols, carbonyls, quinones, Appendix 11) [154]. On the other hand, the O1s line is found to be composed of 5 contributions, consistent with the carbon oxidized species observed at the C1s line [154] (Appendix 11). In general, the identified oxidized and carbonized species are largely reported in the literature for the AC synthesis regardless of the different starting raw material and the final applications [155][103][156], indicating their potential origins during the carbonization or the activation process. The heteroatoms compared to carbon (oxygen and hydrogen, namely) are reported to be inserted within the carbon matrix by ether and olefin type bond during carbonization process [106]. Besides, these heteroatoms can also be chemisorbed on the carbonaceous structure during the activation process [109].

Information about the nitrogen and iodine speciation can be deduced from their respective peaks deconvolution as depicted in Figure 28. In the case of nitrogen (N1s), two peaks located at 398 eV (N1) and 400 eV (N2) are observed (Figure 28). The N1 peak corresponds to three-coordinated nitrogen N sigma-bonded to carbons (with sp^3 bonds), as in amines ($N\text{-}H_3$) and in TEDA ($N\text{-}C_3$)[157]. The N2 peak is rather associated with N-C sp^2 bonds, as for quaternary amines, that may be attributed to a nitrogen interaction with a carbon atom in the graphitic structure [158]. It is difficult to relate the TEDA quantity to the N1 speciation since N1 is already present on the unimpregnated AC and 5%KI AC (Figure 28). Therefore, it is assumed that the N1 speciation is not only contributed by the TEDA but also by other potential nitrogen functional groups on the AC surface. In general, it is observed that the speciation of the N1 and N2 remains the same for all the tested AC sample, indicating their similar surface characteristics. For iodine (I3d), two different components can be also displayed: 619 eV (I1) and 621 eV (I2) (Figure 28). The dominant contribution I1 is due to ionic I^- characteristic of the KI signature. While, the small one I2 is associated to less negative iodine ($I^{\delta-}$). A ratio between I1 and I2 of about 80/20 was found for all the tested samples, as a comparison with the reference KI product mostly made from the I1 peak (94%) (Figure 28). The presence of the peak I2 for the tested AC sample may indicate the potential interaction of iodine with surface defects of the AC, leading to the formation of more covalent iodine species. The presence of this contribution may explain also the observed deviation from

acetonitrile extraction, since the developed analytical method was only sensitive to I^- component (Section 4.1).

Finally, a rather similar speciation of nitrogen and iodine can be observed when comparing the single and co-impregnated AC. Therefore, it can be proposed that there is no particular interaction between TEDA and KI molecules within the tested AC.

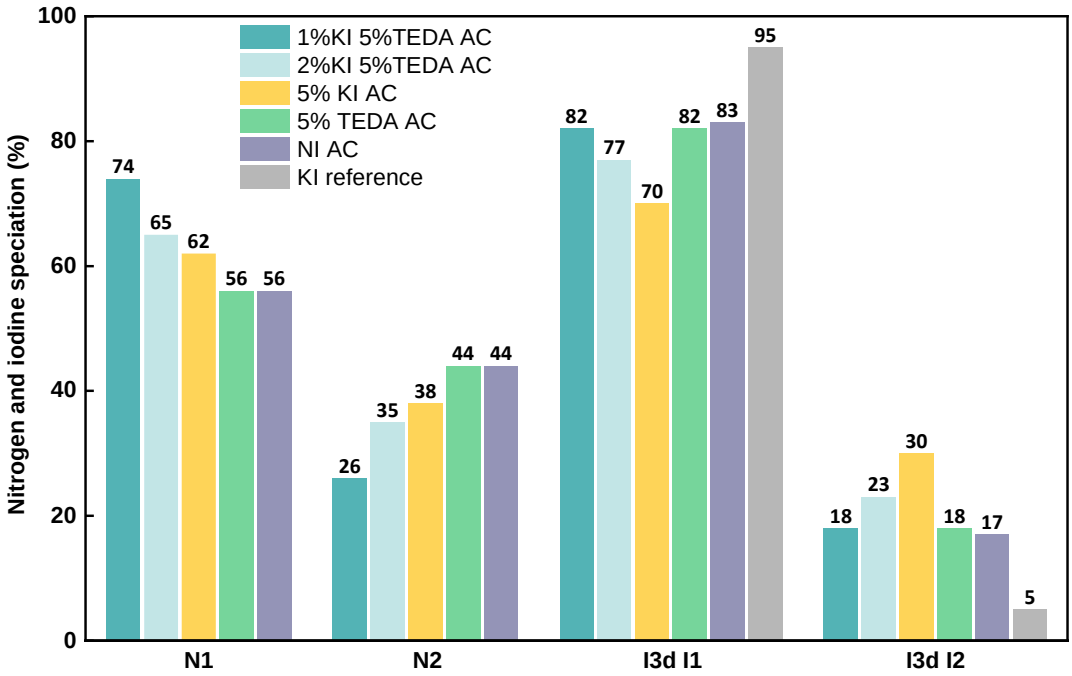

Figure 28. Nitrogen and iodine speciation for some AC

Additional elements regarding the investigated AC can be deduced from XRD and SEM/EDX analysis. As depicted in Appendix 12, these broad XRD patterns indicate the typical amorphous carbon structure in consistent with the previous XPS analysis with sp^2 and sp^3 carbon speciation [159]. More particularly, the XRD signals at $2\theta = 22°$ and 43.5° are generally assigned to the *(002)* and *(100)* reflections of the disordered graphitic wall layers related to the porous structure of the AC [153].

Regarding the KI and TEDA localizations, no new X-ray diffraction peaks typical of KI and TEDA lines were observed for all the investigated AC, indicating the absence of agglomeration of the impregnants (> 100 nm) on the external surface (Appendix 12). Therefore, it can be proposed that these agents are well-dispersed within the internal porosity in a molecular way. This observation

was also confirmed by SEM/EDX investigations. Indeed, no substantial changes before and after impregnation were noticed according to the different recorded SEM images. An example for the (2%KI + 5%TEDA) AC is presented in Figure 29 with increasing magnifications. More particularly, the 65000 magnification (Figure 29 (a)) reveals the presence of macropores presenting the typical geometry of a coconut shell based AC [89]. Other magnifications (Figure 29 (b) and (c)) show the existence of some particles heterogeneously distributed on the carbon surface. According to their EDX analysis, neither KI nor TEDA are identified. However, other elements can be depicted (such as magnesium, sodium, chlorine, silicon, etc.) which are reported to be inherent to the raw material and the further fabrication steps [89]. Hence, KI and TEDA seem to be well dispersed within the internal porosity of the studied materials in agreement with XRD characterizations. The comparison between EDX and XPS (Appendix 13) allows to give insights on the relative elemental distribution between the surface (XPS, depth about 1 nm) and the bulk (EDX, hundreds of nanometers) for a given AC. On the one hand, rather similar concentrations of carbon, iodine and potassium between the bulk and the surface were found. On the other hand, different distributions for oxygen and nitrogen may be observed. For oxygen, a higher concentration at surface was measured, in agreement with the potential occurrence of surface oxidation by atmospheric contamination (namely, humidity). However, a lower nitrogen amount was obtained at the surface than the bulk, due to the possible desorption of physiosorbed TEDA molecules under vacuum (as observed for pure TEDA with XPS).

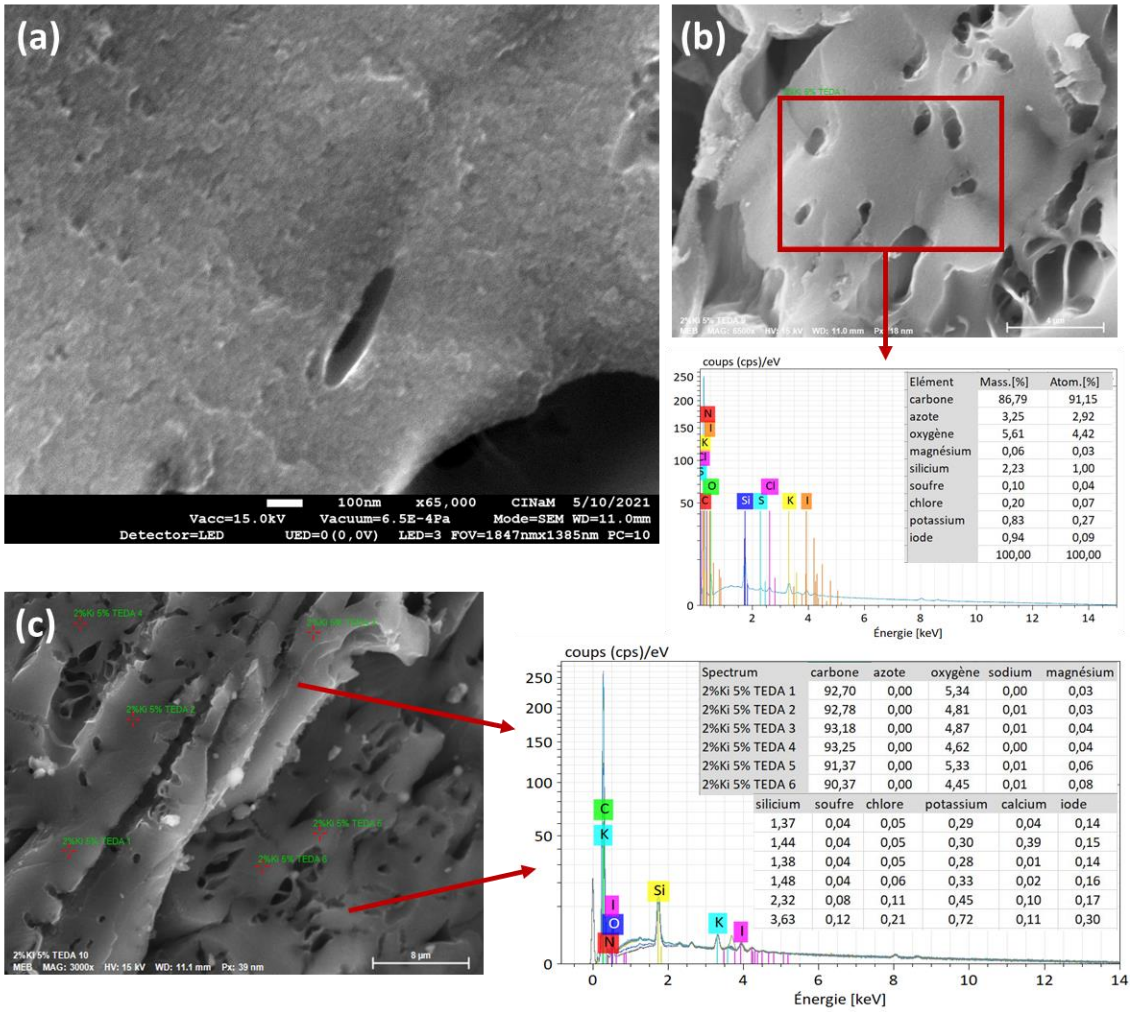

Figure 29. Selected SEM images of the 2%KI 5%TEDA AC: (a) magnification × 65000; (b) magnification × 6500 and EDX analysis in the rectangular area; (c) magnification × 3000 and EDX analysis at six locations

4.3 Textural properties

N_2 porosimetry at 77 K

The effect of KI and TEDA presence within the tested AC is now discussed in terms of porosimetric properties as deduced form N_2 adsorption/desorption isotherms at 77 K. The obtained N_2 adsorption isotherms display a type I isotherms, typical of microporous materials [160] (Appendix 4). A very small hysteresis can also be depicted indicating the presence of narrow mesopores [161], whose contribution was found to be negligible (< 6 %). The associated porosimetric data (S_{BET} and V_{micro}) are summarized in Table 20, as average values from two

replicates with k = 2. All these AC exhibit high specific surface area around 1000 $m^2 \cdot g^{-1}$, with an important contribution from the microporous volume (V_{micro} / V_{pore} > 94%). The observed microporous character of the tested AC is in agreement with AC made from coconut shell in the nuclear field. This raw material is reported to be associated with highly microporous AC after being activated [89][92]. Besides, the mean pore diameter deduced from the HK method is around 0.5 nm, making it suitable for the CH_3I trapping (kinetic diameter of 0.5 - 0.6 nm [52]) by physisorption phenomena.

Table 20. Textural properties of the investigated AC from N_2 porosimetry at 77 K

Impregnation type	Total molar impregnation ratio (%)	S_{BET} (m^2/g)	V_{micro} (cm^3/g)	d_{micro} (nm)	V_{pore} (cm^3/g)
Unimpregnated	0.000	1142 ± 67	0.453 ± 0.031	0.473 ± 0.003	0.472 ± 0.032
0.1% KI	0.007	1174 ± 67	0.469 ± 0.026	0.474 ± 0.001	0.492 ± 0.030
0.5% KI	0.036	1171 ± 154	0.470 ± 0.066	0.480 ± 0.009	0.496 ± 0.075
1% KI	0.072	1213 ± 134	0.486 ± 0.058	0.482 ± 0.017	0.513 ± 0.061
1% TEDA	0.107	1217 ± 90	0.489 ± 0.043	0.485 ± 0.016	0.513 ± 0.051
0.5%KI + 1%TEDA	0.143	1097 ± 197	0.439 ± 0.083	0.478 ± 0.018	0.458 ± 0.086
2% KI	0.145	1174 ± 0	0.469 ± 0.002	0.479 ± 0.003	0.493 ± 0.003
1%KI + 1%TEDA	0.179	1089 ± 81	0.435 ± 0.028	0.479 ± 0.003	0.454 ± 0.029
2% KI + 1% TEDA	0.252	1104 ± 54	0.445 ± 0.014	0.487 ± 0.009	0.472 ± 0.011
3% TEDA	0.321	1097 ± 59	0.441 ± 0.028	0.488 ± 0.006	0.464 ± 0.029
5% KI	0.361	1132 ± 69	0.456 ± 0.032	0.484 ± 0.014	0.483 ± 0.034
5% TEDA	0.535	1022 ± 31	0.410 ± 0.012	0.492 ± 0.002	0.433 ± 0.009
0.5%KI + 5%TEDA	0.571	944 ± 57	0.378 ± 0.021	0.492 ± 0.012	0.394 ± 0.020
1%KI + 5%TEDA	0.607	950 ± 83	0.382 ± 0.033	0.492 ± 0.004	0.403 ± 0.035
2%KI + 5%TEDA	0.679	972 ± 39	0.396 ± 0.008	0.508 ± 0.020	0.420 ± 0.013
7% TEDA	0.749	938 ± 90	0.380 ± 0.035	0.501 ± 0.008	0.401 ± 0.035
10% TEDA	1.070	824 ± 146	0.332 ± 0.059	0.515 ± 0.003	0.343 ± 0.076
0.5%KI + 10%TEDA	1.106	696 ± 116	0.282 ± 0.043	0.518 ± 0.024	0.298 ± 0.014
1%KI + 10%TEDA	1.142	641 ± 62	0.258 ± 0.020	0.519 ± 0.010	0.268 ± 0.002
2%KI + 10%TEDA	1.214	693 ± 44	0.282 ± 0.017	0.526 ± 0.003	0.293 ± 0.003

In addition, both the S_{BET} and V_{micro} present a general decreasing evolution with the total impregnation molar ratio as depicted in Figure 30. For example, the S_{BET} progressively decreases from (1217 ± 90, Table 20) $m^2 \cdot g^{-1}$ for 1%TEDA AC until reaching (693 ± 44 $m^2 \cdot g^{-1}$, Table 20) for (2% KI + 10% TEDA) AC. Indeed, the impregnation is known to induce the partial blocking of the porosity on the AC surface (especially the micropores), leading to the decrease of the textural properties [63][116]. Such a micropore blockage becomes more significant for total molar impregnation ratio exceeding 0.4 % (around 3 w.t% TEDA or 5 w.t% KI). The observed decrease of microporosity may be assigned to the presence of KI and TEDA within or in the openings of micropores. This observation seems to be in line with previous XRD and SEM/EDX analysis indicating the presence of such agents within the internal porosity without agglomeration on the external surface. Moreover, the linear decrease of the textural properties (V_{micro} and S_{BET}) as a function of the global molar amount of impregnants, seems to follow the same trend whatever the type of impregnation (TEDA or co-impregnated). This result may consolidate the previous investigations by XPS indicating the absence of any interaction between TEDA and KI for the co-impregnated adsorbents.

Nevertheless, a closer look for low impregnation contents (< 0.1 %) shows a slight increase (or higher variability) of the S_{BET} and V_{micro} as a comparison with the unimpregnated AC. This unexpected increase is also reported in the literature [162][163][164]. It can be postulated that a small amount of impregnation may create more heterogeneity on the AC surface, inducing a slight overestimation of the microporosity.

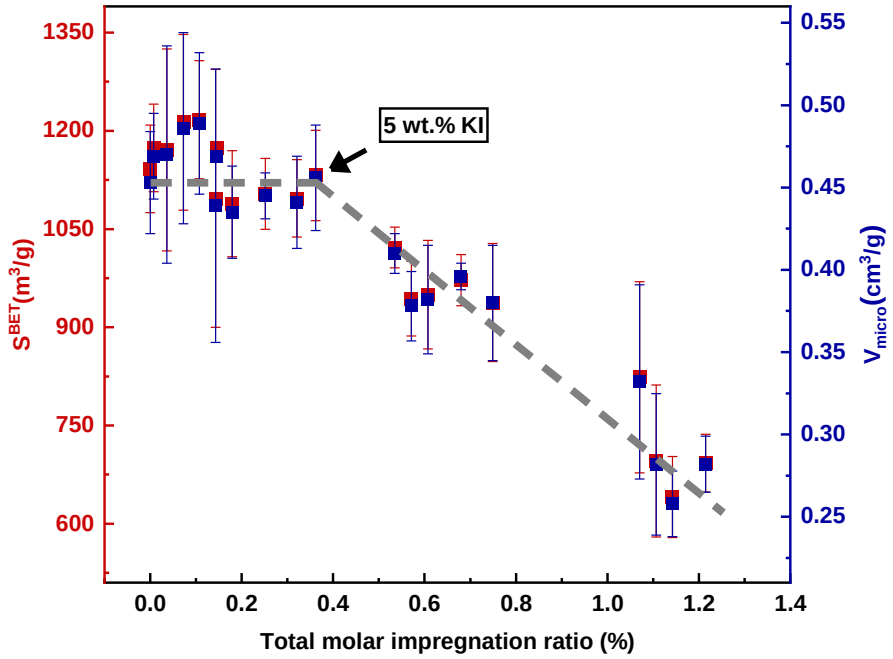

Figure 30. Evolution of S_{BET} and V_{micro} as a function of total impregnation ratio

H_2O adsorption isotherms

Apart from the N_2 porosimetry at 77 K, additional investigations about the tested AC can be obtained from water adsorption isotherms, which are reported to be dependent both on the chemical composition and on the textural properties of adsorbents [63][165][166]. The isotherms displayed in Figure 11 (a) and (b) represent an adsorption isotherm of type V according to IUPAC classifications [143]. This S-shape isotherms indicates that the adsorbent/adsorbate interactions are weak in the beginning. This trend is related to the hydrophobic surface characterizing the AC. As shown in Figure 11 (a), the water uptake for the KI impregnated AC generally increases with the KI impregnation ratio at low RH, which is due to the nucleation effect introduced by the impregnant as surface functional group. At high RH, however, the water uptake is found to be related to the microporosity of the AC. It is reported that the water uptake at high RH is mainly controlled by the microporosity of the AC due to the micropore filling phenomena [165][166].

In contrast, the TEDA impregnated AC seem to be less sensible to water molecule compared to KI impregnated AC at low RH. Indeed, a quasi-similar water uptake can be noticed regardless of the TEDA impregnation ratio, with a lower value compared to KI impregnation (Figure 11 (b)). The influence of the water uptake towards the retention performance of the CH_3I for different AC will be further discussed in Chapter III.

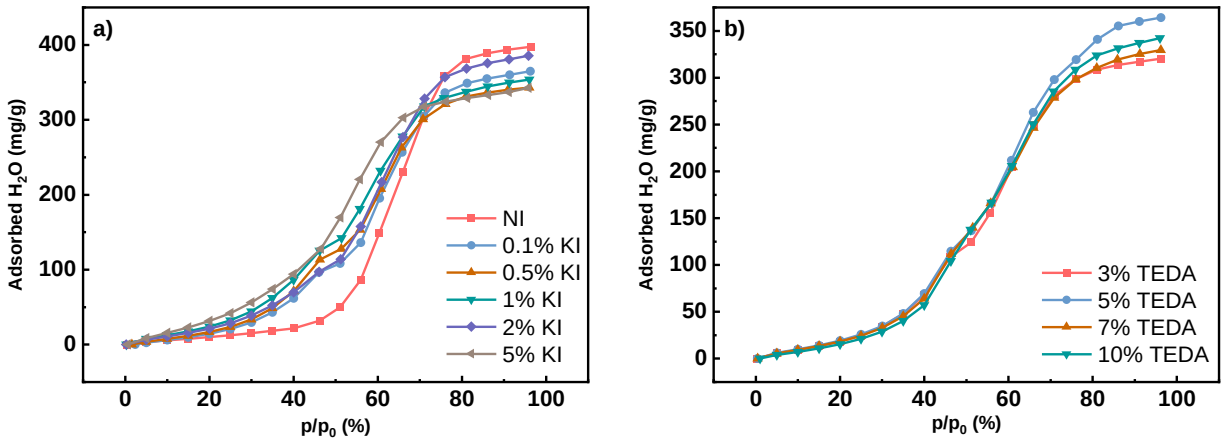

Figure 31. Water adsorption isotherms at 25 °C for (a) KI impregnated AC; (b) TEDA impregnated AC

5. Conclusions

This chapter was devoted to the physico-chemical characterization of the AC using different analytical techniques.

Regarding the impregnant quantity, a quasi-linear relationship was observed comparing experimental and theoretical contents for all the tested AC. Nevertheless, a deviation of 23%, 15% and 27% from the expected amount, as reported by the manufacturer, was found for the tested TEDA, KI and co impregnated AC respectively. More particularly, the experimental value obtained by acetonitrile extraction is found to be underestimated compared to CHNS analysis. The observed deviation for acetonitrile extraction is probably due to its insufficient accessibility towards certain TEDA and KI sites within the internal microporosity. Considering the unmeasurable TEDA and KI by acetonitrile extraction and the quasi-similar deviation of about 20%, it can be concluded that KI and TEDA are well impregnated in terms of quantity.

Additional information regarding the impregnant speciation and the AC sample surface can be deduced from the XPS. On the one hand, the carbonaceous nature (88 - 90 at.% in carbon) of the tested AC were confirmed by both XPS, EDX and CHNS analysis, and their similar C1s (285 eV) and O1s (530 eV) speciation also confirm the same batch characteristics for the AC production. On the other hand, the similar speciation of nitrogen and iodine for the single and co-impregnated AC indicates the absence of interaction between TEDA and KI molecules within the tested AC. Besides, the obtained elemental composition (especially for iodine and nitrogen) from the XPS

and EDX analysis is found to present a higher variability as compared to global characterization (acetonitrile extraction and CHNS analysis), which is probably due to the different sensibilities in depth for the XPS and EDX analysis. Further XRD and SEM/EDX analyses show the absence of agglomeration of the impregnants (> 100 nm) on the external surface, indicating that KI and TEDA are well dispersed within the internal porosity of the studied materials. The comparison between EDX and XPS has also provided information about elemental distribution (C, O, N, I, K) between the surface and the bulk for some of the tested AC.

The porous structure of the investigated AC is determined firstly by the porosimetry with nitrogen at 77 K. The obtained N_2 adsorption isotherms for all the AC exhibit a type I, typical of microporous materials. All these AC present high specific surface area around 1000 $m^2 \cdot g^{-1}$, with an important contribution of microporosity (V_{micro} / V_{pore} > 94%). The calculated mean pore diameter of about 0.5 nm makes the tested AC suitable for the CH_3I trapping by physisorption phenomena. In addition, both the S_{BET} and V_{micro} present a general decreasing evolution with the total impregnation molar ratio due to the partial blocking of the porosity on the AC surface by impregnation. Such a micropore blockage becomes more significant for total molar impregnation ratio exceeding 0.4 % (around 3 w.t% TEDA or 5 w.t% KI). Apart from the N_2 porosimetry at 77 K, additional investigations about the tested AC are obtained using water adsorption isotherms. The water uptake for the KI impregnated AC under low RH generally increases with the KI impregnation ratio, which is due to the nucleation effect introduced by the impregnant as surface functional group. At high RH, however, the water uptake is found to be related to the microporosity of the AC. In contrast, the TEDA impregnated AC seem to be less sensible to water molecules as compared to KI impregnated AC.

These results allow us to better understand their trapping behaviors towards CH_3I as described later in the next chapters, by attempting to establish a structure - activity relationship (Chapters III and IV).

Chapter III: AC performances towards the capture of γ-labelled CH_3I (DF measurements)

1. Introduction

In the previous chapter, the intrinsic characteristics of AC have been finely investigated regarding the chemical and surface composition as well as the textural properties. In this chapter, the performances of AC towards the capture of γ-labelled CH_3I are explored at semi-pilot scale. The objective is to establish a structure – activity correlation between the physico-chemical characteristics of AC and the decontamination factor (DF) under specified dynamic conditioning, temperature, relative humidity, adsorbent bed thickness, iodine flow velocity and iodine concentrations. Firstly, the experimental setup and the used protocols are presented in detail. Then, the AC performances at different operating conditions (RH = 40 and 90% at room temperature) are investigated. Finally, discussions on the effect of the isotopic exchange along with a proposed hypothesis based on the results obtained in this chapter are presented.

2. Materials and methods

2.1 General description: principle and methodology

The retention tests were carried out using the PERSÉE facility (see diagrams and photographs in Figure 32 and Figure 33) which is dedicated to evaluate the performance of nuclear grade AC before being used in the French nuclear facilities. The PERSÉE test bench consists of a glove box for γ-labelled CH_3I generation in gaseous phase and a metallic structure for fixed-bed adsorption experiments. Schematically, a retention test can be summarized as follows:

- Before the adsorption experiment, the AC are placed in equilibrium with a given concentration of water vapor during at least 16 h;
- During the experiments, up to four AC can be tested simultaneously for the capture of γ-labelled CH_3I. These tested adsorbents are placed in the upstream section, while the non-

retained CH_3I by the investigated materials are captured by the reference AC placed in the downstream section (Figure 32);

- The retention test consists on an injection of a given amount of γ-labelled CH_3I followed by an elution under the same conditions (face velocity, temperature and RH);
- Finally, the DF displayed by the tested AC towards γ-labelled CH_3I are deduced from the comparison between the measured activities from both upstream and downstream sections for each branch. The temperature and RH are measured continuously by different sensors inside the test bench.

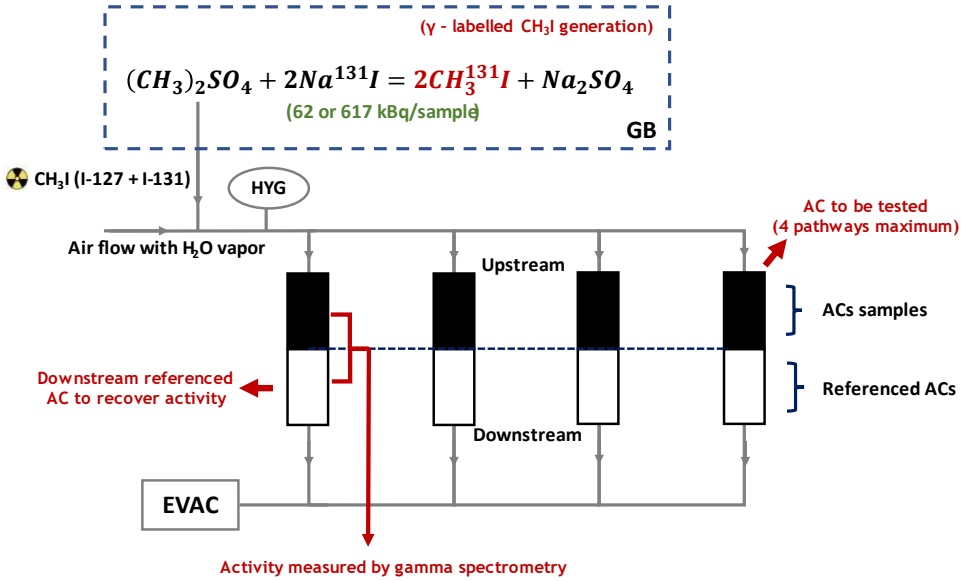

Figure 32. Schematic view of PERSÉE test bench (pulsed mode)

Figure 33. Photograph of the PERSÉE test bench

It should be noticed that the tests carried out in the PERSÉE facility are based on the standardized protocols (ASTM D3803 [128], NF M62-206 [167]) which were established to evaluate the performance of commercial *nuclear grade* AC. The operating conditions are referenced to particular conditions where a high RH is expected. In the present study, the influence of KI and TEDA impregnation was studied using a RH ranging from 40 to 90 % (T = (20 ± 1) °C). The operating conditions of the ASTM 3803 and NF M62-206 standards, as well as of those used in the current tests at PERSÉE, are summarized in Table 21.

Table 21. Summary of the operating conditions of ASTM3803, NFM62-206 and PERSÉE (k = 2) [128][167]

	Residence time (s)	Linear velocity ($cm \cdot s^{-1}$)	T (°C)	RH (%)	Equilibrium with H_2O (h)	γ-labelled CH_3I injection (min)	Air elution (min)
ASTM D3803	0.25	20.3 ± 0.5	30 ± 0.2	94.5 ± 1.5	16 ± 1	60 ± 1	60 ± 1
NF M62-206	≥ 0.25	≤ 25	/	various	≥ 16	30	≥ 60
PERSÉE	0.2	25	20 ± 1	40 and 90 (± 5)	≥ 16	30 ± 0.5	60 ± 0.5

The details of the experimental protocols (main steps, instrumentation and γ-spectrometry measurements) are presented in the next section.

2.2 Experimental protocols

Schematically, the test procedure comprises four main steps:

(i) Sample preparation
(ii) Pre-equilibration under humidity
(iii) Retention test
(iv) Activity measurement

2.2.1 Sample preparation

The AC sample (8×16 mesh, corresponding to 2 - 3 mm) to be tested (upstream section, Figure 32) is placed within a specific cylindrical sample holder with an internal diameter of 40 mm using a

metallic ring and a metallic grid fixed on the bottom side of the sample holder (Figure 34). After adding another metallic grid on the top side, the system (AC + sample holder) is kept under agitation using appropriate rates during about 1 minute. This agitation not only assures the compactness and homogeneity of the tested AC bed, but also adjusts the apparent density of the tested AC to be around 0.5 $g \cdot cm^{-3}$, in agreement with the iodine traps currently used in the French nuclear industry [42]. The bed depth was checked experimentally after the agitation step. A reference value of (50.5 ± 0.5) mm was fixed with the aim to follow the ASTM D3803 specifications [128]. Then, a metallic spring and another metallic ring are added on the top side of the filled sample holder in order to guarantee the integrity of the tested sample as well as the seal connection with the other parts of the setup.

On the other hand, the downstream reference AC was also conditioned through the same geometry as the adsorbent placed in the upstream stage. This adsorbent which is devoted to trap the fraction of the γ-labelled CH_3I not retained by the tested adsorbent, was the same for all the retention tests for comparison purposes. It should be highlighted that at RH = 90 %, the DF of the downstream referenced AC is about 100, indicating its capture efficiency of γ-labelled CH_3I is about 99%. Hence, an uncertainty of about 1% for the downstream activity can be estimated. On the contrary, this uncertainty at RH = 40% can be neglected considering the performance of the downstream AC ($DF > 10^4$).

Figure 34. Different components for AC sample preparation

2.2.2 Pre-equilibration under humidity

As specified in the ASTM3803 and NF M62-206 standards, a 16h duration pre-equilibration under humidity is performed for all the AC samples (both upstream and downstream section) [128][167]. The first objective of this treatment is to achieve the equilibrium between the samples and the desired RH before the adsorption test. The second objective is to balance the temperature perturbation of AC facing high RH due to the exothermic character of water vapor adsorption [128]. Two RH were targeted in our study (RH = 40 % corresponding to H_2O 9320 ppmv and RH = 90 % corresponding to H_2O 22600 ppmv at T = (20 ± 1) °C).

An example is given regarding the determination of the water vapor breakthrough curve (BTC) by AC using the same sample preparation protocols (ambient temperature, RH = 40 %, linear velocity = 10 $cm \cdot s^{-1}$, residence time = 0.5 s, bed depth = 5 cm [168]). It can be noticed that around 300 min is required to reach 100% breakthrough for the water vapor, during which a temperature increase of around 10° C can also be observed (Figure 35). It can be deduced that a duration of 16 h is sufficient to reach the equilibrium in both temperature and RH for the retention tests at PERSÉE (linear velocity = 25 $cm \cdot s^{-1}$, residence time = 0.2 s, bed depth = 5 cm).

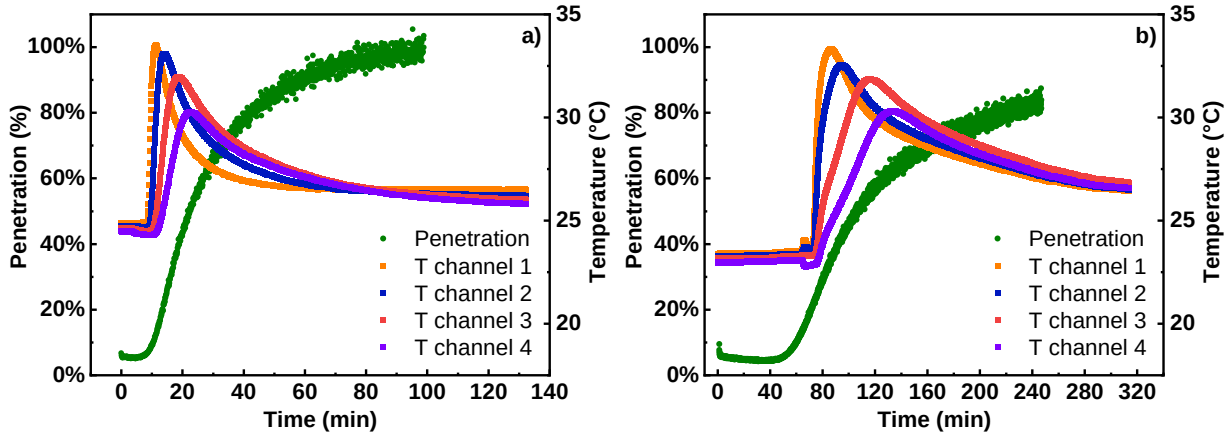

Figure 35. Temperature profiles in the adsorbed phase and water vapor BTC: (a) unimpregnated AC; (b) 5% KI impregnated AC [168]

In our test bench, ultra-pure water with a controlled flow (*LVF, Horiba*) is used to generate water vapor. More precisely, water is injected successively in two evaporators with different temperatures (415 °C and 180 °C). The RH generation in automatic mode is performed using PID regulation of the water flowmeter setpoint and a dedicated bench probe (*HMT330, Vaisala*) placed

before the samples for RH measurement (Figure 36). In the meantime, the obtained RH for each branch before the upstream AC is measured continuously using specific sensors (*HC2A-IC102*, *Rotronic*) (Figure 36). An example of the RH evolution during the pre-equilibration step is presented in Figure 37.

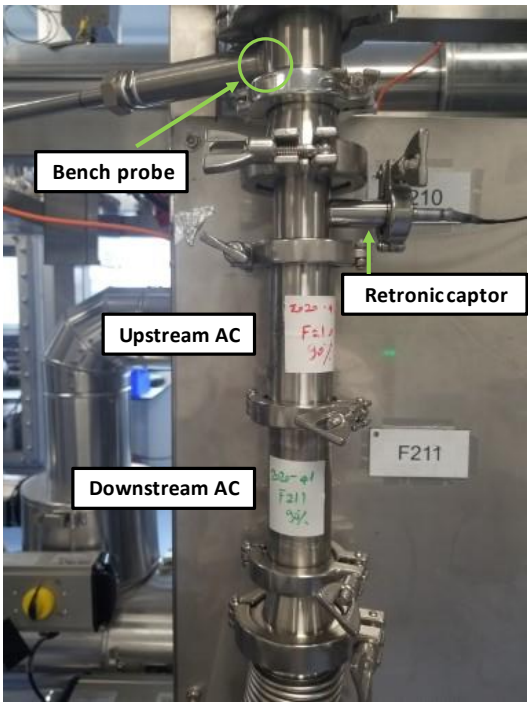

Figure 36. Positions of different sensors for RH measurements

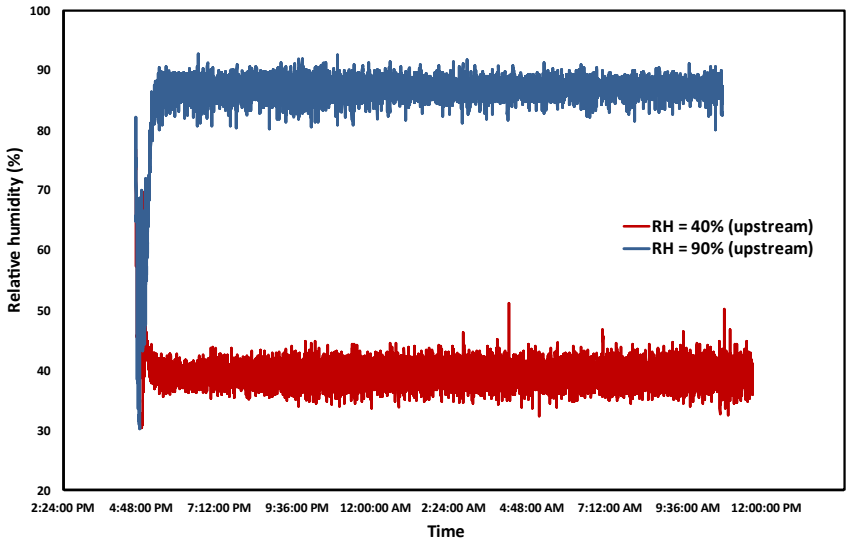

Figure 37. Example of RH evolution during pre-equilibration under water vapor (RH of 40 % and 90 % at T = (20 ± 1) °C)

2.2.3 Retention test

The retention test occurs with a gas flowrate of 17.5 $L \cdot min^{-1}$ (NTP) that corresponds to a linear velocity of 25 $cm \cdot s^{-1}$ at the tested temperature. After a pre-equilibration under humidity of at least 16 h with the indicated flow rate, a pulse of γ-labelled CH_3I (duration of 30 min, around 600 ppbv) is generated in the glove box according to the following reaction [167]:

$$(CH_3)_2SO_4 + 2Na^{131}I \rightleftharpoons 2CH_3^{131}I + Na_2SO_4 \quad (24)$$

The γ-labelled CH_3I generation protocol has been already developed at PERSÉE facility to evaluate the retention performances of commercial *nuclear grade* AC. More particularly, a specific glass vessel (Figure 38) is used within the glove box to regulate the γ-labelled CH_3I generation. Two reactants are added into the vessel through the solution entrance:

- the γ-labelled NaI solution prepared from a mixture containing 2 mL of stable NaI (2 $g \cdot L^{-1}$, *AC grade, Fisher Scientific*) and the required amount of $Na^{131}I$ solution (*Curium*) depending on the targeted RH;
- 0.5 ml of dimethyl sulfate solution (*AC grade, Fisher Scientific*).

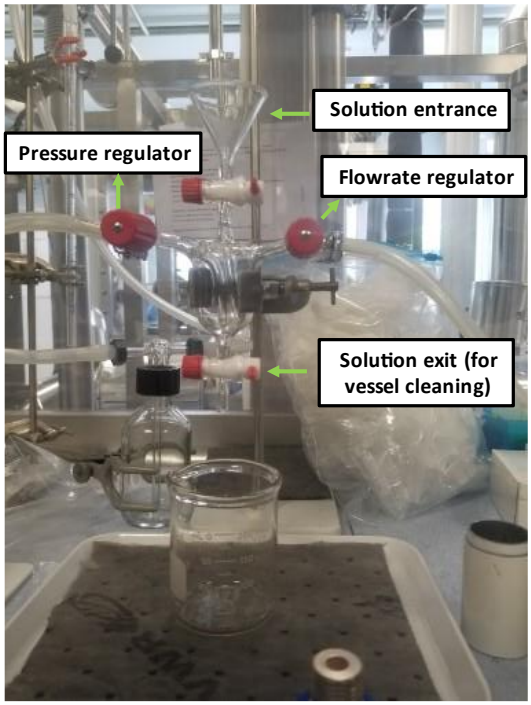

Figure 38. Glass vessel in the glove box for γ-labelled CH_3I flowrate regulation

It should be noticed that the initial $Na^{131}I$ activity depends on the targeted RH as reported in the Table 22. Indeed, the AC exhibit higher performances for CH_3I retention under moderate RH (RH = 40 %) as compared with RH = 90 %. Hence, a higher activity of $Na^{131}I$ is required (Table 22) in order to increase the expected activity in the downstream AC (generally close to the DL for moderately humid conditions). After 30 min of the γ-labelled CH_3I generation, an elution of 60 min with the same flowrate is carried out in order to take into account the desorption of physiosorbed $CH_3{}^{131}I$ [167].

Table 22. Summary of the experimental conditions (per sample) at PERSÉE

T (°C)	RH (%)	Initial activity (KBq)	Molar ratio ($CH_3{}^{131}I$/ CH_3I)	Molar ratio ($CH_3{}^{131}I/H_2O$)	Molar ratio (CH_3I/H_2O)	Linear velocity ($cm \cdot s^{-1}$)	Residence time (s)
20 ± 1	40 ± 5	617	8×10^{-8}	5×10^{-9}	7×10^{-5}	25	0.2
	90 ± 5	62	8×10^{-9}	2×10^{-10}	3×10^{-5}		

Finally, *ex-situ* γ measurements were carried out on both the upstream and downstream AC. The counting protocol are presented in detailed in the next section.

2.2.4 Activity measurement

Once the retention experiment is finished, all the AC samples are removed from the metallic structure for an *ex-situ* γ spectrometry characterization in order to determine the decontamination factor (DF). More precisely, the tested AC are firstly removed from the sample holder and placed in a separated Teflon bottle in order to acquire a controlled counting geometry. Then, a hyper-pure Germanium detector (HPGe) (*Cryo-Pulse 5 Plus, Canberra*) is used for activity measurements in order to deduce the DF according to the following relationship:

$$DF = \frac{A_{upstream} + A_{downstream}}{A_{downstream}} \quad (25)$$

Where $A_{upstream}$ upstream activity (Bq);
$A_{downstream}$ downstream activity (Bq).

As shown in Figure 39, the AC sample is placed in front of the γ-spectrometer at a distance d, and lead bricks are added around the gamma detector and the AC sample to avoid radioactive exposure for operators and exterior disturbance during measurement. According to the ^{131}I decay scheme (Appendix 14), it can be noticed that the gamma emission of ^{131}I at 364.5 keV (81.2% abundance) can be used to calculate the activity of the AC through the following relationship:

$$A = \frac{N(E)}{\eta(E) \times I(E) \times t} \quad (26)$$

Where A activity of the sample during day and time of the measurement (Bq);
$N(E)$ Net counting surface of the peak at the given energy;
$\eta(E)$ detection efficiency at the given energy;
$I(E)$ emission abundance of the measured radionuclide at the given energy (%);
t measurement time (s).

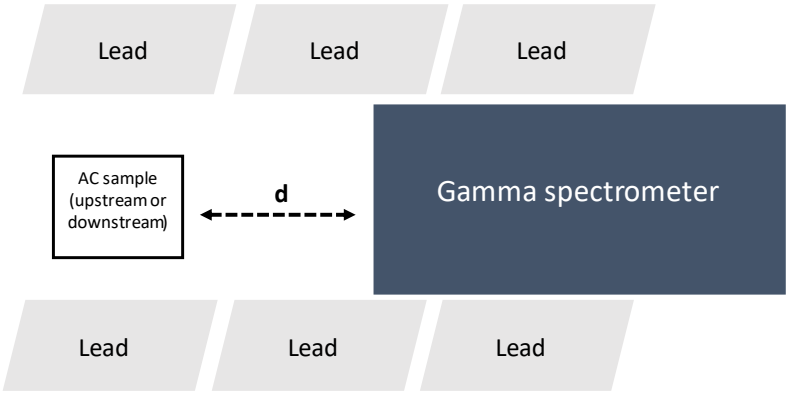

Figure 39. Schematic view of activity measurements

According to Eq. (26), the ^{131}I activity measurement depends on the detection efficiency η, the total net counting N as well as the measurement time t. In practice, the measurement configurations are adjusted regarding these three aspects in order to improve the measurement quality.

For a given radionuclide (^{131}I), the detection efficiency η is dominated by the counting geometry (sample geometry and distance between the sample and the detector). More particularly, the measurement distance d is adjusted to be 0 and 10 cm. The measurement method with d = 10 cm is used for the upstream AC samples in order to avoid the potential detector saturation due to their sufficiently high radioactivity. Accordingly, the measurement method with d = 0 (in contact) is used for the downstream AC due to their expected low radioactivity. The counting duration was also varied to have a high net counting surface for the downstream AC (Appendix 15). The activity measurement requires specific AC standards preparation as well as the γ-spectrometer calibration for the detection efficiency η, which is presented in Appendix 16.

In the next section, the AC performances displayed by the DF (T = 20 °C, RH = 40 and 90 %) using aforementioned experimental protocols are investigated. The relationships between the DF and the physico-chemical characteristics deduced from Chapter II are also evaluated.

3. Results and discussion

3.1 Retention performances of AC at (T = 20 °C, RH = 40 %)

3.1.1 Behavior of co-impregnated AC

To begin with, attention is firstly focused on the co-impregnated AC since they represent the current impregnant combination in the French nuclear industry. The DF values for the tested AC at (T = 20 °C, RH = 40 %) are summarized in Table 23 and shown in Figure 40. The reported DF are average values from up to 14 replicates with k = 2. In this configuration (T = 20 °C, RH = 40 %), the co-impregnated AC exhibit excellent filtering properties with DF magnitude ranging from 10^4 to 10^5 (Table 23). Therefore, the DF determined in these conditions are found to be in agreement with the required performances for AC currently implemented in the French nuclear industry [43]. A closer look to the DF evolution indicates a different behavior depending on the impregnation nature. When fixing the TEDA quantity, a decrease of DF values can be reported as a function of KI content (Figure 40, curves in black, red and blue). For example, a reduction in performances (DF) is noticed from (91958 ± 19879) to (12575 ± 2046) when varying KI contents from 0.5 to 2 w.t% for a fixed TEDA quantity of 1 w.t% (Table 23). However, progressive TEDA impregnation from 1 to 5 w.t% (whatever the fixed loading of KI) contributes to the enhancement of $CH_3{}^{131}I$ retention performances (Figure 40). For higher TEDA contents, a slight decrease of DF can be observed. Thus, it seems that the best retention performances at this condition (T=20°C, RH = 40%) are displayed by (0.5%KI + 5%TEDA) AC with a DF value of (173182 ± 43473, Table 23). This composition seems to agree well with the reported composition of nuclear grade activated carbons (%KI < 1 w.t%, TEDA content of 5 w.t% [43]). Nevertheless, uncertainty is still remaining concerning the role played by KI in the removal of $CH_3{}^{131}I$ through the tested methodology. Indeed, higher DF value was even obtained without KI and for TEDA content of 5 w.t% (220228 ± 46423, Table 23).

Table 23. Summary of DF for different AC at (T = 20 °C, RH = 40 %, k = 2): residence time = 0.2 s, linear velocity = 25 cm·s^{-1}, pre-equilibration under humidity for 16 h

Co-impregnation			TEDA impregnation		KI impregnation	
KI%	TEDA%	DF	TEDA%	DF	KI%	DF
0.5	1	91958 ± 19879	1	106286 ± 35606	0	10917 ± 4981
0.5	5	173182 ± 43473	3	210578 ± 62883	0.1	6378 ± 1557
0.5	10	123006 ± 21794	5	220228 ± 46423	0.5	3689 ± 1097
1	1	37772 ± 10984	7	167621 ± 46755	1	2895 ± 769
1	5	79281 ± 7743	10	128365 ± 32189	2	1587 ± 486
1	10	86905 ± 23751			5	236 ± 29
2	1	12575 ± 2046				
2	5	49410 ± 11971				
2	10	39445 ± 6884				

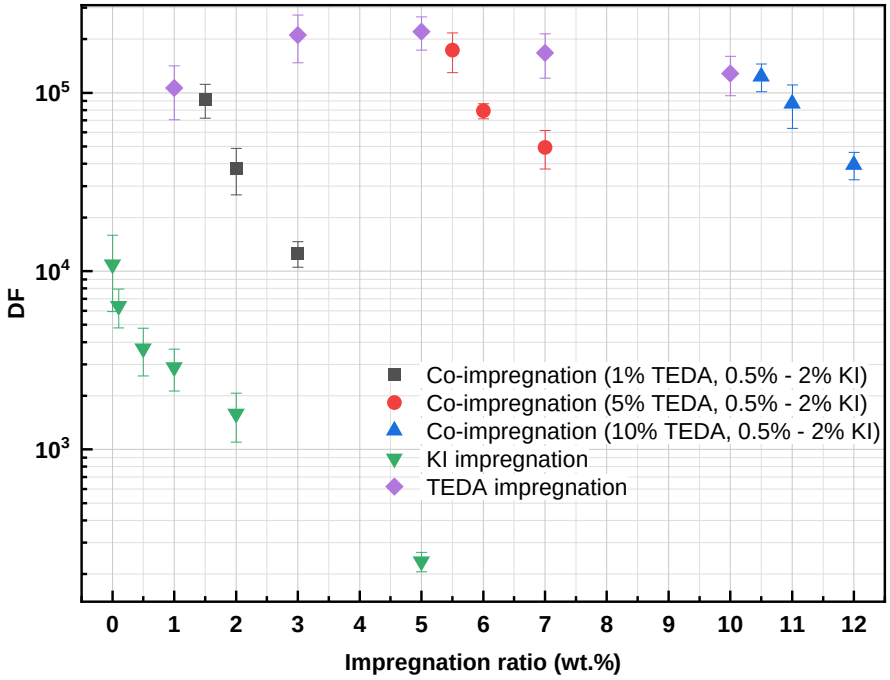

Figure 40. DF evolution for different AC as a function of KI and TEDA contents at (T = 20 °C, RH = 40 %): residence time = 0.2 s, linear velocity = 25 cm·s^{-1}, pre-equilibration under humidity for 16h

In order to study the effects of KI and TEDA on the trapping performance of $CH_3{}^{131}I$ and to understand more precisely the role played by each of the two impregnants, the AC performances of the single impregnated AC is investigated in the next section.

3.1.2 Behavior of single impregnated AC

The specific behaviors of the impregnants are now discussed using single impregnated AC. On the one hand, the TEDA impregnated AC present the highest DFs among all the investigated adsorbents. Besides, DF evolution towards TEDA impregnation similar to the co-impregnated materials is observed (Figure 40, curve in purple). Indeed, an enhancement of DF is observed from (106286 ± 35606) to (220228 ± 46423) when increasing TEDA contents from 1 to 5 w.t% (Table 23). However, for higher TEDA contents, a slight DF decrease is observed until reaching a value of (128365 ± 32189) when TEDA amount is about 10 w.t% (Table 23). On the other hand, the DF displayed by KI impregnated AC are found to be lower than that of the co-impregnated and TEDA impregnated AC (Table 23). More particularly, a paradoxical decrease of DF (Figure 40, curve in green) is observed with the increase of KI content from (10917 ± 4981) for unimpregnated AC to only (236 ± 29) for 5 w.t% KI AC (Table 23). This decreasing feature is also found to be consistent with the behavior displayed by co-impregnated AC when fixing the TEDA quantity, confirming the absence of any interaction between KI and TEDA molecules as observed in the previous chapter. Same orders of magnitude of DF for KI impregnated AC were also reported in the literature with RH ranging from 30 % to 40 % (T = 20 – 30 °C) [5][43][117]. However, up to now no attempt was performed to better assess the role played by KI by comparing, for instance, with the unimpregnated AC. In the next section, the effect of KI impregnation is further investigated using the deduced physico-chemical characteristics from Chapter II in order to explain the obtained DF evolution at (T = 20 °C, RH = 40 %).

3.1.3 Discussions about the observed features for KI and TEDA AC

In order to explain the DF evolutions obtained in this first set of conditions (Figure 40), it is necessary to evaluate all the potential involved mechanisms. More precisely, three mechanisms are distinguished: (i) the physisorption phenomena controlled by the microporosity and the micropore filling of H_2O during the equilibration phase; (ii) the chemisorption *via* TEDA reactivity which was found to be dependent on the humidity and (iii) the isotopic exchange reaction due to KI impregnation. Under moderately humid conditions (T = 20 °C, RH = 40 %), the physisorption mechanism was generally reported to be dominant compared to chemisorption phenomena or the potential isotopic exchange [131]. Therefore, a specific attention is devoted to assess the influencing parameters towards physisorption in this first set of conditions.

On the one hand, the microporosity of the KI and TEDA impregnated AC present different features depending on the impregnation ratio. Indeed, according to the previous characterization of the porous structure in Chapter II, the decreasing evolution of the microporosity cannot be observed for low impregnation ratio (< 0.4 % in molar, Figure 30 of Chapter II), which corresponds to the studied KI impregnated AC and 3% TEDA AC (Table 20, Chapter II). In contrast, a more significant reduction of the microporosity was obtained for other TEDA AC because of a higher impregnation molar ratio (value ranging from 3 w.t% to 10 w.t% corresponding to molar fractions of 0.32 % and 1.07 %, respectively). The extent of the reduction of microporosity can reach about 27 % for a TEDA content of 10 w.t%. To sum-up, the starting microporosity can be considered to be similar for KI impregnated AC but decreasing for TEDA impregnated AC especially after 3 w.t% in TEDA.

On the other hand, the available microporosity for CH_3I trapping can be influenced by the pre-adsorbed H_2O during the pre-equilibration step performed before retention test (Section 2.2.2). This adsorbed amount can be deduced from H_2O adsorption isotherms recorded at T = 25 °C (Chapter II). More precisely, a particular attention will be devoted to the water uptake at RH = 30% (T = 25 °C) in order to have the same absolute humidity as for the CH_3I retention experiment (T = 20 °C, RH = 40 %). The correspondent results for different AC are reported in Table 24. Different behaviors can be highlighted depending on the investigated adsorbent. On the one hand, a significant increase of the adsorbed H_2O amount was observed with KI impregnation (Figure 41 (a)). For example, an increase of water uptake from about 15 $mg \cdot g^{-1}$ to about 56 $mg \cdot g^{-1}$ was obtained when moving from un-impregnated AC to 5%KI AC (Table 24). Indeed, KI molecules may play as primary clustering or nucleation sites towards water vapor adsorption at low RH, therefore allowing to reduce the hydrophobic character of AC [63]. On the other hand, the adsorbed amount of H_2O using the same conditions (T = 25 °C, RH = 30 %) seems to be quasi-similar for the different TEDA AC tested (Figure 41 (a)), indicating a lower effect due to nucleation for TEDA as compared with KI. Moreover, a lower water uptake was generally obtained for TEDA impregnated materials (a value ranging from 29 to 35 $mg \cdot g^{-1}$, Table 24).

Table 24. Main characterization data of the tested AC from N_2 and H_2O porosimetry versus their ability for $CH_3{}^{131}I$ trapping (DF and η)

Impregnation	V_{micro} (cm^3/g)	Adsorbed H_2O at RH = 30%* (mg/g)	Adsorbed H_2O at RH = 95% (mg/g)	H_2O filling fraction at RH = 30% (%)	Available V_{micro} (cm^3/g)	DF	Trapping efficiency η** (%)
Unimpregnated	0.453	15.4	397.4	4	0.435	10917	99.9908
0.1 w.t% KI	0.469	29.7	364.8	8	0.431	6378	99.9843
0.5 w.t% KI	0.470	33.4	343.1	10	0.424	3689	99.9729
1 w.t% KI	0.486	44.4	353.9	13	0.425	2895	99.9655
2 w.t% KI	0.469	38.6	385.4	10	0.422	1587	99.9370
5 w.t% KI	0.456	56.1	342.4	16	0.381	236	99.5763
3 w.t% TEDA	0.441	34.1	320.4	11	0.394	210578	99.9995
5 w.t% TEDA	0.410	34.8	364.3	10	0.371	220228	99.9995
7 w.t% TEDA	0.380	33.1	329.5	10	0.342	167621	99.9994
10 w.t% TEDA	0.332	28.9	342.4	8	0.304	128365	99.9992

** The conditions of the adsorption isotherms of H_2O (T=25°C, RH = 30%) are equivalent to the conditions of the retention test (T=20°C, RH = 40%) in terms of absolute humidity*
*** $\eta = 100 \times (1-1/DF)$, chapter I*

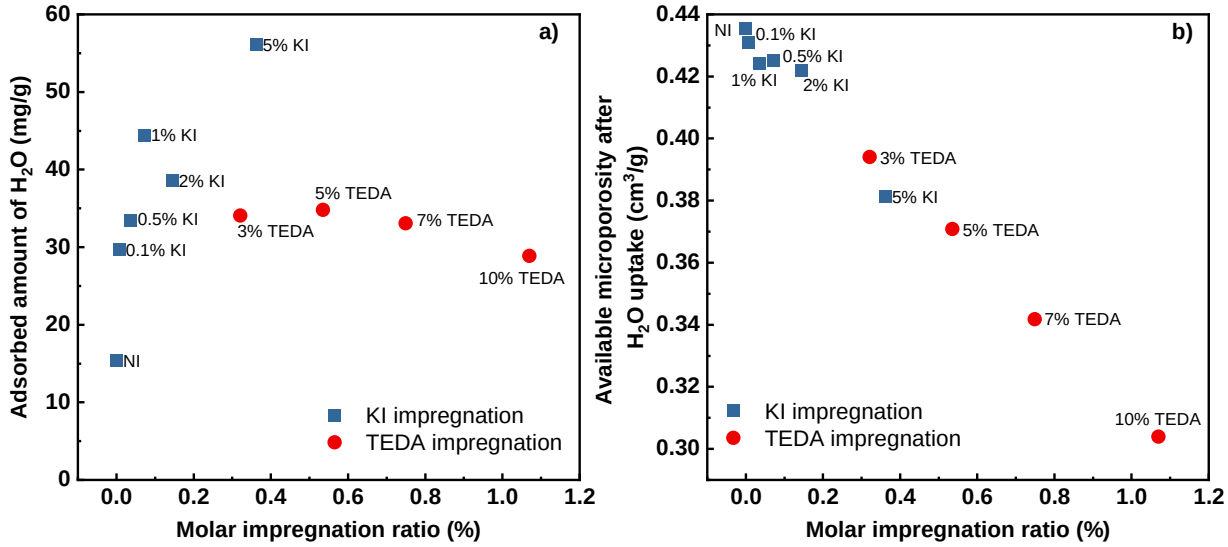

Figure 41. a) Pre-adsorbed H_2O versus molar impregnation ratio at T = 25 °C, RH = 30 % as deduced from adsorption isotherms experiments; b) Available microporous volume after water uptake at T = 25 °C, RH = 30 % versus molar impregnation ratio

Regarding these considerations, it is necessary to define the fraction of microporosity that will be available for $CH_3{}^{131}I$ retention under the tested conditions. In that respect, the H_2O filling fraction can be estimated from the ratio between the obtained uptake at RH = 30% and the adsorbed amount at saturation (*i.e.* at RH = 95 %). The available microporous volume can then be calculated by multiplying the starting V_{micro} and the fraction of residual pores (1-H_2O filling fraction). As depicted in Figure 41 (b), the available microporosity after water uptake decreases for both KI and TEDA impregnation, with a decrease magnitude up to 12% and 30 % for 5 w.t% of KI and 10 w.t% of TEDA, respectively (Table 24). This reduction is attributed to different reasons depending on the molecule nature. For KI, this decrease is related to the enhancement of adsorbed H_2O at low RH after KI progressive loading. For TEDA, this trend is assigned to the decrease of microporosity because of the presence of TEDA within or at the openings of AC pores (Table 24). Therefore, the contribution of physisorption in all cases is expected to decrease after KI and TEDA impregnation.

Now, if we consider the DF evolution for both KI and TEDA, it can be noticed that DF evolution is actually more "logical" for TEDA impregnation than for KI impregnation. For TEDA impregnated AC, the contribution of the physisorption is proven to be decreasing because of the presence of TEDA molecules within or at the openings of micropores. In the meantime, the contribution of the chemisorption is expected to increase with TEDA content. More precisely, the reactivity of TEDA at such moderately humid conditions (T = 20 °C, RH = 40 %) is reported to be dominated by an alkylation mechanism based on CH_3I dissociation followed by the formation of stable ammonium [124]. Hence, The DF evolution for TEDA impregnation at RH = 40% can be considered as a compromise between these two opposite mechanisms. According to the obtained results, the optimum TEDA impregnation corresponding to these two mechanisms seems to be 5 w.t%, where the accessible microporosity is decreased only by 15% against 23% with 7 w.t% of TEDA, for instance.

It is reasonable to think that the DF evolution for KI impregnated AC at the studied conditions should be the same as displayed by TEDA impregnated AC. Indeed, there are also two mechanisms that work oppositely with KI content: the physisorption and the isotopic exchange led by KI. However, it seems that the DF evolution for KI AC at (T = 20 °C, RH = 40 %) is dominated by physisorption and more particularly by the pre-adsorbed amount of water vapor during the equilibration step. This unusual observation is firstly evidenced in Figure 42 (a) which shows the

decreasing evolution of DF versus the adsorbed amount of H_2O, in agreement with the reduction of the available microporosity for CH_3I retention. Then, the relation between AC performances and the physisorption is further presented in Figure 42 (b), where a linear relationship can be noticed. Here, the trapping efficiency η is used instead of *DF* for mathematical reasons. *DF* is widely used in the nuclear field due to its mathematical form, allowing to distinguish easily between different adsorbents especially when the trapping efficiency is sufficiently high. As presented in Table 24, all the KI impregnated AC display similar trapping efficiency (higher than 99%), but their DF remain easily distinguishable. Nevertheless, the use of the trapping efficiency η allows to represent the "trapping capacity" of a given adsorbent, which is easier to evaluate the trapping performance versus certain adsorbent parameters (Figure 42 (b)). Finally, it can be concluded that the trapping performance of the γ–labelled CH_3I for KI impregnated AC at moderately humid conditions is only dominated by the physisorption influenced itself by the water pre-adsorption. Therefore, in other words this trend may indicate the absence of the isotopic exchange under the first set of conditions. This unexpected observation is part of an important hypothesis for the isotopic exchange in this chapter, which will be later discussed in Section 3.3. The role played by TEDA and KI for $CH_3{}^{131}I$ removal at more humid conditions is evaluated in the next section.

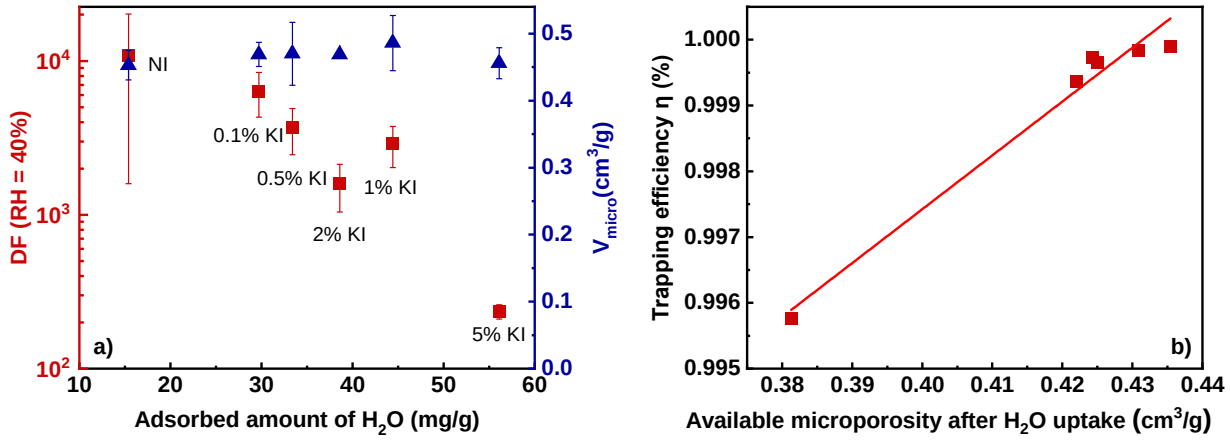

Figure 42. a) Evolution of DF and V_{micro} versus the adsorbed amount of H_2O (T = 25 °C, RH = 30 %) for KI impregnated AC; b) Trapping efficiency η versus the available microporosity for KI impregnated AC

3.2 Retention performances of AC at (T = 20 °C, RH = 90 %)

3.2.1 Behavior of co-impregnated AC

In this section, attention is focused on the retention performances at (T = 20 °C, RH = 90 %). Using the same methodology as that of Section 3.1, the DF of the tested AC are summarized in the Table 25 and shown in Figure 43. The reported DF are average values from up to four replicates with k = 2. A drastic decrease of DF is observed at this second set of conditions, with corresponding DF around 1000 times lower than those obtained at the previous conditions (T = 20 °C, RH = 40 %). As presented in the last section, the co-impregnated AC were firstly evaluated under current conditions. The DF of the tested co-impregnated AC are ranging from (31 ± 2.6) to (109 ± 25) in humid conditions. As a comparison, a DF of about 100 is required for nuclear grade AC in these conditions, *i.e.* in the presence of a large excess of water vapor [43]. This order of magnitude is also reported in several studies in the literature [89][169]. More particularly, a greater beneficial effect due to TEDA impregnation as a comparison with KI can be observed. Indeed, TEDA contents of 5 or 10 w.t% are required to guarantee satisfactory retention performances towards CH_3I (DF about 100, for KI content lower than 2 w.t%, Table 25). However, a negligible contribution of KI for $CH_3{}^{131}I$ removal can be reported considering these tests. A detrimental effect is even highlighted when increasing KI contents from 1 to 2 w.t% for fixed TEDA loadings of 5 or 10 w.t% (curves in red and blue, Figure 43). Indeed, the corresponding DF are only about (53 ± 14) and (60 ± 5.4) for (2%KI + 5%TEDA) AC and (2%KI + 10%TEDA) AC, respectively (Table 25).

In addition, just a slight increase in DF performances is observed from (91 ± 6.5) to (106 ± 20) when increasing KI content from 0.5 to 1 w.t% and for a fixed TEDA quantity of 5 w.t% (Table 25). Considering the tested co-impregnated AC, the optimal retention performances are found for (1%KI + 5%TEDA) AC. The same impregnation combination is also reported for the commonly used *nuclear grade* AC [6]. For the co-impregnated AC, the KI contribution may be masked because of the simultaneous presence of TEDA, presenting higher affinity for $CH_3{}^{131}I$ removal in moderately or highly humid conditions [131][63]. Using the same methodology as that of Section 3.1, the effect of each impregnation for single impregnated AC is separately discussed in the following sections.

3.2.2 Behavior of single impregnated AC

TEDA impregnated AC

An increasing relationship can be evidenced between DF and TEDA content up to 7 w.t% (Figure 43, curve in purple). More particularly, a DF increase from (32 ± 5.8) to (103 ± 4.6) can be highlighted for TEDA loadings of 1 w.t% and 7 w.t%, respectively (Table 25). A less pronounced increase in DF can be outlined for TEDA content of 10 w.t% (DF = (115 ± 5.9)). The observed DF are the same order of magnitude as the reported values in the literature under similar conditions for TEDA impregnated AC [5][170].

KI impregnated AC

Similar to the TEDA impregnated AC, the DF are also observed to increase with KI impregnation at (T = 20 °C, RH = 90 %), but to a less important extent. When varying KI content from 0 to 5 w.t%, a slight increase of DF from (1.96 ± 0.08) to (9.71 ± 0.87) can be highlighted (Table 25 and Figure 43, curve in green), indicating the inability of KI-impregnated AC to retain $CH_3{}^{131}I$ at the considered conditions compared to TEDA impregnation. Besides, the DF for a KI content of 2 w.t% and 5 w.t% are found to be similar (9.60 ± 1.32) and (9.71 ± 0.87) respectively (Table 25). This trend indicates a potential saturation of the AC performances for KI impregnation under current conditions. The inability of KI-impregnated AC to retain $CH_3{}^{131}I$ seems to be consistent with the literature, where a magnitude of more than 600 of the DF decrease are outlined for RH ranging from 40 to 98% (residence time = 0.2 s) [5].

In general, single impregnated AC present nearly the same DF evolutions as co-impregnated AC. Therefore, the absence of any interaction between TEDA and KI molecules can be proposed, consistently with characterization results in Chapter II. An attempt to explain these observed trends is presented in the next section.

Table 25. Summary of DF for different AC at (T = 20 °C, RH = 90 %, k = 2): residence time = 0.2 s, linear velocity = 25 cm·s^{-1}, pre-equilibration under humidity for 16 h

Co-impregnation			TEDA impregnation		KI impregnation	
KI%	TEDA%	DF	TEDA%	DF	KI%	DF
0.5	1	33 ± 8.0	1	32 ± 5.8	0	1.96 ± 0.08
0.5	5	91 ± 6.5	3	66 ± 2.4	0.1	3.96 ± 0.98
0.5	10	100 ± 19	5	88 ± 15	0.5	5.82 ± 0.61
1	1	35 ± 5.0	7	103 ± 4.6	1	7.33 ± 0.60
1	5	106 ± 20	10	115 ± 5.9	2	9.60 ± 1.32
1	10	109 ± 25			5	9.71 ± 0.87
2	1	31 ± 2.6				
2	5	53 ± 14				
2	10	60 ± 5.4				

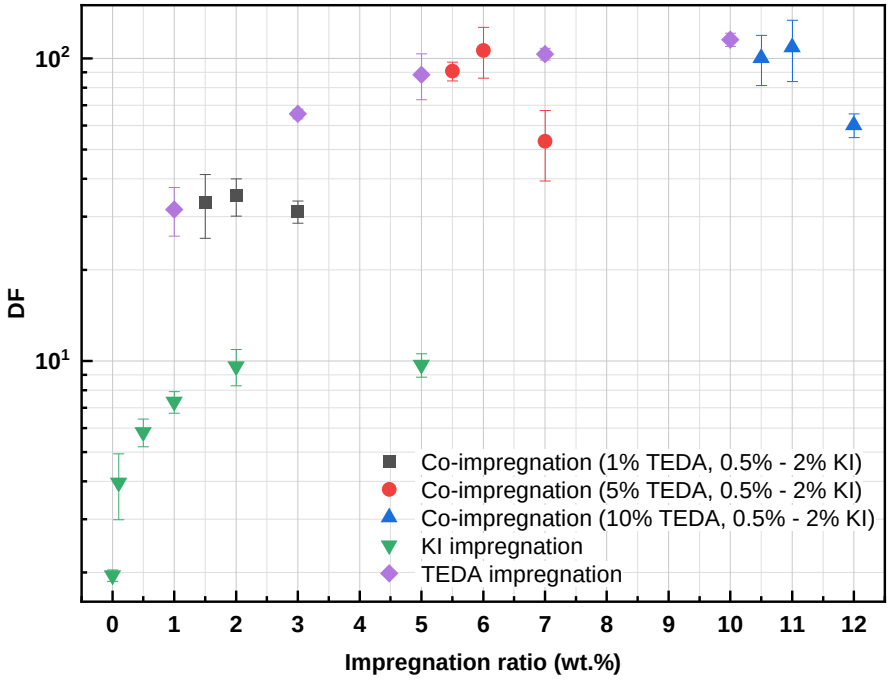

Figure 43. DF evolution for different AC as function of KI and TEDA contents at (T = 20 °C, RH = 90 %): residence time = 0.2 s, linear velocity = 25 cm·s^{-1}, pre-equilibration under humidity for 16 h

3.2.3 Discussions about the observed features for KI and TEDA AC

In these conditions, the significant changes of the DF evolution compared to RH = 40 % indicates the change of each trapping mechanism contribution (physisorption, chemisorption and the

isotopic exchange). Using the same strategy as described in Section 3.1, the contribution of the physisorption can be firstly investigated using the adsorption isotherms of H_2O. As summarized in Table 26, all the tested AC present significant amount of pre-adsorbed H_2O regardless of the impregnation type (adsorbed amount higher than 300 $mg \cdot g^{-1}$). The water molecules are reported to be firstly adsorbed on the AC surface due to the strong chemisorption of the water molecules with functional groups as mentioned in the previous section [171][172]. Then, water clusters are progressively formed on the AC surface through the formation of hydrogen bonds [171][172], corresponding to the micropore filling by the water molecules. The increase of the pre-adsorbed amount of H_2O compared to RH = 40 % leads to the huge increase of the micropore filling fraction to around 90% (Table 26), indicating a strong competitive adsorption between CH_3I and H_2O. Consequently, the deduced available microporous volume for the impregnated AC is found to be less than 0.08 $cm^3 \cdot g^{-1}$ (Figure 44), which is almost negligible compared to the first set of conditions. To sum up, it can be concluded that the contribution of the physisorption is significantly reduced at RH = 90 % since the accessibility to the active sites for physisorption is largely hindered by H_2O [7]. The significant reduction of the physisorption for all the tested AC under current conditions explains the drastic diminution of DF compared to RH = 40 %.

Table 26: Summary of the pre-adsorbed H_2O amount for different AC deduced from the adsorption isotherms of H_2O

Impregnation	V_{micro} (cm^3/g)	Adsorbed H_2O at RH = 70%* (mg/g)	Adsorbed H_2O at RH = 95% (mg/g)	H_2O filling fraction at RH = 70% (%)	Available V_{micro} (cm^3/g)	DF	η (%)
Non impregnated	0.453	305	397.4	77	0.11	2.0	50.000
0.1 w.t% KI	0.469	304.7	364.8	84	0.08	4.0	74.773
0.5 w.t% KI	0.47	300.9	343.1	88	0.06	5.8	82.813
1 w.t% KI	0.486	317.8	353.9	90	0.05	7.3	86.365
2 w.t% KI	0.469	328.4	385.4	85	0.07	9.6	89.583
5 w.t% KI	0.456	317.4	342.4	93	0.03	9.7	89.703
3 w.t% TEDA	0.441	281.3	320.4	88	0.05	66	98.475
5 w.t% TEDA	0.41	298	364.3	82	0.07	88	98.869
7 w.t% TEDA	0.38	278.7	329.5	85	0.06	103	99.033
10 w.t% TEDA	0.332	285.4	342.4	83	0.06	115	99.133

** The conditions of the adsorption isotherms of H_2O (T = 25°C, RH = 70%) are equivalent to the conditions of the retention test (T=20°C, RH = 90%) in terms of absolute humidity.*

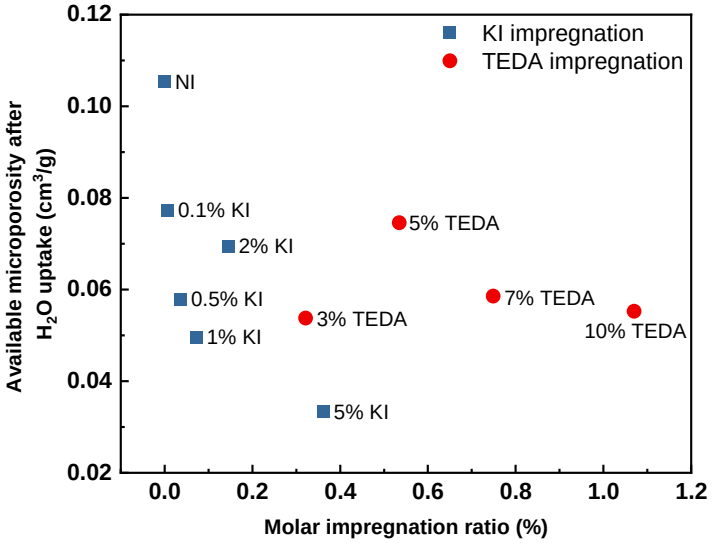

Figure 44. Available microporous volume after water uptake at T = 25 °C, RH = 70 % versus molar impregnation ratio

Apart from the significant decrease of DF at RH = 90 % compared to RH = 40 %, the DF were found to increase with both TEDA and KI impregnations (Figure 43), which is clearly assigned to

the chemisorption and the isotopic exchange, respectively, since there is no other mechanism responsible for such increase of the AC performance in these conditions. Taking into account the low available microporosity that still remains at RH = 90 %, it can also be proposed that as a preliminary step for the adsorption phenomena [26][132], the physisorption is no longer dominant for the CH_3I removal under current conditions. Nevertheless, the extent of DF increase due to the KI impregnation is less important as compared with TEDA, which is due to the affinity of TEDA towards CH_3I under humidity. Unlike the CH_3I dissociation mechanism for TEDA at RH = 40 %, a protonation mechanism between CH_3I, H_2O and TEDA results in the formation of a molecular complex of TEDA/CH_3I under humid conditions, enhancing the chemical interaction of TEDA with CH_3I [131][173]. Besides, the limitation of the DF increase between 2 w.t% and 5 w.t% in KI may be assigned to the increase of the diffusion resistance by pre-adsorbed H_2O and deposited KI [131]. Further discussion on the isotopic exchange is presented in the next section.

3.3 Discussions on the isotopic exchange

In the previous sections, the effect of the isotopic exchange led by KI was investigated at RH = 40 % and 90 % using adapted procedures from standardized methods according to the ASTM D3803 and NF M62-206 norms [128][167]. The obtained DF evolutions for KI impregnated AC show rather different features. On the one hand, the isotopic exchange led by KI seems to be absent at RH = 40%. On the other hand, the isotopic exchange was observable at RH = 90 %, but with poor AC performance (especially compared to TEDA impregnated AC). These unusual observations raise the question about the current use of KI in the *nuclear grade* AC: does it truly improve the AC performance towards the $CH_3{}^{131}I$ trapping? Furthermore, another question can be asked regarding the results obtained in this chapter: why the effect of the isotopic exchange does seem to depend on the operating conditions (especially the water content)?

If we take a closer look in the literature, there is only one publication that clearly investigated the effect of isotopic exchange led by KI. The performance of a 5 w.t% KI_3 impregnated AC (equal amount of KI and I_2) was evaluated through the BTC measurement [135]. Under their operating conditions employed (4625 $Bq \cdot m^{-3}$ of $CH_3{}^{131}I$, RH = 86 %, residence time = 0.75 s, linear velocity = 6.6 $cm \cdot s^{-1}$), it was observed that the penetration of $CH_3{}^{131}I$ is less than that of stable CH_3I (Figure 45), which justifies the presence of the isotopic exchange during the adsorption experiment [135].

More particularly, the effect of the isotopic exchange becomes more significant during the breakthrough phase: the cumulative penetrations (ratio between the total quantity of outlet CH_3I and the total injected CH_3I) at t = 120 min (Figure 45) for radioactive and stable CH_3I are around 10 % and 60 %, respectively. Besides, no specific effect is observed at the beginning of the BTC (retention phase).

The aforementioned BTC measurements are actually in good agreement with our DF measurements in this chapter. As summarized in Table 27, the conversion of DF to penetration P at RH = 40 % indicates that the tested KI impregnated AC are still in the retention phase. Accordingly, the isotopic exchange cannot be observed. However, the high value of penetration P at RH = 90 % indicates the AC breakthrough for the tested KI impregnated AC. Under these conditions, the effect of the isotopic exchange is clearly observed. Hence, a hypothesis is made based on the DF results of this chapter, that the effect of the isotopic exchange for KI can only be observed after the AC breakthrough. Meanwhile, similar AC performances during the retention phase should be expected for different KI contents. In order to prove the proposed hypothesis, the BTC measurements dedicated for both stable and γ-labelled CH_3I is required, which will be presented in the next chapter.

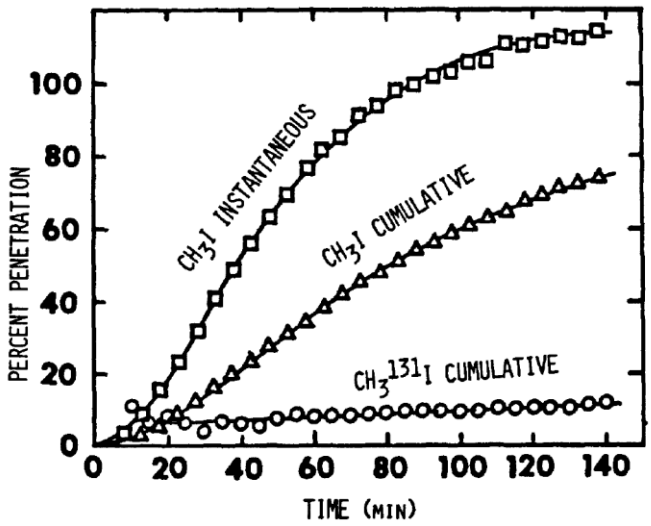

Figure 45. Comparisons of $CH_3{}^{127}I$ and $CH_3{}^{131}I$ penetration on a 5% KI_3 AC (4625 $Bq \cdot m^{-3}$ of $CH_3{}^{131}I$, RH = 86 %, residence time = 0.75 s, linear velocity = 6.6 $cm \cdot s^{-1}$) [135]

Table 27. Summary of the AC' performances for KI impregnation

KI impregnation	RH = 40 %			RH = 90 %		
	DF	P (%)	Phase	DF	P (%)	Phase
Unimpregnated	10917	0.01	Retention phase → absence of the isotopic exchange	2.0	50	Breakthrough phase → observation of the isotopic exchange
0.1 w.t%	6378	0.02		4.0	25	
0.5 w.t%	3689	0.03		5.8	17	
1 w.t%	2895	0.03		7.3	14	
2 w.t%	1587	0.06		9.6	10	
5 w.t%	236	0.42		9.7	10	

4. Conclusions

In this chapter, the behavior of KI and/or TEDA impregnated AC towards the capture of $CH_3{}^{131}I$ was investigated under different RH in order to gain insights about the role played by these impregnants for the retention of $CH_3{}^{131}I$. A specific attention was also devoted to assess the effect of isotopic exchange from experiments based on standardized protocols.

The investigation of γ-labelled CH_3I retention behaviors at RH = 40 % and 90 % reveals different features. At (T = 20 °C, RH = 40 %), all the tested AC exhibit good performance of $CH_3{}^{131}I$ trapping, with a DF up to 2.2×10^5 in good agreement with the required performances for AC currently implemented in the French nuclear industry. The similar DF evolution between single and co-impregnated AC allows to confirm the absence of any interaction as observed in the characterization section. The DF evolution for TEDA impregnated AC exhibits an increase up to 5 w.t% then followed by a slight decrease. However, a decreasing DF evolution with KI impregnation is observed. Under these conditions, the dominant trapping mechanism (physisorption) is found to be decreasing for both TEDA and KI impregnation but for different reasons. On the one hand, the decreasing physisorption for KI is due to the increased amount of adsorbed H_2O resulting from the nucleation effect of KI impregnation, and leading to the diminution of the available microporosity. On the other hand, the physisorption for TEDA impregnation is found to decrease with the microporosity due to the high impregnation ratio and the presence of such molecules within or at the openings of micropores. Because of the well dispersed TEDA content that contributes to the chemisorption, the DF evolution for TEDA at RH = 40 % is found to be a compromise between the diminution of the available microporosity and

the increase of the chemisorption *via* TEDA, with an optimal TEDA impregnation at 5 w.t%. In contrast, the isotopic exchange by KI is found to be absent, with the AC performance for KI impregnation dominated by the physisorption itself determined by the pre-adsorbed water.

At (T = 20 °C, RH = 90 %), a drastic decrease of DF is observed for all the AC, with DF about 1000 times lower than that at RH = 40%. The optimal impregnation at RH = 90 % is obtained with 1% KI and 5% TEDA, in agreement with the composition of the *nuclear grade* AC. The increase of the DF with TEDA and KI at RH = 90 % is found to be directly related to the chemisorption and the isotopic exchange, respectively. The importance of the corresponding chemisorption and the isotopic exchange is evidenced by the significant decrease of the available microporosity (fraction of pore filled with water exceeding 90%), indicating that the physisorption as the preliminary step of adsorption phenomena is no longer dominant under current conditions. The extent of the DF increases when using TEDA is found to be more important as compared with KI, thanks to its higher reactivity with CH_3I under different conditions consistently with several literature studies.

The different DF evolutions for KI impregnated AC at RH = 40 % (absence of the isotopic exchange) and 90% (presence of the isotopic exchange with poor AC performance) highlight the importance of the different phases during the adsorption test. An assumption is therefore proposed that the isotopic exchange is only observed during the breakthrough phase at least when considering the literature. In order to prove the proposed hypothesis, additional investigations of the AC performances were further conducted at the lab scale. The main objective was to elucidate the importance of the isotopic exchange reaction by measuring the BTC of both $CH_3{}^{131}I$ and $CH_3{}^{127}I$ for KI impregnated AC, which is presented in the next chapter in more details.

Chapter IV: AC performances towards the capture of stable/γ-labelled CH_3I (breakthrough curves measurements)

1. Introduction

Based on the hypothesis proposed in the previous chapter, it is assumed that the observation of the isotopic exchange may require to reach the breakthrough phase of the tested AC. However, the current use of the PERSÉE facility for evaluating the AC performances under moderately humid conditions only displays the retention phase observation considering their high DF at RH = 40 %. Furthermore, the use of DF makes it difficult to quantitatively evaluate such isotopic exchange. Hence, another experimental approach for a relatively long-time scale, which can globally evaluate the AC performance from total retention to complete breakthrough, must be considered. The investigation of the AC performances as a function of time in adsorption field of research leads naturally to the breakthrough curves (BTC) measurements. One the one hand, the BTC for stable CH_3I adsorption can be achieved using a classic fixed-bed adsorption experiment. On the other hand, the BTC for γ-labelled CH_3I adsorption remains a scientific and technical challenge. Here comes the following issue: how to measure the BTC for the γ-labelled CH_3I adsorption in order to investigate the contribution of the isotopic exchange?

The previously cited publication [135] describes a specific experimental setup dedicated to the BTC measurement of both stable and γ-labelled CH_3I adsorption. As shown in Figure 46, the *in-situ* inlet/outlet concentration of both stable and γ-labelled CH_3I are measured by GC-ECD and γ spectroscopy using NaI scintillators, respectively. However, this kind of experimental setup requires a large amount of preparation at the laboratory scale, especially regarding the adjustment between different measurement techniques.

Based on the current facilities available of the LECEV laboratory, a newly-designed experimental setup has been developed. The general idea is to measure the BTC towards both stable and γ-labelled CH_3I adsorption separately through two different experimental setups: one for the stable

CH_3I, while the other (newly designed) is dedicated to the γ-labelled CH_3I. In this way, each experimental setup can be compact and relatively easy to handle and manipulate separately. The operating conditions will be as similar as possible for these two setups (Table 28), in order to ensure the comparability between these two configurations.

The objectives of the BTC comparisons between stable and γ-labelled CH_3I is to directly quantify the contribution due to isotopic exchange over time focusing on KI impregnated AC in a certain experimental configuration ([CH_3I] = 10 ppmv, T = 20 - 30 °C, RH = 0 %, Table 28). In order to achieve this goal, the first part of this chapter (Section 2 and 3) focuses on the characteristics of each experimental setup especially for the newly designed one. Then, the second part of this chapter (Section 4) is dedicated to the exploitation of the obtained BTC results (stable and γ-labelled CH_3I).

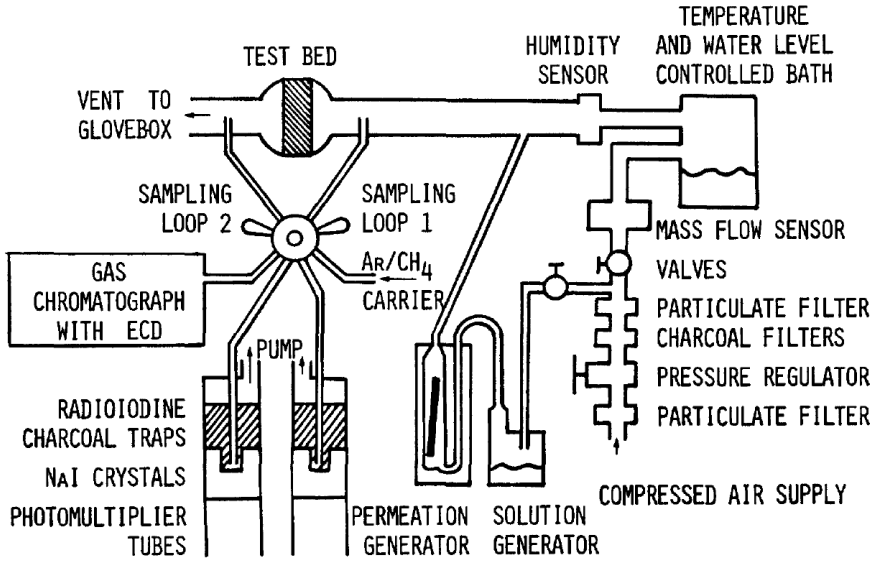

Figure 46. Experimental setup for simultaneous CH_3I and $CH_3{}^{131}I$ penetration measurements [135]

Table 28. Operating conditions for BTC measurements during the present study

Breakthrough curve type	Temperature (°C)	RH (%)	C_0 (CH_3I)	Residence time (s)	Linear velocity ($cm \cdot s^{-1}$)
Stable CH_3I	20 - 30	0	10 ppmv	0.2	25
γ-labelled CH_3I					

2. AC performances towards the capture of stable CH_3I: experimental part

The BTC measurement of stable CH_3I adsorption at dry conditions is carried out through an experimental setup named BRIOCH (Figure 47). This bench is composed of three main parts: (1) gas generation, (2) AC sample bed inside the oven and (3) gas chromatography equipped with a PDECD (Pulsed Discharge Electron Capture Detector).

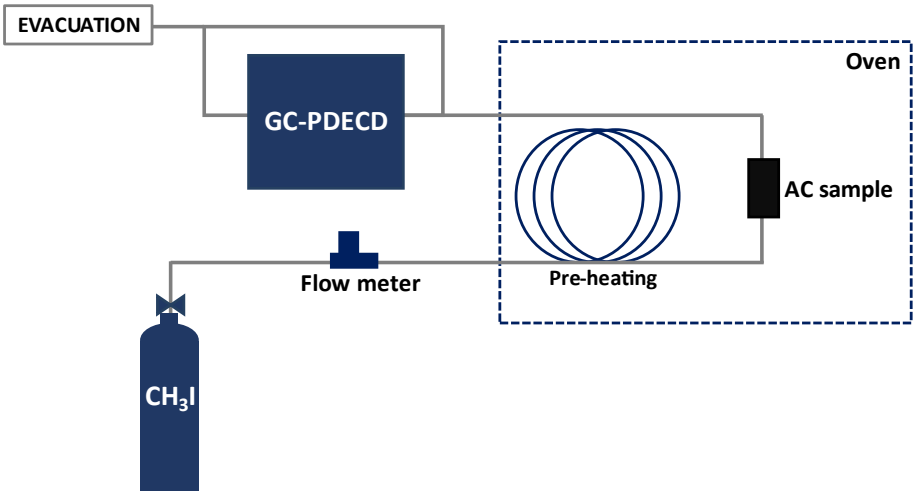

Figure 47. Schematic view of the BRIOCH setup

Gas generation

Certified CH_3I gas bottles (*Air Products*, [CH_3I] = 160 ppmv ± 0.5%/N_2) were used for BRIOCH. The CH_3I was diluted by pressurized air in order to obtain a CH_3I concentration of 10 ppmv according to Table 28. The selection of a 10 ppmv inlet concentration allows the obtention of complete BTC in a reasonable time (around 20 h) while remaining close to maximum CH_3I concentrations in nuclear industry effluents [60]. The gas bottle was connected to the inlet of the AC sample holder. The flows of the pressurized air and CH_3I were controlled by mass flow meters (*SLA5800*, *Brooks*), with a total flowrate of 6.63 $L \cdot min^{-1}$ (NTP) corresponding to a linear velocity of 25 $cm \cdot s^{-1}$ at 30 °C.

AC sample bed

The AC sample is prepared using similar protocols as described in Chapter III, with the inner diameter of the sample holder reduced to 25 mm (bed depth = 50 mm, residence time = 0.2 s).

Prior to each experiment, the AC sample was manually grinded. The granulometry of the grinded AC was selected through a mechanical sieving ranging from 1 mm to 1.4 mm in order to avoid preferential schemes [174]. An *ex-situ* pretreatment at 100 °C overnight was also carried out to remove the moisture content of the AC.

GC-PDECD instrument

The outlet line of the AC sample holder was connected to the gas chromatography *(Clarus 680, PerkinElmer)* equipped with a high-sensitivity PDECD (*Valco instruments)* specific for electro-negative compounds, especially halogenated molecules detection [175]. This instrument allows the continuous and online precise measurements of CH_3I gaseous concentration during retention tests. It consists of three main parts:

(i) gas injector

The gas injector allows the introduction of gaseous compounds within the GC-PDECD system thanks to an appropriate sampling loop (schematic view in Appendix 17). The injection loop placed in a metal pad was regulated at 120°C in order to ensure a good thermal homogeneity of the injection system without inducing decomposition of the inlet gaseous CH_3I into the column. A controlled volume of CH_3I gaseous sample (V = 250 µL) is injected into the column inlet (Appendix 17) before reaching the detector using helium as a carrier gas (*BIP ECD, Air Products*). The helium flowrate was maintained at 6 $mL \cdot min^{-1}$. Furthermore, an online dilution using the same carrier gas is achieved by a split injection to avoid the potential saturation in the column and detector. The split flow rate was fixed at 30 $mL \cdot min^{-1}$. Finally, an additional pneumatic valve is used to separate most of the atmospheric gases and the targeted analyte (CH_3I) in a first column before entering the second column (Appendix 17).

(ii) columns

Two slightly polar columns (*Rtx-502.2, RESTEK*) are installed in a thermostatic chamber of the GC-PDECD system. This *Rtx-502.2* column is composed of 5% diphenyl and 95% dimethyl polymethyl siloxane. The polyvalent nature of this column allows to separate CH_3I from other compounds based mainly on the difference in polarity. The length of the columns is set to 30 m. The column temperature that is important for the molecule separation and the retention time, is

optimized to be 80 °C. In this configuration, a chromatogram is obtained with a CH_3I retention time of about 24 min (Appendix 18), allowing to have enough experimental points to finely monitor the evolution of the CH_3I concentration (taking into account a duration of about 20 h for a total BTC).

(iii) detector

Contrarily to the standard Electron Capture Detector (ECD), in which the ionization source is a radioactive substance, the PDECD relies on a very short-wavelength UV and, additionally, on the electrons emitted by a high-voltage electric discharge in ultrapure helium [59]. A supply of "dopant" gas (3% xenon in helium, *Air Products*) in the detector volume provides a wealth of thermalized electrons. In the electrical field created by a bias electrode, these electrons are eventually gathered by a collector electrode: they constitute the detector standing current. When a compound with high electron affinity enters the detector volume through the capillary column, the decrease of the standing current is the PDECD response (see [175] and Appendix 19 for more details). In practice, the detector temperature is set to 300°C, and the length of the column inside the detector is set to 10.3 cm.

Preliminary tests were conducted in order to obtain a sufficiently high signal-to-noise ratio while avoiding signal saturation at 10 ppm for the BTC measurements. A summary of the optimized parameters of GC-PDECD is shown in Table 29. The CH_3I concentration monitoring was performed using *TotalChrom Navigator* software (Run time = 26 min). The calibration curve was established for initial CH_3I concentrations ranging from 2 ppbv to 10 ppmv (Figure 48). Accordingly, DL of about 0.8 ppbv was calculated for the studied analytical configuration.

In the next section, the newly designed experimental setup as well as the gas phase γ-labeled CH_3I generation methods is presented.

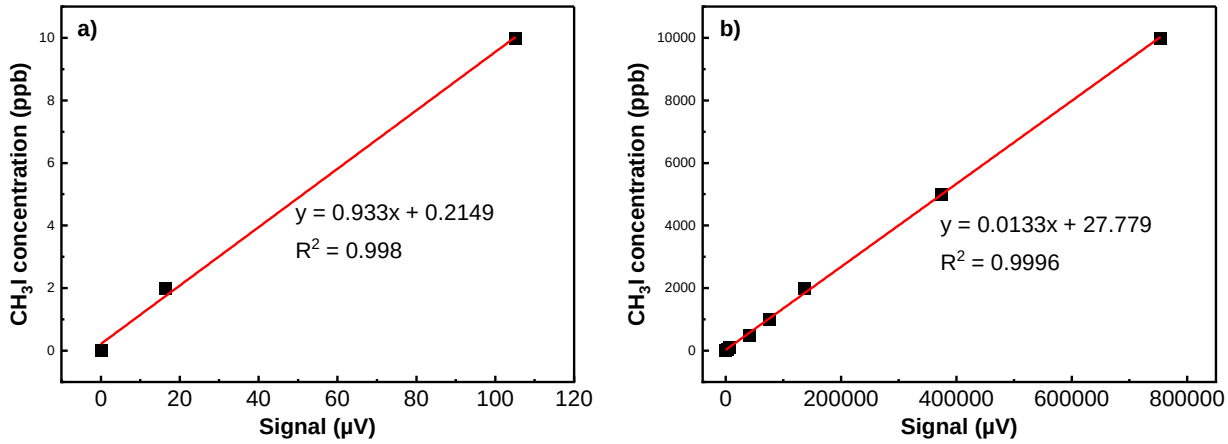

Figure 48. Calibration of the GC-PDECD for CH_3I with different concentration ranges: (a) 0 – 10 ppbv; (b) 10 – 10000 ppbv

Table 29. Summary of the GC-PDECD parameters chosen in this PhD project

Chromatogram information	
Retention time of CH_3I (min)	24
Run time for each chromatogram (min)	26
CH_3I concentration measurement range	2 ppbv – 10 ppmv
Sampling system of the GC	
Injection temperature (°C)	120
He flowrate (mL/min)	6
Split flowrate (mL/min)	30
Sampling duration by the valve V3 (min)	0.19
Closure of the valve V5 (min)	11
Columns of the GC	
Column type	Rtx-502.2 (RESTEK)
Column length (m)	30
Column temperature (°C)	80
Height of the column in the detector (cm)	10.3
PDECD detector	
Detector temperature (°C)	300
Attenuation coefficient	- 4
Pressure of dopant gas (bar)	2.6

3. AC performances towards the capture of γ-labelled CH_3I: experimental part

3.1 Experimental setup

3.1.1 General description

Unlike the above measurement of the stable CH_3I using GC-PDECD, the BTC measurement in radioactive case deals with other various considerations such as different measurement techniques, the γ-labelled generation in continuous mode as well as the safety and radioprotection considerations. More precisely, such an experimental setup must meet the following requirements:

- Operability to continuously generate a steady flow of γ-labelled CH_3I;
- Ability to characterize the obtained flow of γ-labelled CH_3I at the inlet and outlet of the adsorbent bed;
- Easy manipulation for data acquisitions and the use of an adapted measuring technique;
- Compact size in order to keep the whole setup inside a glove box for radioprotection considerations.

The first criterion represents one of the biggest challenges for the BTC measurement towards radioactive species. For this reason, most of the retention test for active species in the literature are carried out only in pulsed mode in a similar way as described in the previous chapter. The second criterion requires an adequate *ex-situ* measurement technique (γ-spectrometry). The last two criteria are related to the compactness of the experimental setup installed inside a glove box, which takes into account the safety consideration. The compact size also means that an *ex-situ* measurement of the activity for upstream/downstream section is required.

Hence, an experimental setup that successfully satisfies all these four criteria is designed and it is schematized in Figure 49 and Figure 50. Schematically, it can be divided into three main parts: A, B and C. Part A is dedicated to the generation of a steady flow of γ-labelled CH_3I using permeation tube placed within a permeation oven at a fixed temperature (see Section 3.2). Here, the use of the dilution flows 1 and 2 are with different purposes. More precisely, the dilution flow 1 (air or concentrated CH_3I depending on the experimental configuration, see Section 4.1) is used for the

gas phase γ-labeled CH_3I generation. The dilution flow 2 (air) is used to regulate the total flowrate to 6.86 $NL \cdot min^{-1}$ in order to obtain a linear velocity of 25 $cm \cdot s^{-1}$ at T = 20 °C. The flowrates of both dilution flows are summarized in Table 30.

Then, we distinguish afterwards parts B and C, whose principle and schematic design are similar. The principle of these two pathways consists of γ-labelled CH_3I continuous sampling on dedicated AC cartridges before further γ-spectrometry measurements with different purposes. On the one hand, part B is used to characterize the obtained γ-labelled CH_3I flow at the inlet of the bed adsorbent. This part is so-called the "*bypass section*". On the other hand, part C is used for the acquisition of BTC by continuous samplings at the outlet of the tested AC. This part is denoted as the "*main setup section*".

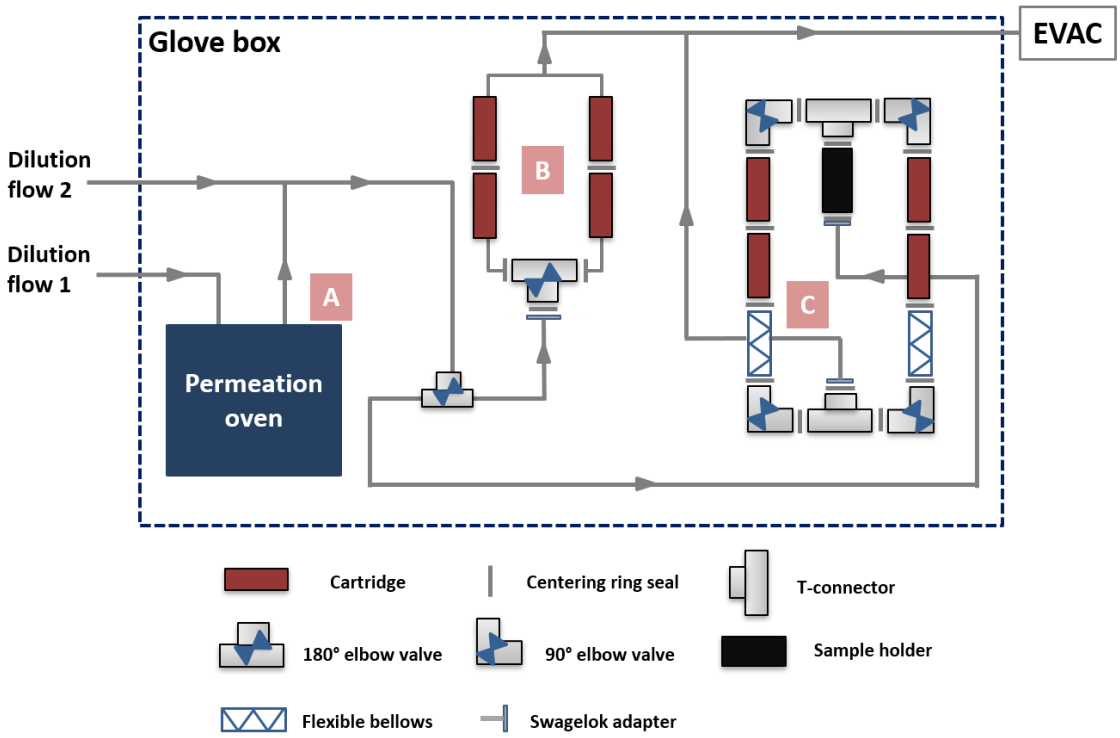

Figure 49. Schematic view of the experimental setup for γ-labelled CH_3I BTC measurement

Table 30. Summary of the different flowrates corresponding to a residence time of 0.2 s for dynamic adsorption experiments

Dilution flow 1 ($NL \cdot min^{-1}$)	0.4 (default)*
Dilution flow 2 ($NL \cdot min^{-1}$)	6.46
Total flowrate ($NL \cdot min^{-1}$)	6.86
Inner diameter of the sample holder (mm)	25
Bed depth of the sample** (mm)	50
Linear velocity ($cm \cdot s^{-1}$)	25
Residence time (s)	0.2

** The default value of the 0.4 $NL \cdot min^{-1}$ for dilution flow 1 has been used as a reference during past investigations at IPSN* [176]

*** The sample holder and AC granulometry for this experimental setup are the same as that for the first configuration (stable CH_3I adsorption).*

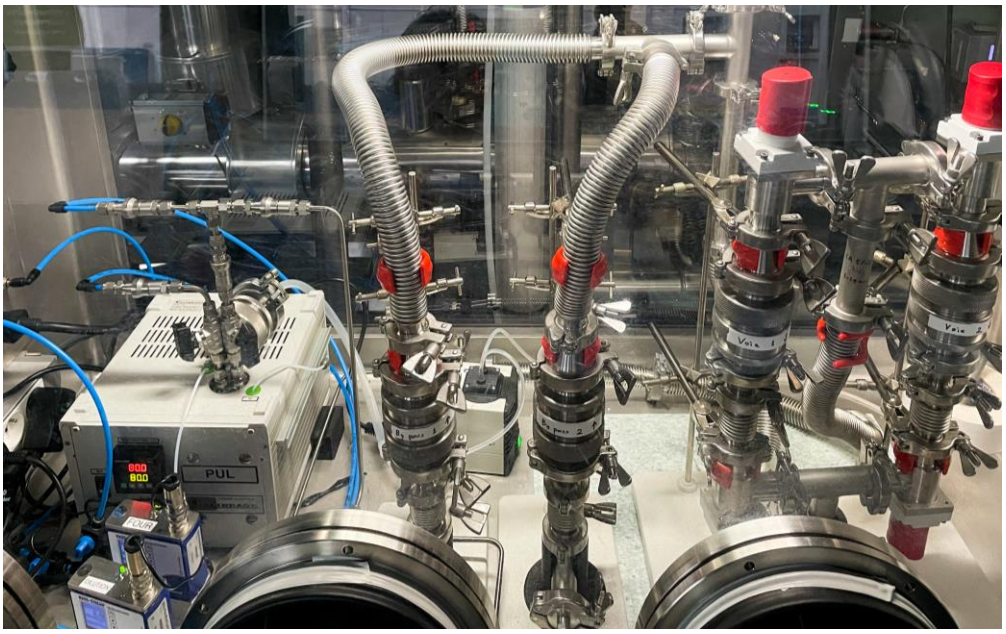

Figure 50. Photo of the experimental setup for γ-labelled CH_3I BTC measurement

3.1.2 Sampling principle

The use of two pathways for both the *bypass* and *main setup sections* takes into account the *ex-situ* activity measurements. More specifically, the γ-labelled CH_3I flow will be in contact with the commercial cartridge for a certain duration, and these cartridges will be changed regularly to be measured by γ-spectrometry. By this way, the $CH_3{}^{131}I$ flowrate ($Bq \cdot min^{-1}$) can be determined. Due to the manual character of the cartridge change and the corresponding *ex-situ* measurement, parts

B and C must be equipped with two pathways in order to guarantee a continuous generation of the γ-labelled CH_3I flow during the change of a given cartridge.

In general, once the flow of γ-labelled CH_3I is generated, it will be firstly characterized through the *bypass section* before further BTC measurement. A specific uptake method was used: during the bypass characterization, the flow will pass through one of these two pathways, then the direction of the flow is switched to the other after a certain duration. The upstream cartridge kept in contact with the flow will be replaced by a new one. The old one will be characterized by γ-spectrometry in order to measure the generated $CH_3{}^{131}I$ flowrate ($Bq \cdot min^{-1}$). The uptake will be repeated between these two pathways using the same method. Once the flowrate is stable, the γ-labelled CH_3I flow is finally switched to the *main set up section* to perform the BTC measurement using the same uptake method at the outlet of the tested adsorbent (Figure 49, Figure 50). The details of the cartridge calibration for the gamma spectroscopy are presented in Appendix 20.

3.2 Gas phase γ-labeled CH_3I generation methods

Two different methods are reported in the literature to generate the γ-labeled CH_3I in gas phase. The objective is to the choose the most appropriate method for our study.

γ-labeled CH_3I generation in pulsed mode

The γ-labeled CH_3I generation in pulsed mode is the same method used in Chapter III. This method is based on the methyl groups (from dimethyl sulfate) substitution by the sodium of radioactive NaI through the following reaction [167]:

$$(CH_3)_2SO_4(aq) + 2Na^{131}I(aq) \rightleftharpoons 2CH_3^{131}I(g) + Na_2SO_4(aq) \qquad (27)$$

The generated γ-labeled CH_3I is transferred immediately into the vapor phase at ambient temperature due to its high volatility (vapor pressure of 54.4 kPa at 20 °C [177]). However, this generation method in pulsed mode is not able to maintain a stable and continuous generation of γ-labeled CH_3I flow for a long duration.

γ labeling of CH_3I in liquid phase + gaseous generation using permeation tube

Faced with the inconveniences of the previous method, another approach is therefore considered. In the present study, an isotopic exchange method for CH_3I γ-labeling in liquid phase followed by a gaseous generation is chosen. More precisely, this method firstly involves the isotopic exchange of iodine molecules in liquid phase between the $CH_3{}^{127}I$ and $Na^{131}I$. The isotopic exchange reaction is presented as follow [178][179]:

$$CH_3^{127}I(aq) + Na^{131}I(aq) \rightleftharpoons CH_3^{131}I(aq) + Na^{127}I(aq) \quad (28)$$

Once the γ-labelled CH_3I in liquid phase is obtained, the generation in the gaseous phase is performed trough the permeation tube. More details about the second method are presented in the next section.

3.2.1 γ labeling of CH_3I in liquid phase

Reaction conditions

The isotopic exchange reaction takes place in the liquid phase. Hence, it is necessary to choose an appropriate solvent to facilitate the reaction kinetics. In that respect, it was reported that the reaction rate of the isotopic exchange between radioactive sodium iodide and methyl iodide was greatly dependent on the solvent nature (as summarized in Table 31) [180].

Table 31. Isotopic exchange reaction rate constants between methyl iodide and sodium iodide in different solvents at 20 °C [180]

Solvent	Reaction constant ($L \cdot mol^{-1} \cdot s^{-1}$) $\times 10^4$
H_2O	2.9
methanol	50
ethanol	140
methanol/ H_2O	63
acetone	43000

According to Table 31, acetone enables the highest rate constant. Consequently, the equilibrium of the isotopic exchange reaction will be reached more rapidly using acetone as compared with other solvents. Therefore, acetone is chosen to optimize the isotopic exchange reaction for the present study.

Experimental protocols

The experimental protocols for the isotopic exchange reaction was firstly developed within IRSN (Appendix 21 [176]). According to this protocol, the isotopic exchange reactions occur between stable CH_3I and $Na^{131}I$/NaOH using acetone as a solvent. A stirring step is required in order to enhance the reaction kinetics. Finally, water is added for the final γ-labelled CH_3I recovery thanks to a decantation process. More precisely, the aqueous phase will be present on the bottle top (contains water and acetone mixture) while the organic phase at the bottom (contains mostly γ-labelled CH_3I, density = 2.28 $g \cdot cm^{-3}$) as shown in Figure 51.

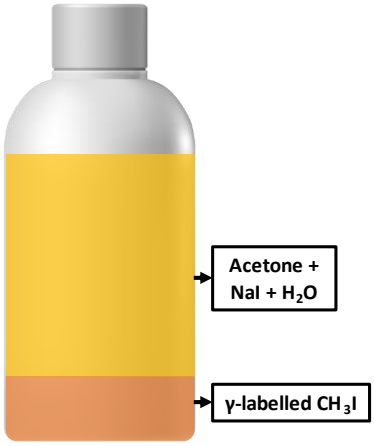

Figure 51. Theoretical distribution of different phases after decantation

The detailed optimization of the original experimental protocols regarding the effect of several parameters (initial $Na^{131}I$ activity, acetone and H_2O volumes, stirring duration) is presented in the Appendix 22. The objective of the protocol optimization is to obtain a high isotopic labeling efficiency of around 90% for a given initial $Na^{131}I$ activity as demonstrated in Appendix 22. Finally, the characteristics of the optimized experimental parameters are summarized in Table 32.

Table 32. Summary of the optimized experimental protocols

Initial $Na^{131}I$ activity (*AC grade*)	10 MBq
Volume of $Na^{131}I$ (µL)	between 300 and 600 µL
Volume of acetone (*AC grade*, mL)	1
Volume of the CH_3I (*AC grade*, mL)	1
Volume of the H_2O (*MiliQ*, mL)	14
Stirring duration	15 min

3.2.2 γ-labelled CH_3I generation in gas phase

The γ-labelled CH_3I generation in the gas phase is achieved using a permeation tube. The permeation tube uses a permeable membrane to deliver a small flow of chemical vapor [181]. It is essentially a hollow, non-porous cylinder, hermetically closed at its ends and containing the substance to be diffused (Figure 52). This substance is generally in liquid form. In addition, the tube wall is a membrane usually in Teflon FEP (fluorinated ethylene propylene copolymer) or PTFE (polytetrafluoroethylene). Indeed, these polymers are known to be chemically inert to a large number of substances [182]. As schematized in Figure 52, the tube is placed in a thermostatically controlled chamber (permeation chamber) and a stable amount of γ-labelled CH_3I is diffused into the vapor phase through a dilution flow (dilution flow 1 of Figure 49). In this way, a steady permeate flow of γ-labelled CH_3I can be generated during three to four weeks.

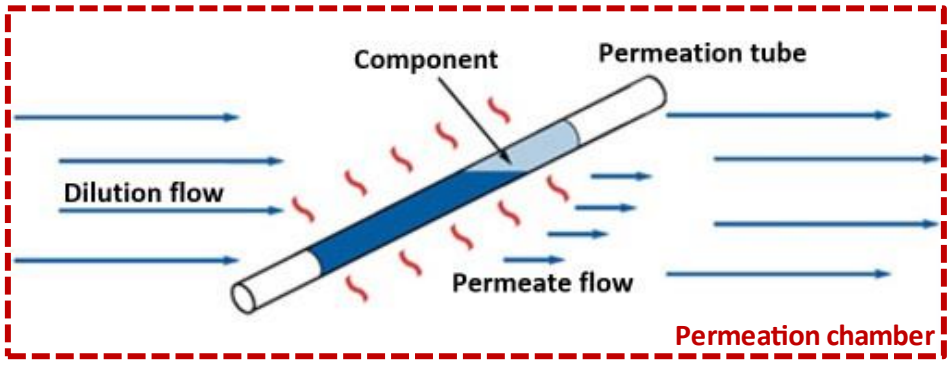

Figure 52. Scheme of a permeation tube [181]

At a given dilution flowrate, the concentration of the permeate vapor (total CH_3I), which depends on the membrane permeability, can be expressed from the following relationship:

$$C(total\ CH_3I\ in\ ppmv) = \frac{Permeate\ flowrate}{Dilution\ flowrate^*} \times 10^6 \quad (29)$$

** In practice, the dilution flowrate corresponds to the total flowrate of the dilution flows 1 and 2 as indicated Figure 49.*

Starting from Fick's second law, Barrer [183] established the equation giving the permeate flowrate of a cylindrical tube in the stationary state:

$$Q_p = \frac{2 \times \pi \times L_p \times P_0{}' \times (p_i - p_e)}{lnr_e - lnr_i} \quad (30)$$

Where Q_p permeate flowrate ($cm^3 \cdot s^{-1}$, NTP);
L_p the permeation tube length (cm);
P_0' permeation coefficient ($cm^2 \cdot s^{-1} \cdot Pa^{-1}$, NTP);
p_i internal partial pressure (Pa);
r_i internal tube radius (cm);
p_e external partial pressure (Pa);
r_e external tube radius (cm).

The permeation coefficient is related to the temperature according to the following expression [183]:

$$P_0{}' = P' \times \exp(-E_p/RT) \quad (31)$$

Here P' is a constant and E_p is the activation energy of permeation. Hence, it can be deduced that for a given permeation tube, the permeate flow can be regulated by the operating temperature of the tube (permeation oven).

For a sake of clarity, two types of CH_3I "concentrations" should be considered for this study:

- the $CH_3{}^{131}I$ flowrate (expressed in $Bq \cdot min^{-1}$);
- the concentration of the total CH_3I permeate (expressed in ppm).

In practice, only the $CH_3{}^{131}I$ flowrate (expressed in $Bq \cdot min^{-1}$) can be directly measured using the aforementioned uptake method described in Section 3.1.2. The ratio between ^{131}I and (^{131}I+^{127}I) (defined as the isotopic dilution factor (G_{IDF})) in the permeate CH_3I flow is considered to be the

same as that in the permeation tube. Therefore, once the $CH_3{}^{131}I$ flowrate in $Bq \cdot min^{-1}$ is measured, the permeate CH_3I concentration in ppmv can be determined using the G_{IDF}. For a permeation tube containing 1 mL of γ-labelled CH_3I with an activity of 10 MBq, the determination of the G_{IDF} is summarized in Table 33.

Table 33. Summary of the calculation of the G_{IDF}

Characteristics of the $CH_3{}^{131}I$ in the permeation tube				
$Na^{131}I$ activity (MBq)	Isotopic labelling efficiency	$CH_3{}^{131}I$ activity (MBq)	Half-life of ^{131}I (s)	$CH_3{}^{131}I$ quantity (mol)
10	90%	9	692902	1.5×10^{-11}
Characteristics of the CH_3I in the permeation tube				**G_{IDF} of $^{131}I/I$**
CH_3I volume (mL)	CH_3I density (g/cm^3)	CH_3I molar mass (g/mol)	CH_3I quantity (mol)	
1	2.28	141.94	0.0161	9×10^{-10}

For the BTC measurements which will be shown in Section 4.2, the $CH_3{}^{131}I$ flowrate is measured to be around 150 $Bq \cdot min^{-1}$. Using the G_{IDF} deduced from Table 33, the permeate CH_3I concentration can be calculated to be around 0.87 ppmv (Table 34).

Table 34. Determination of the permeate CH_3I concentration in ppmv*

$CH_3{}^{131}I$ flowrate ($Bq \cdot min^{-1}$)	Half-life of ^{131}I (s)	Isotopic dilution factor of $^{131}I/I$	Permeate CH_3I flowrate ($mol \cdot min^{-1}$)
150	692902	9×10^{-10}	2.7×10^{-7}
CH_3I molar volume (20°C) ($L \cdot min^{-1}$)	Permeate CH_3I flowrate ($NL \cdot min^{-1}$)	Total flowrate ($NL \cdot min^{-1}$)	Permeate CH_3I concentration (ppmv)
24.05	6×10^{-6}	6.86	0.87

** Here, only air is used for the dilution flow 1 and 2 as indicated in the Figure 49.*

Experimentally, the generated γ-labelled CH_3I in liquid phase is immediately transferred into the permeation tube (*Vampa Combustion, Pillard*, Figure 53 (a)). Then, the tube is placed in the permeation chamber (*Serv' instrument*). The chamber will be afterwards hermetically closed and placed inside the permeation oven (*Serv' instrument,* Figure 53 (b)). The operating temperature of the permeation oven, according to the permeation tube manual, is set to 80 °C.

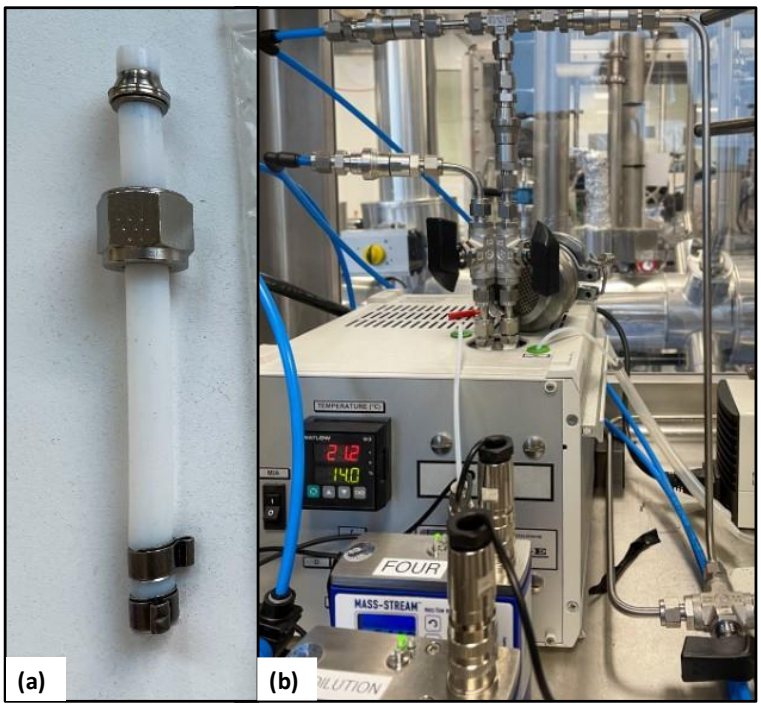

Figure 53. (a) Photo of the permeation tube; (b) photo of the permeation oven

Once the permeation process is started, three successive well-defined phases characterized by the change in the permeation rate over time are observed:

- equilibrium phase;
- steady phase;
- depletion phase.

The equilibrium phase is characterized by the time required to achieve a steady state. This transient state exists after each filling and after each temperature change. In our case, the duration required to reach the equilibrium is found to be around 10 h. The steady phase of a permeation tube (up to 3 - 4 weeks) ends with the depletion of the liquid phase of the substance. The pressure inside the tube is no longer constant, inducing therefore the permeation rate decrease.

3.3 Preliminary test for the capture of γ-labelled methyl iodide

The objectives of the preliminary tests are as follow:

- To verify the feasibility of the methodology described above for the generation and online monitoring of the $CH_3{}^{131}I$ flowrate ($Bq \cdot min^{-1}$);
- To calculate the permeate CH_3I concentration with the optimized protocol and adjust the total CH_3I concentration to 10 ppmv.

3.3.1 Feasibility test

The feasibility test represents the first manipulation of this experimental setup using only the *bypass section* to characterize the evolution of the generated $CH_3{}^{131}I$ flowrate ($Bq \cdot min^{-1}$) with the operating conditions summarized in Table 35.

Table 35. Summary of the operating conditions of the feasibility test

Initial $Na^{131}I$ activity	1 MBq
Permeation temperature	80 °C
Dilution flow 1 (For the γ-labeled CH_3I generation) (Default flowrate = 0.4 $NL \cdot min^{-1}$)	Air 0.2, 0.4 and 1 $NL \cdot min^{-1}$
Dilution flow 2 (For the total flowrate regulation)	Air 6.66, 6.46 and 5.86 $NL \cdot min^{-1}$
Total flowrate	6.86 $NL \cdot min^{-1}$
γ spectroscopy measurement configuration	d = 10 cm

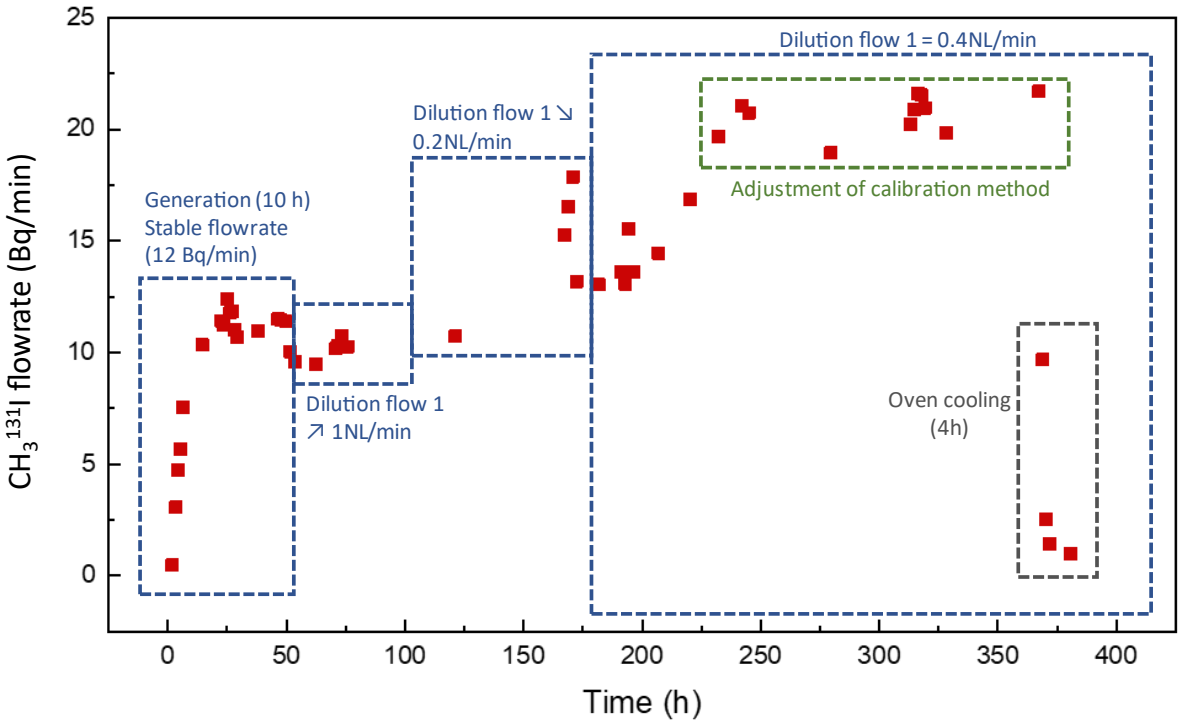

Figure 54. γ-labelled CH_3I concentration evolution for the feasibility test

As depicted in Figure 54, the steady generation of γ-labelled CH_3I in gas phase takes place in approximately 10 h and corresponds to a $CH_3{}^{131}I$ flowrate of about 12 Bq·min^{-1}. Firstly, the effect of the dilution flow 1 is investigated using a flowrate range between 0.2 and 1 NL·min^{-1} (NTP). It is found that the flowrate variation of the dilution flow 1 leads to a less stable $CH_3{}^{131}I$ flowrate. According to Eq. (29), the obtained $CH_3{}^{131}I$ flowrate should be independent of the dilution flow 1 since the total flowrate remains always unchanged. The variation of the $CH_3{}^{131}I$ flowrate may be assigned to the γ spectroscopy measurement configuration that was not yet optimized during preliminary investigations. Indeed, using d = 10 cm for a low activity measurement (around 15 Bq·min^{-1}) should be avoided in order to improve the measurement quality. Hence, the calibration method of the commercial cartridge is then modified using d = 0 (Appendix 20). Finally, a stable $CH_3{}^{131}I$ flowrate of (20.65 ± 0.53) Bq·min^{-1} is obtained considering the tested conditions (green area of Figure 54).

3.3.2 CH_3I concentration calculation

As illustrated in the previous section, using 1 MBq of the initial $Na^{131}I$ for the permeation corresponds to a $CH_3{}^{131}I$ flowrate of around 20 Bq·min^{-1}. Then, it is decided that a higher initial

$Na^{131}I$ activity of 10 MBq must be chosen in order to improve the measurement quality of γ spectroscopy during the BTC measurement for a reasonable measurement time. An even higher $Na^{131}I$ activity is technically feasible but should be avoided in practice regarding the worker exposure and ASN authorization.

More precisely, the $CH_3{}^{131}I$ flowrate in $Bq \cdot min^{-1}$ should be linearly dependent on the activity of the $CH_3{}^{131}I$ in the permeation tube according to the following expression:

$$CH_3^{131}I\ flowrate\ (Bq/min) = \frac{D_p \times A(CH_3I)}{V(CH_3I) \times \rho(CH_3I) \times 10^6} \quad (32)$$

Where D_p the certificate flowrate of the permeation tube depending on the temperature of the permeation oven ($\mu g \cdot min^{-1}$);
$V(CH_3I)$ the γ-labelled CH_3I volume (mL);
$A(CH_3I)$ the $CH_3{}^{131}I$ activity (Bq);
$\rho(CH_3I)$ the liquid CH_3I density (2.28 $g \cdot cm^{-3}$).

Here, D_p is a characteristic constant of the permeation tube at the temperature of operation. The volume of γ-labelled CH_3I is fixed at 1 mL for our studies considering the limited volume of the permeation tube (less than 2 mL). Hence, for a given permeation temperature, the gaseous $CH_3{}^{131}I$ flowrate depends only on the liquid $CH_3{}^{131}I$ activity, which is governed by the initial $Na^{131}I$ activity.

Extrapolating the feasibility test (the increase of initial $Na^{131}I$ from 1 to 10 MBq will be accompanied by an increase in $CH_3{}^{131}I$ flowrate from 20 to 200 $Bq \cdot min^{-1}$), a permeate CH_3I concentration of 1.2 ppmv can be deduced using the same calculation from Table 33 and Table 34. However, a total CH_3I concentration of 10 ppmv is required for the comparison purpose with stable CH_3I adsorption experiment. Therefore, the dilution flow 1 should be fed by a given concentrated CH_3I bottle (*Air products*) rather than air in order to reach such a concentration. According to the calculations reported in Table 36, the concentration of this CH_3I bottle should be 160 ppmv.

Table 36. Summary of the total CH_3I concentration calculation (for a $CH_3{}^{131}I$ flowrate of 200 $Bq \cdot min^{-1}$)

Dilution flow 1		
Gas type	Concentration (ppmv)	Flowrate ($NL \cdot min^{-1}$)
CH_3I	160	0.4
Dilution flow 2		
Gas type	Concentration (ppmv)	Flowrate ($NL \cdot min^{-1}$)
Pressurized air	/	6.46
Summary		
Permeate CH_3I concentration (ppmv)	Total CH_3I concentration (ppmv)	
1.2	10.5	

It should be outlined that for the γ-labelled CH_3I BTC measurement presented in the next section, a $CH_3{}^{131}I$ flowrate of around 150 $Bq \cdot min^{-1}$ instead of 200 $Bq \cdot min^{-1}$ (as expected from Eq. (32)) is obtained using initial $Na^{131}I$ = 10 MBq. Hence, it can be noticed that the permeate CH_3I concentration is slightly altered from 1.2 to 0.87 ppmv. This slight change of the permeate CH_3I concentration will not influence significantly the total CH_3I concentration since the majority of the 10 ppmv CH_3I is contributed by the CH_3I bottle of 160 ppmv as shown in Table 36. The operating conditions for the BTC measurements in Section 4 are summarized in Table 37.

In the next section, attention is focused on the results and the discussion of the different BTC towards the stable and the γ-labelled CH_3I with special emphasis on the KI impregnated AC. The relative contribution of the isotopic exchange by KI will be evaluated using different approaches.

Table 37. Summary of the operating conditions of the γ-labelled CH_3I BTC measurements

Permeation oven	
Initial $Na^{131}I$ activity	10 MBq
Final $CH_3{}^{131}I$ activity	Around 9 MBq
Temperature	80 °C
Gas flow	
Dilution flow 1 (160 ppm CH_3I)	0.4 NL·min^{-1}
Dilution flow 2 (Air)	6.46 NL·min^{-1}
$CH_3{}^{131}I$ flowrate	150 Bq·min^{-1}
Permeate CH_3I concentration	0.87 ppmv
Total CH_3I concentration	10.2 ppmv
G_{IDF} (including the 160 ppmv of CH_3I in the dilution flow 1)	8×10^{-11}
γ spectroscopy	
measurement configuration	d = 0

4. Results and discussions

4.1 Methodology of the data processing

The quantification of the isotopic exchange contribution requires data processing of the observed BTC to deduce the adsorption properties such as the adsorption capacity (at a given breakthrough or saturation), the rate constant, the mass transfer zone (MTZ), etc. In the meantime, the fixed bed adsorption model should be carefully chosen in order to better estimate some particular value of penetrations (as deduced from the utilization of the AC in the nuclear context, Chapter I). As described in Chapter I, both the Thomas and the improved Thomas model allow to deduce the adsorption capacity at saturation as well as the rate constant. However, it has been observed that the application of the improved Thomas model for the BTC measurements during this PhD project generally presents a better fitting quality especially at the beginning of the BTC. The different fitting results at the beginning of the BTC is due to the slightly unsymmetric nature of the obtained BTC [74]. An example of the BTC of 5%KI AC for the trapping of stable CH_3I is shown in Figure 55. Hence, only the improved Thomas model is used in this chapter for the BTC data processing. It should also be noticed that the adsorption capacity at saturation deduced from both the improved Thomas model and the trapezoidal integration method [28] is nearly the same (Appendix 24),

justifying the advantage using the BTC model for data processing. The improved Thomas model is referenced to Thomas model for simplicity purpose hereafter.

The adsorption parameters were quantified for both stable and radioactive CH_3I as follows:

- The adsorption capacity for a given breakthrough is calculated using the trapezoidal integration method [28] applied to the fitted curve according to the Thomas model;
- The adsorption capacity at saturation (Q_{Th}) and the rate constant (K_{Th}) are deduced directly form the Thomas model;
- The MTZ is deduced from Eq. (9) presented in Chapter I, using $t_{5\%}$ and $t_{95\%}$ corresponding to C_{outlet}/C_{inlet} = 0.05 and 0.95, respectively [60][65].

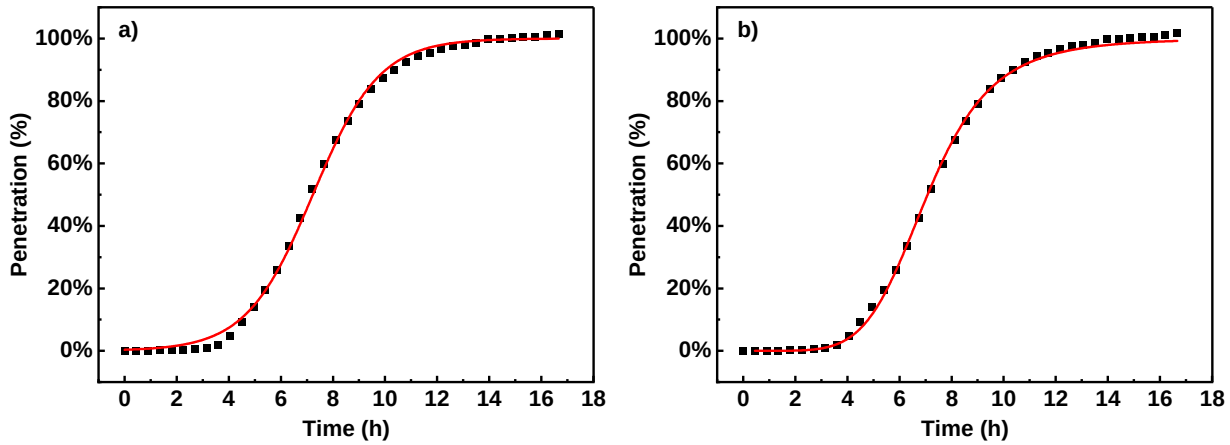

Figure 55. Example of the BTC fitting for 5%KI AC towards the stable CH_3I: (a) Improved Thomas model; (b) Thomas model

4.2 Investigation of the AC performance towards the trapping of stable CH_3I

The obtained BTC for different AC are presented in Figure 56 and the corresponding parameters are summarized in Table 38. Firstly, the unimpregnated AC displayed a total retention phase with a duration of 5 hours (Figure 56), corresponding to a DF of about 12600 (C_{inlet}/DL). Subsequently, the penetration P(C_{inlet}/C_{outlet}) increases progressively until reaching the complete saturation of the adsorbent bed (P = 100%) after around 12 hours (Figure 56). This leads to adsorption capacities at 5% breakthrough ($Q_{5\%}$) and saturation (Q_{Th}) of 14 and 22 $mg \cdot g^{-1}$, respectively (Table 38). Same

magnitude of the adsorption capacity at saturation for unimpregnated AC with similar porosimetric properties was reported in the literature under similar operating conditions [56].

Similar performances were observed for KI impregnated AC in general with quasi-overlapping BTC (Figure 56). This trend is in agreement with their similar microporosity as stated in Chapter II (see Table 38). However, a closer look to the data gathered in the Table 38 indicates a slight decrease of adsorption capacity at saturation. The variations of the adsorption capacity at saturation are explained by the uncertainties and the slight variation in the sample mass required for a bed depth of 5 cm after KI impregnation (Table 38). In Chapter II, the porous structure of the KI impregnated AC was found to be similar due to the low impregnation ratio of KI. However, the presence of KI even in low quantity may induce different adsorption kinetics. As shown in Figure 57, a decreasing evolution of the $Q_{5\%}$ towards the MTZ can be noticed. The existence of diffusional limitations is reported to facilitate the preferential pathways inside the adsorbent, leading to the decrease of the corresponding retention properties [60]. The presence of KI may induce more diffusional limitations of the CH_3I molecules towards the micropores, leading therefore to the decrease of the rate constant K_{Th} (Figure 57). Under the studied conditions (30 °C, RH = 0), the physisorption mechanism is expected to be dominant in accordance with the literature [78][131]. This is confirmed with a fraction of physiosorbed CH_3I of about 100% for the 1%KI AC (Appendix 23), indicating the absence of any strong interaction between KI molecules and $CH_3{}^{127}I$. This trend is in line with our previous works under batch reactor configuration [133]. To sum-up, the investigation of KI-impregnated AC behavior towards stable CH_3I indicates as expected the occurrence of unspecific interactions only, which are dependent mainly on the microporosity accessibility by the adsorbate [184].

For TEDA impregnated AC, a significant improvement can be observed in terms of the retention phase duration, with a total duration of about 12 h against 5 h for the previous AC (Figure 56). This enhancement in the filtering properties is accompanied by an increase in $Q_{5\%}$ and Q_{th} from 14 and 22 $mg \cdot g^{-1}$ (unimpregnated AC) to 28 and 40 $mg \cdot g^{-1}$ (3% TEDA AC), respectively. When using a higher TEDA content (5 w.t%), an increase but with a lesser extent (30 and 44 $mg \cdot g^{-1}$ for $Q_{5\%}$ and Q_{Th}, respectively, Table 38) was observed. Our attempt to study the evolution of the Q_{Th} (in molar) as a function of the TEDA content (in molar) has indicated a linear relationship with a slope of about 0.35 (Appendix 25). This factor is significantly lower than the theoretical value of

2 according to the alkylation reaction mechanism (S_N2) expected to occur between the two nitrogen atoms of TEDA and CH_3I [78] [124][131]:

$$2CH_3I + TEDA \rightarrow 2I^- - (2CH_3 - TEDA)^+ \quad (33)$$

The difference between the experimental and theoretical values is mainly assigned to the occurrence of both physical interactions and chemisorption for TEDA impregnated AC under the chosen conditions. Moreover, a more beneficial effect from TEDA is expected under more aggressive conditions (higher temperatures and in the presence of water vapor to reduce the physisorption). Similar trends have been also outlined in previous works indicating generally a very low TEDA utilization in dry conditions, low temperatures and low inlet concentration [78][131][173].

The occurrence of strong interactions for CH_3I removal after TEDA impregnation was also confirmed by our previous batch reactor studies, indicating a significant enhancement of the Langmuir coefficient (b) as a comparison with unimpregnated or KI impregnated AC [184].

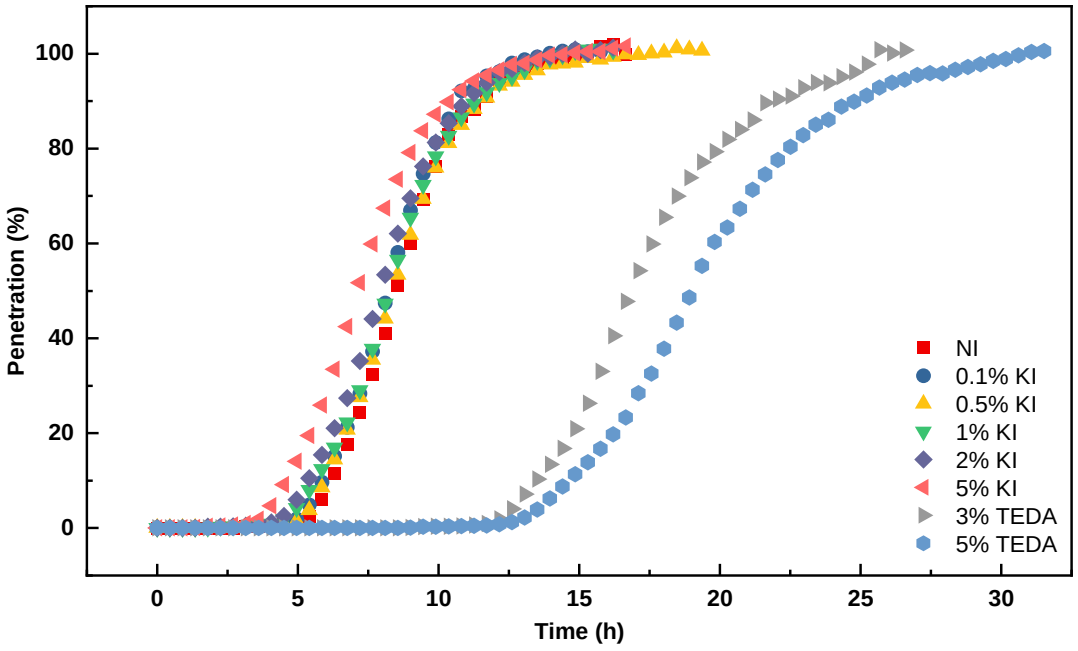

Figure 56. Stable CH_3I BTC for different AC (C_{inlet} = 10 ppmv, T = 30 °C, bed depth = 50 mm, linear velocity = 25 cm·s^{-1}, residence time = 0.2 s)

Table 38. Summary of the deduced parameters from the BTC measurements towards stable CH_3I (C_{inlet} = 10 ppmv, T = 30 °C, bed depth = 50 mm, linear velocity = 25 $cm \cdot s^{-1}$, residence time = 0.2 s)

AC type	Mass (g)	V_{micro} ($cm^3 \cdot g^{-1}$)	S_{BET} ($m^2 \cdot g^{-1}$)	$Q_{5\%}$ ($mg \cdot g^{-1}$)	Q_{Th} ($mg \cdot g^{-1}$)	K_{th}	R^2 (Thomas model)	MTZ
Unimpregnated	9.98	0.453	1142	14	22	7.4	0.9989	53%
0.1 w.t% KI	10.51	0.469	1174	13	20	7.6	0.9995	54%
0.5 w.t% KI	11.09	0.470	1171	12	20	6.8	0.9986	58%
1 w.t% KI	10.85	0.486	1213	12	20	6.7	0.9991	59%
2 w.t% KI	10.93	0.469	1174	11	19	6.5	0.9992	60%
5 w.t% KI	11.17	0.456	1132	9	17	5.7	0.9987	65%
3 w.t% TEDA	11.03	0.441	1097	28	40	9.3	0.9968	47%
5 w.t% TEDA	11.25	0.410	1022	30	44	8.6	0.9985	50%

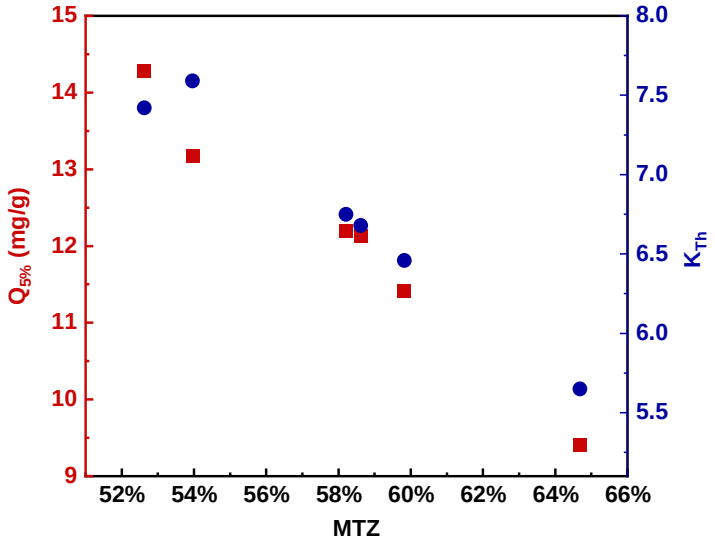

Figure 57. Evolution of the $Q_{5\%}$ and K_{th} towards the MTZ for the KI impregnated AC

In the next section, the effect associated to KI is discussed for the capture of the γ-labelled CH_3I, to isolate and quantify the isotopic exchange contribution for the total trapping.

4.3 Investigation of the AC performance towards the trapping of γ-labelled CH_3I

4.3.1 General evolutions of the obtained BTC towards γ-labelled CH_3I

(a) Difficulties related to the BTC acquisition under the applied conditions

Before presenting the results of the BTC obtained for the trapping of γ-labelled CH_3I, it is necessary to underline the difficulties encountered during manipulation for the BTC acquisitions towards $CH_3{}^{131}I$. As demonstrated previously in Section 3.1.2 (sampling principle), the BTC acquisitions require manual uptakes to determine the flowrate ($Bq \cdot min^{-1}$) of the downstream section. The inlet CH_3I concentration of 10 ppmv results in a relatively short duration of the BTC (less than 24 h for most of the cases, see next section). In this case, the period of night where the manual uptake is impossible would lead to insufficient experimental points (especially for less efficient sorbents, namely the unimpregnated, 0.1% KI and 0.5%KI AC, Figure 58). The lack of the experimental data between the retention and saturation phases for certain BTC results to a less accurate estimation of the adsorption parameters ($Q_{5\%}$, MTZ, K_{Th}, etc.). Nevertheless, first elements on the isotopic exchange process can be determined thanks to the BTC fitting with Thomas model for the trapping of both stable and γ-labelled CH_3I.

(b) Breakthrough curves towards γ-labelled CH_3I

Using the same methodology, the obtained BTC for different AC towards γ-labelled CH_3I are presented in Figure 58, with the corresponding fitted curves of the Thomas model. Firstly, no significant change in the retention phase duration (around 5 h, Figure 58) was observed for γ-labelled CH_3I adsorption using KI impregnated AC as a comparison with stable CH_3I adsorption experiments (Section 4.2.1, Figure 56). This similar retention phase area is rather untypical especially compared to TEDA impregnated AC in the previous section (Figure 56), where an increase of the retention phase can be noticed. In that respect, the behaviors of KI and TEDA impregnated AC during the retention phase seem to be consistent with the previous DF measurements at RH = 40 %. Indeed, the similar retention phase for KI impregnated AC towards the trapping of both stable and γ-labelled CH_3I confirms the absence of isotopic exchange under moderately humid conditions when considering the adsorption experiment at the beginning

(retention phase). In contrast, a significant enhancement of the retention of CH_3I is observed due to the reactivity of TEDA interacting *via* an alkylation mechanism in these conditions.[124]

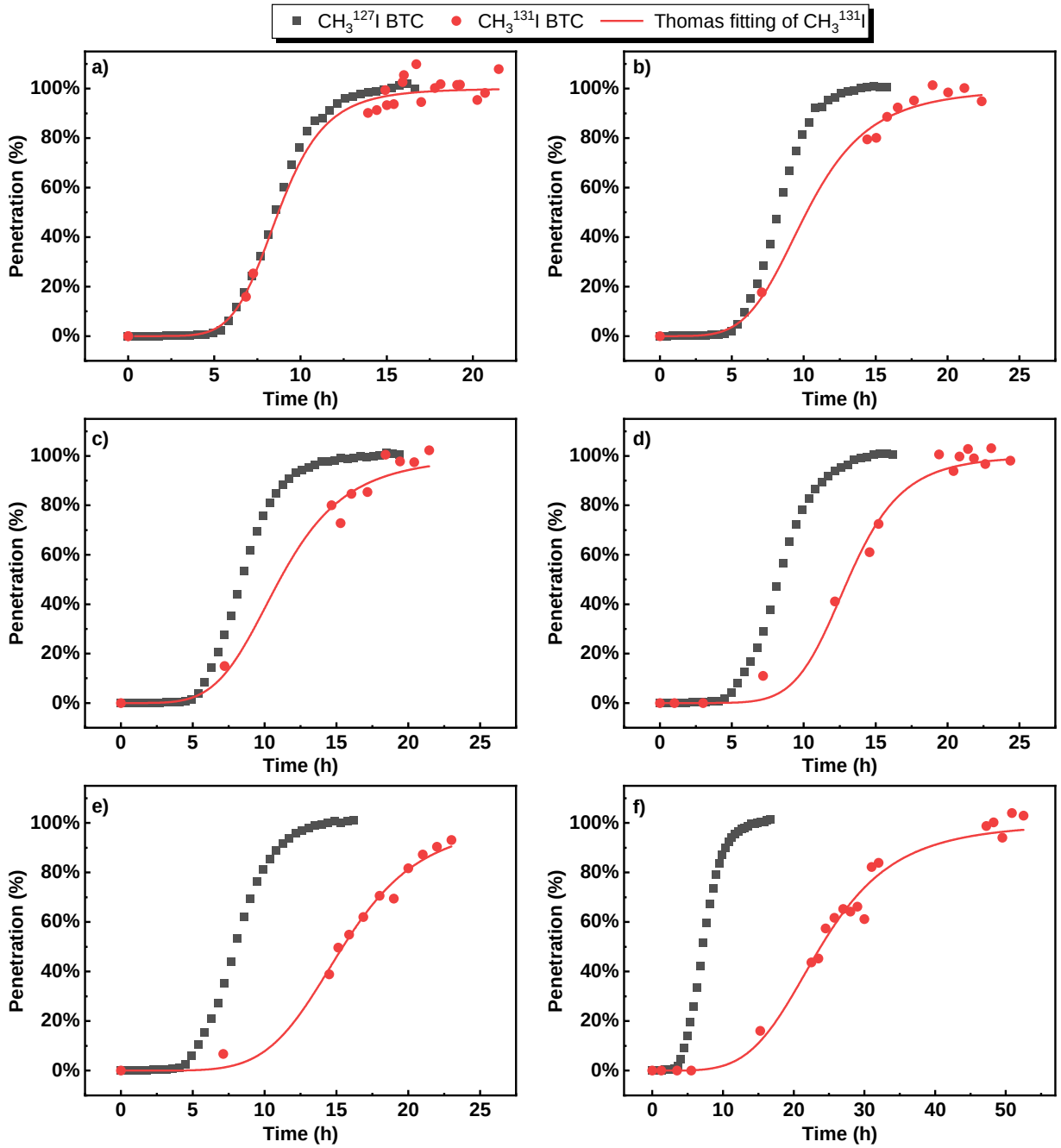

Figure 58. γ-labelled CH_3I BTC for: (a) unimpregnated AC; (b) 0.1% KI AC; (c) 0.5% KI AC; (d) 1% KI AC; (e) 2% KI AC; (f) 5% KI AC (C_{inlet} = 10 ppmv, T = 20 °C, bed depth = 50 mm, $CH_3{}^{131}I$ flowrate around 150 $Bq \cdot min^{-1}$, linear velocity = 25 $cm \cdot s^{-1}$, residence time = 0.2 s)

More importantly, a progressive improvement of the AC performance regarding the trapping of γ-labelled CH_3I during breakthrough phase is observed after KI impregnation. According to Figure 58, the enhancement of the AC performance during breakthrough phase is observed with an

increase in $t_{95\%}$ from 14 h for unimpregnated AC to 46 h for 5% KI AC (Table 39). This behavior is due to the isotopic exchange between ^{127}I (from KI) and ^{131}I (from γ-labelled CH_3I) [7]. Indeed, retention tests performed for unimpregnated AC (Figure 58 (a)) and 5%TEDA AC (Appendix 26) indicate similar trapping performances for stable and γ-labelled CH_3I, in agreement with the study of G. O. Wood *et al.* [135]. Thus, only KI seems to play beneficial role for the γ-labelled CH_3I uptake as a comparison with stable CH_3I, according to the postulated isotopic exchange reaction described in the literature [132][135]. This isotopic redistribution seems to be more significant during the breakthrough phase of the tested AC. This trend is in line with the previous data of Chapter III. Indeed, a slight increase of the DF towards γ-labelled CH_3I was observed in humid conditions (T = 20 °C, RH = 90 %) after KI impregnation. Because of competitive adsorption phenomena, the presence of high content of water vapor induced the shifting of the adsorption process to the breakthrough phase (penetration up to 50%, Table 27) for KI impregnated AC more rapidly, without introducing other trapping mechanism like TEDA (protonation mechanism). Therefore, the hypothesis proposed in Chapter III can finally be confirmed: the effect of the isotopic exchange for KI can only be observed after the AC breakthrough.

Therefore, it seems that KI and TEDA molecules present not only different CH_3I trapping mechanisms, but lead also to different behaviors in the BTC. The TEDA effect mainly results in the increase of the retention phase duration accompanied by an enhancement of the trapping stability, while the KI effect contributes rather to a larger breakthrough phase. According to the publication of G. O. Wood *et al.* [135], the isotopic exchange delays the desorption of $CH_3{}^{131}I$ which is progressively exchanged with stable KI according to a first order kinetics.

In the following Sections (4.3.2 and 4.3.3), two different approaches to quantify the relative contribution of the isotopic exchange is presented.

4.3.2 Relative contribution of the isotopic exchange: adsorption behaviors without the isotopic dilution factor (G_{IDF})

In this section, we present a first attempt to quantify the relative contribution of the isotopic exchange, not taking G_{IDF} into consideration. In other words, we assume that behaviors of $CH_3{}^{131}I$ and $CH_3{}^{127}I$ are the same for BTC presented in Section 4.3.1, corresponding to a total $CH_3{}^{131}I$ concentration equivalent to 10 ppmv. The advantage of this method is to allow a direct comparison

of the BTC between stable and radioactive CH_3I, with the deduced adsorption parameters remaining of the same magnitude. Indeed, the Thomas model fitting for a given BTC is independent to the inlet concentration of $CH_3{}^{131}I$. For a given BTC, the change of C_{inlet} leads to the proportional change of the deduced adsorption parameters (Q_{Th} and K_{Th}). In this way, the Q_{Th} and K_{Th} between stable and radioactive CH_3I can be directly compared without altering their evolution towards the KI contents.

Using this strategy, the adsorption parameters such as Q_{Th} and K_{Th} for both stable and radioactive CH_3I are summarized in Table 39. A significant increase of the adsorption capacity at saturation towards $CH_3{}^{131}I$ after KI impregnation can be noticed. Taking the 5% KI AC as an example, the Q_{Th} is found to increase from 17 to 55 $mg \cdot g^{-1}$. This increase extent seems to be dependent mainly on the KI content, which highlights the beneficial role of KI for $CH_3{}^{131}I$ trapping, as a comparison with $CH_3{}^{127}I$. This enhancement may be due to the isotopic exchange reaction involved in KI impregnated AC. Considering the calculated Q_{Th} without taking G_{IDF} into account, the relative contribution of both physisorption and isotopic exchange reaction are presented in Figure 59. Owing to the same adsorption capacities for the unimpregnated AC (Table 38 and Table 39), the physiosorbed amount will be the same for a given AC between the two configurations (stable and radioactive). The gain in Q_{Th} (expressed in percentage) between stable and radioactive CH_3I is linked to isotopic exchange. This methodology presents a first simplifying approach to determine the relative contribution of isotopic exchange for different KI impregnated AC. This first approach allows to highlight an increasing evolution of the relative contribution due to the isotopic exchange from 19% (0.1% KI AC) to about 70% (5%KI AC) (Figure 59).

Table 39. Summary of the deduced parameters from the BTC ($CH_3^{131}I$ flowrate = 150 Bq·min^{-1}, T = 20 °C, bed depth = 50 mm, linear velocity = 25 cm·s^{-1}, residence time = 0.2 s)

AC type	Q_{Th} (mg·g^{-1})*	K_{th}	Real Q_{Th} (Bq·g^{-1})**	Real Q_{Th} (mg·g^{-1})**	R^2 (Thomas model)	$t_{95\%}$ (h)
Non impregnated	22	6.4	7400	1.8×10^{-9}	0.9944	14
0.1 w.t% KI	25	4.8	8200	2.0×10^{-9}	0.9916	18
0.5 w.t% KI	27	4.7	9000	2.2×10^{-9}	0.9844	21
1 w.t% KI	32	7.7	10700	2.6×10^{-9}	0.9946	19
2 w.t% KI	38	5.7	12600	3.1×10^{-9}	0.9927	26
5 w.t% KI	55	4.5	18300	4.4×10^{-9}	0.9967	46

** These parameters are calculated considering a $CH_3^{131}I$ concentration of 10 ppmv (without G_{IDF})*

*** These parameters are calculated using the real $CH_3^{131}I$ concentration (with G_{IDF})*

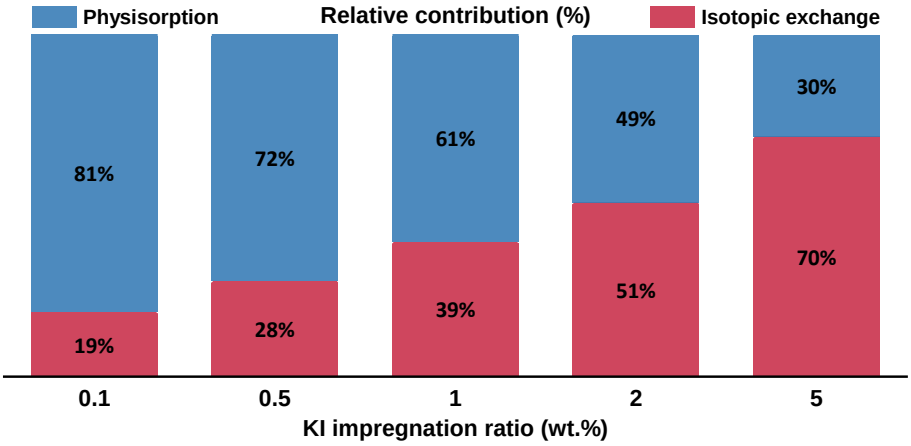

Figure 59. Relative contribution of the isotopic exchange considering the adsorption capacity at saturation for KI impregnated AC ((Q($CH_3^{131}I$)-Q($CH_3^{127}I$))/Q($CH_3^{131}I$), without G_{IDF})

Besides, it can be noticed that the rate constant K_{Th} deduced for the γ-labelled CH_3I retention presents generally a higher variability when compared with the first configuration (Figure 60). This higher variability is mainly due to the difficulties of the BTC acquisition as previously described in Section 4.3.1 (especially for the unimpregnated, 0.1% KI and 0.5% KI AC). Nevertheless, for 1% KI, 2% KI and 5% KI AC, a decreasing evolution of the rate constants towards the KI content can be noticed regarding the trapping of the γ-labelled CH_3I. The decreasing feature of K_{Th} is probably explained by the increase of adsorption sites participating in the isotopic exchange, leading to an increase of the reaction time to complete the isotopic exchange reaction.

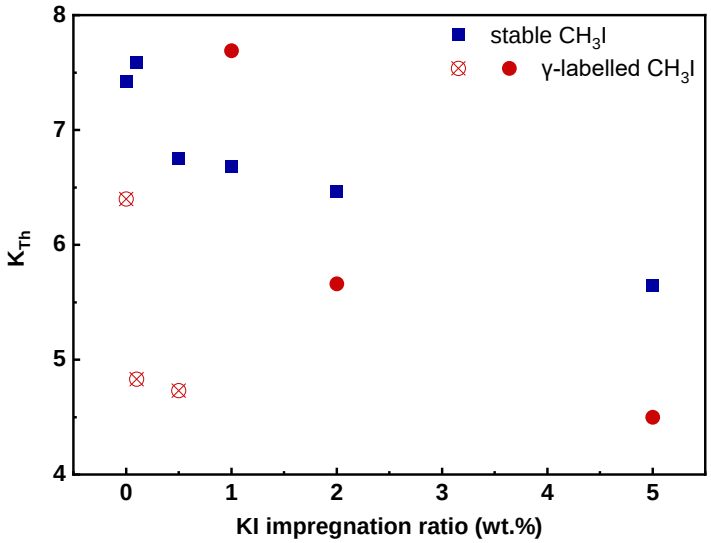

Figure 60. Evolution of the rate constant K_{Th} towards the KI impregnation

In this section, the contribution of the isotopic exchange is highlighted using adsorption capacity at saturation without G_{IDF}. The difference of the $CH_3{}^{131}I$ inlet concentration due to G_{IDF} will be normalized while calculating the relative contribution of isotopic exchange using another approach, which is presented in the next section.

4.3.3 Extrapolation to the application of iodine traps in the nuclear context (consideration of G_{IDF})

Context and methodology

As stated in the previous section, the effect of the isotopic exchange by KI brings interesting features to radioactive CH_3I retention, with a significant improvement of the adsorption capacity at saturation (a relative contribution calculated from an isotopic exchange of 70% for 5%KI AC). However, the current use of the iodine trap of AC within the ventilation networks mainly focuses on their performances far away from saturation. As described in Chapter I (Page 11), DF of 10 and 100 can be highlighted for the majority of the ventilation networks, corresponding to a penetration of 10% and 1%, respectively. Hence, rather than focusing on the adsorption capacity at saturation, attentions should be given to the AC performance at different penetrations ratios (breakthroughs) in order to better evaluate the AC practical use in the nuclear facilities.

The presence of KI has proven to be beneficial after AC breakthrough, inducing a progressive enrichment of ^{131}I within the AC due to the isotopic exchange reaction, as shown in the previous section. However, two issues still remain regarding the quantification of the isotopic exchange:

- The aforementioned adsorption capacity for $CH_3{}^{131}I$ was calculated using 10 ppmv inlet concentration without taking into account G_{IDF};
- The utilization of the inlet $CH_3{}^{131}I$ real concentration makes it difficult to quantify the relative contribution of the isotopic exchange considering the orders of magnitude difference between $CH_3{}^{127}I$ and $CH_3{}^{131}I$.

In this section, a second approach for the isotopic exchange quantification is proposed taking into account the different isotopic dilution factors. In the previous section, G_{IDF} for the γ-labelled CH_3I flow is determined. Similarly, the isotopic dilution factor between the adsorbed $CH_3{}^{127}I$ and $CH_3{}^{131}I$ within the KI impregnated AC (R_{IDF}) can be determined using the following expression:

$$R_{IDF} = \frac{Q(CH_3^{131}I)}{Q(CH_3I)} \tag{34}$$

Where R_{IDF} isotopic dilution factor between the adsorbed $CH_3{}^{127}I$ and $CH_3{}^{131}I$;
$Q(CH_3{}^{131}I)$ calculated real $CH_3{}^{131}I$ adsorption capacity at a given penetration ($mol \cdot g^{-1}$);
$Q(CH_3I)$ calculated CH_3I adsorption capacity at a given penetration ($mol \cdot g^{-1}$).

This isotopic dilution factor within the adsorbed phase R_{IDF} is then determined from the fitted BTC according to the Thomas model for active and stable configurations respectively. These adsorption capacities were calculated at the same time for both configurations, with the aim to reach a given AC breakthrough. The isotopic exchange process for the KI impregnated AC induces an enrichment effect of the adsorbed $CH_3{}^{131}I$ towards adsorbed CH_3I inside the AC (R_{IDF}) as a comparison with the initial gaseous phase composition (G_{IDF}). The obtained value of the R_{IDF} can be then compared to the G_{IDF} to determine the relative contribution of isotopic exchange using the following expression:

$$Relative\ contribution\ (\%) = \frac{R_{IDF} - G_{IDF}}{R_{IDF}} \tag{35}$$

Since the adsorption capacity (at a given breakthrough) is proportional to $CH_3^{131}I$ inlet concentration, the following expression can be obtained:

$$Q(CH_3^{131}I) = Q'(CH_3^{131}I) \times G_{IDF} \quad (36)$$

Here, the Q'($CH_3^{131}I$) is the adsorption capacity calculated for an inlet $CH_3^{131}I$ concentration of 10 ppmv. Using Eq. (34) and Eq. (36), Eq. (35) can be reformulated as:

$$Relative\ contribution\ (\%) = \frac{Q'(CH_3^{131}I) - Q(CH_3I)}{Q'(CH_3^{131}I)} \quad (37)$$

Our objective is to extrapolate this relative contribution (%) for different $CH_3^{131}I$ penetrations through the use of Thomas model. It can be noticed from Eq. (37) that the relative contribution calculation can be simplified using the inlet $CH_3^{131}I$ concentration of 10 ppmv to calculate the adsorption capacity at a given penetration, as presented in the previous section. Using a $CH_3^{131}I$ penetration of 100% for Eq. (37) corresponds to the results presented in Figure 59. Therefore, the second approach leads to a more generalized expression allowing the determination of this mechanism importance at different AC breakthrough levels.

Results of the relative contribution of isotopic exchange versus $CH_3^{131}I$ penetration

Based on this methodology, the evolution of the isotopic exchange relative contribution towards $CH_3^{131}I$ penetrations is presented in Figure 61. According to Figure 61 (a), all the tested KI AC present a linear increase of the isotopic exchange relative contribution when the penetration ratio reaches around 25%. For example, an increase of the isotopic exchange relative contribution can be calculated for 5%KI AC from 58% to 71% at penetrations of 25% and 100% respectively. The increasing trend of this relative contribution indicates its time-dependent nature. A closer look in Figure 61 (b) presented in logarithmic scale, allows to reveal more information for the low penetration values. The relative contribution due to the isotopic exchange for several penetration ratios is summarized in Table 40. It can be observed that the effect related to the isotopic exchange starts to be evidenced experimentally from a certain penetration ratio. This threshold depends both on KI content and the present methodology limitations. Indeed, increasing the KI loading will enhance the breakthrough phase as observed previously. Thus, more experimental points can be measured between the retention and the saturation phase despite the manual sampling and the inlet

concentration used. In that respect, the extrapolation of isotopic exchange relative contribution to penetrations less than or equal to 10% (Table 40) cannot be feasible for 0.1% and 0.5% KI AC considering the lack of the experimental data for the Thomas model fitting (Figure 58). However, the extrapolation of this contribution to penetrations of 1% was found to be possible for the 5%KI AC thanks to its higher efficiency and the sufficient data experimentally measured between the retention and the saturation phase (Figure 58).

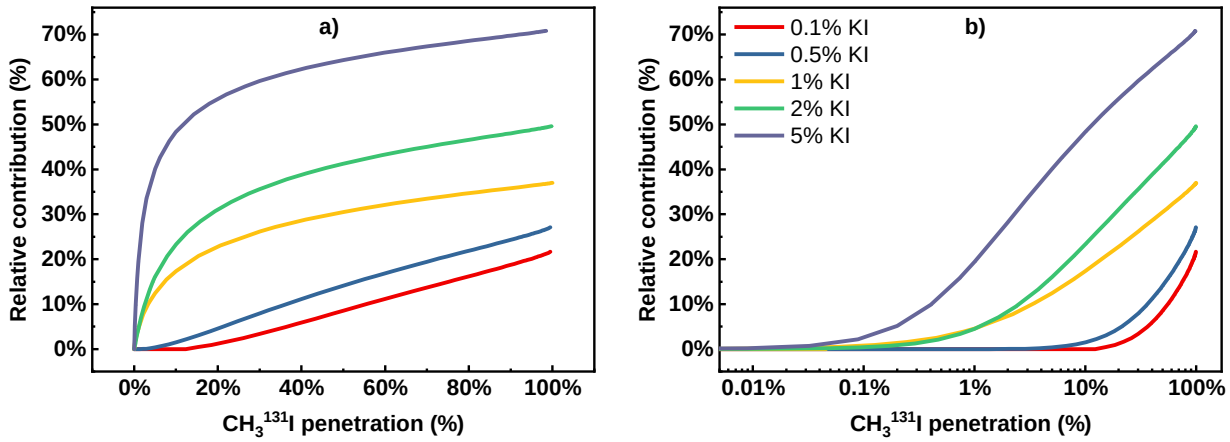

Figure 61. Evolution of the relative contribution of isotopic exchange toward $CH_3{}^{131}I$ penetration: (a) penetration in linear scale; (b) penetration in logarithmic scale

Table 40. Relative contribution of isotopic exchange at different penetration ratio

KI (w.t%)	1% penetration	5% penetration	10% penetration	30% penetration	70% penetration	100% penetration
0.1	0%	0%	0%	3%	14%	22%
0.5	0%	0%	0%	8%	19%	27%
1	5%	12%	17%	26%	33%	37%
2	4%	16%	23%	36%	45%	50%
5	19%	40%	48%	60%	67%	71%

Our interest on the isotopic exchange effect is mainly focused on the low penetration ratio as indicated in Table 3 (Chapter I). Here, attention is focused on 2% KI and 5% KI AC since they represent the only cases where the Thomas model fitting is “reliable”, especially for the retention phase, regarding the number of experimental data compared to less efficient KI AC. At 1% of $CH_3{}^{131}I$ penetration, the calculated relative contribution due to the isotopic exchange seems to be non-negligible (4% and 19% for 2% KI and 5% KI AC respectively, Figure 61 and Table 40).

These first calculations outline the importance of isotopic exchange phenomena for KI AC even at low penetrations. However, further experiments should be performed to consolidate these results and to ensure a more accurate determination of the retention behavior in the AC expected working range within the ventilation circuits of nuclear facilities [44]. In that respect, some improvements can be proposed for the present methodology. More particularly, a lower inlet CH_3I concentration (5 ppmv for example) should be used especially for AC with low KI contents. In addition, a more automatized uptake method is required to limit the time gap, especially during the night. The optimized experimental methodology should be applied afterwards to gain insights about the isotopic exchange importance in KI/TEDA co-impregnated AC, with the aim to extrapolate to *nuclear grade AC.* Finally, more investigations should be performed to explore the influence of experimental conditions (T, RH) on the isotopic exchange efficiency.

5. Conclusions

In this chapter, the occurrence of the isotopic exchange reaction is evaluated based on the hypothesis proposed in Chapter III. More particularly, the effect of the isotopic exchange is investigated by measuring the BTC towards both stable and γ-labelled CH_3I separately through two different experimental setups. Consequently, a newly designed experimental setup has been developed for the BTC measurement of the γ-labelled CH_3I.

Different trends were observed depending on the investigated experimental configuration. Regarding the stable CH_3I trapping, similar performances were observed for unimpregnated and KI impregnated AC. This result is in line with their similar microporosity as stated in Chapter II and with the occurrence of only physical interactions for the considered adsorbents. A significant improvement of the retention phase duration was observed after TEDA impregnation. This enhancement in the trapping properties is accompanied by an increase in $Q_{5\%}$, Q_{Th} and in the trapping stability thanks to the occurrence of strong interactions between TEDA and CH_3I molecules.

Regarding the γ-labelled CH_3I trapping, no significant change in the retention phase was observed using KI impregnated AC compared to stable CH_3I adsorption experiments. Nevertheless, a significant enhancement of the AC performances during breakthrough phase is observed after KI

impregnation, which is due to the isotopic exchange reaction occurrence. Indeed, additional tests have indicated the absence of a such phenomenon for the unimpregnated and 5%TEDA AC.

Two approaches were presented to quantify the relative contribution due to the observed isotopic exchange. The first approach focuses on the adsorption capacity at saturation without considering the G_{IDF} ([$CH_3{}^{131}I$] equivalent to 10 ppmv). Accordingly, an increasing relative contribution due to isotopic exchange reaction was calculated from 19% to 70% for KI contents of 0.1% and 5% respectively. Based on the expected working range of AC in the nuclear field, the determination of the importance of this mechanism as a function of the methyl iodide penetration is required. Consequently, an expression more generalized than the first approach has been demonstrated. This approach was based on the concept of iodine 131 progressive enrichment within the adsorbed phase as compared with the initial gaseous phase composition. More particularly, the relative contribution due to this mechanism was calculated at different filter breakthrough levels using the Thomas model applied for both stable and radioactive experimental sorption curves. The isotopic exchange effect was found to be evidenced experimentally from a certain threshold depending both on KI content and experimental methodology limitations. On the one hand, the lack of sufficient experimental data between the retention and the saturation phases for 0.1 and 0.5%KI AC makes impossible to extrapolate their behavior to breakthrough levels lower than 10%. On the other hand, extrapolated relative contributions due to isotopic exchanges of about 4% to 19% were calculated for 2% and 5%KI AC, respectively, for 1% of breakthrough. These first calculations, even needed to be further consolidated, highlight the importance of the isotopic exchange reaction at low penetrations.

The methodology based on the BTC determination has shown the importance related to the isotopic exchange reaction. Besides, first elements about the quantification of this mechanism were afforded by the presented methodology as a comparison with the previous DF investigations (Chapter III). However, technical improvements should be proposed by varying the initial inlet CH_3I concentration and automatizing the uptake method. The objective is to finely monitor the behavior of the tested sorbents towards γ-labelled CH_3I from very low penetrations (0.1 to 1%) in agreement with the studied context. Additional investigations should be also conducted in order to isolate and quantify the isotopic exchange contribution for *nuclear grade AC* (TEDA + KI co-impregnation) and for a large panel of experimental conditions (T, RH).

General conclusions and perspectives

The main aim of this PhD work was to isolate and quantify the role played by KI based on the isotopic exchange mechanism postulated in the literature. In that respect, complementary test methodologies (from DF determination to complete BTC curves measurements) have been developed and implemented for a large panel of AC impregnations (unimpregnated AC, KI or TEDA impregnated AC, KI + TEDA co-impregnated AC). More precisely, up to 20 AC were considered. A first objective was to establish correlations between the AC parameters as deduced from physico-chemical characterizations and their retention performances based on DF measurement. Then, a specific attention was devoted to the KI-impregnated AC through breakthrough curves measurements towards both stable and radioactive CH_3I.

Three main steps can be distinguished with the aim to accomplish these PhD work goals:

- Firstly, a combination of physico-chemical characterization is used to probe the main characteristic parameters (chemical composition, morphology and porous structure) that may influence CH_3I removal efficiency by the studied AC. Impregnant quantity (TEDA, KI) is deduced from an extraction procedure followed by UV-Visible spectroscopic analysis. Surface composition as well as the morphology of some of the tested adsorbents are obtained from XRD, XPS and SEM/EDX characterizations. The porous structure of the different impregnated AC is determined by N_2 porosimetry at 77 K. H_2O adsorption isotherms at T = 25 °C were also recorded in order to finely investigate the effect of water vapor on the studied AC depending on the impregnation nature.
- Secondly, the performances of AC towards the capture of γ-labelled CH_3I are investigated at semi-pilot scales. The decontamination factor (DF) is measured according to test procedures adapted from standardized methods devoted to the *nuclear grade AC*. An attempt to establish structure–activity correlations between the physico-chemical characteristics and the measured DF is presented. Such investigations were also helpful to better assess the role played by KI and TEDA separately. First insights about the occurrence of isotopic exchange reaction were also provided. Based on the obtained results,

an assumption is made regarding the isotopic exchange reaction observation only after AC breakthrough.

- Based on this hypothesis, the BTC comparison towards stable ad radioactive CH_3I under similar conditions is required. In that respect, a novel experimental setup is developed. This study was focused on KI impregnated AC under a specific experimental configuration. The BTC comparison allows to directly quantify the temporal evolution of the contribution due to isotopic exchange. The attention is focused more particularly on the low penetrations in agreement with the AC working range in the nuclear context.

As reported in Table 41, the most important new findings gained from this PhD project can be summarized as follows:

The AC retention performance towards the capture of the γ-labelled CH_3I not only depends on the physico - chemical properties of the AC, but also on the testing methodology especially in the case of KI impregnation. Indeed, the retention tests for the AC using methods based on DF determination and the BTC measurements reveal different features. Regarding the DF determination, the dominant retention mechanism of the tested AC is found to be dependent on the RH (T = 20 °C). At RH = 40 %, the AC performance is governed by the physisorption compared to the chemisorption of TEDA and the isotopic exchange of KI. Physisorption phenomena are known to be dependent mainly to the microporous network availability. More particularly, the available microporosity for CH_3I capture through physisorption, was found to be decreased after water vapor uptake (pre-equilibration step), whatever the impregnation type. On the one hand, the decreasing available microporosity after KI impregnation is due to the affinity displayed by KI towards the water molecules at low RH. On the other hand, the decreasing available microporosity results from the micropore blockage due to TEDA presence within the internal porosity, as evidenced from N_2 adsorption isotherms at 77 K. Under these conditions, the isotopic exchange is found to be absent since the KI AC performance is correlated only with the available microporosity. At RH = 90 %, a drastic decrease of the available microporosity is observed according to H_2O adsorption isotherms. Therefore, the retention performances are rather governed by TEDA or KI reactivity than physisorption. In that respect, satisfactory retentions performances are guaranteed after TEDA impregnation thanks to its high affinity towards the capture of CH_3I. In addition, a slight contribution due to isotopic exchange reaction was observed. Based on DF measurements,

it has been proposed that this reaction can be evidenced experimentally only after the AC breakthrough.

Based on this hypothesis, BTC measurements are conducted. Accordingly, a novel experimental setup for the γ-labelled CH_3I retention is developed. Firstly, the BTC comparisons between the stable and γ-labelled CH_3I show a similar retention phase for all the tested KI AC. Secondly, the KI impregnation improves the AC performance after breakthrough, in agreement with the hypothesis based on DF measurements. More importantly, a novel methodology is also developed for the first time to quantify the relative contribution due to the isotopic exchange reaction. Regarding the adsorption capacity at saturation, a relative contribution of around 70% is obtained for the 5%KI AC. Considering the retention behavior at low $CH_3{}^{131}I$ penetration (1%), a relative contribution of around 19% can be extrapolated using the Thomas model for the 5%KI AC. These results need to be further consolidated but outline the important effect of isotopic exchange phenomena for the trapping of radioactive CH_3I considering only KI-impregnated AC. Finally, TEDA and KI presence induce different features for the associated BTC. On the one hand, the high affinity of TEDA towards the capture of CH_3I leads to the retention phase duration increase. The trapping stability is also promoted. On the other hand, the KI action is evidenced experimentally only after the breakthrough through a physical mechanism based on the redistribution of iodine isotopes without any chemical modifications. According to this study, the KI beneficial effect seems to result mainly in a slowdown of the radioactive methyl iodide desorption during the breakthrough phase.

Table 41 Summary of the observed properties and conditions on the quantification of the isotopic exchange of $CH_3^{131}I$ retention

	Properties/conditions		Effect	Remarks
AC characterization	Porous structure		(+)	• Microporous material (V_{micro}/V_{pore} > 94%) • Pore diameter ~ 0.5 nm, suitable for CH_3I retention through physisorption
	Impregnation of KI and TEDA		(+/-)	• Impregnation amount close to the theoretical value, enhancing the retention of $CH_3^{127}I/CH_3^{131}I$ depending on the impregnant nature and the operating conditions (see below) • Quasi-similar microporosity for low molar content • Micropore blocking evidence for molar impregnation ratio > 0.4% (linear decrease of S_{BET} and V_{micro})
	Surface morphology and XPS analysis		(+)	• Same batch characteristics of the tested AC • Similar N and I speciation between the tested co-impregnated and single impregnated AC • TEDA and KI molecules located within the internal porosity
Isotopic exchange by DF	Co - impregnation		(+/-)	• DF in agreement with the *nuclear grade* AC (10^4 to 10^5 at RH = 40%, maximum around 10^2 at RH = 90%) • Similar DF evolutions as comparison with TEDA or KI AC • Effect of KI masked compared to TEDA
	Single - impregnation	RH = 40%	(-)	• KI AC performance governed by physisorption, which is influenced by the pre-adsorbed water → decrease of DF with KI content and absence of isotopic exchange reaction • TEDA AC performance governed by two opposite trends (chemisorption dependent on the TEDA content and physisorption affected by the TEDA presence within the internal porosity) → observed compromise at 5 w.t% of TEDA
		RH = 90%	(+)	• Physisorption no longer dominant under these conditions • AC performance dominated by the chemisorption (TEDA) and isotopic exchange (KI) • Satisfactory retentions performances only in the presence of TEDA • Slight increase of DF with KI → observation of the isotopic exchange
Isotopic exchange through BTC comparison for stable and radioactive CH_3I	TEDA - impregnation		(+/-)	• Quasi-similar BTC towards radioactive and stable CH_3I → absence of isotopic exchange for TEDA/AC • TEDA → chemical reactivity leading to the increase of retention phase duration and the enhancement of trapping stability
	KI - impregnation		(+)	• Similar retention phase for all the tested KI AC • The KI impregnation improves the AC performance after breakthrough → mechanism of redistribution resulted in a slowdown of the $CH_3^{131}I$ desorption during the breakthrough phase • Quantification of the isotopic exchange relative contribution through adsorption capacity at saturation: relative contribution of 70% for 5%KI AC • Quantification of the isotopic exchange relative contribution at low penetration ratio (nuclear context): relative contribution of around 19% for 5%KI AC at 1% $CH_3^{131}I$ breakthrough • Improvements required for the developed experimental setup and the testing methodology

In view of this work, several perspectives can be envisaged:

- The developed experimental setup provides first important elements about the quantification of the isotopic exchange, but technical improvement is required for a better BTC acquisition. For instance, the inlet CH_3I concentration modification and the uptake method improvement are necessary in order to overcome the inconvenience of the time gap during the night. The objective is to guarantee more experimental data for the obtained BTC, which allows a better understanding of the retention behavior especially under low penetrations.
- The BTC and the DF measurement for $CH_3{}^{131}I$ under a larger panel of conditions (effect of RH and temperature, comparison with typical composition of *nuclear grade AC*) should be considered for finely investigating the isotopic exchange.
- Utilization of synthesized supports in the laboratory scale for mechanistic understanding of the isotopic exchange. The objective is to isolate the contribution due to KI while eliminating the other retention mechanisms (physisorption or the chemisorption). A particular attention will also be devoted to the effect of iodine derivatives type for the isotopic exchange.
- In the long term, it is envisaged to describe isotopic exchange theoretically and to predict the retention of $CH_3{}^{131}I$ in a porous material such as AC. The performance of these model materials will then be transposed to those found for commercial AC in order to be able to conclude on the contribution of isotopic exchange in the iodine traps classically used in nuclear facilities. Eventually, a safety coefficient enveloping this contribution should be proposed in a conservative approach and subsequently taken into account during a "non-radioactive" test of the iodine traps.

References

[1] B. Clément, L. Cantrel, G. Ducros, F. Funke, L. Herranz, A. Rydl, G. Weber and C. Wren, "State of the art report on iodine chemistry," *NEA/CSNI/R(2007)1*, 2007.

[2] D. Haefner, T. Tranter, "Methods of gas phase capture of iodine from fuel reprocessing off-gas: a literature survey," *Idaho Natl. Lab.*, 2007.

[3] R. T. Jubin, "A literature survey of methods to remove iodine from off-gas streams using solid sorbents," *ORNL/TM-6607*, 1979.

[4] C. Y. Yin, M. K. Aroua, and W. M. A. W. Daud, "Review of modifications of activated carbon for enhancing contaminant uptakes from aqueous solutions," *Sep. Purif. Technol.*, vol. 52, no. 3, pp. 403–415, 2007.

[5] C. M. Ecob, A. J. Clements, P. Flaherty, J. G. Griffiths, D. Nacapricha, and C. G. Taylor, "Effect of humidity on the trapping of radioiodine by impregnated carbons," *Sci. Total Environ.*, vol. 130–131, no. C, pp. 419–427, 1993.

[6] B. Collinson, L. R. Taylor, and P. Meddings, "Trapping performance of 1.5% KI 207B charcoal for methyl iodine in CO2 at high temperature and pressure," in *Proceedings of the 20th DOE/NRC nuclear air cleaning conference. Sessions 1--5*, 1989, pp. 537–559.

[7] J. Huve, A. Ryzhikov, H. Nouali, V. Lalia, G. Augé, and T. J. Daou, "Porous sorbents for the capture of radioactive iodine compounds: a review," *RSC Adv.*, vol. 8, no. 51, pp. 29248–29273, 2018.

[8] V. R. Deitz, "Interaction of radioactive iodine gaseous species with nuclear-grade activated carbons," *Carbon N. Y.*, vol. 25, no. 1, pp. 31–38, 1987.

[9] J. Zhou, S. Hao, L. Gao, and Y. Zhang, "Study on adsorption performance of coal based activated carbon to radioactive iodine and stable iodine," *Ann. Nucl. Energy*, vol. 72, pp. 237–241, 2014, doi: 10.1016/j.anucene.2014.05.028.

[10] Y. S. Kim, "Study on adsorption characteristics and deterioration patterns of an impregnated active carbon under a simulated service condition of the filtering system at a nuclear power plant," in *Proceedings of the 20th DOE/NRC nuclear air cleaning conference*, 1989, pp. 602–618.

[11] C. Monsanglant-Louvet, A. Brunisso, L. Bouilloux, and L. Ricciardi, "Orientation du programme 'IODE' du SCA dans le domaine de l'épuration des gaz radioactifs," *IRSN 2019-00295*, 2019.

[12] J. Rouxel, J. G. Coutard, S. Gidon, O. Lartigue, S. Nicoletti, B. Parvitte, R. Vallon, V. Zéninari and A. Glière, "Development of a miniaturized differential photoacoustic gas sensor," *Procedia Eng.*, vol. 120, pp. 396–399, 2015.

[13] EDF, "La nucléaire en chiffres," *Electricité de France*, 2022. .

[14] CEA, "The nuclear fuel cycle," *Commis. à l'Energie At. aux énergies Altern.*, 2005.

[15] WNA, “Chernobyl Accident 1986,” *World nuclear association*, 2022. .

[16] IAEA, “Fukushima Daiichi Accident Update Log,” *International Atomic Energy Agency*, 2017. .

[17] J. Repussard, T. Charles, D. Champion, and J. R. Jourdain, “Press briefing of February 2012: Situation in Japan one year after the Fukushima Daiichi accident-Summary of the Fukushima accident’s impact on the environment in Japan, one year after the accident,” *Rep. IRSN*, 2012.

[18] M. L. Perrin, A. Thomassin, E. Gaillard-Lecanu, V. Chambrette, and J. Brenot, “IODE 131,” *IRSN*, 2001.

[19] LNHB, “Iodine-129 - Emissions and decay scheme,” *Laboratoire National Henri Becquerel*, 2021. .

[20] N. S. Kwatra, M. B. Parisi, and B. L. Shulkin, “Radioisotope Therapies: Iodine-131, I-131-MIBG, and Beyond,” in *Imaging in Pediatric Oncology*, Springer, 2019, pp. 275–303.

[21] M. E. Kitto, E. M. Fielman, S. E. Fielman, and E. A. Gillen, “Airborne 131I at a background monitoring site,” *J. Environ. Radioact.*, vol. 83, no. 2, pp. 129–136, 2005.

[22] N. R. Gilfillan and H. Timmers, “Detection and tracing of the medical radioisotope 131I in the Canberra environment,” *EPJ Web Conf.*, vol. 35, p. 4002, 2012.

[23] B. J. Riley, J. D. Vienna, D. M. Strachan, J. S. McCloy, and J. L. Jerden Jr, “Materials and processes for the effective capture and immobilization of radioiodine: A review,” *J. Nucl. Mater.*, vol. 470, pp. 307–326, 2016.

[24] K. D. Kok, P. J. Fehrenbach, and A. I. Miller, “Nuclear fuel cycle,” in *Nuclear engineering handbook*, CRC Press, 2016.

[25] N. R. Soelberg T. G. Garn, M. R. Greenhalgh, J. D. Law, R. Jubin, D. M. Strachan and P. K. Thallapally, “Radioactive iodine and krypton control for nuclear fuel reprocessing facilities,” *Sci. Technol. Nucl. Install.*, vol. 2013, 2013.

[26] F. Kepák, “Removal of gaseous fission products by adsorption,” *J. Radioanal. Nucl. Chem. Artic.*, vol. 142, no. 1, pp. 215–230, 1990.

[27] M. Chebbi, B. Azambre, C. Volkringer, and T. Loiseau, “Dynamic sorption properties of Metal-Organic Frameworks for the capture of methyl iodide,” *Microporous Mesoporous Mater.*, vol. 259, pp. 244–254, 2018.

[28] M. Chebbi, “Piégeage d’espèces iodées volatiles sur des adsorbants poreux de type zéolithique dans le contexte d’un accident nucléaire grave.” Université de Lorraine, 2018.

[29] Q. Cheng, W. Yang, Z. Li, Q. Zhu, T. Chu, D. He and C. Fang, “Adsorption of gaseous radioactive iodine by Ag/13X zeolite at high temperatures,” *J. Radioanal. Nucl. Chem.*, vol. 303, no. 3, pp. 1883–1889, 2015.

[30] P. Paviet-Hartmann, W. Kerlin, and S. Bakhtiar, “Treatment of gaseous effluents issued from recycling–A review of the current practices and prospective improvements,” Idaho National Laboratory (INL), 2010.

[31] IRSN, “MIRE Project,” *Inst. Radioprot. Sûreté Nucléaire*, 2020.

[32] IRSN, “PASSAM project,” *Inst. Radioprot. Sûreté Nucléaire*, 2017.

[33] B. Azambre, M. Chebbi, and A. Hijazi, “Effects of the cation and Si/Al ratio on CH3I adsorption by faujasite zeolites,” *Chem. Eng. J.*, vol. 379, p. 122308, 2020.

[34] M. Chebbi, B. Azambre, C. Monsanglant-Louvet, B. Marcillaud, A. Roynette, and L. Cantrel, “Effects of water vapour and temperature on the retention of radiotoxic CH3I by silver faujasite zeolites,” *J. Hazard. Mater.*, p. 124947, 2020.

[35] L. Cantrel, L. Herranz, S. Guieu, T. Albiol, R. Collet, T. Lind, T. Kärkelä, C. Mun, D. Jacquemain, M. Chebbi and B. Azambre, “Overview of ongoing and planned R&D works on delayed radioactive releases and filtered containment venting systems efficiencies in a severe accident,” *Int. Congr. Adv. Nucl. Power Plants, ICAPP*, 2015.

[36] J. Pelcé, B. Noc and L. Reynes, “Containment venting system: motivations and objectives,” in *OECD Specialist Meeting on Filtered Containment Venting System*, 1988, pp. 21–29.

[37] E. Jouen, “Containment venting system - Sand bed filter: discription, operating procedure, implementation program,” in *OECD specialist Meeting on Filtered Containment Venting System*, 1988, pp. 257–278.

[38] M. Hoyle, G. R. Astbury and M. H. Chen, “Thermal stability of activated carbon in an adsorber bed,” in *Institution Of Chemical Engineers Symposium Series*, 1997, vol. 141, pp. 247–260.

[39] L. E. Herranz, T. Lind, K. Dieschbourg, E. Riera, S. Morandi, P. Rantanen, M. Chebbi and N. Losch, “Technical bases for experimentation on source term mitigation. The EU-PASSAM project,” 2014.

[40] R. T. Jubin, “Airborn Waste Management Technology Applicable for Use in Reprocessing Plants for Control of Iodine and Other Off-Gas Constituents,” Oak Ridge National Lab., TN (USA), 1988.

[41] ISO, “ISO 17873:2004. Nuclear Facilities - Criteria for the description and operation of ventilation systems for nuclear installations other than nuclear reactors,” *ISO/TC85/SC2*, 2004.

[42] CAMFIL, “Acticarb,” *Data sheet*, 2022.

[43] P. Decourcière, “Evolution de la filtration des iodes dans les centrales nucléaires,” in *Iodine Removal From Gaseous Effluents In The Nuclear Industry*, 1981, pp. 347–390.

[44] Y. Testini, “Note de doctrine : Contrôle des pièges à Iodes des systèmes de ventilation des centrales REP,” *EDF*, 2007.

[45] O. Talu and A. L. Myers, “Rigorous thermodynamic treatment of gas adsorption,” *AIChE J.*, vol. 34, no. 11, pp. 1887–1893, 1988.

[46] P. Guan, D. R. Mckenzie, and B. A. Pailthorpe, “MD simulations of Ag film growth using the Lennard-Jones potential,” *J. Phys. Condens. Matter*, vol. 8, no. 45, p. 8753, 1996.

[47] D. Leinekugel-le-Cocq, “Contribution à la modélisation dynamique simplifiée d’un procédé d’adsorption modulée en pression (PSA).” Université Claude Bernard-Lyon I, 2004.

[48] L. Sun and F. Meunier, “Adsorption - Aspects théoriques Aspects théoriques - J2730,” *Tech. l’ingénieur*, 2003.

[49] R. Chauveau, “Modélisation multiparamètre du phénomène d’adsorption: détermination du temps de percée des cartouches de masques à gaz.” Université de Lorraine, 2014.

[50] B. Zdravkov, J. J. Čermák, J. Janků, V. Kučerová, and M. Šefara, “Pore classification in the characterization of porous materials,” *Chem. List.*, vol. 102, no. 6, pp. 434–438, 2008.

[51] J. A. Menéndez-Díaz and I. Martín-Gullón, “Chapter 1 Types of carbon adsorbents and their production. Actived carbon surfaces in environmental remediation.,” in *Interface Science and Technology*, vol. 7, no. C, Elsevier, 2006, pp. 1–47.

[52] B. S. Choi, G. Il Park, J. H. Kim, J. W. Lee, and S. K. Ryu, “Adsorption equilibrium and dynamics of methyl iodide in a silver ion-exchanged zeolite column at high temperatures,” *Adsorption*, vol. 7, no. 2, pp. 91–103, 2001.

[53] F. Rodríguez-Reinoso, “Activated Carbon and Adsorption,” *Encycl. Mater. Sci. Technol.*, vol. 2, pp. 22–34, 2001.

[54] E. J. Bottani and J. M. D. Tascon, “Energetics of physical adsorption of gases and vapors on carbons,” in *Chemistry and Physics of Carbons*, vol. 29, 2004, pp. 209–423.

[55] I. Langmuir, “The adsorption of gases on plane surfaces of glass, mica and platinum.,” *J. Am. Chem. Soc.*, vol. 40, no. 9, pp. 1361–1403, 1918.

[56] H.-K. Lee and G.-I. Park, “Adsorption characteristics of elemental iodine and methyl iodide on base and TEDA impregnated carbon,” *Nucl. Eng. Technol.*, vol. 28, no. 1, pp. 44–55, 1996.

[57] G. F. Cerofolini, M. Jaroniec, and S. Sokołosvski, “A theoretical isotherm for adsorption on heterogeneous surface,” *Colloid Polym. Sci.*, vol. 256, no. 5, pp. 471–477, 1978.

[58] C. C. Travis, “Mathematical description of adsorption and transport of reactive solutes in soil: A review of selected literature,” Oak Ridge National Lab., 1978.

[59] D. S. Forsyth, “Pulsed discharge detector: theory and applications,” *J. Chromatogr. A*, vol. 1050, no. 1, pp. 63–68, 2004.

[60] M. Chebbi, B. Azambre, L. Cantrel, M. Huvé, and T. Albiol, “Influence of structural, textural and chemical parameters of silver zeolites on the retention of methyl iodide,” *Microporous Mesoporous Mater.*, vol. 244, pp. 137–150, 2017.

[61] C. Moulin, C. Gerente, M. Chebbi, B. Azambre, C. Volkringer, and L. Cantrel, “Rapport bibliographique sur le piégeage des iodes volatils par des matériaux adsorbants dans le cadre du projet MIRE,” *IRSN 2016-00028*, 2016.

[62] M. R. Bassford, G. Nickless, P. G. Simmonds, A. C. Lewis, M. J. Pilling, and M. J. Evans, “The concurrent observation of methyl iodide and dimethyl sulphide in marine air; implications for sources of atmospheric methyl iodide,” *Atmos. Environ.*, vol. 33, no. 15, pp. 2373–2383, 1999.

[63] K. Ho, S. Moon, H. C. Lee, Y. K. Hwang, and C. H. Lee, “Adsorptive removal of gaseous methyl

iodide by triethylenediamine (TEDA)-metal impregnated activated carbons under humid conditions," *J. Hazard. Mater.*, vol. 368, pp. 550–559, 2019.

[64] M. M. R. Khan, M. W. Rahman, M. S. I. Mozumder, K. Ferdous, H. R. Ong, K. M. Chan and D. M. R. Prasad, "Performance of a submerged adsorption column compared with conventional fixed-bed adsorption," *Desalin. Water Treat.*, vol. 57, no. 21, pp. 9705–9717, 2016.

[65] J. M. López, M. V. Navarro, T. García, R. Murillo, A. M. Mastral, F. J. Varela-Gandía, D. Lozano-Castelló, A. Bueno-López and D. Cazorla-Amorósb, "Screening of different zeolites and silicoaluminophosphates for the retention of propene under cold start conditions," *Microporous mesoporous Mater.*, vol. 130, no. 1–3, pp. 239–247, 2010.

[66] C.-G. Lee, J. H. Kim, J. K. Kang, S. B. Kim, S. J.Park, S. H. Lee and J. W. Choi, "Comparative analysis of fixed-bed sorption models using phosphate breakthrough curves in slag filter media," *Desalin. Water Treat.*, vol. 55, no. 7, pp. 1795–1805, 2015.

[67] G. S. Bohart and E. Q. Adams, "Some aspects of the behavior of charcoal with respect to chlorine.," *J. Am. Chem. Soc.*, vol. 42, no. 3, pp. 523–544, 1920.

[68] H. C. Thomas, "Heterogeneous ion exchange in a flowing system," *J. Am. Chem. Soc.*, vol. 66, no. 10, pp. 1664–1666, 1944.

[69] Y. H. Yoon and J. H. NELSON, "Application of gas adsorption kinetics I. A theoretical model for respirator cartridge service life," *Am. Ind. Hyg. Assoc. J.*, vol. 45, no. 8, pp. 509–516, 1984.

[70] K. H. Chu, "Breakthrough curve analysis by simplistic models of fixed bed adsorption: In defense of the century-old Bohart-Adams model," *Chem. Eng. J.*, vol. 380, p. 122513, 2020.

[71] H. Nakajima, *Mass Transfer: Advances in Sustainable Energy and Environment Oriented Numerical Modeling*. BoD–Books on Demand, 2013.

[72] H. Patel, "Fixed-bed column adsorption study: a comprehensive review," *Appl. Water Sci.*, vol. 9, no. 3, p. 45, 2019.

[73] K. H. Chu, "Fixed bed sorption: setting the record straight on the Bohart–Adams and Thomas models," *J. Hazard. Mater.*, vol. 177, no. 1–3, pp. 1006–1012, 2010.

[74] R. Apiratikul and K. H. Chu, "Improved fixed bed models for correlating asymmetric adsorption breakthrough curves," *J. Water Process Eng.*, vol. 40, p. 101810, 2021, doi: 10.1016/j.jwpe.2020.101810.

[75] S. U. Nandanwar, K. Coldsnow, A. Porter, P. Sabharwall, D.E. Aston, D. N. McIlroy and V. Utgikar, "Adsorption of radioactive iodine and krypton from off-gas stream using continuous flow adsorption column," *Chem. Eng. J.*, vol. 320, pp. 222–231, 2017.

[76] C. Le Gall, P. Nérisson, L. Cantrel, B. Azambre, and A. Piton, "Piégeage de l'iodure de méthyle sur des zéolithes échangées a l'argent en conditions représentatives d'un accident nucléaire grave," *IRSN 2021-00134*, 2021.

[77] H. Houjeij, M. Chebbi, and C. Le Gall, "Trapping of methyl iodide by silver-loaded zeolites in various configurations - Works performed within the frame of the extension of MIRE project," *IRSN*

2021-00881, 2021.

[78] G.-I. Park, I.-T. Kim, J.-K. Lee, S.-K. Ryu, and J.-H. Kim, "Effect of Temperature on the Adsorption and Desorption Characteristics of Methyl Iodide over TEDA-Impregnated Activated Carbon," *Carbon Lett.*, vol. 2, no. 1, pp. 9–14, 2001.

[79] G.-I. Park, B.-S. Park, I.-H. Cho, J.-H. Kim, and S.-K. Ryu, "Adsorption and desorption characteristics of methyl iodide on silver ion-exchanged synthetic zeolite at high temperature," *Nucl. Eng. Technol.*, vol. 32, no. 5, pp. 504–513, 2000.

[80] C. Le Gall, "Rapport bibliographique sur le vieillissement des zéolites échangées à l'argent vis-à-vis du piégeage des espèces iodées volatiles étudiées dans le cadre du projet MIRE," *IRSN 2020-00248*, 2020.

[81] F. J. Herrmann, B. Herrmann, V. Hoeflich, C. Beyer, and J. Furrer, "Removal Effkiency of Silver Impregnated Filter Materials and Performance of IodineFilters in the Off-Gases of the Karlsruhe Reprocessing Plant WAK," 1996.

[82] L. Wu, J. A. Sawada, D. B. Kuznicki, T. Kuznicki, and S. M. Kuznicki, "Iodine adsorption on silver-exchanged titania-derived adsorbents," *J. Radioanal. Nucl. Chem.*, vol. 302, no. 1, pp. 527–532, 2014.

[83] B. Li, X. Dong, H. Wang, D. Ma, K. Tan, S. Jensen, B. J. Deibert, J. Butler, J. Cure, Z. Shi, T. Thonhauser, Y. J. Chabal, Y. Han and J. Li, "Capture of organic iodides from nuclear waste by metal-organic framework-based molecular traps," *Nat. Commun.*, vol. 8, no. 1, pp. 1–9, 2017.

[84] D. F. Sava, M. A. Rodriguez, K. W. Chapman, P. J. Chupas, J. A. Greathouse, P. S. Crozier and T. M. Nenoff, "Capture of volatile iodine, a gaseous fission product, by zeolitic imidazolate framework-8," *J. Am. Chem. Soc.*, vol. 133, no. 32, pp. 12398–12401, 2011.

[85] J. H. Yang, Y. J. Cho, J. M. Shin, and M. S. Yim, "Bismuth-embedded SBA-15 mesoporous silica for radioactive iodine capture and stable storage," *J. Nucl. Mater.*, vol. 465, pp. 556–564, 2015.

[86] B. Azambre, M. Chebbi, and N. Ibrahim, "Structure–Activity Relationships between the State of Silver on Different Supports and Their I2 and CH3I Adsorption Properties," *Nanomaterials*, vol. 11, no. 5, p. 1300, 2021.

[87] A. Hijazi, B. Azambre, G. Finqueneisel, F. Vibert, and J. L. Blin, "High iodine adsorption by polyethyleneimine impregnated nanosilica sorbents," *Microporous Mesoporous Mater.*, vol. 288, p. 109586, 2019.

[88] CARBIO12, "Filtration of radioactive gases and raioactive particles: impregnated activated carbon C1220 IG 98," *Carbio 12 Prod.*

[89] C. M. González-García, J. F. González, and S. Román, "Removal efficiency of radioactive methyl iodide on TEDA-impregnated activated carbons," *Fuel Process. Technol.*, vol. 92, no. 2, pp. 247–252, 2011.

[90] W. M. A. W. Daud and W. S. W. Ali, "Comparison on pore development of activated carbon produced from palm shell and coconut shell," *Bioresour. Technol.*, vol. 93, no. 1, pp. 63–69, 2004.

[91] J. Laine and S. Yunes, "Effect of the preparation method on the pore size distribution of activated carbon from coconut shell," *Carbon N. Y.*, vol. 30, no. 4, pp. 601–604, 1992.

[92] C. G. Doll, C. M. Sorensen, T. W. Bowyer, J. I. Friese, J. C. Hayes, E. Hoffmann, and R. Kephart, "Abatement of xenon and iodine emissions from medical isotope production facilities," *J. Environ. Radioact.*, vol. 130, pp. 33–43, 2014.

[93] H. M. Mozammel, O. Masahiro, and S. C. Bhattacharya, "Activated charcoal from coconut shell using ZnCl2 activation," *Biomass and Bioenergy*, vol. 22, no. 5, pp. 397–400, 2002.

[94] K. Sartova, E. Omurzak, G. Kambarova, I. Dzhumaev, B. Borkoev, and Z. Abdullaeva, "Activated carbon obtained from the cotton processing wastes," *Diam. Relat. Mater.*, vol. 91, pp. 90–97, 2019.

[95] Z. Gao, Y. Zhang, N. Song, and X. Li, "Biomass-derived renewable carbon materials for electrochemical energy storage," *Mater. Res. Lett.*, vol. 5, no. 2, pp. 69–88, 2017.

[96] P. Patnukao and P. Pavasant, "Activated carbon from Eucalyptus camaldulensis Dehn bark using phosphoric acid activation," *Bioresour. Technol.*, vol. 99, no. 17, pp. 8540–8543, 2008.

[97] A. Kongsuwan, P. Patnukao, and P. Pavasant, "Binary component sorption of Cu (II) and Pb (II) with activated carbon from Eucalyptus camaldulensis Dehn bark," *J. Ind. Eng. Chem.*, vol. 15, no. 4, pp. 465–470, 2009.

[98] T. Budinova, E. Ekinci, F. Yardim, A. Grimm, E. Björnbom, V. Minkova and M. Goranova, "Characterization and application of activated carbon produced by H3PO4 and water vapor activation," *Fuel Process. Technol.*, vol. 87, no. 10, pp. 899–905, 2006.

[99] M. Danish and T. Ahmad, "A review on utilization of wood biomass as a sustainable precursor for activated carbon production and application," *Renew. Sustain. Energy Rev.*, vol. 87, pp. 1–21, 2018.

[100] C. C. Chien, Y. P. Huang, W. C. Wang, J. H. Chao, and Y. Y. Wei, "Efficiency of Moso Bamboo Charcoal and Activated Carbon for Adsorbing Radioactive Iodine," *Clean - Soil, Air, Water*, vol. 39, no. 2, pp. 103–108, 2011.

[101] C. Srinivasakannan and Z. M. Abu Bakar, "Production of activated carbon from rubber wood sawdust," *Biomass and Bioenergy*, vol. 27, no. 1, pp. 89–96, 2004.

[102] M. A. F. Mazlan *et al.*, "Activated carbon from rubber wood sawdust by carbon dioxide activation," *Procedia Eng.*, vol. 148, pp. 530–537, 2016.

[103] A. A. Ceyhan, Ö. Şahin, O. Baytar, and C. Saka, "Surface and porous characterization of activated carbon prepared from pyrolysis of biomass by two-stage procedure at low activation temperature and it's the adsorption of iodine," *J. Anal. Appl. Pyrolysis*, vol. 104, pp. 378–383, 2013.

[104] S. Kutluay, O. Baytar, and Ö. Şahin, "Equilibrium, kinetic and thermodynamic studies for dynamic adsorption of benzene in gas phase onto activated carbon produced from elaeagnus angustifolia seeds," *J. Environ. Chem. Eng.*, vol. 7, no. 2, p. 102947, 2019.

[105] F. Rodriguez-Reinoso, "The role of carbon materials in heterogeneous catalysis," *Carbon N. Y.*, vol. 36, no. 3, pp. 159–175, 1998.

[106] M. Hervy, “Valorisation de chars issus de pyrogazéification de biomasses pour la purification du syngas : lien entre propriétés physico-chimiques et efficacité du traitement.” Ecole des Mines d’Albi-Carmaux, p. 306, 2016.

[107] L. Lu, C. Kong, V. Sahajwalla, and D. Harris, “Char structural ordering during pyrolysis and combustion and its influence on char reactivity,” *Fuel*, vol. 81, no. 9, pp. 1215–1225, 2002.

[108] P. J. F. Harris, Z. Liu, and K. Suenaga, “Imaging the atomic structure of activatedcarbon,” *J. Phys. Condens. Matter*, vol. 20, no. 36, p. 362201, 2008.

[109] F. Rodríguez-Reinoso and M. Molina-Sabio, “Textural and chemical characterization of microporous carbons,” *Adv. Colloid Interface Sci.*, vol. 76–77, pp. 271–294, 1998.

[110] A. K. Srivastava, A. Saxena, B. Singh, and S. K. Srivas, “Development and evaluation of impregnated carbon systems against iodine vapours,” *Carbon Lett. (Carbon Lett.)*, vol. 8, no. 4, pp. 274–279, 2007.

[111] H. Sun, P. La, Z. Zhu, W. Liang, B. Yang, and A. Li, “Capture and reversible storage of volatile iodine by porous carbon with high capacity,” *J. Mater. Sci.*, vol. 50, no. 22, pp. 7326–7332, 2015.

[112] A. J. Juhola, “Iodine adsorption and structure of activated carbons,” *Carbon N. Y.*, vol. 13, no. 5, pp. 437–442, 1975.

[113] S. Kitani, T. Noro, and T. Kohara, “Removal of Methyl Iodide by Impregnated Charcoals from Flowing Air under Humid Condition,” *J. Nucl. Sci. Technol.*, vol. 9, no. 4, pp. 197–202, 1972.

[114] D. A. Collins, L. R. Taylor, and R. Taylor, “Development of impregnated charcoals for trapping methyl iodide at high humidity,” 1967.

[115] G. O. Wood, G. J. Vogt, and C. A. Kasunic, “Methyl iodide retention on charcoal sorbents at parts-per-million concentrations,” in *Proceedings of the 15th DOE/NRC Nuclear Air Cleaning Conference*, 1978, pp. 352–367.

[116] S. W. Park, W. K. Lee, and H. Moon, “Adsorption and desorption of gaseous methyl iodide in a triethylenediamine-impregnated activated carbon bed,” *Sep. Technol.*, vol. 3, no. 3, pp. 133–142, 1993.

[117] F. Billard, A. Charamathieu, M. F. Thal, J. Caron, and J. Van der Meersch, “Etude de l’efficacité des charbons actifs vis-à-vis de l’iodure de méthyle marqué à l’iode 131,” *CEA/STEP/GAM*, 1966.

[118] A. Sadighzadeh, M. Gourani, and F. Mizani, “Effect of impregnating materials in activated carbon on Iodine-131 (131I) removal efficiency,” *Radiat. Prot. Environ.*, vol. 37, no. 3, p. 179, 2014.

[119] C. Landaverde-Alvarado, A. J. Morris, and S. M. Martin, “Gas sorption and kinetics of CO2 sorption and transport in a polymorphic microporous MOF with open Zn (II) coordination sites,” *J. CO2 Util.*, vol. 19, pp. 40–48, 2017.

[120] J. L. Kovach, “Parametric Studies of Radioiodine, Hydrogen Iodide, and Methyl Iodide Removal,” in *Proceedings of the 22nd DOE/NRC Nuclear Air Cleaning Conference*, 1992, vol. 22, p. 646.

[121] A. J. Juhola and J. V. Friel, “Effect of Pore Structure on the Activated Carbon’s Capability To Sorb

Airborne Methylradioiodine," in *Proceedings of the 15th DOE/NRC Nuclear Air Cleaning Conference*, 1979, pp. 335–351.

[122] H. Shiomi, Y. Yuasa, A. Tani, M. Ohki, and T. Nakagawa, "Parametric Study on Removal Efficiency of Impregnated Activated Charcoal and Silver Zeolite for Radioactive Methyl Iodide.," in *Proceedings of the 17th DOE/NRC Nuclear Air Cleaning Conference*, 1983, vol. 1, pp. 199–222.

[123] M. Nakamura, T. Ohba, P. Branton, H. Kanoh, and K. Kaneko, "Equilibration-time and pore-width dependent hysteresis of water adsorption isotherm on hydrophobic microporous carbons," *Carbon N. Y.*, vol. 48, no. 1, pp. 305–308, 2010.

[124] H. Chun, J. Kang, and B. Han, "First principles computational study on the adsorption mechanism of organic methyl iodide gas on triethylenediamine impregnated activated carbon," *Phys. Chem. Chem. Phys.*, vol. 18, no. 47, pp. 32050–32056, 2016.

[125] S. W. Park, H. S. Park, W. K. Lee, and H. Moon, "Effect of water vapor on adsorption of methyl iodide to triethylenediamine-impregnated activated carbons," *Sep. Technol.*, vol. 5, no. 1, pp. 35–44, 1995.

[126] L. Bouilloux, B. Marcillaud, C. Monsanglant-Louvet, and A. Roynette, "Épuration de l'iodure de méthyle par du charbon actif-Comparaison des résultats des plateformes TEAM, STEAM et PERSÉE," *IRSN 2018-00094*, 2018.

[127] J. G. W. H. Deuber, "Retention of elemental radioiodine by deep bed carbon filters under accident conditions," in *Proceedings of the 17th DOE Nuclear Air Cleaning Conference*, 1982, pp. 248–277.

[128] ASTM, "ASTM D3803-91(2014). Standard Test Method for Nuclear-Grade Activated Carbon," *B. Stand.*, 2014.

[129] J. Trejbal and P. Švecová, "Preparation of alkyl-1, 4-diazabicyclo [2.2.2] octanes over zsm-5 zeolite," *Pet. Coal*, vol. 54, no. 4, pp. 335–339, 2012.

[130] E. Aneheim, D. Bernin, and M. R. S. J. Foreman, "Affinity of charcoals for different forms of radioactive organic iodine," *Nucl. Eng. Des.*, vol. 328, pp. 228–240, 2018.

[131] K. Ho, H. Chun, H. C. Lee, Y. Lee, S. Lee, H. Jung, B. Han, and C. H. Lee, "Design of highly efficient adsorbents for removal of gaseous methyl iodide using tertiary amine-impregnated activated carbon: Integrated experimental and first-principles approach," *Chem. Eng. J.*, vol. 373, pp. 1003–1011, 2019.

[132] J. L. Kovach, "History of radioiodine control," in *Proceedings of 25th DOE/NRC Nuclear Air Cleaning and Treatment Conference*, 1998, pp. 304–319.

[133] B. Azambre and M. Chebbi, "Evaluation of Silver Zeolites Sorbents Towards their Ability to Promote Stable CH3I Storage as AgI Precipitates," *ACS Appl. Mater. Interfaces*, vol. 9, no. 30, pp. 25194–25203, 2017.

[134] M. Chebbi, B. Azambre, L. Cantrel, and A. Koch, "A Combined DRIFTS and DR-UV–Vis Spectroscopic In Situ Study on the Trapping of CH3I by Silver-Exchanged Faujasite Zeolite," *J. Phys. Chem. C*, vol. 120, no. 33, pp. 18694–18706, 2016.

[135] G. O. Wood and F. O. Valdez, "Nonradiometric and radiometric testing of radioiodine sorbents using methyl iodide," in *Proceedings of the 16th DOE Nuclear Air Cleaning Conference*, 1980, pp. 448–464.

[136] P. Billemont, B. Coasne, and G. De Weireld, "Adsorption of carbon dioxide, methane, and their mixtures in porous carbons: effect of surface chemistry, water content, and pore disorder," *Langmuir*, vol. 29, no. 10, pp. 3328–3338, 2013.

[137] Y. S. Aim, "Ultraviolet spectrometric method of analyzing chemical impregnants of a nuclear grade active carbon and its applications for managing the carbon filter at a nuclear regulatory laboratory and plants," in *Proceedings of the 19th DOE/NRC Nuclear Air Cleaning Conference*, 1987, pp. 221–236.

[138] D. Di Benedetto and P. Breuil, "Spectrophotométrie d'absorption dans l'ultraviolet et le visible," *Tech. l'ingénieur Spectrométries*, 2007.

[139] S. S. Kiani, Y. Faiz, A. Farooq, M. Ahmad, N. Irfan, M. Nawaz and S. Bibi, "Synthesis and adsorption behavior of activated carbon impregnated with ASZM-TEDA for purification of contaminated air," *Diam. Relat. Mater.*, vol. 108, p. 107916, 2020.

[140] J.-Y. So and H.-R. Cho, "Thermal characteristics of spent activated carbon generated from air cleaning units in Korean nuclear power plants," *Nucl. Eng. Technol.*, vol. 49, no. 4, pp. 873–880, 2017.

[141] C. W. F. T. Pistorius, "Melting curves of the potassium halides at high pressures," *J. Phys. Chem. Solids*, vol. 26, no. 9, pp. 1543–1548, 1965.

[142] M. Bée, J. L. Sauvajol, A. Hédoux, and J. P. Amoureux, "Molecular reorientations of triethylenediamine (TEDA) in its plastic solid phase: An incoherent quasielastic neutron scattering study," *Mol. Phys.*, vol. 55, no. 3, pp. 637–652, 1985.

[143] M. Thommes, K. Kaneko, A. V. Neimark, J. P. Olivier, F. Rodriguez-Reinoso, J. Rouquerol and K. S. W. Sing, "Physisorption of gases, with special reference to the evaluation of surface area and pore size distribution (IUPAC Technical Report)," *Pure Appl. Chem.*, vol. 87, no. 9–10, pp. 1051–1069, 2015.

[144] S. Brunauer, P. H. Emmett, and E. Teller, "Adsorption of gases in multimolecular layers," *J. Am. Chem. Soc.*, vol. 60, no. 2, pp. 309–319, 1938.

[145] F. Rouquerol, J. Rouquerol, P. Llewellyn, and R. Denoyel, "Texture des matériaux divisés Aire spécifique des matériaux pulvérulents ou nanoporeux," *Tech. l'ingénieur*, 2017.

[146] J. Rouquerol, P. Llewellyn, and F. Rouquerol, "Is the BET equation applicable to microporous adsorbents," *Stud. Surf. Sci. Catal*, vol. 160, no. 07, pp. 49–56, 2007.

[147] G. Horváth and K. Kawazoe, "Method for the calculation of effective pore size distribution in molecular sieve carbon," *J. Chem. Eng. Japan*, vol. 16, no. 6, pp. 470–475, 1983.

[148] B. Sellergren and A. J. Hall, "Fundamental aspects on the synthesis and characterisation of imprinted network polymers," in *Techniques and Instrumentation in Analytical Chemistry*, vol. 23, Elsevier, 2001, pp. 21–57.

[149] M. Önal, Y. Sarikaya, and T. Alemdaroğlu, "Investigation of the microporous and mesoporous structures of the Reşadiye (Tokat/Turkey) bentonite and its fractions," *Turkish J. Chem.*, vol. 25, no. 2, pp. 241–249, 2001.

[150] L. F. Velasco, D. Snoeck, A. Mignon, L. Misseeuw, C. O. Ania, S. van Vlierberghe, P. Dubruel, N. de Belie, and P. Lodewyckx, "Role of the surface chemistry of the adsorbent on the initialization step of the water sorption process," *Carbon N. Y.*, vol. 106, pp. 284–288, 2016.

[151] S. C. Lee, S.Y. Kim, W. S. Lee, S. Y. Jung, B. W. Hwang, D. Ragupathy, D. D. Lee, S. Y. Lee, and J. C. Kim, "Effects of textural properties on the response of a SnO2-based gas sensor for the detection of chemical warfare agents," *Sensors*, vol. 11, no. 7, pp. 6893–6904, 2011.

[152] S.-G. Ro and H.-K. Lee, "Method and apparatus for manufacturing TEDA-impregnated active carbon in fluidized bed type absorbing tower by generating TEDA vapor by means of hot air." Google Patents, Aug. 11, 1998.

[153] H. Estrade-Szwarckopf, "XPS photoemission in carbonaceous materials: A 'defect' peak beside the graphitic asymmetric peak," *Carbon N. Y.*, vol. 42, no. 8–9, pp. 1713–1721, 2004.

[154] M. E. Schuster, M. Hävecker, R. Arrigo, R. Blume, M. Knauer, N. P. Ivleva, D. S. Su, R. Niessner, and R. Schlögl, "Surface sensitive study to determine the reactivity of soot with the focus on the European emission standards IV and VI," *J. Phys. Chem. A*, vol. 115, no. 12, pp. 2568–2580, 2011.

[155] J. Yang and K. Q. Qiu, "Preparation of activated carbon by chemical activation under vacuum," *Environ. Sci. Technol.*, vol. 43, no. 9, pp. 3385–3390, 2009.

[156] J. M. V. Nabais, P. Nunes, P. J. M. Carrott, M. M. L. Ribeiro Carrott, A. M. García, and M. A. Díaz-Díez, "Production of activated carbons from coffee endocarp by CO2 and steam activation," *Fuel Process. Technol.*, vol. 89, no. 3, pp. 262–268, 2008.

[157] Y. Hayashi, G. Yu, M. M. Rahman, K. M. Krishna, T. Soga, T. Jimbo and M. Umeno, "Spectroscopic properties of nitrogen doped hydrogenated amorphous carbon films grown by radio frequency plasma-enhanced chemical vapor deposition," *J. Appl. Phys.*, vol. 89, no. 12, pp. 7924–7931, 2001.

[158] J. T. Titantah and D. Lamoen, "Carbon and nitrogen 1s energy levels in amorphous carbon nitride systems: XPS interpretation using first-principles," *Diam. Relat. Mater.*, vol. 16, no. 3, pp. 581–588, 2007.

[159] E. F. Sheka, Y. A. Golubev, and N. A. Popova, "Amorphous state of sp2 solid carbon," *Fullerenes, Nanotub. Carbon Nanostructures*, vol. 29, no. 2, pp. 107–113, 2021.

[160] S. Brunauer, L. S. Deming, W. E. Deming, and E. Teller, "On a theory of the van der Waals adsorption of gases," *J. Am. Chem. Soc.*, vol. 62, no. 7, pp. 1723–1732, 1940.

[161] F. R. Ribeiro and M. Guisnet, *Les zéolithes, un nanomonde au service de la catalyse*. EDP sciences, 2006.

[162] J. Sreńscek-Nazzal, U. Narkiewicz, A. W. Morawski, R. J. Wróbel, and B. Michalkiewicz, "The increase of the micoporosity and CO2 adsorption capacity of the commercial activated carbon CWZ-22 by KOH treatment," *Microporous mesoporous Mater.*, 2016.

[163] Z. Liu, X. Zhou, F. Wu, and Z. Liu, "Microwave-Assisted Preparation of Activated Carbon Modified by Zinc Chloride as a Packing Material for Column Separation of Saccharides," *ACS omega*, vol. 5, no. 17, pp. 10106–10114, 2020.

[164] N. Bouchemal, M. Belhachemi, Z. Merzougui, and F. Addoun, "The effect of temperature and impregnation ratio on the active carbon porosity," *Desalin. water Treat.*, vol. 10, no. 1–3, pp. 115–120, 2009.

[165] J. Alcañiz-Monge, A. Linares-Solano, and B. Rand, "Mechanism of adsorption of water in carbon micropores as revealed by a study of activated carbon fibers," *J. Phys. Chem. B*, vol. 106, no. 12, pp. 3209–3216, 2002.

[166] J. Alcañiz-Monge, A. Linares-Solano, and B. Rand, "Water adsorption on activated carbons: study of water adsorption in micro-and mesopores," *J. Phys. Chem. B*, vol. 105, no. 33, pp. 7998–8006, 2001.

[167] AFNOR, "NF M62-206, Installation de ventilation nucléaire - Méthode de contrôle du coefficient d'épuration des pièges à iode," *Normes Natl. Doc. normatifs Natx.*, 1984.

[168] U. D. Djiogo Yemele, "Prédiction des courbes de percée : adsorption de l'iodure de méthyle ou de la vapeur d'eau par une sélection de charbons actifs commerciaux," *M2 Rep. IRSN*, 2021.

[169] H. C. Lee, D. Y. Lee, H. S. Kim, and C. R. Kim, "Performance evaluation of TEDA impregnated activated carbon under long term operation simulated NPP operating condition," *Nucl. Eng. Technol.*, vol. 52, no. 11, pp. 2652–2659, 2020.

[170] B.-S. Choi, S.-B. Kim, J. Moon, and B.-K. Seo, "Evaluation of decontamination factor of radioactive methyl iodide on activated carbons at high humid conditions," *Nucl. Eng. Technol.*, vol. 53, no. 5, pp. 1519–1523, 2021.

[171] D. D. Do and H. D. Do, "A model for water adsorption in activated carbon," *Carbon N. Y.*, vol. 38, no. 5, pp. 767–773, 2000.

[172] T. Ohba, H. Kanoh, and K. Kaneko, "Structures and stability of water nanoclusters in hydrophobic nanospaces," *Nano Lett.*, vol. 5, no. 2, pp. 227–230, 2005.

[173] K. Ho, D. Park, M.-K. Park, and C.-H. Lee, "Adsorption mechanism of methyl iodide by triethylenediamine and quinuclidine-impregnated activated carbons at extremely low pressures," *Chem. Eng. J.*, vol. 396, p. 125215, 2020.

[174] V. J. Inglezakis and S. G. Poulopoulos, "Adsorption, ion exchange and catalysis," in *Adsorption, ion exchange and catalysis - Design of Operations and Environmental Applications*, 2006, pp. 31–56.

[175] V. Instruments, "Pulsed Discharge Detector Models D-2 and D-2-I Instruction Manual," *Rev 2/14.*

[176] L. Laloubère, "Réalisation d'un dispositif de génération d'iode organique en continu," *Mémoire d'ingénieur C.N.A.M.* Conservatoire national des arts et métiers, 2001.

[177] A. Karhu, "Gas phase chemistry and removal of CH3I during a severe accident," Nordisk Kernesikkerhedsforskning, 2001.

[178] G. Lugt and L. C. Scholten, “Methods used at KEMA for measuring iodine adsorption on charcoal and experiences with charcoal filters installed in a nuclear power plant,” 1973.

[179] D. Ducret, C. Galland, J. M. Maurel, and J. Vendel, “Génération continue et contrôlée d’iodure de méthyle marqué à l’iode 131, étude de faisabilité,” *SERAC/LECEV/92-26*, 1992.

[180] D. H. F. Atkins and G. M. Arkell, *The preparation of radioiodine labelled methyl iodide by an exchange process*. Health Physics and Medical Division, Atomic Energy Research Establishment, 1965.

[181] L.-M. Sun, “Perméation gazeuse,” *Tech. Ingénieur*, 2004.

[182] G. D. Mitchell, “A review of permeation tubes and permeators,” *Sep. Purif. Methods*, vol. 29, no. 1, pp. 119–128, 2000.

[183] R. M. Barrer, *Diffusion in and through Solids*. Cambridge University Press, 1941.

[184] C. Monsanglant-louvet, M. Chebbi, B. Marcillaud, and A. Roynette, “Synthèse des travaux effectués par l’IMT/Atlantique et l’IRSN/SCA sur la rétention de l’iodure de méthyle dans les charbons actifs,” *IRSN 2019-00733*, pp. 1–48, 2019.

[185] F. Ambroz, T. J. Macdonald, V. Martis, and I. P. Parkin, “Evaluation of the BET Theory for the Characterization of Meso and Microporous MOFs,” *Small Methods*, vol. 2, no. 11, p. 1800173, 2018.

[186] LNHB, “Iodine-131 - Emissions and decay scheme,” *Lab. Natl. Henri Becquerel*, 2021.

[187] B. Marcillaud and C. Monsanglant-louvet, “Optimisation de la chromatographie en phase gazeuse pour l’analyse de l’iodure de méthyle non-radioactif,” *IRSN 2017-00123*, 2017.

[188] J. E. Lovelock, R. J. Maggs, and R. J. Wade, “Halogenated hydrocarbons in and over the Atlantic,” *Nature*, vol. 241, no. 5386, pp. 194–196, 1973.

[189] W. E. Wentworth, Y. Wang, W. Odegard, E. C. M. Chen, and S. D. Stearns, “Pulsed-discharge electron-capture detector: Kinetic model, response factors, and temperature dependence,” *J. Chromatogr. Sci.*, vol. 34, no. 8, pp. 368–375, 1996.

[190] LNHB, “Barium-133 - Emissions and decay scheme,” *Lab. Natl. Henri Becquerel*, 2021.

[191] C. A. Kalfas, M. Axiotis, and C. Tsabaris, “SPECTRW: a software package for nuclear and atomic spectroscopy,” *Nucl. Instruments Methods Phys. Res. Sect. A Accel. Spectrometers, Detect. Assoc. Equip.*, vol. 830, pp. 265–274, 2016.

[192] D. J. Wren and A. C. Vikis, “Vapour Pressure of CH3I in the temperature range 176 to 227 K,” *J. Chem. Thermodyn.*, vol. 14, no. 5, pp. 435–437, 1982.

[193] U. Osha, “Globally harmonized system of classification and labelling of chemicals (GHS),” *J United Nations Econ. Comm. Eur.*, vol. 224, 2013.

[194] ILO-WHO, “Methyl iodide,” *Int. Chem. Saf. Cards (ICSC 0509)*, 2012.

[195] J. Kestin, M. Sokolov, and W. A. Wakeham, “Viscosity of liquid water in the range −8°C to 150°C,”

J. Phys. Chem. Ref. Data, vol. 7, no. 3, pp. 941–948, 1978.

Appendix

Appendix 1. Summary of the homemade AC impregnation / extraction protocols and results

Table S1. Summary of the impregnation and extraction protocols for activated carbons

	AC quantity (g)	Solvent type	Duration
Impregnation	5	200 mL of aqueous TEDA solution (5000 $m \cdot L^{-1}$)	overnight
		200 mL of aqueous KI solution (2000 $m \cdot L^{-1}$)	
Extraction	0.5	100 mL of acetonitrile	overnight

Table S2. Results of the impregnation-extraction

	Impregnation ratio	Measured impregnation ratio			Average	Efficiency
KI impregnated AC	0.68%	0.66%	0.68%	0.66%	0.67%	98.5%
TEDA impregnated AC	7.16%	7.31%	6.70%	6.23%	6.74%	94.2%

Appendix 2. Yellow coloration during KI extraction

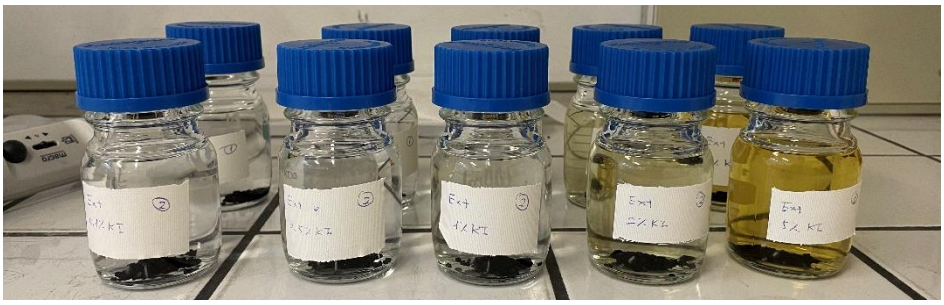

Figure S1. Yellow coloration during KI extraction (KI concentration increases from left to right)

Appendix 3. Example of the KI and TEDA concentration determination for co-impregnated AC

Supposing the calibration equations for KI:

- λ = 225 nm, absorbance = y1 (concentration)

- λ = 247 nm, absorbance = y2 (concentration)

Supposing the calibration equations for TEDA:

- λ = 225 nm, absorbance = y3 (concentration)
- λ = 247 nm, absorbance = y4 (concentration)

The equations y2 and y3 are already presented in Chapter II 3.1. Examples of y1 and y4 are presented in the Figure S2.

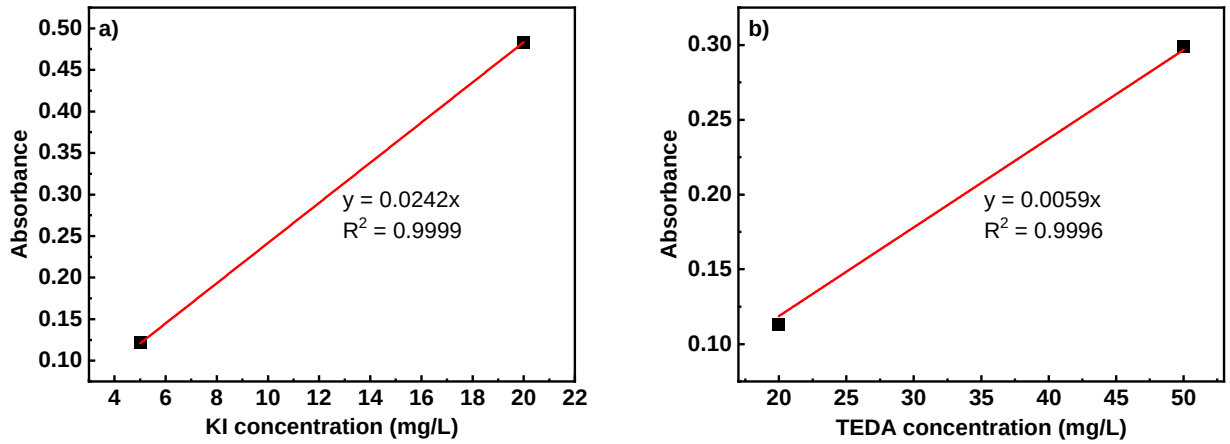

Figure S2. (a) Calibration for KI at 225 nm (y1); (b) Calibration for TEDA at 247 nm (y4)

For a given co-impregnated AC, the absorbances at λ = 225 and 247 nm are measured to be h1 and h2, respectively. Supposing the KI and TEDA concentration for this co-impregnated AC in the solution are a and b mg/L respectively. Then we have:

- a/y2 + b/y3 = h1
- a/y1 + b/y4 = h2

Here, only a and b are unknown. Solving these two equations allows to determine a and b simultaneously.

Appendix 4. N_2 adsorption isotherms for 0.5% KI AC

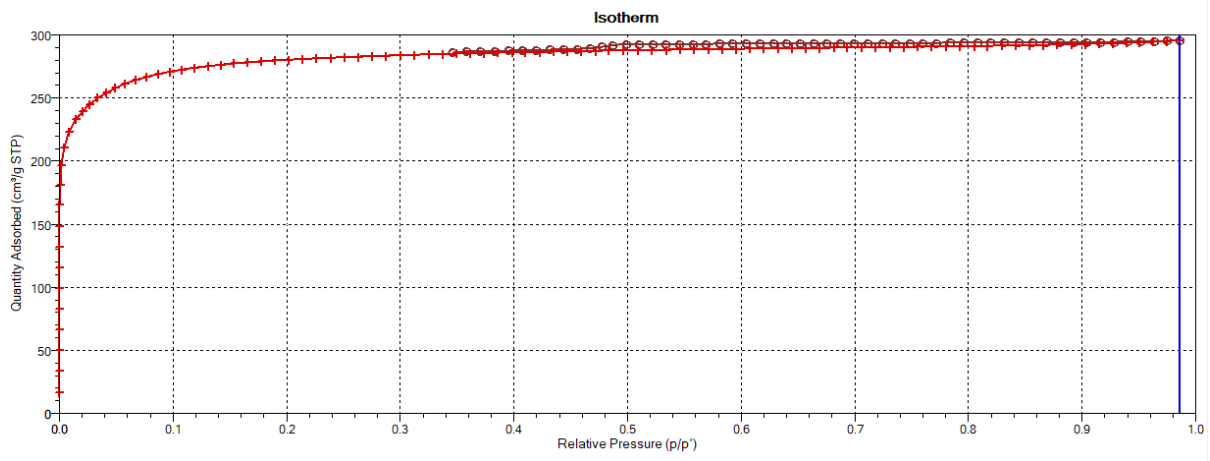

Figure S3. Example of N_2 adsorption isotherms for 0.5% KI AC

Appendix 5. Complementary information about the BET theory

The BET theory describes the multilayer adsorption phenomena which is based on the Langmuir isotherms (monolayer adsorption). The assumptions of Langmuir adsorption isotherms are recalled as follow [55]:

- the adsorbed gas is considered as a perfect gas;
- the maximum adsorption corresponds to a monolayer covering of the surface;
- the adsorbent surface is energetically homogeneous;
- interactions between adsorbed molecules are negligible;
- migration phenomena between adsorption sites are neglected.

As an extension of the Langmuir isotherms, the BET theory considers that [185][144]:

- the solid surface is homogenous and has localized sites;
- gas molecules only interact with adjacent layers;
- the Langmuir theory is applied to the first layer, and gas condensation to liquid phase is applied since the second layer;

- the enthalpy of adsorption for the first layer is constant and greater than the second (and higher) layer.
- the enthalpy of adsorption for the second (and higher) layers is the same as the enthalpy of liquefaction.

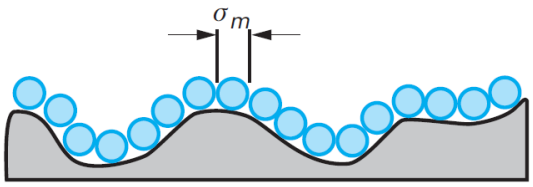

Figure S4. Principle of measuring the specific surface area of an adsorbent [48]

Appendix 6. Example of micropore size distribution for 0.5% KI AC

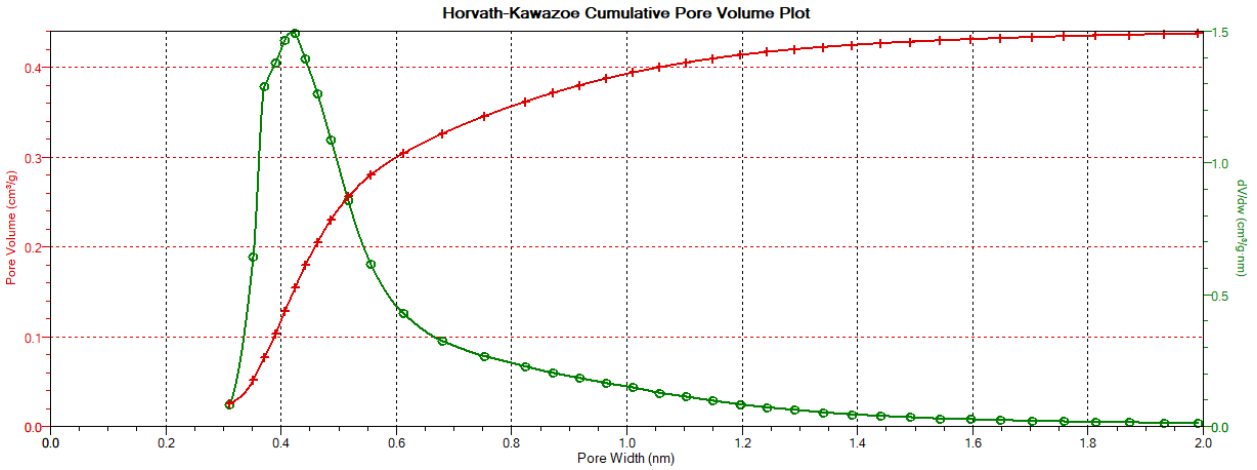

Figure S5. Example of micropore size distribution for 0.5% KI AC

Appendix 7. X-ray photoelectron spectroscopy (XPS)

The data were recorded under ultra-high vacuum using a Resolve 120 hemispherical electron analyzer (PSP Vacuum) and an unmonochromatized X-ray source (Mg Kα at 1253.6 eV, PSP Vacuum) operated at 100 W at an incidence angle of 30° with respect to the analyzer axis. This X-ray excitation energy and detection geometry correspond to an analyzed depth of about 1 nm at the C1s and O1s lines. Survey spectra were collected at pass energy of 50 eV and an energy step

of 0.2 eV. The other lines were collected at 20 eV pass energy (C1s and O1s) and 50 eV (N1s, K1s, I3d, for they are of low intensity, and an increased pass energy increases the transmission), and a step of 0.1 eV. The XPS lines were deconvoluted with the CasaXPS program, after Shirley-type or linear background subtraction. Quantitative estimations of the samples composition were done after correction by the relative sensitivity factors (RSF) provided in the program.

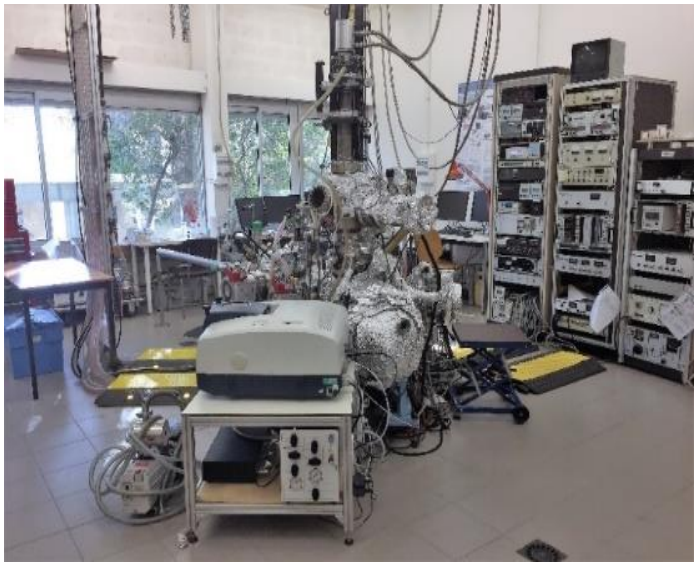

Figure S6. The SUMO experimental setup

Appendix 8. Scanning Electron Microscopy (SEM/EDX)

The scanning electron micrographs as well as the EDX analysis were carried out using a scanning electron microscope (JEOL JSM-7900F) at 15 kV. Energy dispersive X-ray spectroscopy (EDX) were carried out in selected areas of the different samples observed in SEM at 15kV with a Si-Li detector Xflash 6/60 (Brucker AXS Microanalysis GmbH Berlin, Germany).

Appendix 9. X-ray diffraction (XRD)

The XRD experiments were carried out using a device mounted on a Rigaku RU-200BH high-gloss rotating Cu anode. A reflective focusing optic (OSMIC) mainly transmits the Cu Kα radiation (λ = 1.5418Å) and a very small part of the Kβ, the latter being absorbed completely by a

Ni filter. The detector used is 2D, flat image type, model Mar345. For these measurements, the working power was 50 kV and 50 mA and the beam size was 0.5 x 0.5 mm^2. XRD patterns were collected from quartz capillary containing crushed samples.

Appendix 10. Comparison between CHNS analysis and the acetonitrile extraction for the TEDA content determination

Table S3. Comparison between CHNS analysis and acetonitrile extraction for TEDA content determination (k=2)

AC type	CHNS analysis				Acetonitrile extraction
	C w.t%	H w.t%	N w.t%	TEDA w.t%	TEDA w.t%
Unimpregnated	92 ± 4.8	0.40 ± 0.07	< LD	< LD	< LD
3% TEDA	90 ± 6.4	0.74 ± 0.16	1.0 ± 0.17	4.0 ± 0.68	2.2 ± 0.19
7% TEDA	89 ± 3.0	1.05 ± 0.14	1.7 ± 0.14	7.0 ± 0.55	5.5 ± 0.52
0.5%KI + 5%TEDA	88 ± 5.7	0.89 ± 0.15	1.3 ± 0.22	5.3 ± 0.87	3.7
0.5%KI + 10%TEDA	85 ± 7.2	1.33 ± 0.21	2.3 ± 0.36	9.2 ± 1.5	7.1
2%KI + 5%TEDA	87 ± 2.3	0.89 ± 0.04	1.4 ± 0.08	5.4 ± 0.33	4.7

* S w.t% is found to be < LD for all the tested AC

Appendix 11. XPS C1s and O1s speciation for some AC

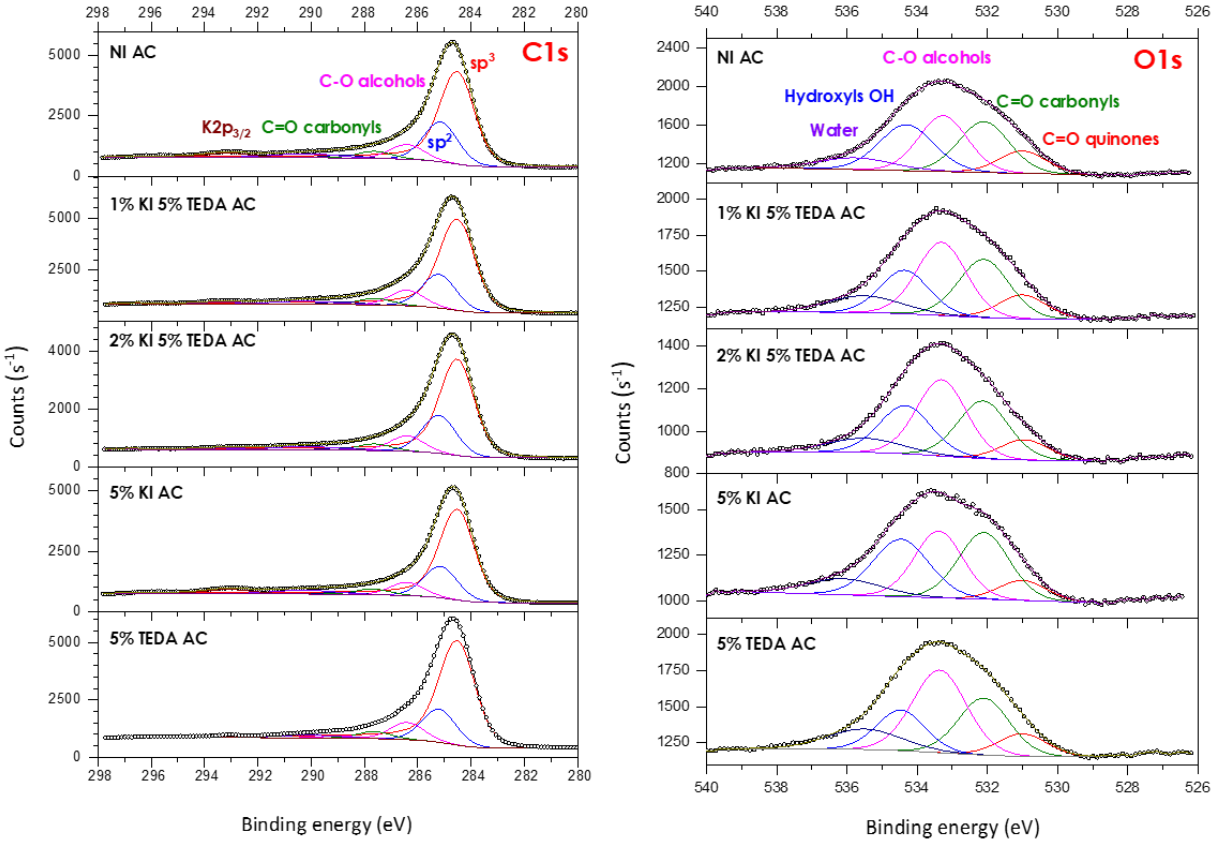

Figure S7. XPS C1s and O1s speciation for some AC

Appendix 12. XRD patterns for some AC

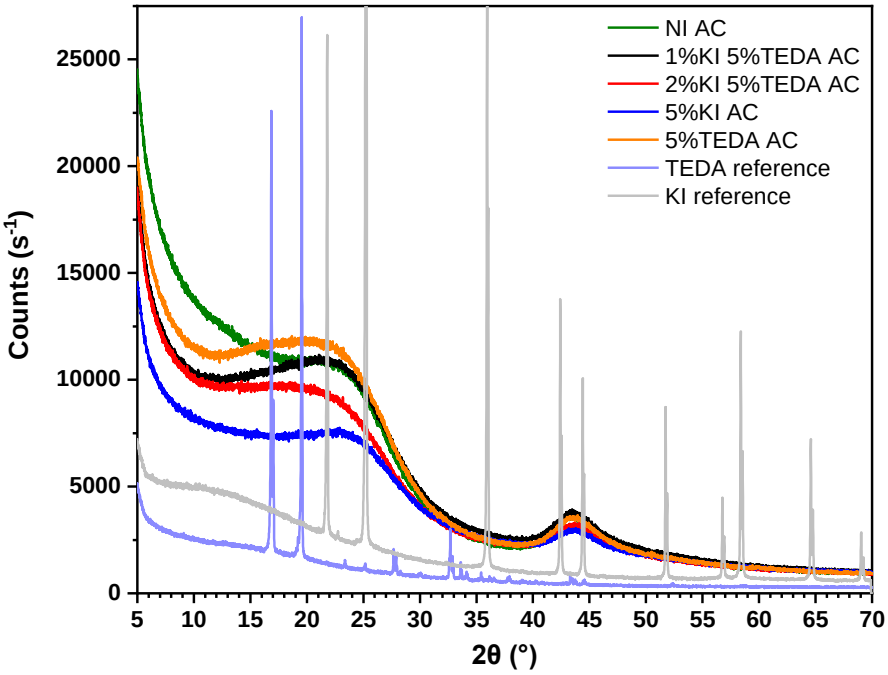

Figure S8. XRD patterns for some AC

Appendix 13. Elemental analysis EDX *vs* XPS

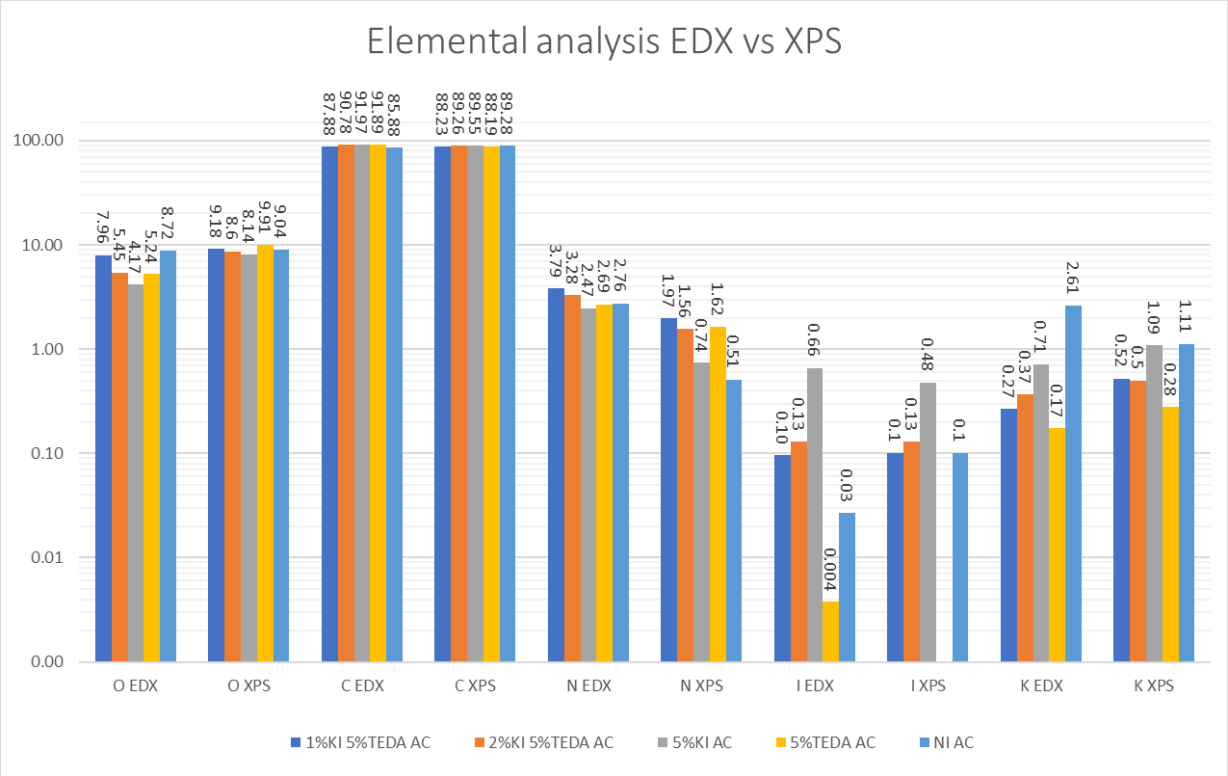

Figure S9. Elemental analysis EDX *vs* XPS

Appendix 14. General scheme of ^{131}I radioactive decay

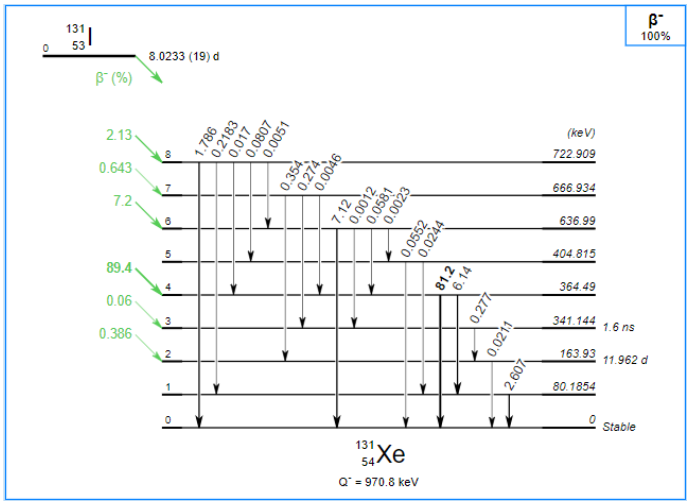

Figure S10. General scheme of ^{131}I radioactive decay [186]

Appendix 15. Determination of the uncertainty of the net counting surface u(N)

The net counting surface *N* is associated with an absolute uncertainty u(N) using Gauss distribution expressed as follow:

$$u(N) = k \times \sqrt{N} \tag{38}$$

k = 2 or 3 corresponds to the confidence levels of 95% or 99.7%, respectively. Hence the relative uncertainty of N is derived:

$$\frac{u(N)}{N} = \frac{k \times \sqrt{N}}{N} = \frac{k}{\sqrt{N}} \tag{39}$$

It can be deduced that a relative uncertainty of 2% can be obtained for N = 10000 (k = 2). More particularly, the counting rate n (s^{-1}) is defined as follows:

$$n = \frac{N}{t} \tag{40}$$

The relative uncertainty of *N* can be reformulated as:

$$\frac{u(N)}{N} = \frac{k}{\sqrt{N}} = \frac{k}{\sqrt{n \times t}} \tag{41}$$

It can be concluded that a large net counting surface N = n × t allows to reduce its relative uncertainty. An example of the AC activity measurement is presented in Table S4. In practice, a measurement time of 10 minutes is sufficient for the upstream AC considering its high net counting rate n. On the contrary, the n for the downstream AC is much lower. The solution is to extend the measurement time in order to improve the measurement quality by increasing N.

Table S4. Example of the AC activity measurements for the retention test at (T = 20 °C, RH = 40 %)

AC type		n (s^{-1})	t (s)	N	u(N)/N	Activity (Bq)
KI impregnation	Upstream	889	667	593021	0.26%	376000
	Downstream	4.64	2408	11166	1.9%	188.5
TEDA impregnation	Upstream	930	677	629358	0.25%	401700
	Downstream	0.103	14440	1483	5.2%	4.161

Appendix 16. AC standard preparation and γ spectrometry calibration

The protocol of the AC standard preparation is developed within the LECEV laboratory (Figure S11): a radioactive NaI solution with a known activity is deposited in the AC standard (fixed mass) using a "micro bottle" to soak it homogenously. Then, a drying step is performed overnight at ambient temperature to ensure the fixation of radioactive iodine within the AC sample. An agitation is performed afterwards in order to ensure the homogenization of the activity within the sample. Finally, the AC standard is placed in the same Teflon bottle as the tested AC. During the calibration, the prepared AC standard is placed in front of the γ spectrometer using the same measurement configuration. The net counting surface at 364.5 keV is recorded, and the detection efficiency η is calculated through the following expression:

$$\eta(E) = \frac{N(E)}{A \times I(E) \times t} \tag{42}$$

Where A activity of the AC standard (Bq);
$N(E)$ total net counting of the peak area at the given energy;
$\eta(E)$ detection efficiency at the given energy;
$I(E)$ emission abundance of the measured radionuclide at the given energy (%);
t measurement time (s).

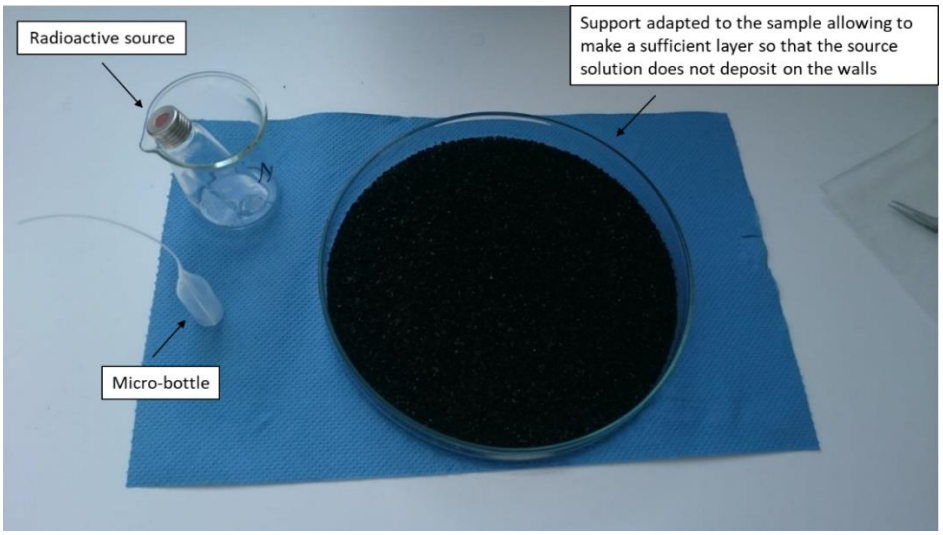

Figure S11. Material necessary for the distribution of the radioactive source

It should be noticed that the background noise of the facility room is already measured and subtracted during the efficiency measurement. Besides, the AC standard is measured four times using the same counting time and different positions. This precaution was carried out in order to take into account the potential inhomogeneity of the deposited radioactivity within the prepared AC standard. The uncertainty of the detection efficiency u(η) is also calculated during calibration. More precisely, the activity of the AC standards is expressed as:

$$A_{standard} = A_{massive}(m_i - m_f) \tag{43}$$

Where $A_{standard}$ activity of the AC standard (Bq);
$A_{massive}$ massive activity of the radioactive solution (Bq/g);
m_i initial mass of the micro bottle (g);
m_f final mass of the micro bottle (g).

The associated uncertainty of the AC standard activity is calculated using the following relationship:

$$\frac{u(A_{standard})}{A_{standard}} = \sqrt{\left(\frac{u(A_{massive})}{A_{massive}}\right)^2 + \frac{u(m_i)^2 + u(m_f)^2}{(m_i - m_f)^2}} \tag{44}$$

Where $u(A_{standard})$ uncertainty of the activity of the AC standard;
$u(A_{massive})$ uncertainty of the massive activity of the radioactive source solution;
$u(m_i)$ uncertainty of the initial micro bottle mass;
$u(m_f)$ uncertainty of the final micro bottle mass.

The associated uncertainty of the detection efficiency u(η) is calculated according to the following relationship considering the uncertainties of the time and the emission abundance are negligeable:

$$\frac{u(\eta)}{\eta} = \sqrt{\left(\frac{u(N)}{N}\right)^2 + \left(\frac{u_{standard}}{A_{standard}}\right)^2} \quad (45)$$

The radioactive NaI solution used for the AC standard preparation was made from the *Curium* enterprise. It should be noted that this enterprise does not provide the calibration certificates with the corresponding uncertainty, making it difficult to evaluate u(η). Here, u(η)/η is manually set to 10% (k = 2) for all the calibrations. For each configuration, the detection efficiency of the γ spectrometry is summarized in the Table S5.

Table S5. Summary of detection efficiencies for each configuration (k = 2)

Configurations	Efficiency	Uncertainty
d = 0 cm	0,030767	10%
d = 10 cm	0,0032469	10%

In Chapter III, the uncertainty of the DF by repetitions is evaluated by determining the standard error of the mean. In practice, precautions are made in order to improve the measurement quality (minimize the uncertainty of the activity measurement). For a given activity measurement A, the uncertainty of the activity u(A) (k = 2) is expressed as:

$$\frac{u(A)}{A} = \sqrt{\left(\frac{u(N)}{N}\right)^2 + \left(\frac{u(\eta)}{\eta}\right)^2} = \sqrt{\frac{2}{N} + (10\%)^2} \quad (46)$$

In practice, a u(A)/A around 10% can be considered a precise activity measurement (for $N \geq 10000$, k = 2). Accordingly, the uncertainty of the DF can be expressed as follow:

$$\frac{u(DF)}{DF} = \sqrt{\frac{u^2(A_{upstream}) + u^2(A_{downstream})}{(A_{upstream} + A_{downstream})^2} + \frac{u^2(A_{downstream})}{A_{downstream}^2}}$$
$$\approx \sqrt{\left(\frac{u(A_{upstream})}{A_{upstream}}\right)^2 + \left(\frac{u(A_{downstream})}{A_{downstream}}\right)^2} \quad (47)$$

Hence, a u(DF)/DF around 14% is recommended in this manuscript for a precise DF measurement.

Appendix 17. General scheme of the GC

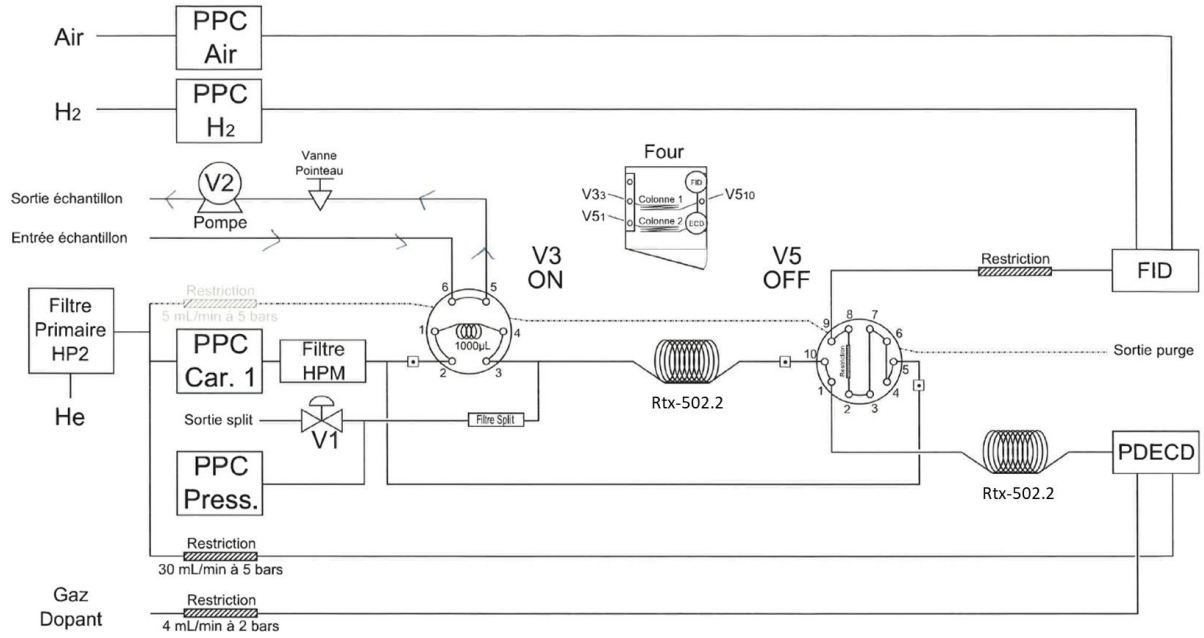

Figure S12. General scheme of the GC (*Clarus 680*) [187]

Appendix 18. Example of a chromatogram for CH_3I

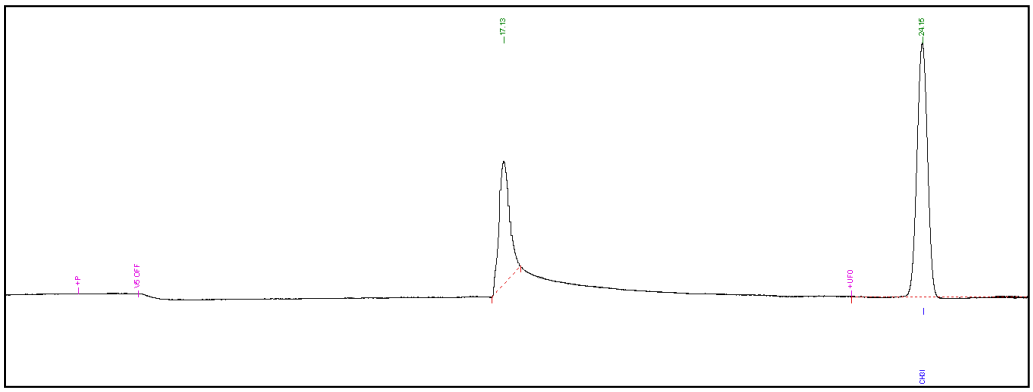

Figure S13. Example of a chromatogram ([CH_3I] around 50 ppbv)

Appendix 19. PDECD

The rationale for investigating into the potential of non-radioactive iodomethane to test iodine traps — especially impregnated activated carbon — relies on the possibility to detect quantitatively $CH_3{}^{127}I$ by gas chromatography at concentrations as low as 1 ppt, its mean concentration in marine air [188], and at still lower concentrations if the air sample is preconcentrated. Such a performance can be achieved by the Electron Capture Detector (ECD).

The main drawback of the ECD is the incorporation of a radioactive substance (*e.g.*, 500 MBq of ^{63}Ni) as the source of free electrons — the β^- particles (< 67 keV) which are thermalized (10^{-2} eV to 10^{-1} eV) by collision with neutrals in the detector, a process that yields near thermal secondary electrons. These electrons are then collected, under a bias voltage of a few tens of volts, by an anode which provides the standing current (*e.g.*, 30 nA) of the detector considered as an ionization chamber.

When electrons attach to an electrophilic gaseous substance in the detector volume (< 1 mL), the standing current is lowered. It is quantified and linearized as the output of the detector (the polarity is reversed by the amplifier). The rate of electron attachment is particularly fast for compounds such as CCl_4, SF_6, $CFCl_3$ (CFC-11) and CH_3I, which makes the ECD extremely sensitive to these gases (mostly by dissociative electron capture).

In the PDECD (Pulsed Discharge ECD), the ionization source is a high voltage (20 kV) discharge in a flow (30 mL/min) of ultra-pure helium which radiates a very short wavelength (< 100 nm) — *i.e.*, ionizing — UV light (Hopfield emission) together with free electrons. Discharge is pulsed (3 kHz) with a comparatively long interval between pulses (300 µs), which allows cooling of the discharge electrodes. Photoionization of a dopant gas (3% Xe in He), fed into the detector as a counter-current gaseous "fountain" (4 $mL \cdot min^{-1}$) downstream from the discharge zone, yields the thermal electrons necessary for the high electron affinity compounds detection. Sample is injected into the detector from the chromatographic column outlet, downstream from the ionization zone (dopant gas outlet).

The sensitivity of the PDECD to most compounds with high electron affinity (*e.g.*, halogenated organic molecules) is basically equal to the sensitivity of the conventional radioactive ECD. However, electron capture coefficient of methyl iodide is a hundredfold higher with PDECD than with conventional ^{63}Ni ECD [189].

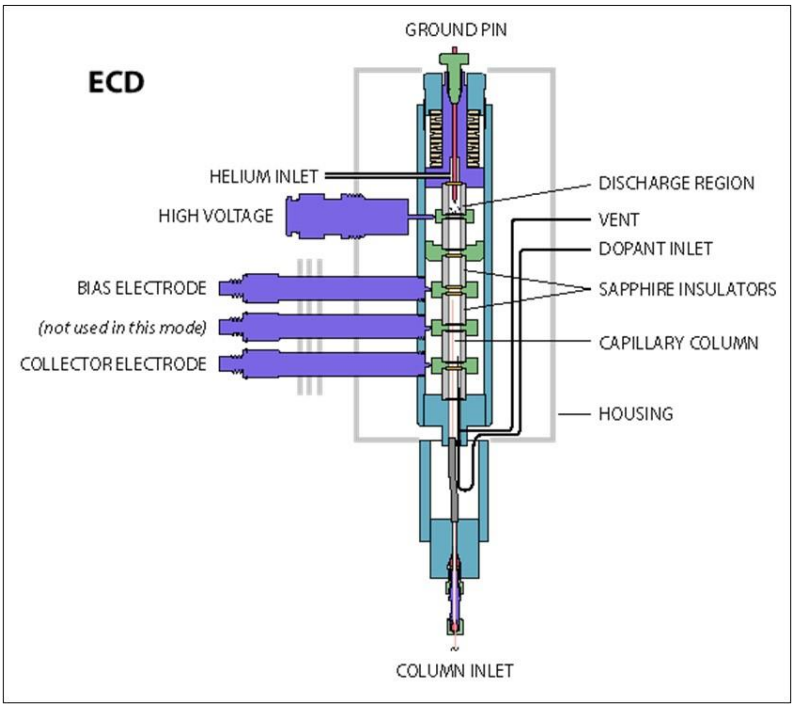

Figure S14. Cross-section of the Pulsed Discharge Electron Capture Detector (PDECD) (in this drawing, the dopant tubing inside the detector is erroneously shorter than the capillary column. See [175])

Appendix 20. Calibration of the cartridge for the γ spectrometry

A commercial cartridge standard calibrated by ^{133}Ba instead of ^{131}I is used (Figure S15) with the similar calibration protocols as previously described in the chapter III for the DF measurements. The ^{133}Ba is chosen to calibrate ^{131}I for two reasons: the first reason is that ^{133}Ba is more stable than ^{131}I with a half-life of 10.51 years. The second reason is that the main γ emission of ^{133}Ba is at 356 keV according to the ^{133}Ba radioactive decay as depicted in Figure S16, which is close to that of ^{131}I (364.5 keV). Hence, the difference of the detection efficiency between 356 keV and 364.5 keV can be considered negligible (Figure S17). For each measurement configuration, the detection efficiency of the γ spectrometry for the commercial cartridge is summarized in Table S6.

Table S6. Summary of detection efficiencies for each configuration (commercial cartridge)

Configurations	d = 0 cm	d = 10 cm	d = 20 cm
Efficiency	0.031139	0.003668	0.001293

Figure S15. Photo of the commercial cartridge standard

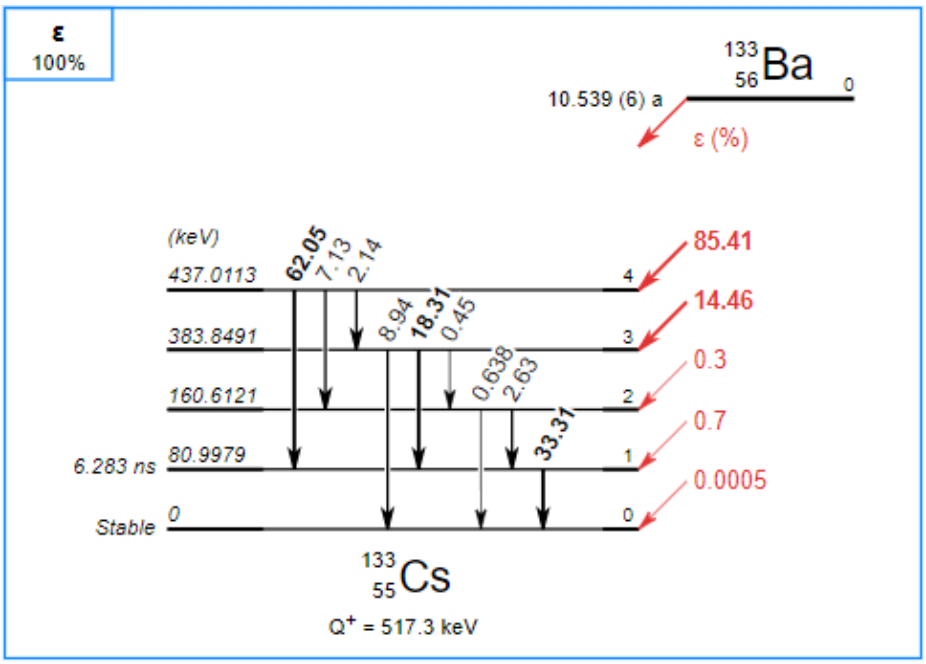

Figure S16. General scheme of ^{133}Ba Radioactive decay [190]

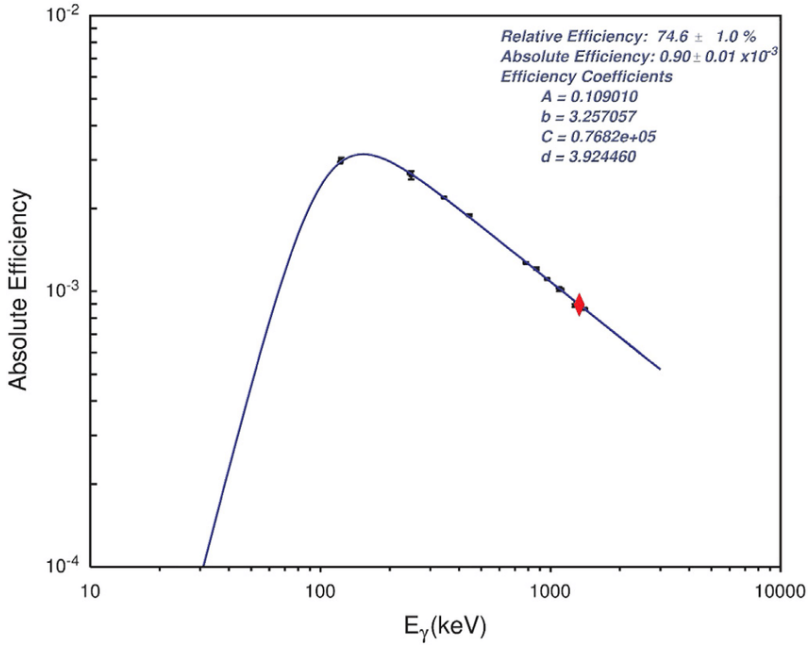

Figure S17. Absolute efficiency curve of an HPGe detector [191]

Appendix 21. Original experimental protocols for the isotopic exchange reaction [176]

- Add 200 µL of radioactive NaI/NaOH solution (4M Bq) into a glass bottle;
- Add 200 µL of acetone into the glass bottle of step 1;
- Add 1 mL of methyl iodide (99% of purity) into the glass bottle of step 2;
- Strong stirring for 15 min;
- Add 8 mL of distilled water into the glass bottle containing the mixture;
- Slight stirring in hand for 20-30 seconds;
- Decantation for several minutes;
- Extract the denser part of the solution using a syringe.

Appendix 22. Optimization of the experimental protocols of the isotopic exchange reaction

1. Preliminary operating mode characterization

Summary of the L. Laloubère's operating mode

The optimization of the radioactive CH_3I labeling efficiency is based on the operating mode proposed by L. Laloubère [176]. This operating mode has been successfully tested in the EPICEA installation [176]. However, it should be noticed that this operating mode was devoted to his specific experimentation. Hence, a preliminary characterization of this protocol is required before a further optimization dedicated for our studies.

Preparation of the isotopic exchange experiments

Before launching the first experience, safety analyses are performed in the laboratory. This isotopic exchange reaction contains both radiologic risks (^{131}I) and chemical risks (strong volatility for CH_3I: vapor pressure of 54.4 kPa at 20 °C [192] as well as strong toxicity [193]). In addition, the final product γ-labelled CH_3I is both radioactive and very volatile. In consequence, a special fume hood dedicated to this experiment is designed (Figure S18) which contains sufficient lead bricks and a ventilation system to ensure the operators' radioprotection and to prevent chemical risks.

Figure S18. Fume hood dedicated to isotopic labeling of CH_3I

The radioactive NaI solution used is a commercial $Na^{131}I$ solution (*Curium*) with a total volume of 3 mL and a total activity of 111 MBq for a given referenced date. The theoretical volume of the NaI solution for each isotopic exchange experiment is calculated knowing the desired final activity of $CH_3{}^{131}I$ and the decay law of ^{131}I. Due to the radioactive decay of ^{131}I, the needed volume of the NaI solution for a given activity varies according to the experiment date. The volume range of the employed radioactive NaI solution is between 300 and 600 µL during our experiments.

Our first approach for the optimization is to verify the operating mode of L. Laloubère by keeping the same experimental conditions as much as possible. However, the activity of $Na^{131}I$ solution is reduced to about 400 kBq during our first preliminary studies. Besides, the mass of each constituent added is measured due to CH_3I volatility. The activity of the initial $Na^{131}I$ solution and the final γ-labelled CH_3I are also measured by γ-spectrometry. Unlike the activity measurement described in Chapter III where the activity of the upstream AC is up to 4×10^5 Bq, the initial activity can reach 10 MBq during these studies. Hence, modifications of measurement conditions are made in order not to saturate the γ-spectrometer. Different lead supports are used during the activity measurement (Figure S19) and the measurement distance d is also varied. Table S7 summarizes the results of the γ-spectrometry calibration for each configuration.

Figure S19. Different lead supports with different thickness for activity measurements

Table S7. Summary of detection efficiencies for each configuration

	d = 10 cm	d = 20 cm	d = 30 cm
Blue support	0.000500056	0.000180967	0.000092133
White support	0.000103245	0.000036345	0.000018862

During experiments, an obvious leakage of the pipette after extracting the methyl iodide is noticed. This can be explained by its low kinematic viscosity (0.18 $mm^2 \cdot s^{-1}$ at 40 °C) [194]. For comparison, the kinematic viscosity of water is about 0.66 $mm^2 \cdot s^{-1}$ at 40 °C [195]. Besides, CH_3I has a high density (2.28 $g \cdot cm^{-3}$). Hence, the use of pipette is not possible for methyl iodide uptake during the experiment. Our solution is to use a specially "cut" syringe needle (Figure S20) to extract methyl iodide. The objective of the cutting is to prevent the potential contamination of the operator from piercing.

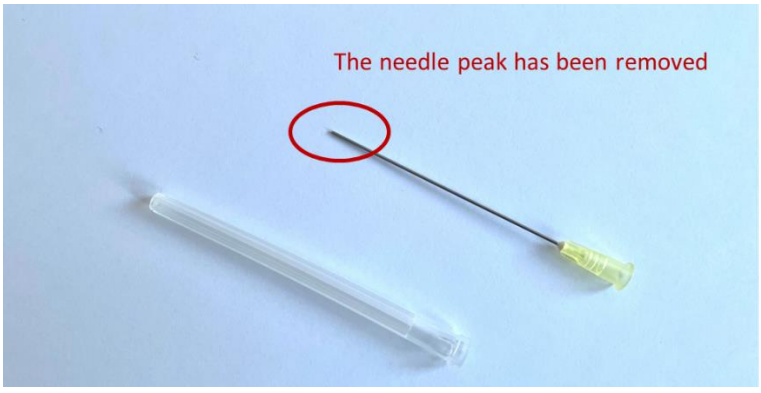

Figure S20. Example of a specially cut syringe needle

Preliminary results of radioactive CH_3I labeling efficiency

The preliminary tests were performed through the following protocols:

1. Add 400 kBq of radioactive NaI solution (total NaI concentration of 2g/L, and a volume range between 300 and 400 µL) into a glass bottle;
2. Measure the initial $Na^{131}I$ solution mass and activity;
3. Add 200 µL of acetone into the glass bottle of step 1 and measure its mass;
4. Add 1 mL of methyl iodide (99% pure) into the glass bottle of step 2 using a syringe and measure its mass;
5. Strong stirring for 15 min;
6. Add 8 mL of distilled water into the glass bottle containing the mixture and measure its mass;
7. Slight stirring in hand for 20-30 seconds;
8. Decantation for 5 minutes;
9. Extract the denser part of the solution using a syringe and measure its mass;
10. Measure the final CH_3I* activity and the residue activity.

The test is done twice and the results of isotopic exchange efficiencies are summarized in Table S8.

Table S8. Summary of the preliminary tests

Test n°	$Na^{131}I$ activity (kBq)	Final $CH_3{}^{131}I$ activity (kBq)	Efficiency (%)	Residue activity (kBq)	Residue percentage (%)	Lost percentage (%)
1	254	20	7.9%	219	86.2%	5.9%
2	416	28	6.7%	368	88.5%	4.8%

Here the isotopic exchange efficiency, the residue percentage and the lost percentage are defined as follow:

$$Efficiency = \frac{final\ CH_3^{131}I\ activity}{initial\ Na^{131}I\ activity} \times 100\% \quad (48)$$

$$Residue\ percentage = \frac{residue\ activity}{initial\ Na^{131}I\ activity} \times 100\% \quad (49)$$

$$Loss\ percentage = \left(1 - \frac{final\ CH_3^{131}I\ activity + residue\ activity}{initial\ Na^{131}I\ activity}\right) \times 100\% \qquad (50)$$

The isotopic exchange efficiency calculated is much lower than that of Laloubère's (76% ± 5%). The origin of this low efficiency does not come from the activity loss during manipulation since the lost percentage is only about 5%. The difference of the isotopic exchange efficiency can probably be explained by the different quantities of $Na^{131}I$. Here, the activity of $Na^{131}I$ is reduced from 4 MBq to 400 kBq. According to Le Chatelier's principle, the reduction of the reactant concentration ($Na^{131}I$) will shift the reaction equilibrium to the left side, meaning the reduction of the $CH_3{}^{131}I$ concentration. Hence the isotopic exchange efficiency is expected to decrease.

In the following parts, the radioactive CH_3I labeling efficiency is optimized through different parameters: the quantity of the solvent or reactant, the effect of decantation, etc.

2. Optimization of the radioactive CH_3I labeling efficiency

In this part, the optimization of the isotopic exchange efficiency will focus on the effect of the solvent (acetone), the reactant ($Na^{131}I$), the decantation process (H_2O) and the reaction duration (agitation). These effects take into account the main parameters governing the isotopic exchange reaction.

Effect of acetone

The low radioactive CH_3I labeling efficiency of the preliminary test is due to the reduction of reactant concentration of $Na^{131}I$. Before increasing the $Na^{131}I$ activity to increase the efficiency, it is important to further investigate the role of acetone as a solvent. The effect of acetone may give insights on other ways to increase the isotopic exchange efficiency. Hence, the first step of the optimization is to investigate the effect of acetone in order to explicit the relation between the isotopic exchange efficiency and the quantity of acetone. The effect of acetone is investigated by keeping the same conditions of the preliminary test except for the acetone quantity. The acetone quantity is varied and the results are presented in Figure S21.

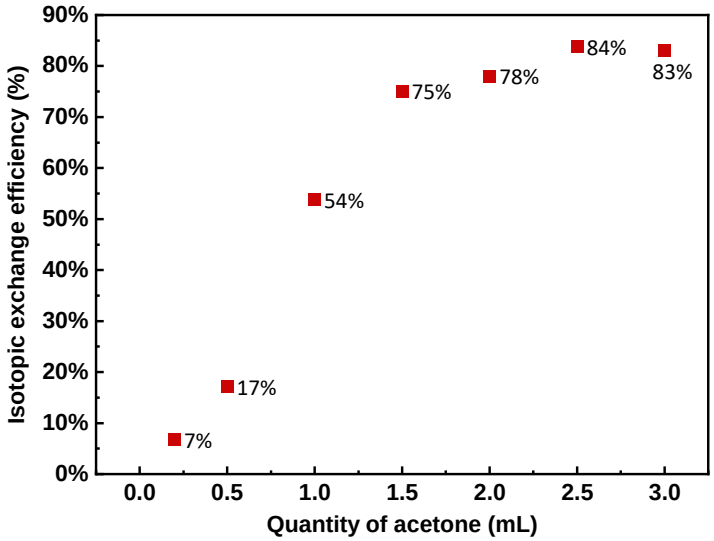

Figure S21. Evolution of the isotopic exchange efficiency versus the quantity of acetone ($Na^{131}I$ = 400 kBq, $V(H_2O)$ = 8 mL, 15 min of stirring)

The isotopic efficiency increases with the acetone quantity then reaches an equilibrium (above 80%) with 2 mL of acetone. The increase of the isotopic exchange reaction efficiency indicates that the reaction equilibrium shifts to the right side since the reactant quantities ($Na^{131}I$ and CH_3I) and other parameters are the same. It can be concluded that the change of the reaction equilibrium is due to the increase of the acetone quantity. Combined with the aforementioned dissociation theory of L. Laloubère, we propose that the acetone promotes the isotopic exchange reaction by facilitating the dissociation of CH_3I, making more CH_3I available for the isotopic exchange reaction.

In order to make sure that the increase of the efficiency with acetone is not related to the operational error, the residue activity is also measured to calculate the activity loss. The results of the activity loss are presented in Figure S22.

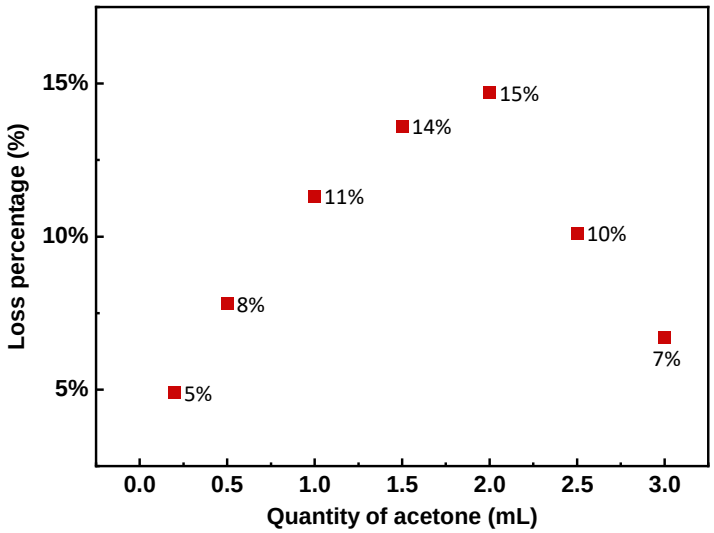

Figure S22. The evolution of the activity loss towards the quantity of acetone

The activity loss is mainly due to the evaporation of $CH_3{}^{131}I$ during manipulation, especially during the transfer of the final product $CH_3{}^{131}I$ to another glass bottle after extraction. In general, the activity loss for all the isotopic exchange experiments is always under 15%. To compare with, the activity loss by L. Laloubère was reported to be between 10% and 15% [176].

The above discussion concludes that acetone facilitates the isotopic exchange. However, a question is raised about the possibility of adding an excessive amount of acetone to ensure an optimal efficiency. This is further investigated in the next part.

Effect of H_2O

As mentioned above, after decantation process by adding distilled water, two phases are formed: the aqueous phase on top and the organic phase at the bottom (it contains mainly γ-labelled CH_3I). In fact, acetone will also be present in the final γ-labelled CH_3I. Hence, a compromise in the added amount of acetone should be find in order to ensure a good isotopic exchange efficiency but without impacting the quality of the final γ-labelled CH_3I. In the work of L.Laloubère, the quantity of acetone in the final γ-labelled CH_3I was investigated using Ultraviolet-visible spectroscopy

[176]. The acetone quantity in the final product with different distilled water quantities added is summarized in Table S9.

Table S9. Evolution of the acetone quantity in the final γ-labelled CH_3I (1 mL) with H_2O quantities (V(acetone) = 200 µL) [176]

Test n°	H_2O volume (mL)	Acetone volume found in the CH_3I*(µL)	Isotopic exchange efficiency (%)
1	2	> 100	74%
2	2.5	> 100	72%
3	5	68	68%
4	8	53	74%
5	10	59	81%

Using 8 mL of H_2O for decantation, about 50 µL of acetone is found in the final product, which is 25% of the acetone added during manipulation of L. Laloubère (200 µL acetone added). Hence, the objective of adding H_2O is not only for decantation but also to reduce the acetone quantity in the final γ-labelled CH_3I.

In the present study, the volume of the glass bottle used for the isotopic exchange is 20 mL, and the maximum volume available for H_2O is around 14 mL. The effect of H_2O towards the isotopic exchange efficiency is shown in Figure S23. It can be noticed that the isotopic exchange efficiency slightly increases with the H_2O volume. It is difficult to conclude whether the increase of the water quantity improves the separation process given the slight difference of the isotopic exchange efficiency. For our case, the acetone quantity used is more than that of L. Laloubère. Therefore, increasing the water quantity allows to decrease the acetone quantity in the final product. For the following experiments, the H_2O volume is increased to 14 mL.

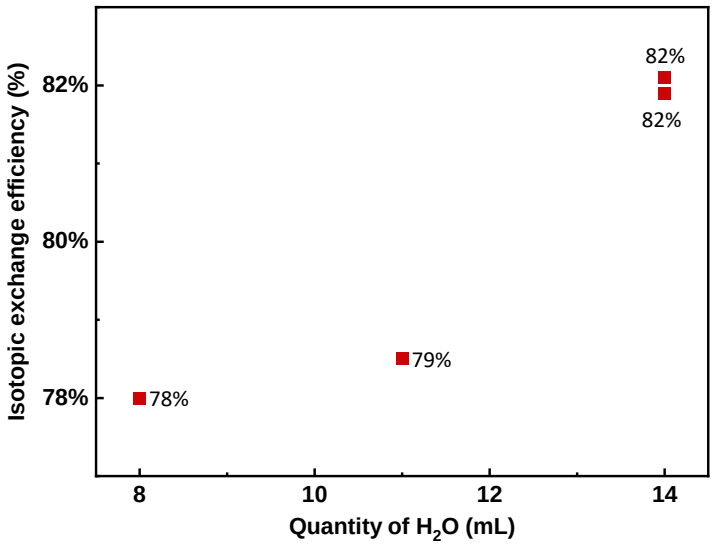

Figure S23. Evolution of isotopic exchange efficiency towards H_2O volume

Effect of $Na^{131}I$ activity

The influence of the initial $Na^{131}I$ activity is investigated using 14mL of H_2O for decantation. The results of the preliminary test show that the reduction of reactant concentration of $Na^{131}I$ leads to the diminution of the isotopic exchange efficiency. Hence, it is of great importance to investigate the effect of the initial $Na^{131}I$ activity. Different activities were tested up to 6 MBq. The associated results are presented in Figure S24.

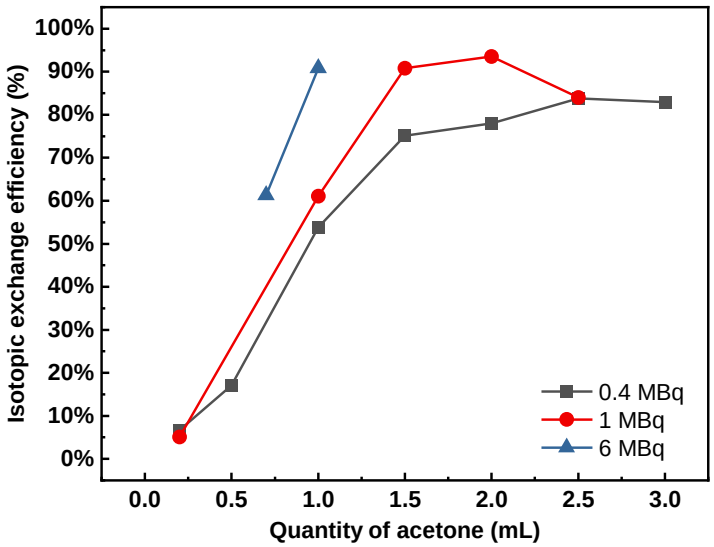

Figure S24. Isotopic exchange efficiency for different $Na^{131}I$ activities ($V(H_2O)$ = 14 mL, 15 min of stirring)

For initial activities of 0.4 and 1 MBq, a progressive increase of the isotopic exchange efficiency is observed for higher acetone volumes up to a value of about 1.5 - 2 mL. For higher acetone volumes, a plateau is obtained. It can be also noticed that the maximal efficiency is a function of the initial activity. Indeed, the best efficiency was equal to 80% and 90% for initial activities of (0.4 MBq) and (1 or 6 MBq), respectively. The relatively low efficiency at 400 kBq can be explained by the insufficient quantity of the reactant ($Na^{131}I$) as compared to CH_3I. Besides, the mass ratio of the initial stable CH_3I and final γ-labelled CH_3I is measured for each test, which is about 90%. This value justifies that the optimal isotopic exchange efficiency is about 90%. It can then be concluded that $Na^{131}I$ and acetone both facilitate the isotopic exchange, but in different ways: (i) the increase of $Na^{131}I$ activity leads to the increase of the reactant hence, the extent of reaction is also increased; (ii) the increase of the acetone creates a more favorable condition for the isotopic exchange reaction.

Effect of the stirring duration

In the work of L. Laloubère, the effect of the stirring duration was not investigated, and it was fixed at 15 min. In this part, the effect of the agitation duration is briefly investigated using 400 kBq of $Na^{131}I$ and 2 mL of acetone, and the results are presented in the Table S10.

Table S10. Evolution of the isotopic exchange efficiency versus different stirring durations

Stirring duration	15 min	60 min
Isotopic exchange efficiency	82.1%	84.3%

The isotopic exchange efficiency slightly increases versus longer stirring durations. However, this slight increase is not significant compared to the large increase of the experiment duration. Hence, the stirring duration is fixed at 15 min.

3. Summary of the protocols of γ-labelled CH_3I generation in liquid phase

The effect of different parameters related to the isotopic exchange reaction are investigated in order to reach an optimal efficiency. The volume of water is fixed at 14 mL, which is dependent on the maximum volume of the bottle. The volume of CH_3I is fixed at 1 mL due to the limited volume of the permeation tube (less than 2 mL). It is found that the isotopic exchange efficiency increases with $Na^{131}I$ activity. Indeed, the increase of the reactant concentration will shift the reaction equilibrium to the right side, leading to the increase of the final product's concentration ($CH_3{}^{131}I$). As for the effect of acetone, the increase of the efficiency with acetone indicates that it is an appropriate solvent for the isotopic exchange reaction and it facilitates the dissociation of CH_3I during the isotopic exchange reaction.

Using a $Na^{131}I$ of 10 MBq, the operating mode of our studies can be summarized as follow:

1. Add 10 MBq of radioactive NaI/NaOH solution (with a volume range between 300 and 600 µL) into a glass bottle;
2. Add 1.5 L of acetone into the glass bottle of step 1;
3. Add 1 mL of methyl iodide (99% pure) into the glass bottle of step 2 using a specially "cut" syringe;
4. Strong stirring for 15 min;
5. Add 14 mL of distilled water into the glass bottle containing the mixture;
6. Slight stirring in hand for 20-30 seconds;
7. Decantation for 5 minutes;
8. Extract the denser part of the solution using a specially "cut" syringe;
9. Measure the final γ-labelled CH_3I activity and the residue activity.

Appendix 23. Fixed bed CH_3I adsorption + desorption of 1% KI AC

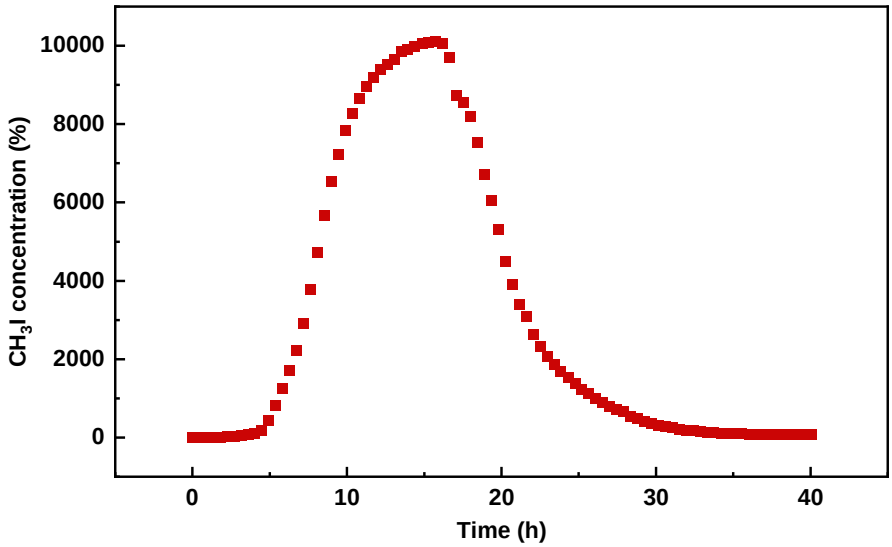

Figure S25. CH_3I adsorption + desorption of 1%KI AC

Table S11. Summary of the adsorption and desorption parameters for 1% KI AC

Adsorption	
Gas	CH_3I (10 ppmv)
Flowrate ($L \cdot min^{-1}$, NTP)	6.63
Temperature (°C)	30
Adsorption capacity ($mg \cdot g^{-1}$)	21.6
Desorption	
Gas	Air
Flowrate ($L \cdot min^{-1}$, NTP)	20
Temperature (°C)	30
Adsorption capacity ($mg \cdot g^{-1}$)	21.5

Appendix 24. Comparison of the adsorption capacity at saturation for $CH_3{}^{127}I$

Table S12. Comparison of the adsorption capacity at saturation for $CH_3{}^{127}I$

	NI	0.1% KI	0.5% KI	1% KI	2% KI	5% KI	3%TEDA	5%TEDA
Trapezoidal method	22.00	20.11	19.69	19.70	18.87	16.83	39.50	43.56
Thomas model	22.09	20.20	19.63	19.63	18.76	16.52	40.11	44.10

Appendix 25. Adsorption capacity for TEDA impregnated AC

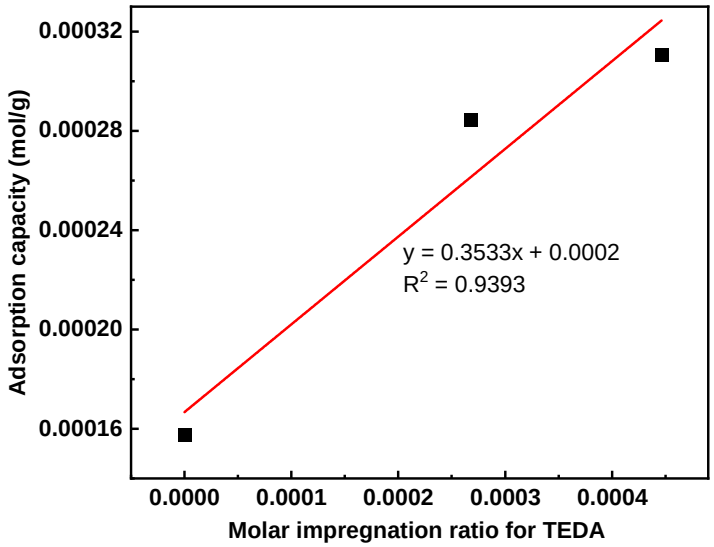

Figure S26. Adsorption capacity versus TEDA impregnation ratio

Appendix 26. Comparisons of the BTC between $CH_3{}^{127}I$ and $CH_3{}^{131}I$ for 5% TEDA AC

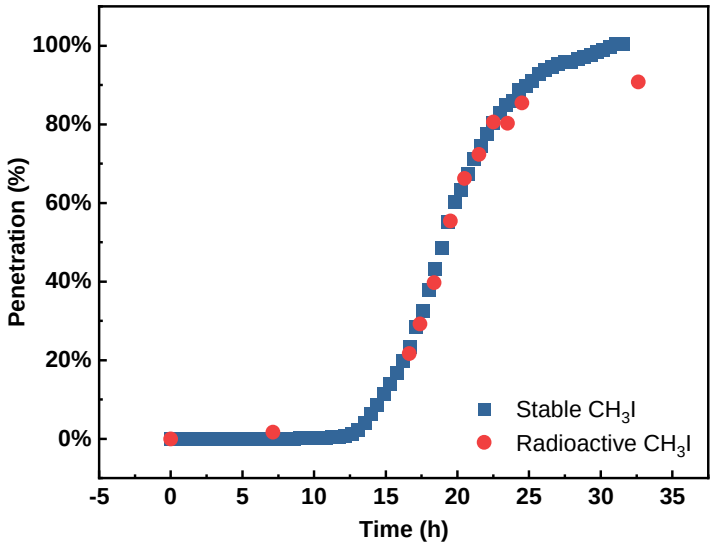

Figure S27. BTC comparisons between $CH_3{}^{127}I$ and $CH_3{}^{131}I$ for 5% TEDA AC

Résumé :
Le charbon actif (CA) de qualité nucléaire est co-imprégné au KI (1 w.t%) et à la TEDA (5 w.t%) pour améliorer l'efficacité du piégeage des espèces iodées, en particulier dans des conditions humides. Malgré l'utilisation extensive des CA imprégnés au KI dans les réseaux de ventilation, un certain nombre de questions est resté non résolu, notamment en ce qui concerne la réactivité de KI basée sur un mécanisme d'échange isotopique. Dans ce contexte, cette thèse vise à étudier la performance des CA pour la rétention de CH_3I radioactif dans différentes configurations expérimentales, dans le but d'observer ce mécanisme avant de quantifier sa contribution dans un second temps.
Différentes combinaisons d'imprégnation du CA commerciale ont été utilisées dans le cadre de la thèse. Ces matériaux présentent une microporosité bien développée (V_{micro} / V_{pore} > 94%), avec un diamètre de micropore d'environ 0.5 nm adapté à la rétention de CH_3I par physisorption. En outre, les imprégnants avec la quantité attendue ont été trouvés localisés dans la porosité interne.
La performance des CA pour la rétention de CH_3I radioactif a été étudiée dans différentes configurations expérimentales. En utilisant des protocoles basés sur la détermination des DF (T = 20 °C, HR = 40% et 90%), l'affinité de l'adsorption d'eau par les CA imprégnés au KI conduit à la réduction des performances, en fonction de la teneur en KI, à HR = 40%. A HR = 90%, le mécanisme de rétention est gouverné par l'échange isotopique comme si 90% de la microporosité était occupée par des molécules d'eau. Une augmentation légère des DF a été ainsi observée après l'imprégnation au KI (DF~10). Une amélioration plus significative a été observée en présence de TEDA (DF~10^2), en raison de sa réactivité. A la lumière de ces considérations, le mécanisme d'échange isotopique semble être mis en évidence expérimentalement pendant la percée du filtre. En conséquence, de nouvelles méthodologies expérimentales ont été développées afin de mesurer les courbes de percée vis-à-vis de CH_3I stable ou radioactif en utilisant notamment les CA imprégnés au KI (T = 20 - 30 °C, conditions sèches). Une amélioration significative des performances du CA pendant la phase de percée est observée après l'imprégnation au KI. Une contribution relative due à l'échange isotopique d'environ 19% a été calculée pour une percée de 1% en utilisant un charbon imprégné à 5 w.t% en KI. Le dispositif expérimental développé pour les mesures en actif a ainsi permis de fournir des premiers éléments importants concernant la quantification de l'échange isotopique.

Mots clés : [iodure de méthyle radioactif, charbon actif, adsorption, échange isotopique, KI, TEDA]

[Evaluation of the contribution of the isotopic exchange mechanism to the removal of radioactive iodine]

Abstract:
The *nuclear grade* activated carbon (AC) is co-impregnated with KI (1 w.t%) and TEDA (5 w.t%) to enhance the trapping efficiency towards iodine species especially under humid conditions. Despite the extensive use of KI impregnated AC within the ventilation networks, scientific obstacles remain unsolved especially regarding the KI reactivity based on an isotopic exchange mechanism. In this context, this PhD project aims to investigate the AC performance towards the capture of γ-labelled CH_3I under different experimental configurations in order to identify this mechanism before its quantification for the trapping of the radioactive CH_3I.
Different impregnant combinations of the commercial AC were employed in this PhD project. These materials present well developed microporosity (V_{micro} / V_{pore} > 94%), with a micropore diameter of around 0.5 nm suitable for the retention of CH_3I *via* physisorption. Besides, the impregnants with the expected amount were found to be located within the internal porosity.
The AC performance towards the capture of γ-labelled CH_3I was investigated under different experimental configurations. Considering DF measurements (T = 20 °C, RH = 40% and 90%), the enhancement of water uptake by KI impregnated ACs leads to the reduction of performances as a function of KI content at RH = 40%. At RH = 90%, the adsorption mechanism was found to be governed by isotopic exchange reaction since 90% of the microporosity was occupied by water molecules. A slight increase of DF was observed after KI impregnation (DF~10). A more significant enhancement of the trapping efficiency was guaranteed thanks to the TEDA presence (DF~10^2). Based on these considerations, the experimental evidence of isotopic exchange mechanism seems to be observed during the filter breakthrough. In consequence, new experimental methodologies have been developed in order to measure both radioactive and stable CH_3I breakthrough curves for the KI impregnated AC (T = 20 - 30 °C, dry conditions). A significant enhancement of the AC performances during breakthrough phase is observed after KI impregnation. A relative contribution due to the isotopic exchange of about 19% was calculated at a $CH_3{}^{131}I$ penetration of 1%, when using an AC impregnated with 5 w.t% KI. The developed experimental setup for radioactive measurements has provided first important elements concerning the quantification of the isotopic exchange.

Keywords: [γ-labelled methyl iodide, activated carbon, adsorption, isotopic exchange, KI, TEDA]